This is to certify that the

dissertation entitled

AN EXPERIMENTAL STUDY OF
SOOT FORMATION AND OXIDATION IN
AXISYMMETRIC COUNTERFLOW DIFFUSION FLAMES

presented by

KEUNCHUL LEE

has been accepted towards fulfillment
of the requirements for

Ph. D. degree in Mechanical Engineering

Arvind Atreya
Major professor

Date December 6, 1991

AN EXPERIMENTAL STUDY OF SOOT FORMATION AND OXIDATION IN AXISYMMETRIC COUNTERFLOW DIFFUSION FLAMES

By

Keunchul Lee

A DISSERTATION

VOLUME I

Submitted to
Michigan State University
in partial fulfillment of the requirements
for the degree of

DOCTOR OF PHILOSOPHY

Department of Mechanical Engineering

1991

IN

The o

oxidation rate

products of c

flames. The

diffusion flar

an axisymme

This

of fuel: CH_4

counterflow

to 1500 K a

experiments

concentratio

To d

three pre-he

and H_2O on

amounts of

temperature

ABSTRACT

AN EXPERIMENTAL STUDY OF
SOOT FORMATION AND OXIDATION
IN AXISYMMETRIC COUNTERFLOW DIFFUSION FLAMES

By

Keunchul Lee

The objectives of this research are: (i) to quantify the formation, growth, and oxidation rates of soot in counterflow diffusion flames and (ii) to quantify the effect of products of combustion (primarily CO_2 and H_2O) on soot oxidation rate in diffusion flames. The technical approach is to conduct a detailed study on a basic unit of turbulent diffusion flame, that is, an one-dimensional laminar diffusion flamelet. For this purpose, an axisymmetric counterflow diffusion flame has been chosen.

This one-dimensional diffusion flame is stabilized between two opposing streams of fuel(CH_4 + inert gas) and oxidizer (O_2 + inert gas) by an unique high temperature counterflow diffusion flame burner. The burner is capable of preheating both streams up to 1500 K at low strain rate. This capability was utilized to conduct a sequence of experiments at pre-heat temperatures of 300 K, 900 K and 1200 K with reduced oxygen concentrations as low as 9.7 %.

To determine soot formation rate, a sequence of experiments was conducted at three pre-heat temperatures with constant fuel concentration. To study the effects of CO_2 and H_2O on soot oxidation, inert gas in oxidizer or fuel stream was replaced by measured amounts of CO_2 or H_2O. These concentrations were calculated to hold the peak flame temperature and the stagnation plane location unchanged. Thus, only the chemical effect

of CO_2 and H_2O

extraction techn

measured. PAH

hydrocarbons. A

The data

diffusion flame

reactions follow

energy for soo

measurements

aromatic hydro

soot destructio

introduced into

of CO_2 and H_2O on soot formation was investigated. Using a laser light scattering and extinction techniques, soot particle size, volume fraction and number density were measured. PAH concentration was determined using a blue-green LIF. Also, stable gases, hydrocarbons, and temperature profiles were measured across the flame.

The data was reduced according to the one-dimensional model for counterflow diffusion flame. This model postulates that the overall soot formation and oxidation reactions follows Arrhenius kinetics. These results showed that the overall activation energy for soot formation is 36 Kcals/mole within 10 % error. The chemical measurements also showed that the primary intermediate species consist of C_2 and aromatic hydrocarbons. It was also found that CO_2 and H_2O are very effective species for soot destruction in the flame. More soot particles are oxidized when CO_2 or H_2O are introduced into the input oxidizer stream.

To

my father Hyunkoo, and my mother Deukrae,
for their encouragement, faith and continual support
throughout my difficult days.

ACKNOWLEDGEMENTS

I would like to thank Dr. A. Atreya for providing me with the opportunity to perform this research and to continue my graduate studies under his direction. His suggestions and guidance were invaluable to the completion of this work.

Dr. A. Dhanak's contributions are gratefully acknowledged. The discussions we had were always enlightening. Specially, his encouragements while I had difficult time were grate helpful to overcome the difficulties.

The careful review of this thesis by Dr. I. Wichman, Dr. Lay, Dr. J. R. Lloyd , and Dr. R. Wasserman is greatly appreciated. The skillful efforts of Mr. L. Eisele and Mr. R. Rose in construction of the burner and optical table are also appreciated. The assistant I received from Dr. Z. Chao and Mr. K. Miller was instrumental to completion of this work.

Finally, I wish to thank my father, and mother for their support, patience and understanding while in graduate school. Also I thank my wife Dukwon, son Sungro and daughter Yunwha for their endless love and understanding. I could not have completed this endeavor without their help and encouragement.

Table of Contents

LIST OF TABLES

LIST OF FIGURES

Figure 4-40

Figure 4-41

Figure 4-42

Figure 4-43

Figure 4-44

Figure 4-45

Figure 4-46

Figure 4-47

Figure

Figur

Figure D-16

Figure D-17

Figure D-18

Figure D-19

Figure D-20

Figure D-21

Figure D-22

Figure D-23

Figure D-24

Figure D-25

Figure D-26

Figure D-27

Figure D-

Roman Le

A_{cor}

A_p

$B(\varepsilon)$

$C(\varepsilon)$

C_p

C_t

C_{tm}

C_{vm}

c

D

D_{CE}

D_{ε}

$D_{\varepsilon\varepsilon}$

$D_{\varepsilon\xi}$

$D_{\xi\xi}$

D_{ε}

dA

dA_p

d_p

d_{ε}, d_{ξ}

dV

E_p, E_O

$F(\theta)$

F_{ε}

$f(A_p)$

f_{ε}

h

I

I_b

I_{ε}

I_{ξ}

K

K_B

K_m

NOMENCLATURE

Roman Letters

A_{coh}	Coherence area.
A_b	Cross sectional area of thermocouple bead.
B(c)	Particle concentration factor.
$C(\tau)$	Photon-autocorrelation function.
C_{pi}	Specific heat at constant pressure of i^{th} species.
C_s	Cunningham correction factor.
C_{sca}	Scattering cross section.
C_{ext}	Extinction cross section.
c	Particle concentration.
D	Soot particle diameter (*nm*).
D_{CE}	Kinetic diffusion coefficient.
D_{ij}	Binary diffusion coefficient.
D_M	Modal value of particle diameter, D.
D_{pq}	Generalized mean diameter and momentum ratio.
D_{SE}	Stokes-Einstein diffusion coefficient.
D_{Th}	Thermophoretic diffusion coefficient of soot particle.
D_t	Translational diffusion coefficient.
dA	Cross sectional area of incident beam.
dA_s	Apparent projected scattering area occupied by all scattering particles.
d_p	Particle diameter.
d_{p1},d_{p2}	Pinhole diameters.
dV	Control volume for scattering.
E_P, E_O	Activation energy of soot production and oxidation.
$F(\theta)$	Monochromatic energy flux scattered at angle θ.
$F_{b\text{-}i}$	Shape factor between thermocouple bead and surrounding surface.
f(A)	Spatial coherence factor.
f_v	Soot particles volume fraction. ($cm^3{}_{soot}/cm^3{}_{space}$)
h	Convective heat transfer rate.
I	Laser light intensity.
I_0	Incident laser light intensity.
I_r	Reference laser beam intensity attenuated only by gas.
I_s	Scattered intensity from the particles.
K	Optical constant.
K_B	Boltzmann constant.
K_{ext}	Extinction coefficient.

A
a
M
M
M
m
m
N
N
n
P D
P_s
Q
Q
Q_{in}
Q_{ex}
Q_m
q
q_{ex}
R
r
R
Re_D
T
T
t
u
ΔV
v
v_2
v_3
W_j
W
x
y
Z
Z_0 Z
z
z_n
z_0

k	Thermal conductivity.
l_m	The mean free path of the molecules in the medium.
M	The mass of particle.
M	The number of correlator channels.
M_j	Atomic weight of atom j.
m	Complex refractive index (= n - ik).
m_p	Mass of suspended particles.
N	Soot particle number density (particles/cm^3).
N	Total sample number.
n	The number of photons detected in a certain time interval.
$P(D)$	Particle size distribution function.
P_θ	Particle form factor.
Q	Monochromatic energy flux scattered at angle θ per unit solid angle from volume for unit incident energy flux.
Q	Heat release rate.
Q_{sca}	Scattering coefficient.
Q_{ext}	Extinction coefficient.
Q_{vv}	Scattering coefficient from vertically polarized scattered and incident light.
q	Amplitude of wave vector of the scattering fluctuation.
q_{rad}	Radiative heat loss from the thermocouple bead.
R	Universal gas constant.
r	Radial distance from the axis.
R_i	Molecular reaction rate of i^{th} species per unit volume.
Re_D	Reynolds number based on burner throat diameter.
T	Total experimental duration for dynamic scattering experiment.
T	Absolute temperature (K).
t	Time variable (seconds).
u	Velocity component in r-direction.
ΔV	Scattering volume.
v	Velocity component in z-direction.
v'^2	Turbulent intensity.
v_{di}	diffusion velocity.
v_i^j	Number of atoms of j in species i.
W_i	Molecular weight of i^{th} species in mixture.
x_i	Mole fraction of i^{th} species in mixture.
y_i	Mass fraction of i^{th} species in mixture.
Z	Lens focal length.
Z_F, Z_O	Normalized atomic mass fraction of fuel and oxygen.
z	Distance along the axis
z_{st}	Measured stagnation plane location.
z_{fl}	Measured flame location.

Greek L

α

ε

ε_i

ε_j

θ

λ

γ

$\vdots$

σ

Γ

τ

ν

υ

ρ

ρ_b

σ

σ_0

σ_0

ω or Ω

ω

$\vdots$

Greek Letters

α	Size parameter ($= \pi D/\lambda$).
ε	Turbulent momentum eddy diffusivity.
ε_0	Constant strain rate.
ε_b	Thermocouple bead emissivity.
θ	Scattering angle.
λ	Laser light wavelength.
λ	Thermal conductivity.
τ	Sampling time.
τ	Particle relaxation time.
ϕ	Azimuthal angle.
Γ	Linewidth of scattered light.
η	Medium viscosity.
μ	viscosity.
ψ	Similarity function.
ψ	Stream function.
ρ	Mass density of surrounding medium.
ρ_p	Particle density.
σ	Stephen-Boltzmann constant.
σ_0	Scattering cross section.
σ_0	Zeroth order of standard deviation in lognormal distribution.
ω or Ω	The solid angle subtended by the source at the detector.
ω	Vorticity.
ξ_i	Atomic mass fraction of ith species.

1.1

Chapter 1

INTRODUCTION

1.1 Introduction

The formation and emission of soot in combustion processes pose problems which have long concerned scientist and engineer alike. Soot emission from a practical combustion appliance reflects poor combustion conditions and, consequently, a loss of efficiency. Also, the particulate loadings of the atmosphere caused by soot released by these combustion processes with gaseous combustion products such as NO_x and hydrocarbons, has recently been recognized as extremely harmful to life by obscuring vision and creating respiratory problems.

On the other hand, soot particles in the flames play an important role in energy transportation by thermal radiation from diffusion flames in industrial furnaces and combustors. The presence of soot in the furnace flame promotes radiation and hence, the efficiency of heat transfer from the flame.

Natural gas diffusion flames are less radiative because very little soots are produced in these flames. This is the most disadvantage of usage of natural gas as a fuel. To promote radiation and hence the efficiency of heat transfer in the natural gas diffusion flames, it is necessary to increase the production of soot without emitting soot particles to the atmosphere.

Under these extremely opposed circumstances, the technical problem is to produce the maximum number of soot particles in such a way that all the particles can be completely oxidized before leaving the reaction zone. Thus, the goal of this research is to develop a quantitative understanding which will enable to control formation and oxidation rate of soot in natural gas turbulent diffusion flames.

1.2 Description of The Research

The aim of this research is to enhance radiative heat transfer from natural gas diffusion flames. As mentioned in previous section, to achieve this aim, it is necessary not only to increase the soot production rate in turbulent diffusion flames, but also to understand soot oxidation processes in these flames.

The particular objective of the present study is to experimentally quantify the formation, growth, and oxidation rates of soot in counterflow diffusion flames. These rates of soot in the diffusion flames were characterized by important factors in turbulent diffusion flames such as temperature, strain rates, and fuel and oxidizer concentrations. For the present study, the soot formation and oxidation rates was quantified for a single fuel of practical importance such as the widely used natural gas. As a fuel, methane was used because methane is a main species of natural gas. This is in contrast with previous studies where obtaining comparative results for fuels with different chemical structure was the primary objective.

It is hard to describe turbulent diffusion flame locally. It was found that the turbulent diffusion flame can be modeled by laminar diffusion flamelet which has a one-dimensional counterflow diffusion flame configuration. Details are discussed in Chapter 2. Therefore, in the present study, one-dimensional axisymmetric counterflow diffusion flames were used to measure characteristic factors of the soot in diffusion flame as well as chemical composition. It is also pointed out that this configuration is convenient for theoretical analysis because of the one-dimensionality.

Sooting structure of flames is very complex. Sooting process can be described by the result of integrated complex chemical processes. Soot production, for example, is reduced as a result of the reduction of oxygen concentration. This does not mention that this soot reduction purely comes from the reduction of oxygen concentration. Because, the different oxygen concentration in flame may changes flame temperature, concentration of combustion products, and even strain rates. It is difficult to identify

single

affecte

combu

T

fore,

this p

need

focu

single effect on the sooting process in the flame. Sooting process of flames can be affected by temperature, fuel and oxygen concentrations, strain rate, concentration of combustion products, etc.

To understand this complicate sooting process and structure of flames, it is, therefore, very advantageous and important to isolate these effects one to the others. For this purpose, an **ideal set of experiments** were designed. These are:

(i) **Soot nucleation and growth (fuel pyrolysis and coagulation)** : This set of experiments is conducted with hot fuel gas (methane) flowing against hot inert gas (N_2) to achieve temperatures at the stagnation plane that are close to the flame temperatures without a flame. Fuel concentration and the fuel and inert stream temperature are used as variables.

(ii) **Soot oxidation by products of combustion** : Part of a hot inert gas is replaced by known concentration of CO_2 and H_2O without changing the flame temperature and the strain rate from experiment (i). The difference between the results of the two experiments (i and ii) provides a quantitative of soot oxidation by major products of combustion. The concentration of CO_2 and H_2O are used as variables.

These ideal experimental conditions are difficult to achieve because the materials needed for building such a burner are not easily available. Thus, initially attention was focused on the following two sets of experiments:

(i) **Determination of soot formation rates** *: To accurately determine the structure of a sooty flame, very low strain rates (2 ~ 3* sec^{-1}*) were used. A set of experiments were performed where an initial sooty flame, which is established by high fuel concentration and low oxygen concentration, with no pre-heat was chosen for the investigation. In subsequent experiments, the oxygen concentration is decreased while increasing the pre-heat temperature to approach a pure sooting flame without oxidation. The oxygen*

concentration was reduced by replacing with nitrogen without significant changes in strain rate and maximum temperature in the flame. The fuel concentration was maintained constant for all experiments. Analysis of these experiments yield the overall soot formation rate and the sooting structure of the diffusion flame with minimum interference from soot oxidation.

(ii) **Determination of soot oxidation rates** *: It is important to understand soot oxidation by main species of combustion products such as* CO_2 *and* H_2O*, because these are the main species in the zone where soots are produced. This set of experiments were performed to verify the* CO_2 *and* H_2O *effects on the soot oxidation rate. Analysis of these experiments will be helpful to determine the effect of exhaust gas recirculation. Experiments were also performed to determine which stream is more effective for these species to be added on the soot oxidation rate. These species pass through a very high temperature zone (~ 2000 K) before reaching sooting zone when they are introduced into oxidizer stream, and they are diffused into sooting zone from the fuel side of stagnation plane when they are introduced into fuel stream.*

Soot particles in the flames can be characterized best by volume fraction f_v (cm^3 of soot/cm^3 of space), number density N (counts/cm^3), and the size of soot particle D (nm). The particles are not uniform in size. Therefore, size distribution of soot particles can also be a parameter which determines the soot volume fraction and the number density. Usually, However, that is relatively narrow. So, some reasonable distribution functions can be used for characterization of the particles at certain position in the flame. From a mechanistic point of view, it is most convenient to consider the soot volume fraction, number density, and particle size as independent variables in the process. These three independent variables are related to each other. Accordingly, if

two of these three are known, the last one can be calculated easily.

To measure these characteristic properties, soot volume fraction, number density, and particles size in a one-dimensional counterflow diffusion flame, it is clear that a very special burner, which can provide a axisymmetric counterflow diffusion flame at high pre-heating temperature, and instrumentation are needed. An ideal axisymmetric counterflow diffusion flame burner was designed and constructed. For the measurements, both intrusive and non-intrusive techniques were employed to measure all the parameters necessary for the present study in the flames. Temperature profile and gas composition were measured by intrusive methods. Temperature was measured by a fine wire thermocouple, and gas composition was measured by a gas chromatograph with a quartz microprobe for gas sampling. A Perkin-Elmer gas chromatograph (model 8500) was employed to measure the concentration of stable species and the light hydrocarbons.

Soot fields were measured by a laser light scattering and extinction optical system. For measuring soot particle size, the dynamic light scattering technique is employed while the classical light scattering/extinction technique is used to determine the particle size, volume fraction, and number density. The details of the apparatus employed are explained in chapter 3 and appendix C.

1.3 Structure of The Thesis

In chapter 2, previous work is reviewed. This includes the review of literature on sooting structures of flames as well as a review soot measurements methods.

Chapter 3 initially describes the burner used in the present study. The axisymmetric counterflow diffusion flame burner has been designed and constructed based on the theoretical calculation and model testing. In section 3.1.1, the requirements of the burner is discussed. Following sections (3.1.2 and 3.1.3) show the results of calculations and model tests for guide flanges. The details of the calculations and model test

are attached in appendix A. The final configuration of the burner and its validity are discussed in section 3.1.4. The heating capability to preheat the inlet gas streams is also discussed in this section. The buoyancy effect in the diffusion flames without pre-heat is also discussed in the section 3.1.5. Since the laser beam location was used as a fixed reference position, Burner has to be capable to move with respect to the laser beam. The burner traverse systems can be found in section 3.1.6. The last section of this part (3.1.7) summaries the burner configurations.

Rest of chapter 3 shows all measuring apparatus and instrumentation used for this research. Apparatus for gas composition measurement are explained in section 3.2. Microprobe, sampling system and method of gas analysis can be found in this section.

Soot field measurements is described in section 3.3. Laser light scattering and extinction measuring equipments and theory for soot field measurement are explained in section 3.3.1. The last part of this section (3.3.2) shows the Laser Induced Fluorescence (LIF) measurement method for Polycyclic Aromatic Hydrocarbon.

Experimental procedures and results are discussed in Chapter 4. This chapter is divided into several parts. First, for experimental procedures is described in section 4.1. This is followed by the measurement methods, data collection and experimental results (4.1, 4.2, 4.3 and 4.4). This chapter also explains the measurement error and error analysis in section 4.5.

In Chapter 5, to analyze the results discussed in chapter 4, the equations for soot field are derived. Parameters are calculated using proper constants and properties. The calculation results based on the Arrehnius form are also discussed.

Chapter 6 concludes this research work. Recommendations for the future work are in this last chapter, too.

Chapter 2

LITERATURE SURVEY

2.1 Diffusion Flames and Sooting Structure

Diffusion Flames

Gaseous fuel flames are commonly divided into two classes, the premixed flame and the diffusion flame. In the premixed flame, the fuel and the oxidizer are premixed, and then the combustible mixture enters into the reaction zone. The final combustion state and the flame characteristics of premixed flame can be determined uniquely with the specifications of chemical and physical conditions of the combustible premixed gases. In the diffusion flame, on the contrary, the fuel and the oxidizer enter the reaction zone separately and are then mixed at the zone where the reaction takes place. The diffusion flame exists at the interface between the fuel and the oxidizer.

Turbulent diffusion flames, which are concerned in this research, are increasingly being viewed as an ensemble of laminar diffusion flamelets (Williams, 1975; Peters, 1983, 1984). In the neighborhood of the reaction zone where soot is being formed and oxidized, turbulent diffusion flames constitute of laminar diffusion flamelets. Figure 2-1 schematically shows the large scale vortices that are formed in the shear layer separating the fuel and the oxidizer streams. Locally, in these vortices, the burning occurs in the little flamelets that exist at the highly convoluted and strained stoichiometric interface between the two streams.

The structure of the diffusion flame has been studied over six decades since the first successful analysis by Burke and Schumann in 1928. They employed flame sheet model. Since the flame sheet model is based on the assumption that the chemical reaction rate in a diffusion flame is infinitely fast, it has been extensively used for theoretical studies. Using this model it becomes possible to calculate the location and the

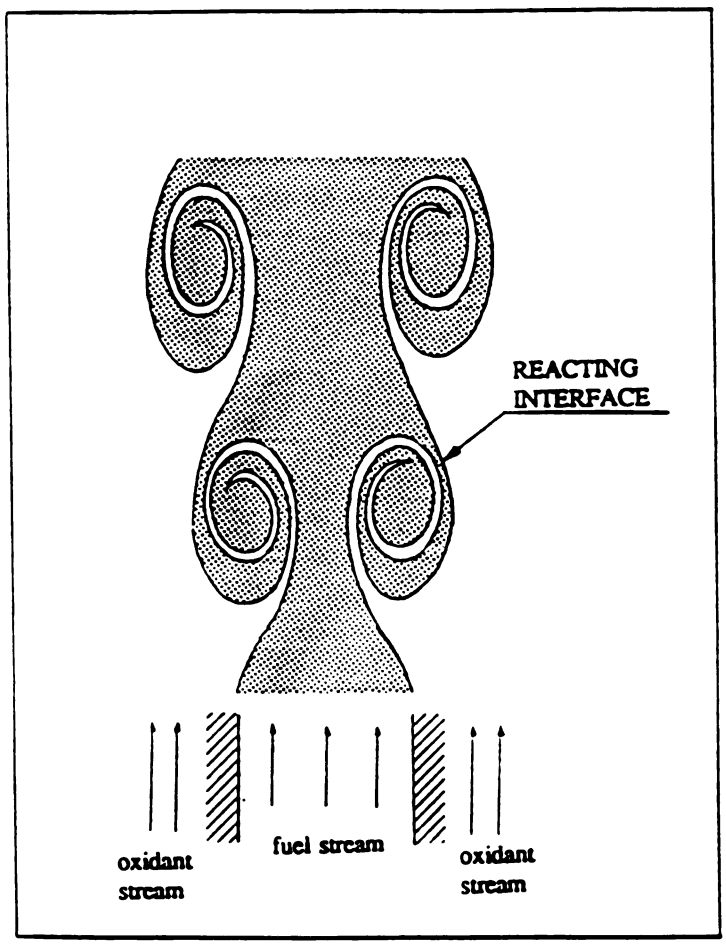

Figure 2-1 Model of laminar diffusion flamelet in turbulent diffusion flame.

shape of the flame, the rate of heat transfer to a solid or a liquid surface, and the burning rate of the fuel.

For the studies of diffusion flames, coaxial coflow diffusion flames and flat coflow diffusion flames have been used. A coaxial diffusion flame can be established when a fuel gas is ejected from a cylindrical tube into a quiescent oxidizer or an oxidizer flow (Smith & Gordon, 1956; Roertgen & Botendahl, 1975; Mitchell, Sarofim, & Clomburg, 1980), and a flat diffusion flame can be established in the boundary region between parallel flows of the fuel and the oxidizer (Parker-Wolfhard burner)(Wolfhard & Parker, 1949; Melvin, Moss, & Clarke, 1971; Smyth & Miller, 1987). In these

flames, however, there is a dead space near the rim of the burner where the flame is not established due to the heat loss and quenching of active radicals at the wall. Therefore, direct inter-diffusion of the fuel and the oxygen occurs in this dead space, producing a small region of premixed gas at the base. Consequently, the characteristics and structure of this type of diffusion flames can be easily affected by this premixed gas.

Wey, Powell, and Jagoda (1989), as an example, investigated the effect of a small amount of oxygen in fuel flow on soot formation in the diffusion flames. Their result showed that even the basic processes of soot formation in a diffusion flame remain valid when small amount of oxygen is introduced to the fuel flows, the soot loadings increases far beyond what would be expected by considering the resultant rise in temperature only.

In these coflow diffusion flames, the conditions along the streamlines may not be same. The profiles of temperature, species concentration, and the time to reach the same distance from the burner (retention time) may be different along different streamlines. This implies that the soot particles may have different formation, growth, and oxidation rates if they flow through different streamlines.

Therefore, the laminar diffusion flame on the coflow burner is thought to be unsuitable for the study of the fundamental processes of the soot formation and oxidation in the diffusion flames.

A pure diffusion flame can be established in the zone of impingement of two opposed gaseous flows of fuel and oxidizer (Spalding, 1961; Liñán, 1974; Carrier, Fendell, & Marble, 1975; Hahn & Wendt, 1981a; Lin & Sohrab, 1987). Such a flame is called the counterflow diffusion flame. Figure 2-2 shows the schematic of the counterflow diffusion flame. This counterflow diffusion flame provides a suitable method to study a pure diffusion flame. This geometry can create a reaction zone or a diffusion flame without premixed gas zone in coflow diffusion flame, and hence, no

premixed characteristics involves in this diffusion flame (Hahn & Wendt, 1981a; Tsuji, 1982).

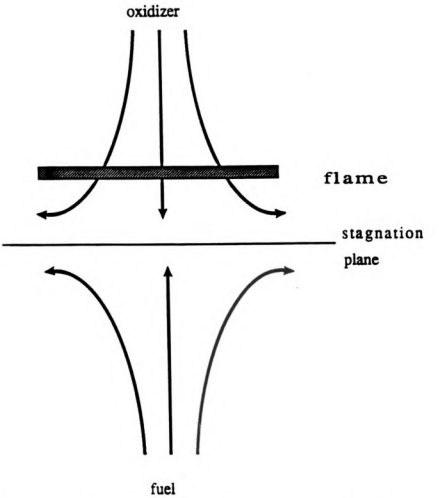

Figure 2-2 Schematic of the structure of one-dimensional counterflow diffusion flame.

Most diffusion flames have two or three dimensional configuration. Thus, it is very difficult to analyze them mathematically. The counterflow diffusion flame, on the other hand, is one-dimensional in temperature, gas concentration, and soot field although two dimensional in velocity and pressure. This one-dimensionality is the biggest advantage in using the flat counterflow diffusion flame. Therefore, for the present research, the axisymmetric counterflow diffusion flame was used to study soot formation and oxidation in diffusion flame.

Sooting Structure in Diffusion Flames

Despite the proliferation of research on soot formation in recent years, a reliable quantitative method for determining the overall rate of soot formation and oxidation is not currently available. In the combustion process, soot usually forms and grows in the temperature range from 1300 K to 1700 K. The total amount of soot formed in the flames is always very small compared to the amount of carbon present in the fuel consumed, and the time available for the soot formation process is of the order of a few milli-seconds. Soot particles looks black and consists mainly of carbon and also contains up to about 10% hydrogen by volume even more when it is young. More detail of physical characteristics of soot can be found elsewhere (Palmer & Cullis, 1965).

Sequential and overlapping steps of soot formation and oxidation have been investigated by numerous researchers. But explanations of soot generated in the combustion process are not uniquely defined in hydrocarbon diffusion flames. As a results of these numerous investigations, the soot formation process in hydrocarbon diffusion flames can be described by a series of distinct steps (Glassman, 1987), which are (i) a fuel pyrolysis, (ii) the production of precursor molecules. (iii) growth which forms numerous small primary soot particles (soot particle nucleation), (iv) particle surface growth, and (v) particle oxidation process (Soot oxidation process may not be a separated process. Soot may be oxidized in any stage of processes in the diffusion flames).

These processes can be briefly described qualitatively.

Particle inception

The first step, called particle inception, is generation of soot seeds from the fuel pyrolysis. Various hypothesis to explain this stage have been made. Haynes and Wagner (1981), for example, suggested that precursors are acetylenic in character and that these acetylenes polymerize and go through a cyclization process to form the virgin soot particles. Since this radical process mechanism involves fuel pyrolysis and

thus depends on chemical structure of the fuel, This mechanism would appear to be slow but to be consistent with experimental observations of soot formation. For the rapid production, Calcote (1981,1983) investigated ions in the flame as major particles of soot precursors. He postulated that molecular ions lead to the formation of soot nuclei. So, number of ions in the flame was used to obtain the rate of soot formation in his research.

It is noted that recent investigations (Homann, 1978; Bertrand & Delfau, 1985; Saito, Williams & Gordon, 1986) have suggested that ionic species do not play a major role in the soot formation processes. However, alternating electric fields have been found to promote soot formation in coflow diffusion flames (Mizutni & Nakahara, 1984). For same explanation, for the rapid soot production, Frenklach, David, and Gardiner (1988), proposed a model which suggested that the precursors are acetylene and its higher analogs ($C_{2n}H_2$), as well as polycyclic aromatic hydrocarbons. These precursors are very small particles in size ($1 \sim 3nm$) and are created in large numbers. Even though these soot precursors are created in large numbers, soot loading is very low because of their small sizes.

These precursor species are then combined as the nucleation reaction proceeds to form the condensed phase material and subsequent absorption of high molecular weight hydrocarbon compounds. The mechanism to form incipient soot particles is not well understood.

Surface growth

These incipient soot particles grow through two different mechanisms. Particles grow by attachment of gas phase species to the surface of the particle phase, known as surface growth. Growth by surface reactions leads to an increase in the volume fraction while number of soot particles remains constant. On the other hand, particles grow by coagulation when the particles collide and coalesce or by agglomeration when the particles combine to form a chain-like configuration. This growth decreases the number

of soot particles while the volume fraction remains constant. These two different mechanisms of soot particle growth makes the flame soot rich.

Soot oxidation

In general, the soot particles that form and grow in flames are, generally speaking, followed by soot oxidation where the soot is burnt in the presence of oxidizing species to form gaseous combustion products. The emission of soot particles from the furnaces and the combustors depends on the balance between the rates of the formation and the oxidation in flames. From the results of present study, oxidation process may occur in any stage of sooting processes.

Most experimental work on soot formation in diffusion flames has investigated overall effects using two or three dimensional flames. The general complexity of the temperature, species, and flow field in these diffusion flames makes it difficult to identify and control the separate parameters which influence soot formation and oxidation.

Fuel species, flow rate, and temperature effects on soot formation

An overall measure of sooting tendency is the gaseous fuel flow rate or flame length of a round laminar jet flame which is at the verge of smoke emission (the smoke point). Fuels with a high sooting propensity produce smoke at low flow rate and short flame length, whereas, low sooting fuels require higher flow rates or longer flame length to emit smoke. The causes for the differences in smoke points between fuels have been examined by Schug, Manheimer, Yaccarino, and Glassman (1980) and Glassman and Yaccarino (1981) in terms of fuel C/H ratio and adiabatic flame temperature. Schug *et al.* (1980) determined that the sooting tendency does not correlate with fuel C/H ratio. Glassman and Yaccarino (1981) found that the C_4 and C_5 olefins show the greatest tendency to soot and that acetylene's great sooting propensity is due entirely to its high flame temperature and not its structure. Kent and Wagner (1984) reviewed temperature and fuel effects on sooting in diffusion flames. They pointed out

in conclusion that fuel structure is an important parameter on soot formation as well as temperature. Roper (1984) added that the effect of buoyancy on the flame gas residence time should be considered in the soot formation.

More accurate measurement techniques, such as laser light scattering and extinction measurements, have made great contributions to soot formation studies. Using this method, Santoro, Semerjian and Dobbins (1983a, 1983b) studied the early particle formation region. In addition, Santoro and Semerjian (1984) examined the effects of fuel flow rate, fuel species and temperature on the soot particle formation in coflow diffusion flames. This study showed that the temperature exerts the strongest influence on soot formation.

Recently, the effect of the strain rate on soot formation in diffusion flames has been examined. Vandsburger, Kennedy, and Glassman (1984) measured soot particles in counterflow diffusion flames with four different oxidizer flow velocities. This experimental work showed that soot volume fraction and the final aggregate size reduces as the oxidizer flow velocity increases. And the number density of soot particles does not vary within velocity range they used. Maximum particle size decreased with increasing oxidizer velocity. This can be explained by examining the soot residence time in the flame. The longer the residence time in the flame, the more the soot volume fraction and the bigger the soot particles form.

The flames with different fuel flow rates are examined by Santoro, Yeh, Horvath, and Semerjian (1987). They observed that large flow rate increases the amount of soot because of the increase in residence time in the annular region of the bigger flame. Also it increases the cross-sectional area and thus in the total amount of soot formed. From this study it is pointed out that there was no significant increase observed in the soot formation rates as a result of increases in the fuel flow rate. Temperature profiles were also examined along the streak lines through the annular region following soot particle formation. In this measurement, the oxidation process begins sooner in the low

flow rate flames, and results in higher temperature at the later stages of the flame. These higher temperatures results in more rapid oxidation of the soot particles in coflow diffusion flames. As the flow rate increases, the amount of soot present increases thus the lower temperatures observed in the oxidation zone because of soot radiation loss. Results reduces the soot oxidation rate.

Most of soot formation and oxidation research has concentrated to isolate various effects from one another. Since soot formation and oxidation is a part of complex chemical and physical reaction processes, the isolation is one of the major tasks not only in soot formation and oxidation research but also in flame research. Axelbaum, Flower, and Law (1989) investigated the effects of dilution and temperature on soot formation. During this experimental work, the effect of fuel dilution and flame temperature are isolated by adding inert to the fuel and oxidizer streams. Flames with different maximum temperatures but the same fuel concentration are used for examination of temperature effect, and flames with different fuel concentrations but the same maximum temperature are used for examination of fuel dilution effect on soot formation and oxidation. This experimental work concluded that the soot volume fraction and the total available surface area vary linearly with initial fuel concentration, and that the specific surface growth rate does not depend on the fuel concentration. It was also found that temperature effect is significant on the soot formation rate. In this experimental work, changes in mass flow rate, which can be changed from the replacing nitrogen by argon, were not concerned.

The influence of addition of oxygen into fuel-side on soot formation in Bunsen diffusion flames has been studied by many authors (Dearden & Long, 1968; Jones & Rosenfeld, 1972; Wright, 1974; Schug et al, 1980; Saito *et al.*, 1986b). In a recent study on methane diffusion flames (Saito *et al.*, 1986b), it was found that addition small amounts, 3% by volume, of oxygen to the fuel side of the flame had negligible effect on methane pyrolysis and soot formation. Relatively much less has been known

about the possible effects of oxygen concentration in oxidizer stream on the soot formation in laminar diffusion flames. Thus far, the extent of the thermal versus chemical influence of oxygen addition into the fuel or the oxidizer stream on soot formation in diffusion flames is not fully understood (Tien & Sohrab, 1990).

2.2 Soot Measurements Methods

Soot particles formed in flames can be studied from measuring them by certain method such as measurement of sooting height or measuring soot particles using laser light scattering and extinction technique. Measuring soot particles in flame is one of main difficult task, because the physical and chemical structure of soot particle is very complex. Soot particles are not unique in chemical point of view. The soot particles are compound of mainly C and H. The shape of soot particles is also not unique. Even individual soot particle which is a part of agglomerated soot particle or a part of chain-like soot particle, is nearly sphere, the shape of the soot particle may be varied along the residence time and its location. These variations of soot particle imply that chemical, physical, and optical properties of soot particles can not be uniquely defined. Therefore, the examination of the measurement method might be very important to measure soot particles and then to understand the insight of soot formation and oxidation in flame.

Sooting height measurement

For the candle type flames, sooting height measurements are common methods to measure sooting trends. Sooting height measurement method has contributed much to the understanding of soot tendency along fuel structures and flow rates qualitatively. This method uses to measure overall or integrated sooting effects of the flames. So, the weak point of this method is that local value of parameters for soot particles can not be measurable.

Intrusive measurement

Direct sampling, as an intrusive technique, are employed to measure the soot field locally in diffusion flames. Direct sampling of the particles has appeared in several forms but the questions related to the validity of the morphological observations make this method hard to be used. Some of direct sampling methods are based on the fact that soot deposition rates on the cold target surfaces immersed in the flames are dominated by particle thermophoresis. These collected particles on the cold surfaces are analyzed under electron microscopy (Jacoda, Prado & Lahaye, 1980; Neoh, Howard & Sarofim, 1984; Prado, Jacoda, Neoh & Lahaye, 1981; Skolnik & McHale, 1980). In this methods, soot particles may be altered when the soot particles are caught by the cold surface. The flame condition around the cold sampling surface, where soot particles are taken, may be altered because of the existence of the cold surface.

Another method consists of using a sampling orifices (Chippett & Gary, 1978; Prado, Lee, Hites, Hoult & Howard, 1977) to collect the particles from the interior of the flame and subsequently to analyze them through electron microscopy technique. These methods, however, involve a few steps which aim at the separation of the sampled particles from the combustion gases withdrawn from the flame. These steps may affect the particle morphology, thus causing a degree of uncertainty of the results obtained using these methods.

Laser light scattering/extinction measurement

Recently laser light scattering and extinction technique has been used for more accurate and *in-situ* measurement of particles in the flames. Initially Millikan (1961, 1962), and Kunugi and Jinno (1967) employed this light scattering technique to measure soot field in flames. The more laser light scattering and extinction measurement techniques were subsequently employed for an *in-situ* analysis of the soot field. These methods have considerably appeal because they are non-intrusive and allow

observation of the soot without intervening in the physical and chemical processes which are present in the flames.

Soot refractive index is strong factor to extract information of soot in the flames from the laser light scattering and extinction measurement. Data for the refractive indices of soot particles in both the visible and infrared wavelength have been obtained by a number of investigators (Dalzell & Sarofim, 1969; Bockhorn, Fetting, Meyer, Reck & Wannemacher, 1981; Lee & Tien, 1981; Charalampopoulos & Felske, 1987). Various combinations of experimental techniques and data reduction schemes have been employed and a fairly wide range of indices have been reported.

Dynamic light scattering measurement

To compensate for this complex problem, the dynamic scattering measurement is being developed to determine the soot particle sizes. This technique measures the fluctuations intensity in the scattered light signal due to the Brownian motion of the soot particles. Initially this method was accessible as Diffusion Broadening Spectroscopy and later, as Photon Correlation Spectroscopy. This method relies on the statistical study of the fluctuations in time of the light scattered by the particles, and particle size can be calculated by the total scattered intensity correlation function. Penner, Bernard, and Jerskey (1976a, 1976b) demonstrated the feasibility of this method for soot particles in C_2H_4/O_2 flat flame. Since this method does not strongly depend on the soot refractive index, more investigation have been made for the soot particle size measurement (Chowdhury, Sorensen, Taylor, Merklin & Lester, 1984; Lhuissier, Gouesbet & Weil, 1989).

Chapter 3

EXPERIMENTAL APPARATUS

The objective of the present study is to quantify soot formation and oxidation rates in a counterflow diffusion flame as a function of temperature, strain rate and fuel and oxidizer concentrations. These variables are important for characterizing the diffusion flame. To enable independent control of temperature, fuel and oxidizer concentrations and to obtain very low strain rates, a special ceramic burner was constructed. In addition, instrumentation is employed to measure temperature, species concentrations, and soot field. This burner and instrumentation are described in this chapter.

Among the equipments, the burner is the most important because the burner will provide the flame which will be measured by various instruments. The high temperature axisymmetric counterflow diffusion flame burner was designed and built to meet the experimental requirements described in section 3.1.1. Design of this burner was guided by two-dimensional numerical calculations of streamlines and later a full scale Plexiglass model was tested in sugar water to increase viscosity and to reduce Reynolds number. Further details are provided in the following sections of this chapter and in appendix A.

Measurement methods are very important in experimental research. Gas composition, temperature profile, soot, and polycyclic aromatic hydrocarbons (PAH) in counterflow diffusion flame were measured for the present work. The equipments and methods are described for each measurement in later sections in chapter 3.

3.1 Axisymmetric Counterflow Diffusion Flame Burner

3.1.1 Requirements for the Burner Design

A high temperature axisymmetric flat diffusion flame burner was constructed to establish flames desired to perform experiments. To satisfy the objectives of the present study, the burner was required to have following capabilities (i) capability of creating an ideal stagnation point flow over large enough area to guarantee one dimensionality, (ii) capability of delivering a uniform slow velocity flow to enable increase the reactant residence time as long as possible, (iii) capability of providing large burner gap to enable increase measurement resolution in the low velocity flow field without any flame distortions, and (iv) capability of heating fuel and oxidizer streams before injected into the reaction zone.

Several different types of counterflow diffusion flame burners have been used in flame research. These burners can be divided into two groups (Tsuji, 1982). In the first group of burners, the flame is established at the interface between a fuel and an oxidizer streams directed each other. A flat axisymmetric diffusion flame is created between the two gas injectors (Hahn & Wendt, 1981a; Puri & Seshadri, 1987). In the second group of burners, the flame is established around a porous sphere or a porous cylinder through which fuel gas is injected into a uniform oxidizer flow (Vandsburger, Kennedy, & Glassman, 1984; Axelbaum, Law, & Flower, 1988).

Among these two types of counterflow diffusion flame burners, axisymmetric counterflow diffusion flame burner (first group) was chosen to study soot formation, growth and oxidation, because it provides a flat diffusion flame, which is one-dimensional in temperature, gas concentrations, and soot fields. Thus, a one-dimensional mathematical model can be used to analyze the experimental results.

To increase measurement resolution, it is advantageous to expand the reaction zone by increasing the reactant residence time. This must be accomplished while maintaining the flow field close to an ideal stagnation point flow. To increase residence

time, it is necessary to maintain low velocities. However, at low velocities, the diffusion flame is easily affected by outside or buoyancy disturbances. Thus, it is desirable to have a burner capable of providing a stable one-dimensional flat diffusion flame in ideal stagnation point flow at very low velocities of order 10 *cm/sec* or less.

Reactant residence time can be also increased by enlargement of the burner gap as well as maintaining low velocities. In the large burner gap with low flow velocities, the stagnation point flow may be distorted easily by outside disturbance and hence the flame becomes unstable. Guide flange was designed and constructed for the burner to provide larger gap without flow distortion and to establish a stable flame. The shapes of the guide flange are calculated based on the Navier Stokes Equations.

The *in-situ* measurements of temperature, species concentrations and soot field should be accomplished for the present study without any disturbances. But the measuring devices in flame are limited in their sizes. And gas flow rate can be controlled more accurately when the flow rate is larger because of limitation of sonic nozzles described in section 4.1. Also, for soot absorption measurements, as well as one-dimensional, the large diameter of flame (>5 *cm*) is needed. Therefore, the size of burner and hence the flow rate was required as large as possible.

To enable soot formation study to be executed in different pre-heat temperature, the burner was required to have capability of pre-heat the fuel and oxidizer streams. The temperature of the pre-heated gas should be uniform along the radial direction. For the fuel stream the pre-heat temperature should be lower than the temperature fuel pyrolyzed. For the oxidizer stream it is desirable as pre-heat temperature as high as possible to enable increase the average temperature of fuel and oxidizer streams.

3.1.2 Model Calculations

The primary target of this burner set is to provide a diffusion flame in the ideal stagnation point flow, and hence one-dimensional flat diffusion flame in the large burner gap without any disturbances. Most of disturbances in the counterflow diffusion flame come from the draft flow around the burner gap and from the flow separation around gas injection tubes.

The flow separation around injection tube may cause temperature short circuit so that the one-dimensional temperature profile along axial direction can be disturbed. Also, this flow separation can cause rotating flow, thus, create velocity components in the radial direction, r, the circumferential direction, ϕ, and axial direction, z. This will make the problem complex. Therefore, it was investigated the shape of the flow guide flange to create flow pattern close to an ideal stagnation point flow in large burner gap with low flow velocity.

Due to the lack of literature on the stagnation point flow, the best way to determine the flow guide flange shape was through experiments. But experiments are so limited. Therefore, a combination of numerical calculation and experiment was used to determine the optimized flange shape.

To calculate streamlines, velocity, and pressure field, steady, incompressible Navier-Stokes equations were employed for the observation area. In the absence of body forces, the dimensionless axisymmetric equations in the vorticity-stream function can be written as (Atreya, Lee, and Foss, 1987):

$$r\left[\frac{\partial(u\,\omega)}{\partial r}+\frac{\partial(v\,\omega)}{\partial z}\right]=\frac{2}{\mathrm{Re}_D}E^2(r\,\omega) \tag{3.1}$$

and

$$E^2(\psi)=2r\,\omega \tag{3.2}$$

where r and z are coordinates of radial and axial direction, respectively. ψ is stream

function and ω is vorticity. Re_D is Reynolds number based on the burner throat diameter. The velocity components of $r-$ and $z-$ directions are:

$$u = \frac{1}{2r}\frac{\partial \psi}{\partial z} \tag{3.3a}$$

$$v = -\frac{1}{2r}\frac{\partial \psi}{\partial r} \tag{3.3b}$$

respectively. And the operator

$$E^2 \equiv \left[\frac{\partial^2}{\partial r^2} - \frac{1}{r}\frac{\partial}{\partial r} + \frac{\partial^2}{\partial z^2} \right]$$

Boundary conditions are

$$\begin{aligned} &\psi = 0 && \textit{on the stagnation plane} \text{ and } \textit{along the } z\textit{-axis}, \\ &\psi = 1 && \textit{along the flange surface}, \\ &\frac{\partial \psi}{\partial r} = 0 && \textit{along the inlet} \text{ and } \textit{outlet}. \end{aligned} \tag{3.4}$$

The origin of cylindrical coordinate system is fixed to the stagnation point and Equations (3.1), (3.2), and (3.3) are solved in the domain for different shapes of the boundary which means the different flange shapes.

Finite difference method was employed for these numerical calculations. Since the boundaries have irregular shapes, it is necessary to transform the boundaries from a Cartesian coordinate system to nonorthogonal coordinate system which is fit to the irregular boundaries. For the calculation, body fitted coordinate system (Thompson, Thomas, & Mastin, 1974; Thompson, Warsi & Mastin, 1982; Anderson, Tannahil & Pletcher, 1984) was adopted. This body fitted coordinate system is very useful to transform various shape of the flange to the Cartesian coordinate system. This transformation improves accuracy of calculation along the boundaries, and hence reduces experimental trials.

Stream lines for three different flange shapes were calculated by the above numerical methods. Further details of numerical calculation are presented in Appendix A. Based on the calculation results, the flange shapes were modified and full-scale Plexiglass burner models were constructed and tested.

3.1.3 Model Testing

A set of full-scale Plexiglass burner models was built to obtain very low Reynolds number flows that correspond to the hot gas flow. A schematic of the experimental apparatus is shown in Figure 3-1. Water flows from two separate bottles into the upper and lower parts of the apparatus. The flow rate is controlled by flowing metered amounts of N_2 into the water bottles from a pressurized cylinder. Figure 3-2 shows the test section of this apparatus. Dye is injected into the flow for flow visualization purposes. The various injection ports are also visible in this photograph. Timed photographs of dye particles are taken to determine the flow velocities. Three different flange shapes and three different burner gaps were examined along the very low Reynolds numbers. The Reynolds number was varied by changing the flow velocity and the viscosity of water by adding sugar. Further details of model testing are described in Appendix A.

Thus, it may be concluded for the burner design that a stable unseparated flow can be obtained for (i) burner gap of at about 2.54 *cm*; (ii) Reynolds number of about 30, which corresponds to a hot gas velocity of 3.0 *cm/sec*; and (iii) ideal inviscid flow regime extending over diameters as large as 7.62 *cm*. Based on these investigations, the burner was designed and constructed.

3.1.4 The Burner Configuration

A burner has been designed to satisfy the requirements mentioned in section 3.1.1. Figure 3.3 shows the schematic of the burner system. The burner system

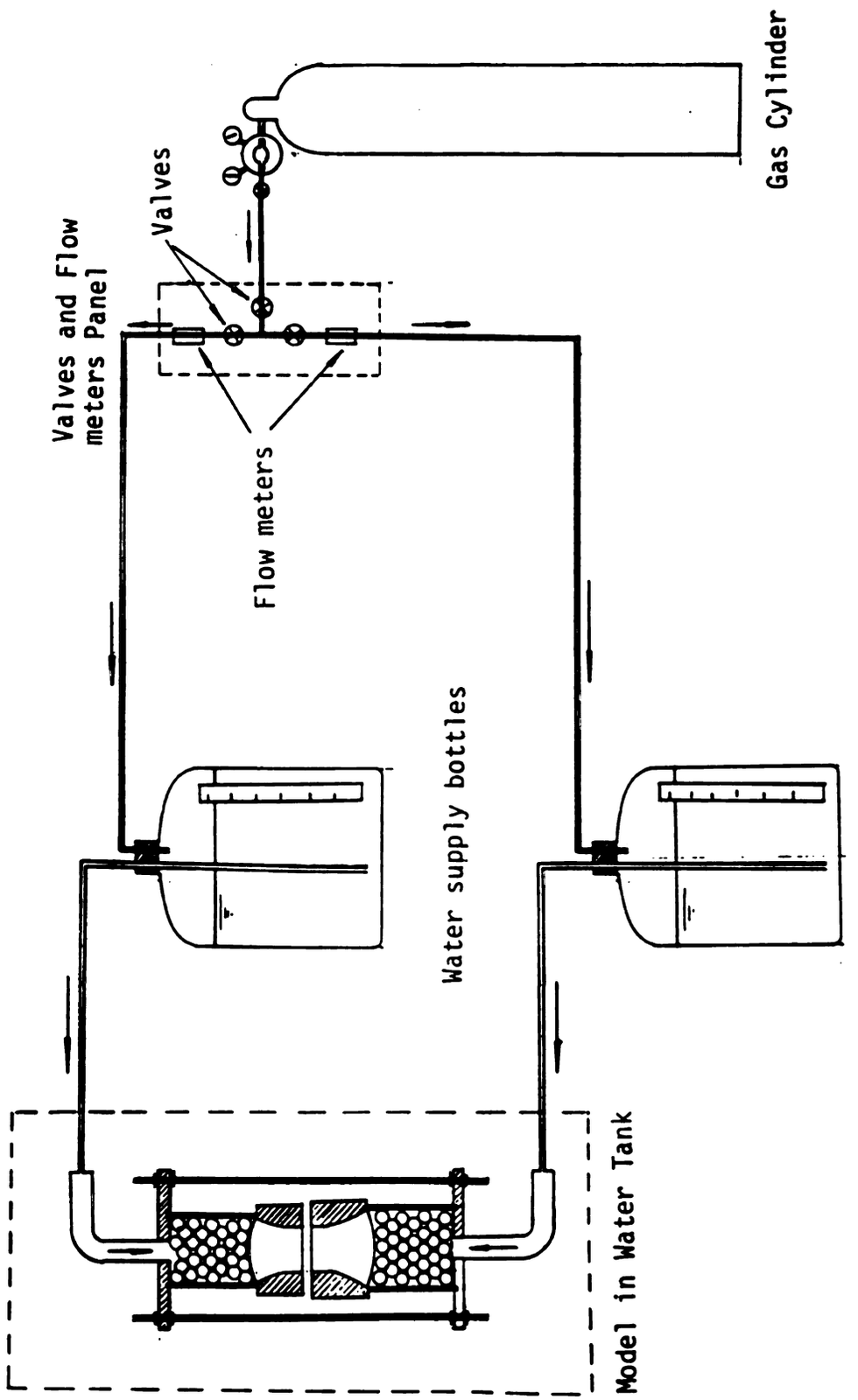

Figure 3-1 Water supply system for the model test. To keep the water flow rate constant, constant N_2 gas pressure is applied to the water supply bottle.

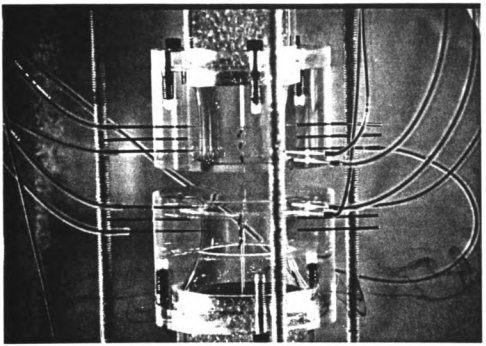

Figure 3-2 Photograph of the test section of the Plexiglass model in sugar-water mixture.

basically consists of two main parts, upper and lower burners. The section views of the upper and lower parts of the burner are also shown in Figure 3-4 and 3-5. The oxidizer, which is a mixture of an O_2 and inert (N_2 or He), is supplied from the upper part and fuel which is a mixture of fuel and N_2 is supplied from the lower part of the burner.

The burners have been constructed in stainless steel housing. There is 2.54 *cm* gap between the inner housing and the outer housing (Figure 3-3 through 3-5). Through this gap inert gas, N_2 flows to prevent from diffusing the air into the reaction zone and to dilute the exhaust gas. Also, screen is installed between upper and lower

parts of burner. This screen is to reduce or to block room air eddies which might be a cause of disturbance of flame when operator moves around the burner system. On the screen, an observation window, quartz window, is located to observe the flame and inside the screen. Through this window, flame is monitored by CCD camera.

The oxidizer supplied by upper part of the burner is heated by passing it through at a porous ceramic heat exchanger which is located inside of the impervious alumina ceramic tube. The porosity of the porous ceramic heat exchanger is 80%. The heat exchanger is made of Zirconia which can stand up to 4000 K. This ceramic heat exchanger is heated primarily by radiative heat transfer from molybdenum disilicide heating elements (Super Kanthal 33) which can sustain at maximum temperature of 2100 K in air.

For the present study, the burner system should provide energy enough to heat up the oxidizer streams up to the desired temperature. To provide axisymmetrical temperature distribution U-shape of electric heating elements should be arranged properly in very limited space. These heating elements are not rigid at high temperature. So, these should be arranged to bend outward by magnetic field force induced by electric current through themselves. The short circuit at high current will not only provide hot spot to break temperature balance but also burn the heating elements. Concerning magnetic field force and limited space, the heating elements are arranged shown in Figure 3-6.

The fuel gas supplied by lower part of the burner is also heated in the same manner as the oxidizer flow in the upper burner. Chrome-Aluminum-Iron alloy wire embedded in high purity Al_2O_3 cement is used to heat the ceramic heat exchanger. For the fuel side the gas pre-heat temperature is lower than the temperature at which the methane begins to be pyrolyzed.

The upper and lower heating elements assemblies are insulated by a fibrous ceramic insulations to reduce heat loss through the cylindrical burner surfaces (refer to

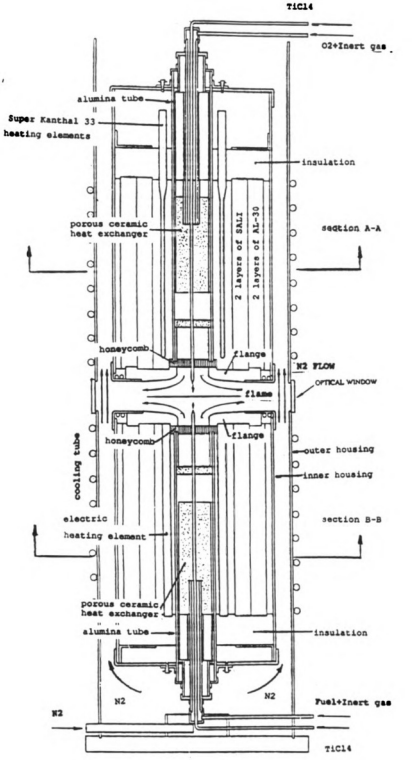

Figure 3-3 Schematic of high-temperature counterflow diffusion flame burner.

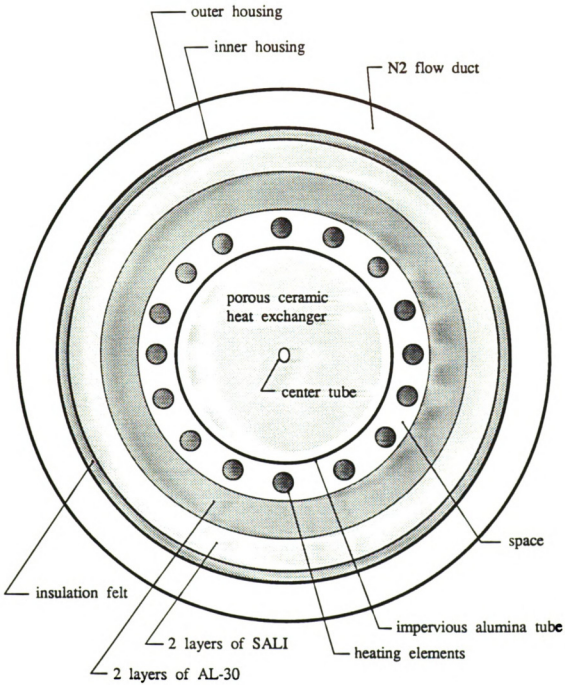

Figure 3-4 Section view of upper part of burner. (section A-A)

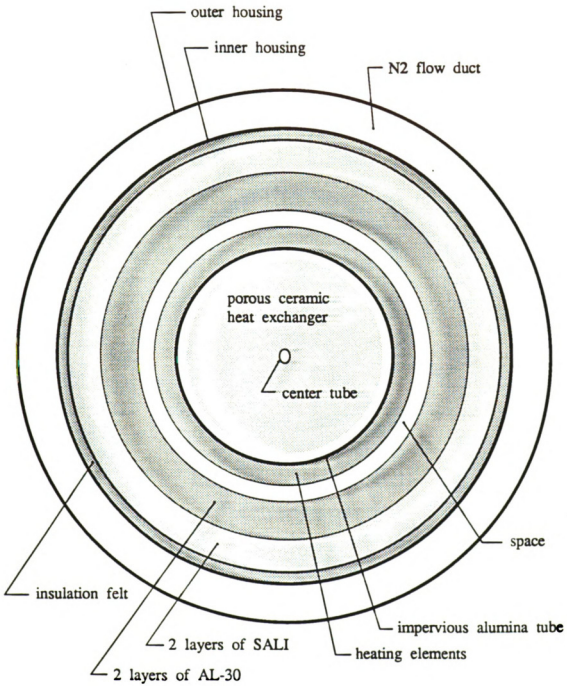

Figure 3-5 Section view of lower part of burner. (section B-B)

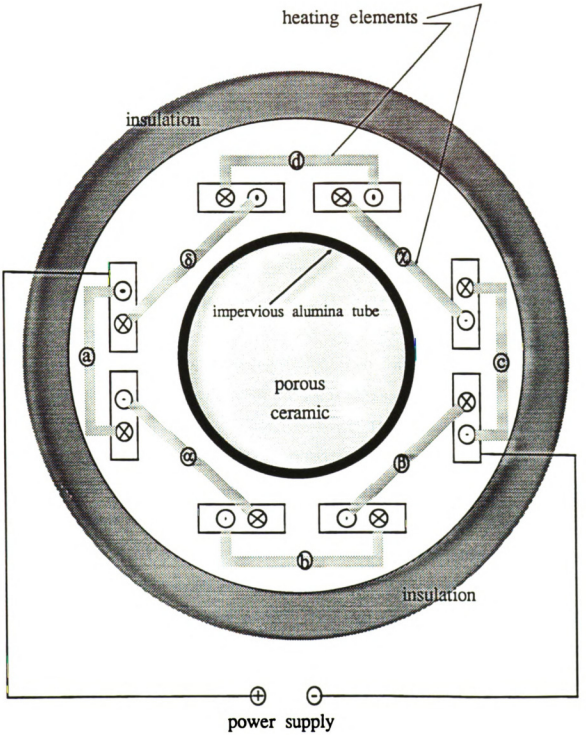

Figure 3-6 Schematic of arrangement of heating elements for upper part of burner

Figure 3-4 and 3-5). Four cylindrical insulations are nested and ceramic glue, which can be used up to 2700 K, and 4 pieces of ceramic bars are used to hold all four nested ceramic insulations. First two layers of insulations from inside are made of a mixture of 80% Al_2O_3 and 20% SiO_2 (SALI, Zircar). Next two layers of insulations are made of 83% Al_2O_3 and 17% SiO_2 (AL-30, Zircar). The assembly of these insulations is reinforced by galvanized sheet metal. The entire system is housed in a cylindrical stainless-steel frame.

Cylindrical ceramic honeycomb is used to straighten the gas flow at the end of the honeycomb. To reduce heat loss by the honeycomb when the hot gas passes through, it is necessary to measure temperature inside the honeycomb to optimize the honeycomb length. Figure 3-7 shows the temperature profile inside the honeycomb along its length. This measurement was performed while the upper burner was at about 1450 K and the lower was at about 900 K. It also shows that most of heat loss takes place at the outer second half of honeycomb length. This temperature profile shows that temperature is almost constant up to 11 *mm* from the inside of the honeycomb. Temperature drops very quickly after that point. Honeycomb temperature is dominated by radiative heat transfer from the heat source, which is porous ceramic heat exchanger. Figure 3-8 shows the relation between honeycomb temperature and view factor from the heat source surface. This figure shows that the length of uniform temperature depends on the honeycomb cell size. To reduce temperature drop at the end of the honeycomb, it is necessary to reduce the length of honeycomb. This reduction of temperature drop along the honeycomb length improves heat loss from the hot gas to the honeycomb cell. This reduction does not affect the maximum honeycomb temperature.

It is clear from the observation (Figure 3-8) that there are two conflicting phenomena with honeycomb length. If the honeycomb length is too short, then the temperature drop along its length will be reduced but it is unclear whether the gas flow

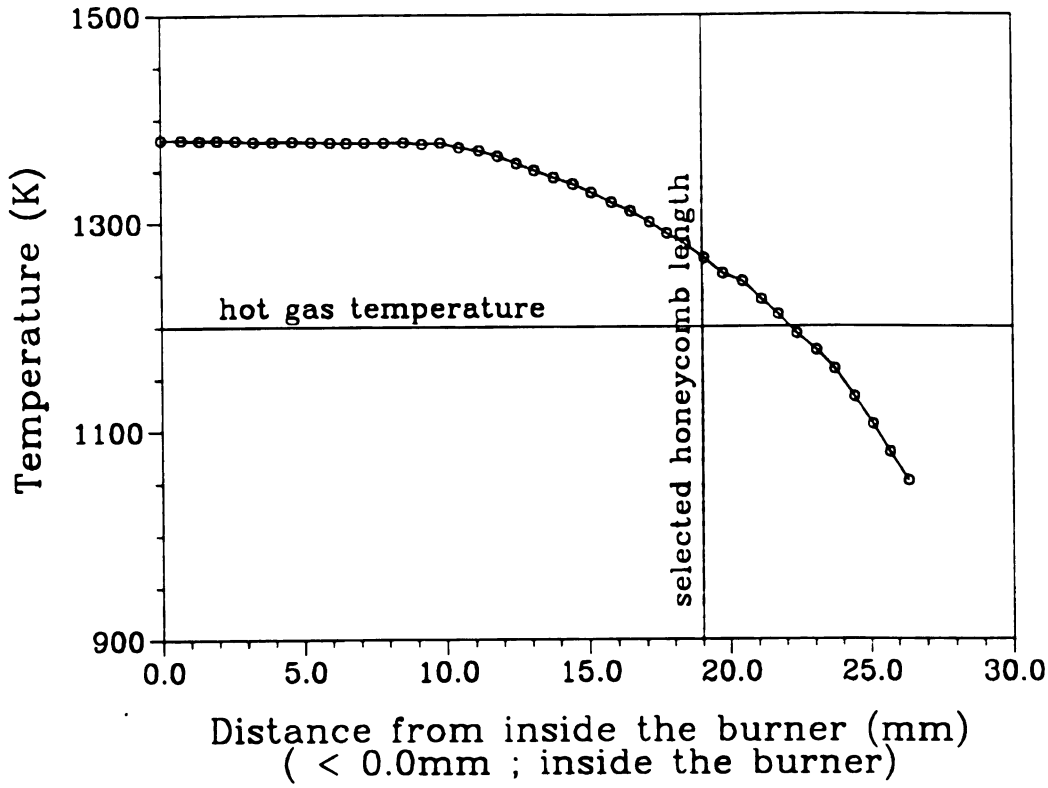

Figure 3-7 Measured temperature profile inside the honeycomb along its length. It also shows the desired temperature for oxidizer stream and the selected honeycomb length.

is straightened enough at the end of honeycomb. On the other hand, if the honeycomb length is too long, straightened flows can be achieved easily but it is hard to get temperature desired at the end of honeycomb.

Very limited amount of literature is available on the effect of honeycombs on the flow (Lumley,1964; 1967; Loehrke & Nagib, 1976). Recall that the gas flows into the honeycomb after passing through the porous ceramic heat exchanger. Therefore, the flow contains r- and ϕ-direction velocity components. To eliminate the r- and ϕ-direction velocity components and to obtain uniform straightened (z-direction) velocity flow, the ratio of honeycomb length to cell size should be approximately greater than

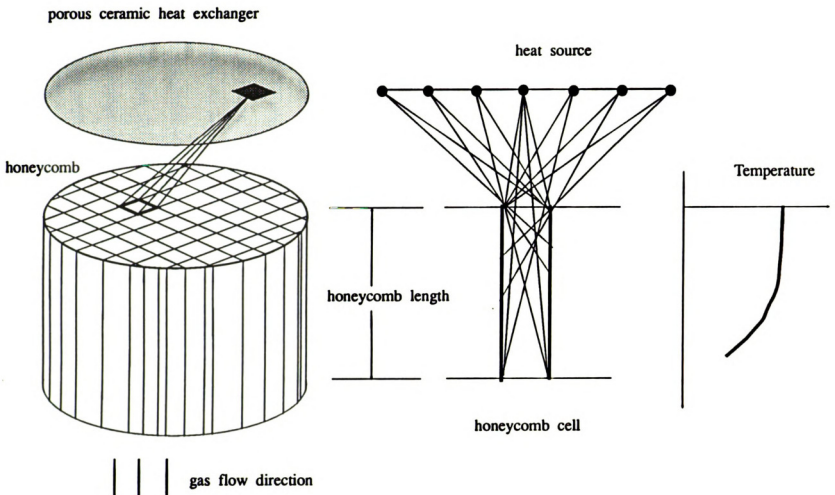

Figure 3-8 Schematic of heat exchange between honeycomb cells and heat source.

or equal to 10.0 (Loehrke & Nagib, 1976). Based on this restriction and temperature measurement, 19 *mm* of length was chosen for the honeycomb cell size of 2 *mm* x 2 *mm* (Normal cell density = 100 cells per 6.45 cm^2).

The burner was tested by flow visualization technique after constructed. Air stream supplied from both upper and lower parts of the burner to establish stagnation point flow. Titanium tetrachloride [1] ($TiCl_4$) was introduced as a tracer into both the air streams through ceramic tubes which were installed at the center of honeycomb for flow visualization (Figure 3-3, 3-4, 3-5). Titanium tetrachloride develops dense white vapor when it is brought in contact with moist air (or gas with small amounts of moisture), as a consequence of the reaction

$$TiCl_4 + 2H_2O \rightarrow TiO_2 + 4HCl \tag{3.5}$$

The most likely particle size of the $TiCl_4$ vapor is about 1.1 μm (Freymuth, Bank & Palmer, 1983). And the range of particle size is between 0.5 to 15 μm. It is well known that the particles in this range are following the gas in the laminar flows.

Thin laser light sheet was used to illuminate a cross sectional plane within the burner gap. Then, the $TiCl_4$ vapor injected from small tubes as scatter of the laser light sheet. Figure 3-9 shows that the flow patterns made by the air streams and visualized with $TiCl_4$ vapor. This photograph confirms that the burner constructed has the ability to provide an ideal stagnation point flow. It is noted that this stagnation plane is comparable to the expanding dye ring of model experiment described in Appendix A.

Also, temperature profiles were measured for air stream flows for verifying one-dimensional flow. To measure temperature profiles the burner have been heated to maintain an average temperature of 600 K and 900 K in the middle of the burners gap.

---

1) The relevant properties of $TiCl_4$: It is nonflamable and nonexplosive, but it reacts strongly with water. Density = 1.722 *g/ml* at 25° C, Molecular weight = 189.71, Freezing point = -24° C.

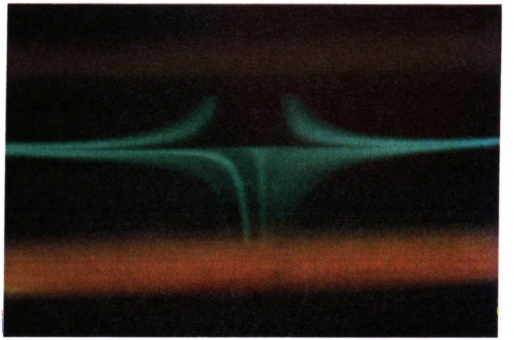

Figure 3-9 Photograph of flow visualization of air steam in the gap between the upper and the lower part of the burner using $TiCl_4$ fume. It shows streamlines and stagnation plane clearly.

Figure 3-10 shows typical temperature profiles in radial-direction with and without flame at 900 K pre-heat condition. Here 0.0 on x-axis stands for center of the burner. The temperature deviation with flame is larger than that without flame. The temperature deviation with the flame is about ± 20° C, and that without the flame is about ± 10° C. The values are present the error range in the r-direction temperature is less than about ± 1 % of average temperature.

Temperature profiles in z-direction for the air streams were also measured. Figures 3-11 show the temperature profiles for 600 K and 900 K pre-heat conditions. For comparison these measured temperature profiles were nondimensionalized by:

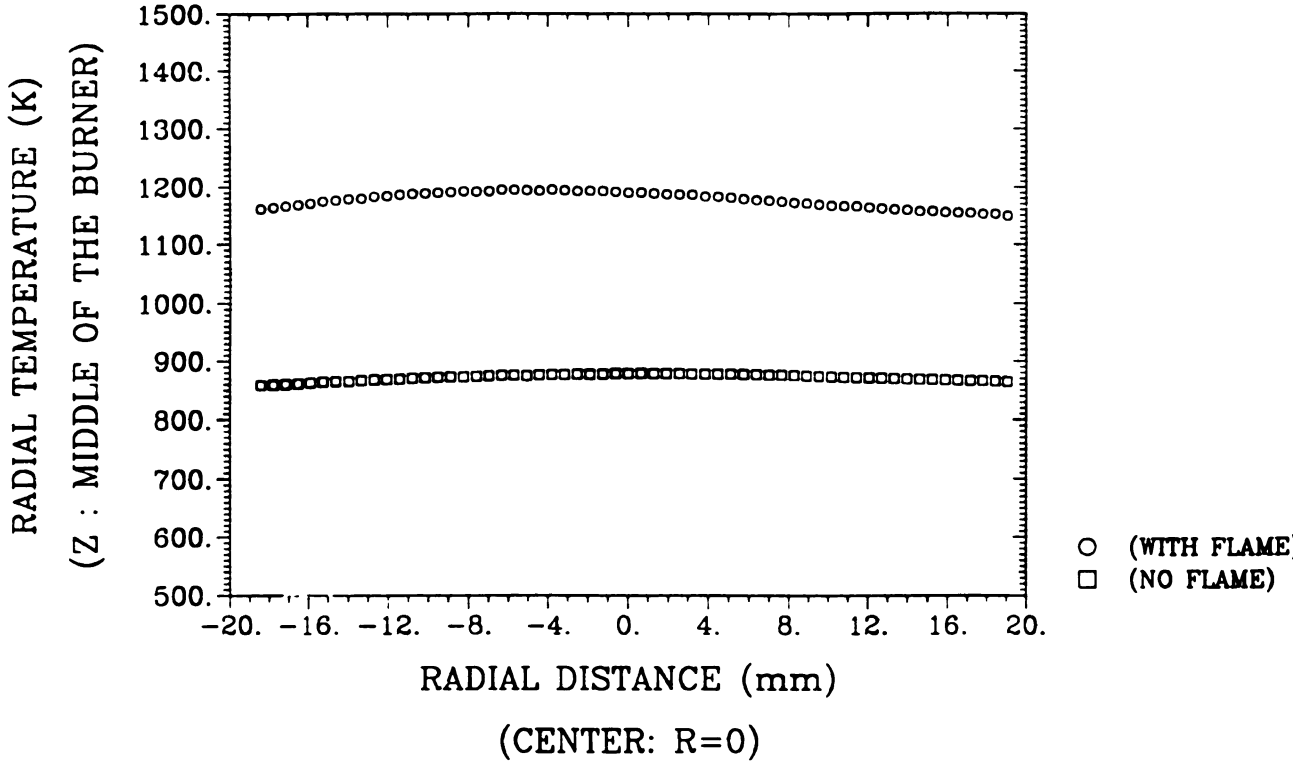

Figure 3-10 Typical temperature profile in radial-direction with and without flame at 900 K pre-heat condition.

$$T^* = \frac{T(z) - T_{low}}{T_{high} - T_{low}} \tag{3.6}$$

$$z^* = \frac{z - z_{avg}}{z_{high} - z_{low}} \tag{3.7}$$

where, T_{high} is 99 % value of the oxidizer side air temperature at nozzle, T_{low} is 1 % higher value of the fuel side air temperature at nozzle, z_{high} and z_{low} are the locations of T_{high} and T_{low}, respectively. In Figure 3-12, these nondimensionalized temperature profiles plotted against nondimensionalized coordinate. These profiles are well fitted each other. These temperature profile measurements for pre-heat air streams showed that the burner system can provide well defined temperature profiles as a conserved quantity.

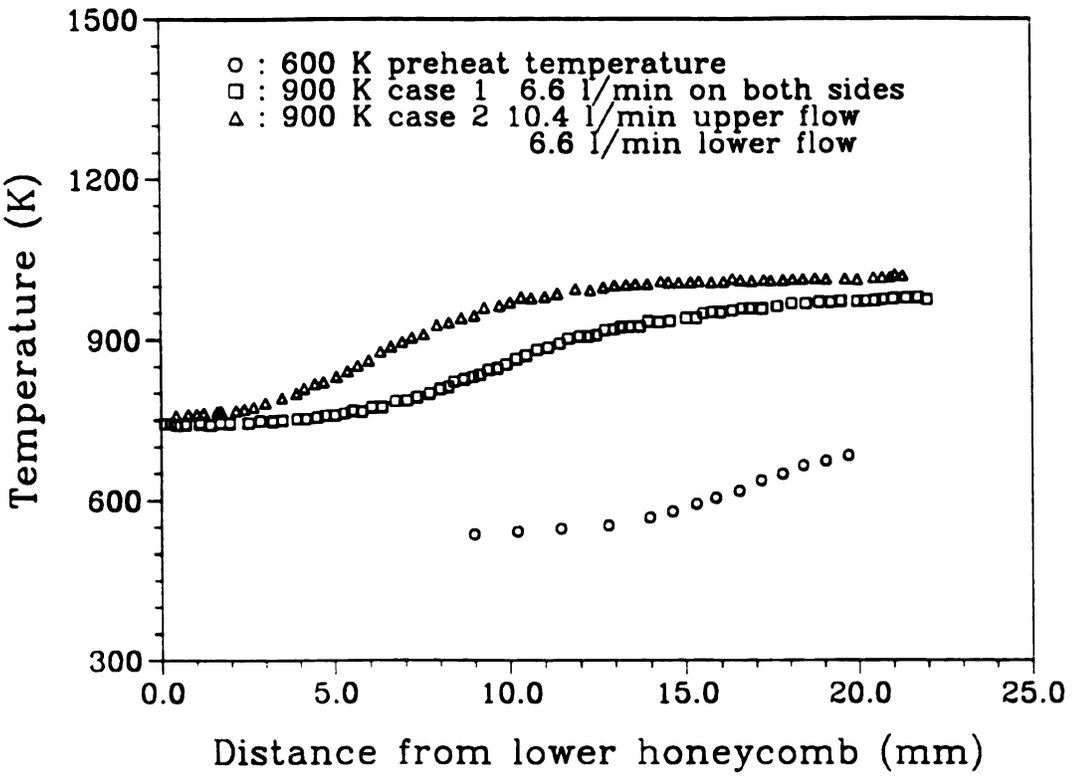

Figure 3-11 Temperature profile of air stream in z-direction for 600 K and 900 K preheat conditions.

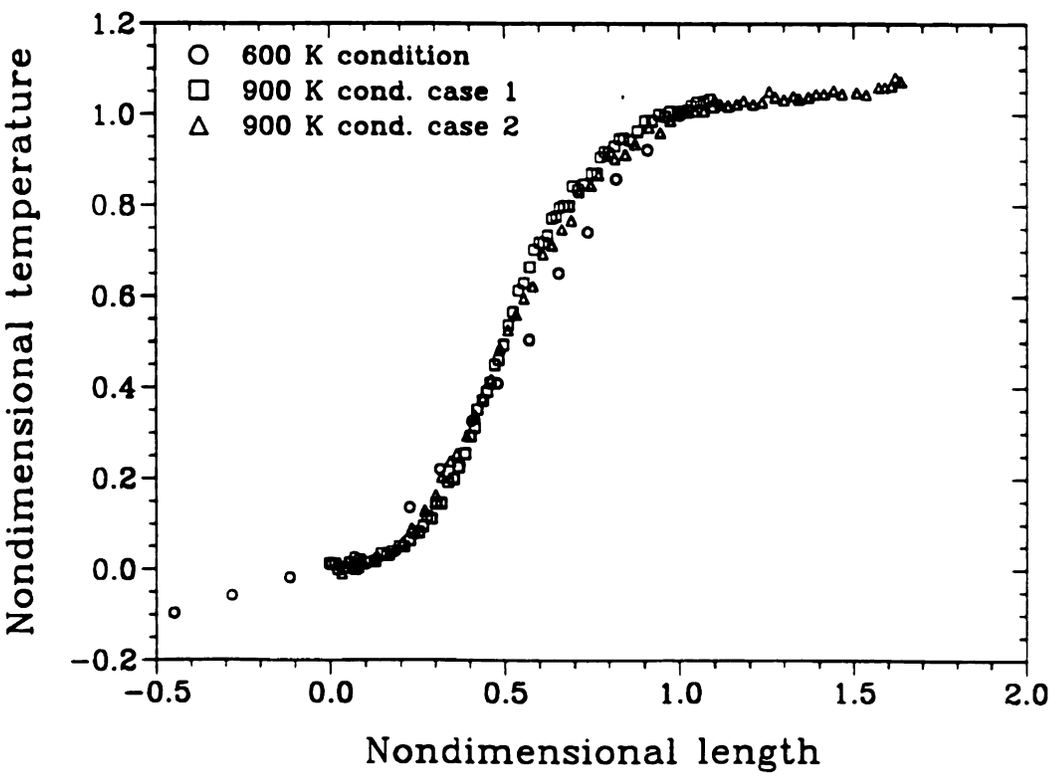

Figure 3-12 Nondimensionalized temperature profile of air stream in z-direction plotted against nondimensionalized coordinate. Temperature and coordinate system are nondimensionalized based on the Equations (3-6) and (3-7), respectively.

In summary, these flow visualization experiment and the temperature measurements showed that the burner system, as designed, has capability of providing ideal stagnation point flow. Also nearly uniform temperature in r–direction (over 4cm in diameter) is possible. This confirms that temperature and soot field are function only of coordinate normal to the flame. This burner system can heat fuel up to about 600 K in lower part and oxidizer over 1200 K in upper part of the burner. The radial temperature profile confirmed that the flange designed no circulation to propagate in the flame zone.

3.1.5 Effect of Buoyancy

As discussed in section 3.1.1, to increase measurement resolution, it is necessary to design the burner to be capable to provide large reactant residence time. Low flow speeds and large burner gaps were used for this purpose. At low speeds and large burner gaps is expected to significantly distort the flow field. This effect was examined based on the Tsuji's data (1982). Figure 3-13 shows that the stable species concentrations in a CH_4/air counterflow diffusion flame. Based on this set of data and temperature profile, density profile was obtained. The density profile for this flame is shown in Figure 3-14. The solid line in this figure shows the density profile obtained from measured species concentrations and measured temperature.

The density profile shows that the density of air side is larger then that of fuel side. This can be cause of distortion of the flame when air flow is supplied above the fuel flow, because of reverse buoyancy in the burner system. For the present study, as mentioned above, the oxidizer was supplied from the upper part and the fuel was supplied from lower part of the burner. This can be serious problem to establish a stable flame at room temperature (without pre-heating). For the higher per-heat conditions (900 K, and 1200 K), the density of oxidizer is reduced by higher pre-heat temperature than fuel pre-heat temperature.

For room temperature experiments, helium gas was used as diluent of oxygen for oxidizer stream instead of nitrogen. This reduces the density of oxidizer stream enough to correct the reverse buoyancy problem. This effect is shown in Figure 3-14 by the dashed curve. The switch of oxygen diluent from nitrogen gas to helium gas made a big improvements and the flame stable.

3.1.6 Burner Mounting

Figure 3-15 shows the burner system assembly and its mounting. The upper and lower burners should be aligned to provide ideal stagnation point flow between the upper and lower parts of burner. Also, the gap between the upper and lower parts of the burner should be adjustable. For these purpose the upper part of burner was mounted on a (x, y, z) traverse which was attached on the steel pipe frame of burner system. So, the upper part can be movable in any direction to adjust its relative location to the lower part of the burner. The upper part can be adjusted within 0.0254 *mm* in x and y directions.

This traverse does not provide a movement to adjust upper part parallel to the lower part. For adjusting the upper part to be parallel to the lower part of burner or to horizontal surface, an aluminum disk was installed between the upper part of burner and the traverse. The upper part of burner is hung by 4 legs from this aluminum disk. The lengths of these 4 legs can be adjusted to set the upper part of burner horizontally.

This burner (both the upper and the lower parts) is sitting on the traverse structure. This traverse can adjust the location of the observation area (the gap between the upper and the lower parts of the burner) from the laser beam position which is fixed on the global coordinate system (X, Y, Z). This traverse has capability of moving the burner with 0.0254 *mm* span in X, Y, and Z- direction.

One more traverse was used to control the measuring probe location based on the flame or stagnation plane location. This traverse can be located any place for

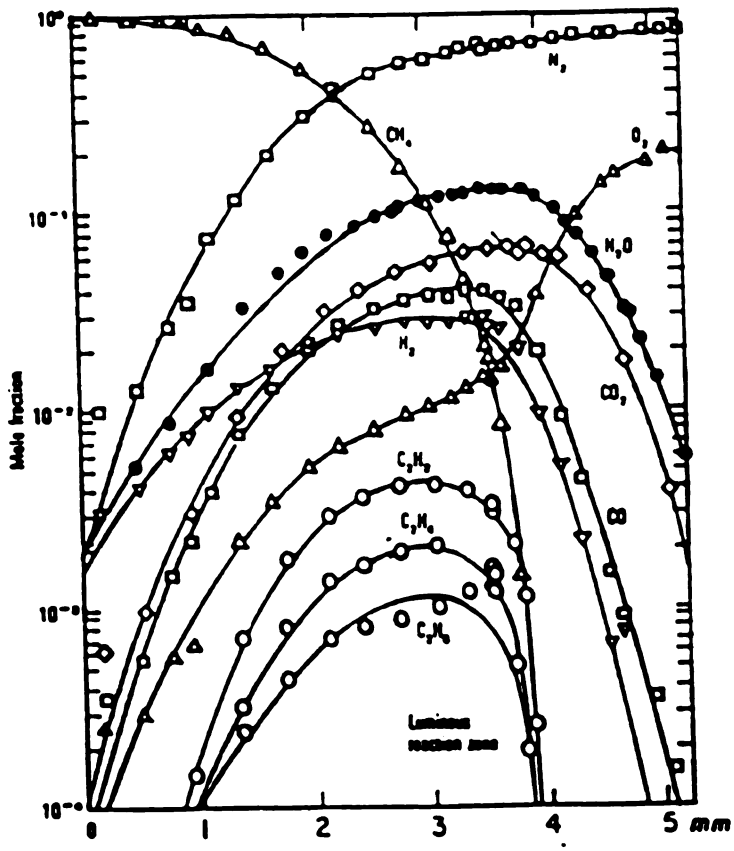

Figure 3-13 The stable species concentration profiles in a CH_4 / Air counterflow diffusion flame (from Tsuji, 1982).

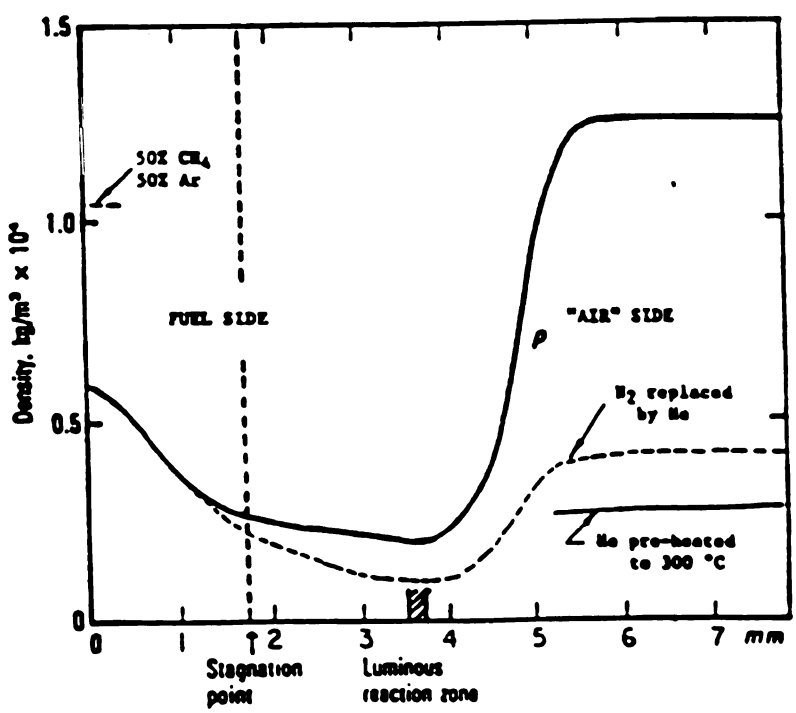

Figure 3-14 Density and temperature profiles. Solid line is the density profile obtained from the measured species concentration in Figure 3-13 and the measured temperature profile. Dashed curve is density profile when helium gas used as oxygen diluent in oxidizer steam instead of nitrogen.

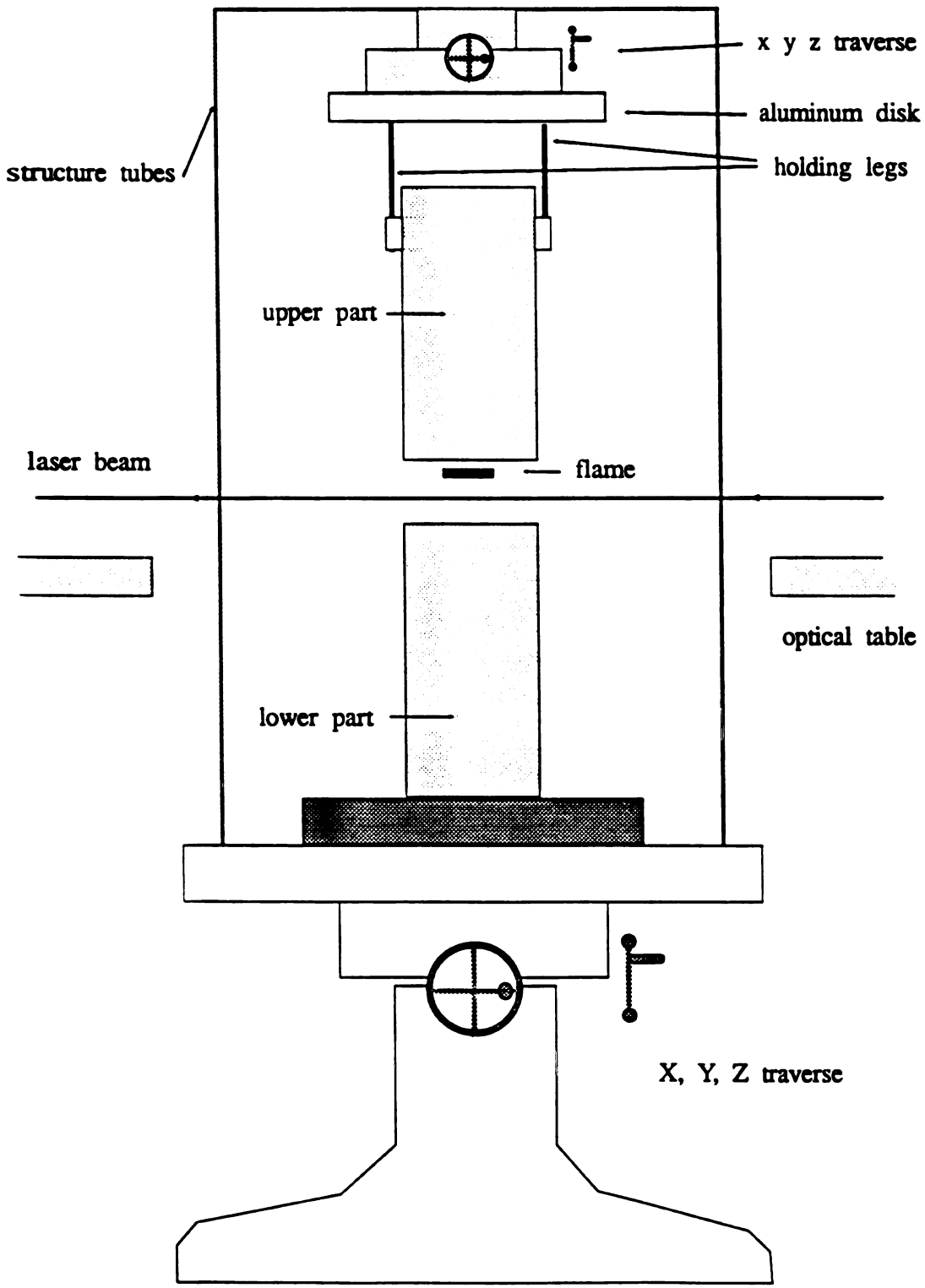

Figure 3-15 Shematic of burner assembly

convenience to use various measuring probes such as thermocouple probes, location indicators, or gas sampling microprobe. This traverse can control x, y, and z-direction and the angle of depression or elevation. This traverse for the probes has capability of moving with 0.0254 *mm* span in x, y, z- direction and 1.0° of angle scale. Figure 3-16 shows the photograph of this traverse for probes.

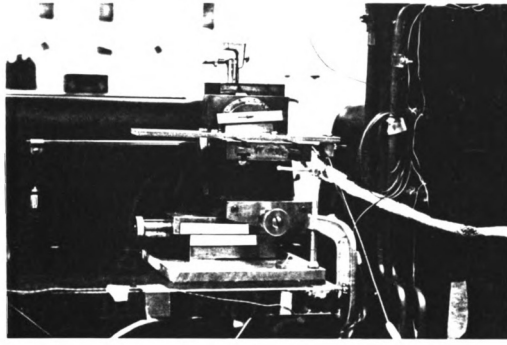

Figure 3-16 Photograph of a traverse used for the measuring probes.

3.1.7 Summary of The Burner Construction

An axisymmetric counterflow diffusion flame burner was designed, constructed and tested as a tool for soot formation, growth and oxidation in diffusion flame. For

the stagnation point flow configuration, the flange shape was chosen from numerical and experimental investigations. Also, it was verified by $TiCl_4$ fume visualization technique (Figure 3-9).

The temperature measurement results (Figures 3-11 and 3-12) show that the burner system is not disturbed from circulation or room air eddies. Also the radial temperature profile (Figure 3-10) shows that the temperature profile is one-dimensional within ± 0.5 % error of average temperature at the measuring location.

For pre-heat conditions, the density of fuel side is always larger than oxidizer side. For room temperature experiment (300 K flame) case, density of fuel stream is smaller than that of oxidizer mixture when O_2 is diluted by N_2. This reversed density distorts the streamline significantly and make the flame unstable. This problem was solved if helium gas, instead of nitrogen, is used as a diluent of O_2 in oxidizer stream.

To conclude, the above investigation made it possible to design and to build a high temperature and a large residence time counterflow diffusion flame burner. Then, the burner was tested. The main advantage of this burner system is that flame, established in nearly stagnation point flow at the burner gap, has one-dimensional configuration in temperature, species concentrations, and soot field, and hence in its receptivity to analysis. This burner system is also capable to provide stable and large diameter (~ 7.0 *cm*) flames at low strain rate flow (~ 3.0 *cm/sec*) in large observation area (the gap between the upper and the lower parts of the burner).

3.2 Gas Sampling System and Composition Measurement

Gas analysis of flames is useful to understand not only chemical process of flame but also sooting history in diffusion flames. Basically the gas analysis gives species concentration profiles which may give the insight of chemical kinetics of flame. This species concentration profile with temperature profile can be used to calculate velocity profile and heat release rate.

Combustion products can be divided into two categories of gases: stable gases and hydrocarbons. The stable gases are main combustion products like H_2, CO_2, CO, and H_2O and gases supplied as fuel and oxidizer such as CH_4, O_2, N_2 and He. Hydrocarbons are the species mainly composed of C and H from the fuel. Usually, to measure these gas concentrations, two methods are used: Probe sampling followed by chromatogram analysis, or *in-situ* analysis by spectroscopic means. For the present study, the probe sampling method was used to measure species profile across the flame.

Measurement of the stable species and hydrocarbons was accomplished by use of sampling probe, sampling system, and gas chromatograph. Gas was sampled by microprobe made of quartz in diffusion flame. This sampled gas was stored in two sample loops, which are for stable gas and hydrocarbon analysis, in sampling system. These stored sample gases were analyzed by gas chromatograph. This gas sampling and analysis system is shown in Figure 3-17. Detailed descriptions for each of the species measurements of the sampling probe, sampling system, gas chromatograph and measuring techniques are explained below.

3.2.1 The Sampling Probe

To sample gas, a sampling probe made of quartz was inserted into diffusion flame. This sampling probe is a device directly contacted with flame. The sample gas is taken at the tip of this sampling probe. For the flame application there are a number

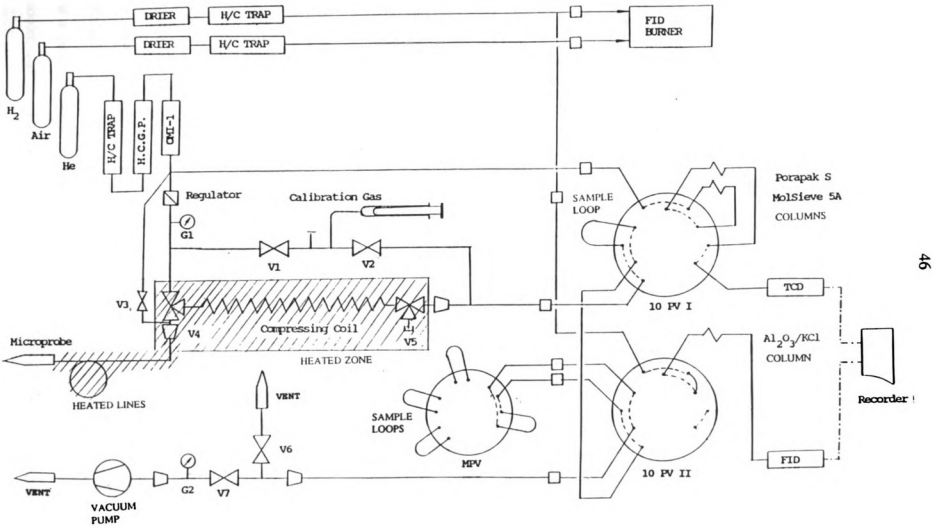

Figure 3-17 Schematic of gas sampling system and chromatography.

of problems which may come from the insertion of the sampling probe in the flame.

Earlier, Fristrom, Prescott, and Grunfelder (1957) examined the problems which may be induced from insertion of sampling probe into the flame or the reactive flow. The problem from the effects of probe in the flame is very complex. The effect of a probe in a flame can be categorized into three, such as aerodynamic, thermal, and catalytic effects. In any reason due to those three effects, this sampling probe should be as small as possible in outside diameter of the probe.

Problems of probe aerodynamics are from internal and external flow. The problem from external flow is the flow disturbance by microprobe itself and the distortion of flow by sample withdrawal. For reducing the flow disturbance problem, the probe shape was designed to minimize disturbance of flame. To improve the flow distortion by sample withdrawal, the sampling rate was optimized based on the microprobe size and critical pressure at the tip of microprobe.

The problem from internal flow of the probe is quenching efficiency of the probe. To freeze reaction at the point of sampling in the flame, it is necessary for the microprobe to have a capability of extremely short quenching time because, in general, half life of reaction is about 500 μsec. This short time quenching can be achieved by rapid adiabatic expansion followed by cooling.

By inserting the microprobe in the flame, the gas temperature around the microprobe may decrease enough to affect the thermal diffusion of reactive species. That is, from the temperature disturbance, reactive species may diffuse to the sampling region. This thermal diffusion of reactive species may cause of losing the accuracy of species measurement.

One of the main effects of probe in the flame is the catalytic effect by the probe surface. This effect can be of two opposing types which are a negative catalytic effect or a positive catalytic effect. The first one may be important when the probe is much cooler than the surrounding gas. This effect usually happens when the microprobe is

water cooled. Positive catalytic effect can be serious problem when the reaction is accelerated by probe surface material.

From the above investigation, the sampling probe must meet the following criteria: (i) minimize the disturbances by it in the flame, (ii) provide rapid decompression and withdrawal of sample to a cool region outside of the flame in order to freeze the reactions, (iii) withdraw the amount of sample required by the analytical instrument in a short time, (iv) minimize the thermal effect around the probe, (v) withdraw sample without catalytic reaction on the surface of the probe, and (iv) provide the desired spatial resolution.

Most of these problems can be solved by the use of a very fine microprobe made of quartz. This quartz microprobe was designed such that the pressure drop across the orifice, which is inlet of the probe, becomes the critical pressure ratio. Thus the sampling mass flow rate depends only on the area of orifice of the probe, and the pressure and temperature within the flame.

The problem of the external flow distortion by inserting microprobe into the reactive stream has been studied by Smith (1981). This study concluded that the external flow distortions can be reduced by reducing inclined angle of microprobe tip and sample size. The limitation of the angle (half angle of the cone) is about 20° at 10^5 Pa, or about 10° at 10^4 Pa. For the present study, the microprobe is made with half angle of about 15°. Also to reduce this kind of flow distortion low sampling rate was chosen.

Fristrom (1983), recently suggested that successful flame sampling does not depend on a rapid temperature drop but, rather, a combination of rapid pressure drop with destruction of radicals on the probe walls. For this method the pressure drop should be large enough to freeze the reaction within time much shorter than the half life of reaction. The sonic orifice of the probe was used for this purpose.

From the isentropic expansion theory, one can calculate the sample temperature at the just inside of microprobe. This quenching process is most important requirement

for the microprobe because the reaction should be frozen immediately after taken. As mentioned above, very low sample flow and very low pressure inside the probe reduces the reaction rate significantly. But the half life of reaction is about 500 μsec so the reduction of pressure is necessary as quick as possible. The microprobe was designed to be sonic orifice and it satisfies the quenching criteria. And it is noted that the time to reduce the pressure is extremely short because it can be accomplished just across the thin shock wave.

For thermal and catalytic effects, quartz probe is one of the best sampling probe. Quartz has a very low emissivity ($\varepsilon \sim 0.02$, Fristrom & Westenberg, 1965), so that the quartz probe temperature at the position of 2000 K in the flame is about 20 K less. Also, quartz is known to have very low activity even in high temperature. Therefore, a quartz microprobe would probably have little or no effects on the thermal disturbance and catalytic effect.

Since the flame is characterized by steep concentration gradient, the flow perturbation set up by the sample withdrawal would be expected to alter the original gradients and thus the composition of the gas entering the probe. Westenberg, Raezer and Fristrom (1957) examined this problem both theoretically and experimentally. This study shows that the concentration gradient effect is insignificant for the quartz microprobe sampling procedure.

It becomes clear that the probe should be as small as possible to increase quenching effect and spatial resolution. On the other hand, the orifice inlet diameter has to be large enough not to be clogged by the soot particles easily and not to take too long to take a sample from the flame. Figure 3-18 shows the design of microprobe used for the present study. Two different orifice sizes (70 and 90 μm) were used to sample gas from diffusion flame. Through these sonic orifices, the gas flows less than 5.0 μg/sec or less than 4 μl/sec. This flow rate small enough not to distort the stream lines in counterflow diffusion flame. The sizes of two sample loops are 250 μl for stable

species and 25 μl for hydrocarbons. For these two sample loops 100 seconds are enough to fill. But most sampling time was used to get low pressure enough to be sonic condition at the orifice. The sampling time was about 12 minutes, for 10 minutes to reach sonic condition at the orifice and for 2 minutes to store the sampled gas. The disturbances by sample withdrawal with such a probe was checked by visually. Figure 3-19 shows the microprobe in a diffusion flame without disturbance.

To prevent from the species condensation on the inside wall of quartz microprobe, the stem of the probe was heated by the electric heating wire wound around the microprobe stem. This quartz microprobe was attached on the fine traverse(see Section 3.1.6) to be located at accurate position.

3.2.2 Sampling system and sampling procedure

Sampling system consists of compressing coil, sample loops, vacuum pump, valves, and plumbings. The sampling procedure is described in this section. While describing the procedure, main components of system like, compressing coil, sample loop, and vacuum pump, which are shown in Figure 3-17, are described.

Before starting sample gas, the whole sampling system was cleaned by helium gas to reduce the sampling error. Cleaning was started from the microprobe. Setting V4 on compressing position isolates the microprobe from the system. After isolating the microprobe, helium gas pushes any residual out from the microprobe by opening V3 for about two minutes. Compressing position of V4 also connects the system to the helium gas to flush the tubes of sampling system. For cleaning sample loops and tubes, another three position valve (V5) is open, and separates from vacuum pump by closing V7. Then, open V6 to vent the helium gas out to the atmosphere. The system needs to clean at least for two minutes. These two cleaning procedures are needed before withdrawing any sample gas from the flame.

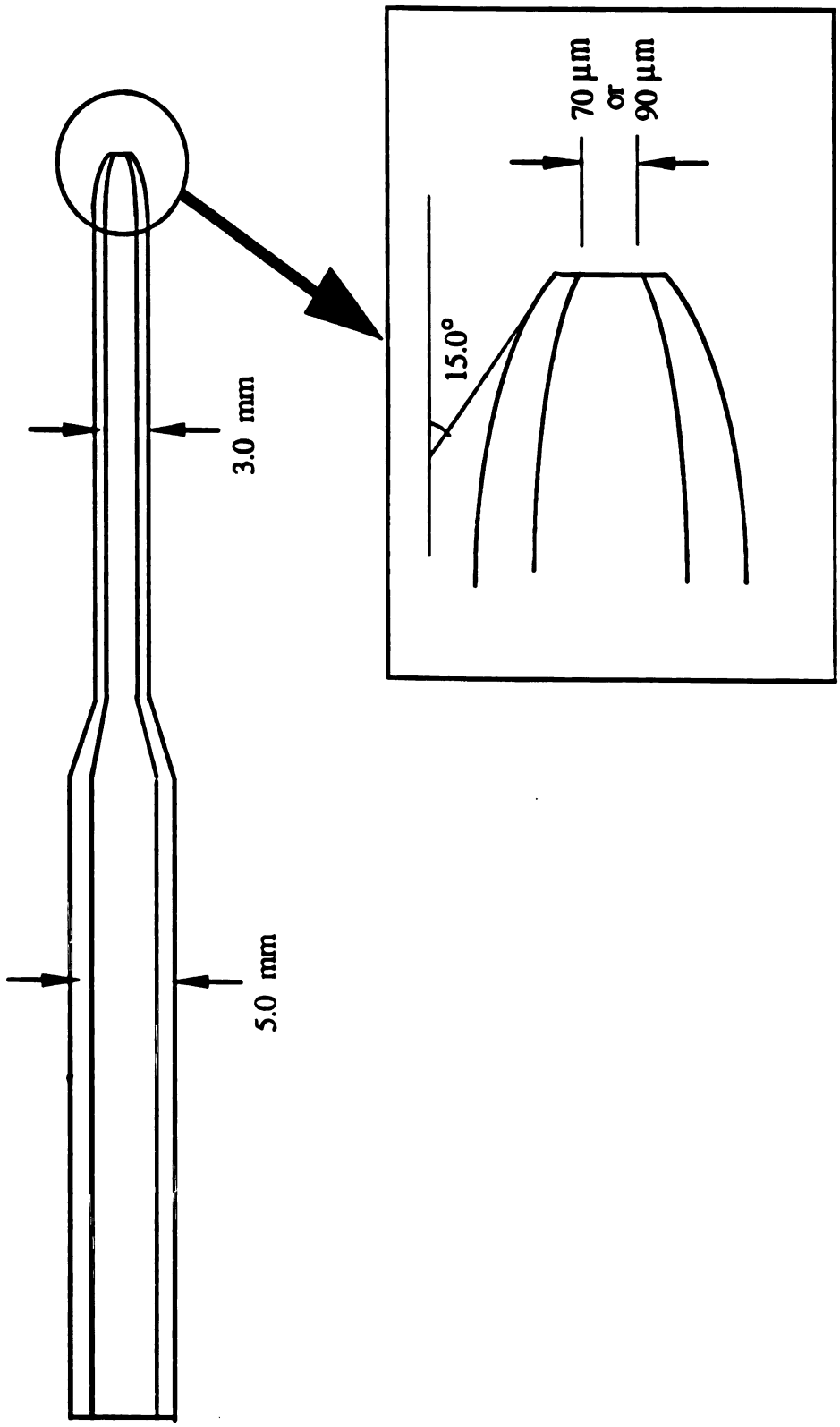

Figure 3-18 Schematic of quartz microprobe

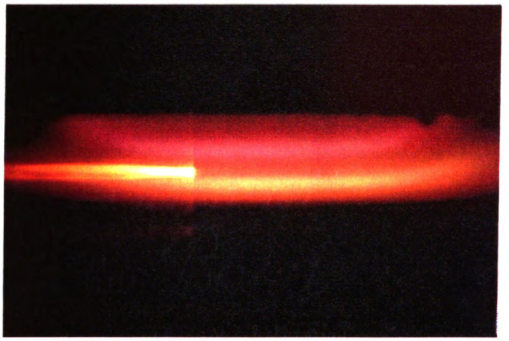

Figure 3-19 Photograph of quartz microprobe in a flame. No evidence is shown that the flame is distorted by the microprobe in the flame.

After cleaning the whole system, calibration gas was injected to check the calibration factors, system and columns in gas chromatograph. For this calibration procedure, V1 and V5 were close to separate injection port from helium gas and open V2 for calibration gas injection port to be connected to the system. Then stable species calibration gas was injected into the injection port. Then the analysis for stable species calibration gas was started. While analyzing calibration gas, another calibration gas for hydrocarbon is injected to be stored in a hydrocarbon sample loop after clean tubes and sample loops.

After started the analysis for stable species calibration gas, microprobe was located at the position where next sample gas would be withdrawn. Turned on vacuum pump, then waited until vacuum gauge (G2) indicates about -730 *mm* Hg. After 10 port valve I (10 PV I) position returned to the sampling position (it automatically returns to sampling position about 1 minute after starting analysis) and the sample loop for hydrocarbon was changed to next loop, microprobe connected to sampling system by changing position V4 and V5. It was then, started to withdraw gas sample by closing V6 and opening V7. This sampling will last at least 12 minutes. It takes about 10 minutes to reach sonic condition at the orifice of the microprobe and about 2 minutes is needed to fill the whole sampling system by the sampled gas from the flame.

At this point the pressure of the sampled gas is about -720 *mm* Hg and it is needed to be pressurized to reach an atmospheric pressure. If a sample gas is injected at low pressure compared with that of carrier gas, the large pressure difference will cause an undesired injection peak and hence loss of measuring accuracy. Large volume of sample loops are also required to store sample gas at low pressure. And a possibility of the outside air pass through into the loops or the tubes is raised. It is also found that it is difficult to inject a low pressure sample gas through the injector of gas chromatograph.

So, the sampled gas was compressed by helium gas. To pressurize the sample gas, close V7 and change V4 to compressing position. Then the sampled gas will be compressed by helium gas preset at slightly higher then atmospheric pressure. To release this excessive pressure, after pressurize the sample gas, open V6 to release excessively pressure and to reach the sampled gas pressure atmospheric. This atmospheric pressure of the sample gas was stored in a 250 µl sample loop for stable species analysis and a 25 µl sample loop for hydrocarbons analysis.

These sample gases in sample loops were ready to be analyzed. There is a 250 µl sample loop to store gas sample for stable species analysis. So, stable species analysis

started immediately after withdrawing each sample gas. And sampling process continued to withdraw next sample gas during the stable species was analyzed. For hydrocarbon analysis, 16 of 25 μl sample loops are installed on the multiposition valve. Sample gases from different locations were stored in 13 sample loops and in the first and 15^{th} loops, hydrocarbon calibration gas was stored. And last loops was used to clean the system before running hydrocarbon analysis. The process for analyzing stable species and hydrocarbon will be discussed in next section.

3.2.3 Species Analysis -- Gas Chromatograph

Gas chromatograph is a device to analyze concentration of various gases in a mixture. The most important parts of a gas chromatograph are columns and detectors. The primary purpose of column is to separate gases from the injected mixture. The detector is a device which indicates gas kind and measures amount of separated components in the mixture.

The basis for gas chromatograph separation is the distribution of a sample between two phases. One of these phases is a stationary bed of large surface area, and the other phase is a gas which perchlorates through the stationary bed. This stationary bed is contained in a column. The gas to be separated (sample gas) is carried through the column by the carrier gas. For the present study, helium gas was used for stable species analysis and hydrogen was used for hydrocarbon analysis.

The column is the heart of the chromatograph. The actual separation of the sample gas is achieved in the column. The sample gas is introduced into the column by the carrier gas. Then selective components in sample gas are adsorbed on the surface of the stationary bed in the column. According to this adsorptive property, the component stays in the column for a certain period (residence time). The selective components of sample gas are separated by this different residence time.

Column length and carrier gas velocity are important factors to separate the selective components from the sample gas. Column length varies from a few inches to more than 50 feet. Longer length gives more theoretical plate and resolution. The carrier gas velocity can be optimized with column length by experimentally. The most efficient carrier gas flow rate is at the minimum of Height Equivalent to a Theoretical Plate (HETP) or a maximum plate (McNair & Bonell, 1969). HETP can be calculated by L/N. Here L is the column length and N is 16 $(x/y)^2$, where y is the distance of two baselines cut by two tangents of the peak curve, and x is the distance from injection to peak maximum (retention time).

Temperature of analysis system specially, injection port and column, is also important to separate gases from the mixture and to reduce analysis time. The temperature should be higher than condensation temperature of the sample gas and lower than the thermal decomposition temperature of the sample gas. Column temperature changes the selective component residence time and hence retention time. For the present study, column temperature varied during the analysis, so that the gas analysis was accomplished in a reasonable time. This temperature programming is described later this section in detail.

Chromatograph has several advantages for analysis of gas from flames: (1) High sensitivity to separate sample gas components, (2) High sensitivity to extremely small amount of species in sample gas with proper detector, (3) Analytical accuracy (1 to 2 %), and (4) Small sample size.

Choosing the proper column is extremely important to analyze the combustion products. For stable species analysis, two columns were used to separate major species from the counterflow diffusion flames. To separate water vapor from the sample gas, MolSieve 5A column was used. Porapak S column separates other stable species such as H_2, CO_2, CO, N_2, O_2, and CH_4. These two columns were installed in series on the 10 port valve I (Figure 3-20). Since the Porapak S column can be destroyed by

water vapor, the system was designed such that water vapor is separated before the sample gas reaches the Porapak S column.

Figure 3-20 shows stable species analysis procedure. Analysis started by switching 10 port valve to operating position. Then the carrier gas (helium) pushed the sample gas from the sample loop to MolSieve 5A column (Figure 3-20 (b)). Moisture in sample gas is adsorbed by MolSieve 5A column and stayed in the column while the other species were moved into Porapak S column by carrier gas (Figure 3-20 (c)). This lasts for 0.93 minutes. After 0.93 minutes, the 10 PV I position switched back and the direction of carrier gas flow reversed. Then all stable species except water vapor separated in Porapak S column flow back into MolSieve 5A column. And H_2O bypassed. Then, water vapor joined to these separated species and all separated stable species entered the detector. For this process, the temperature of inside the oven which contains the columns was programmed. First two minutes the oven temperature was maintained at 70 ° C. Then the temperature started to rise at rate 20 ° C/min until it became 130 ° C. This oven temperature was maintained until the analysis was completed. The amounts of these all separated species were measured by a hot wire detector (HWD or Thermal conductivity detector, TCD).

Figure 3-21 is a test gas chromatogram for Porapak S and MolSieve 5A columns used for the analysis of stable species. For this test, calibration gas was used after conditioning columns at 190° C for 9 hours. And HWD was used to detect the separated species from calibration gas. On this test chromatogram, injection time (BGN) and retention time of each species are shown.

For hydrocarbon measurement, a capillary column was used. A wide bore Al_2O_3/KCl capillary column was installed with a multi-position valve which has 16 sample loops. The volume of these sample loops is 25 µl. This type of aluminum oxide Porous-Layer Open-Tubular (PLOT) column (de Zeeuw, de Nijs & Henrich, 1987) which is deactivated with potassium chloride (KCl) can be used for analysis of C_1 to

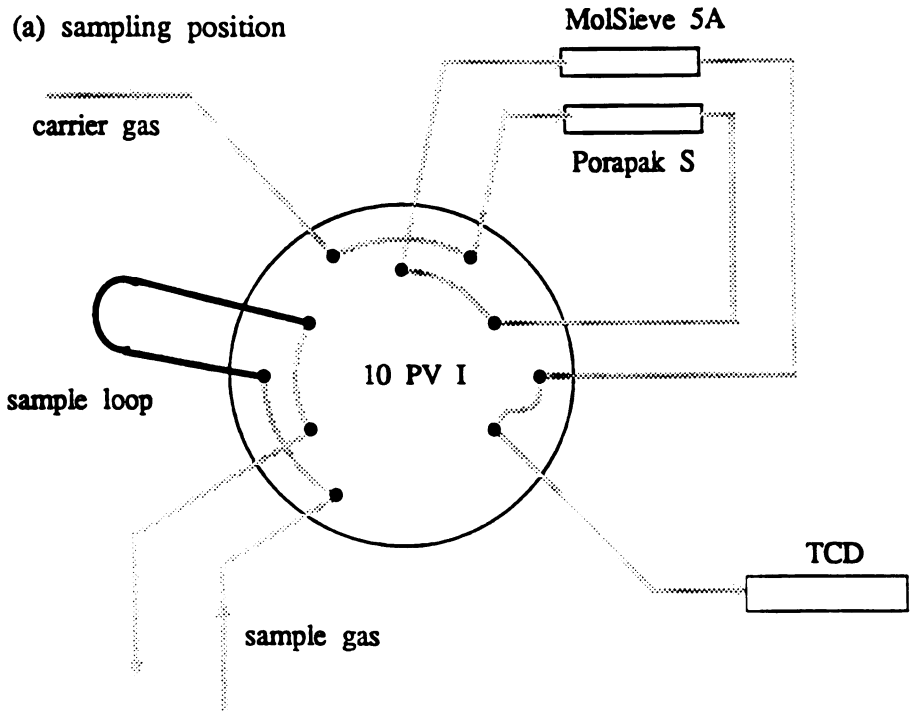

Figure 3-20 10 port valve positions for the stable species analysis. (a) sampling position, (b) Right after switch the position to run analysis, (c) First one minute of analysis, and (d) Final position of analysis.

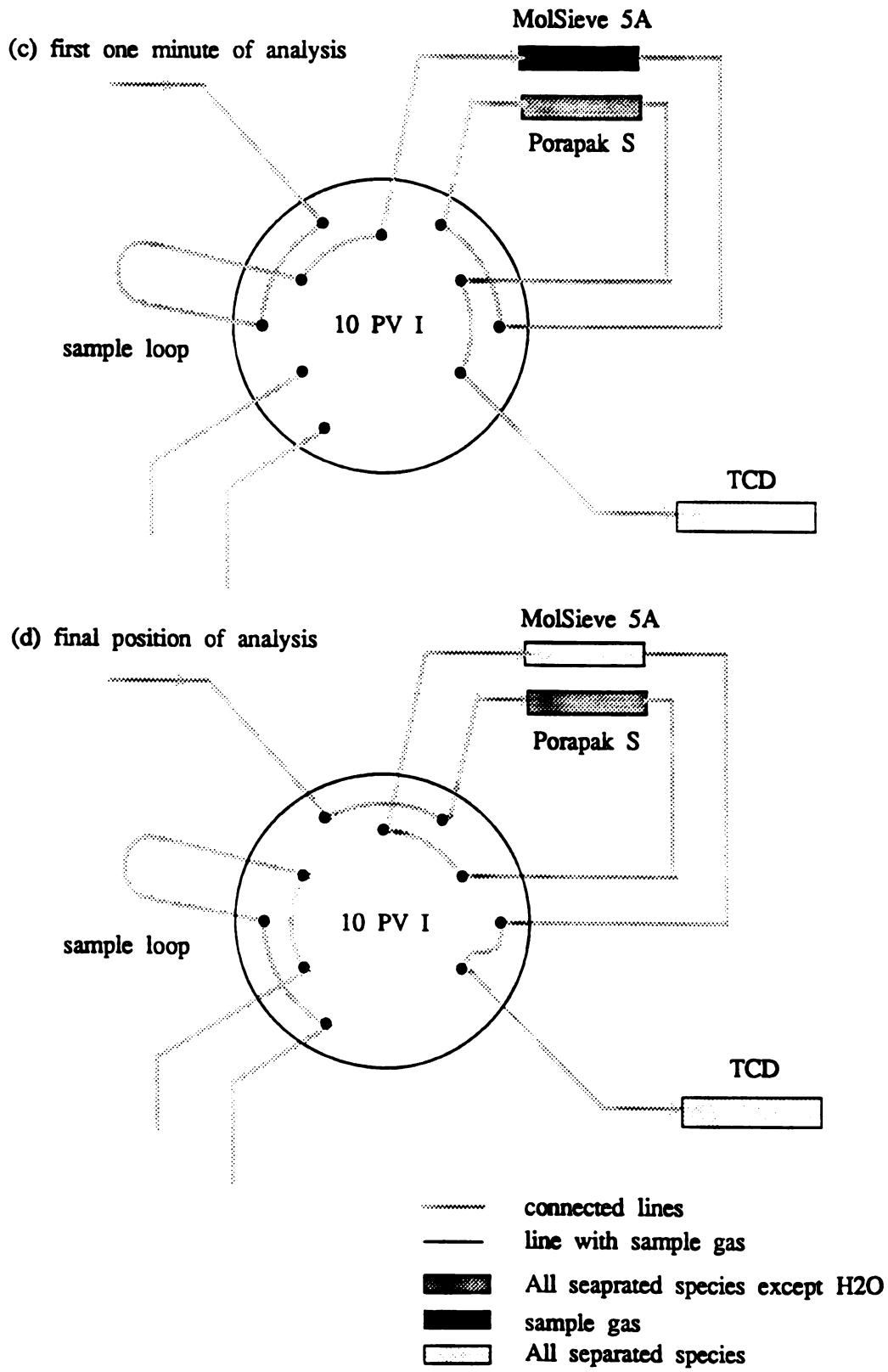

Figure 3-20 continued

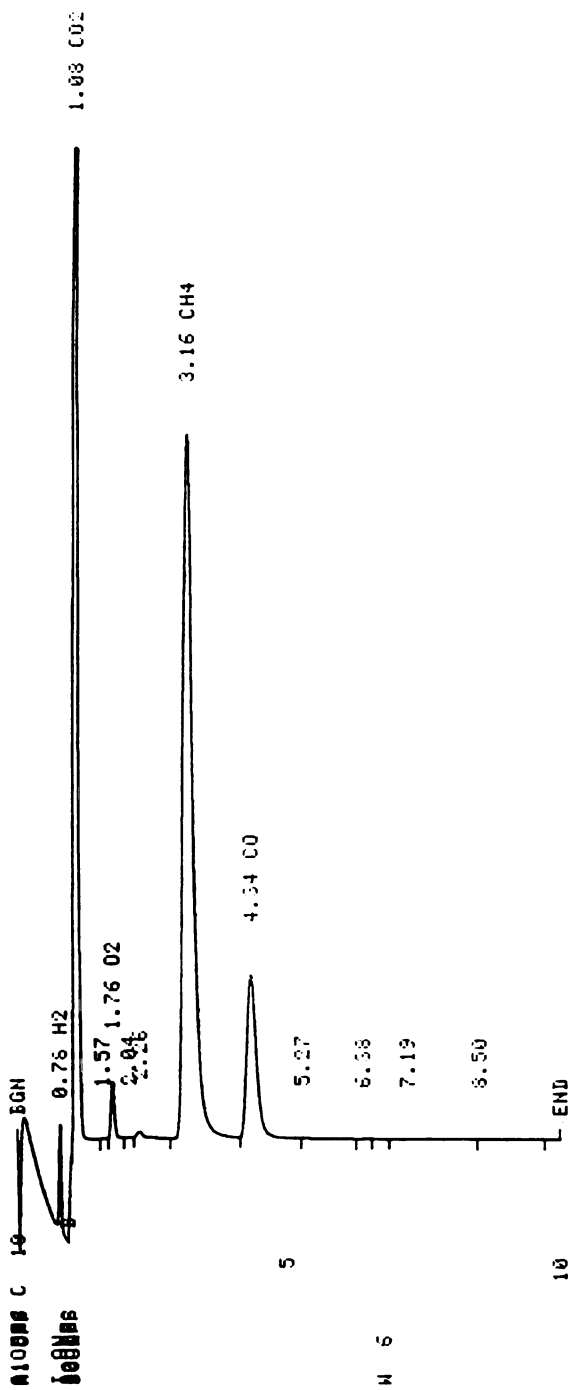

Figure 3-21 Test chromatogram of stable gas analysis using calibration gas.

C_{10}. It has much better resolution and shorter analysis time as compared with the packed column. Also this column can be used with temperature programming up to 200° C to separate light hydrocarbons properly. These capabilities give variety of methods of hydrocarbon measurement.

Figure 3-22 (a) and (b) show the procedure of the hydrocarbon analysis. For this Al_2O_3/KCl capillary column, H_2 gas was used as a carrier gas. Sample gas was stored in one of the 16 sample loops of multi-position valve while stable gas was analyzed (Figure 3-22 (a)). After taking 15 samples including two calibration gas, the system was cleaned by flowing helium gas through the empty sample loop (16^{th} loop). The analysis for hydrocarbons started by changing the 10 port valve II (10 PV II) to analysis position. Then the carrier gas pushes the sample gas to the Al_2O_3/KCl capillary column to separate the hydrocarbons (Figure 3-22 (b)).

For this hydrocarbon analysis, the Al_2O_3/KCl capillary column temperature was varied by changing oven temperature. The oven temperature is 40 ° C when the sample gas is introduced into the column. The oven temperature is increased at the rate of 5 ° C/min up to 200 ° C. Then the oven temperature is maintained constant at 200 ° C until the analysis is completed.

The separated hydrocarbons were introduced into the detector. For the hydrocarbon, flame ionization detector (FID) was used. The FID detector operates on the principle that the electrical conductivity of a gas is directly proportional to the concentration of charged particles within the gas. The effluent gas from the column is mixed with hydrogen and burned in the air. Ions and electrons formed in the flame enter the electrode gap, decrease the gap resistance, thus permitting a current to flow in the external circuit. This electric current is recorded on the chart record. Figure 3-23 is a test chromatogram of hydrocarbon analysis using Al_2O_3/KCl capillary column and FID detector.

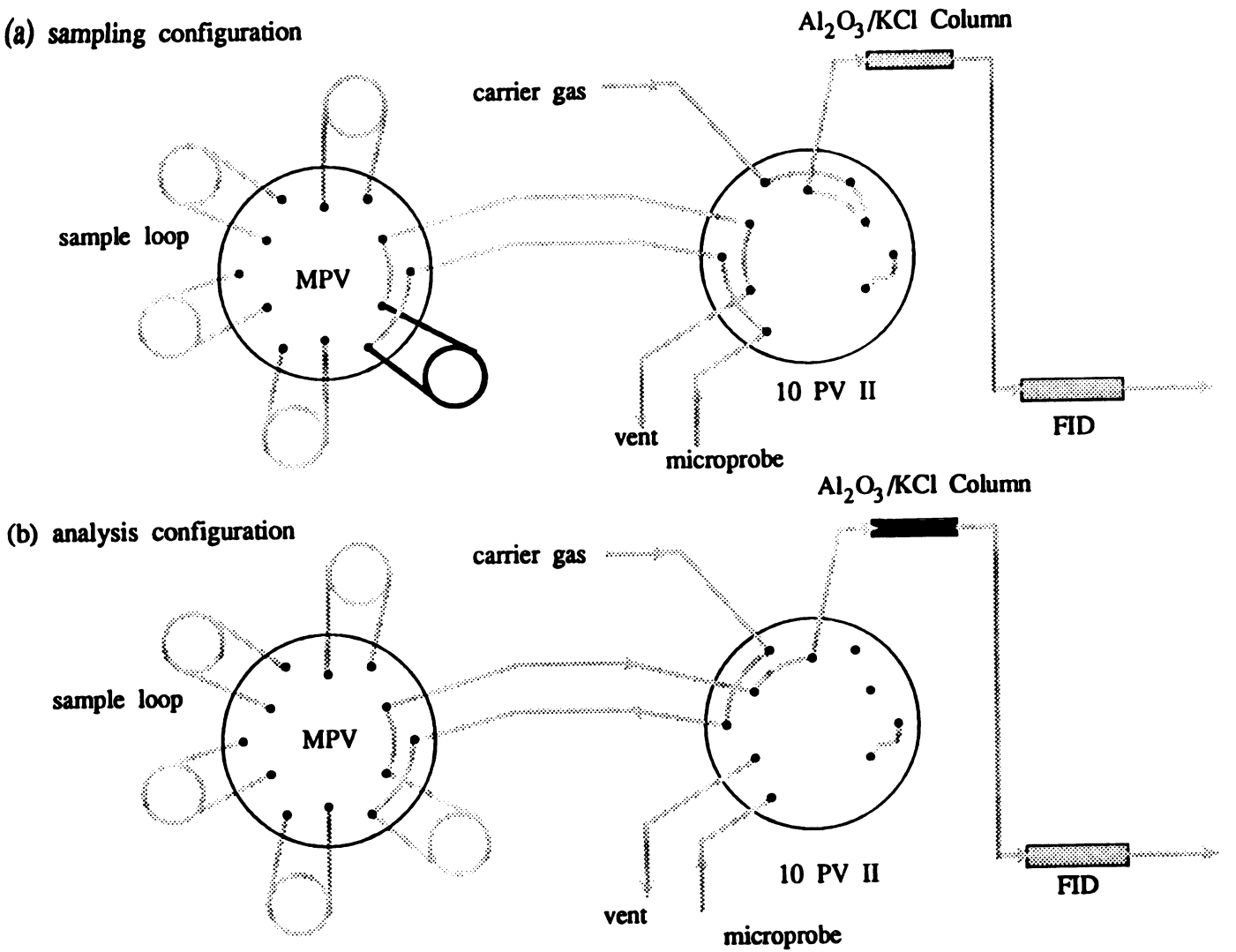

Figure 3-22 10 port valve positions and multiposition valve for hydrocarbon analysis

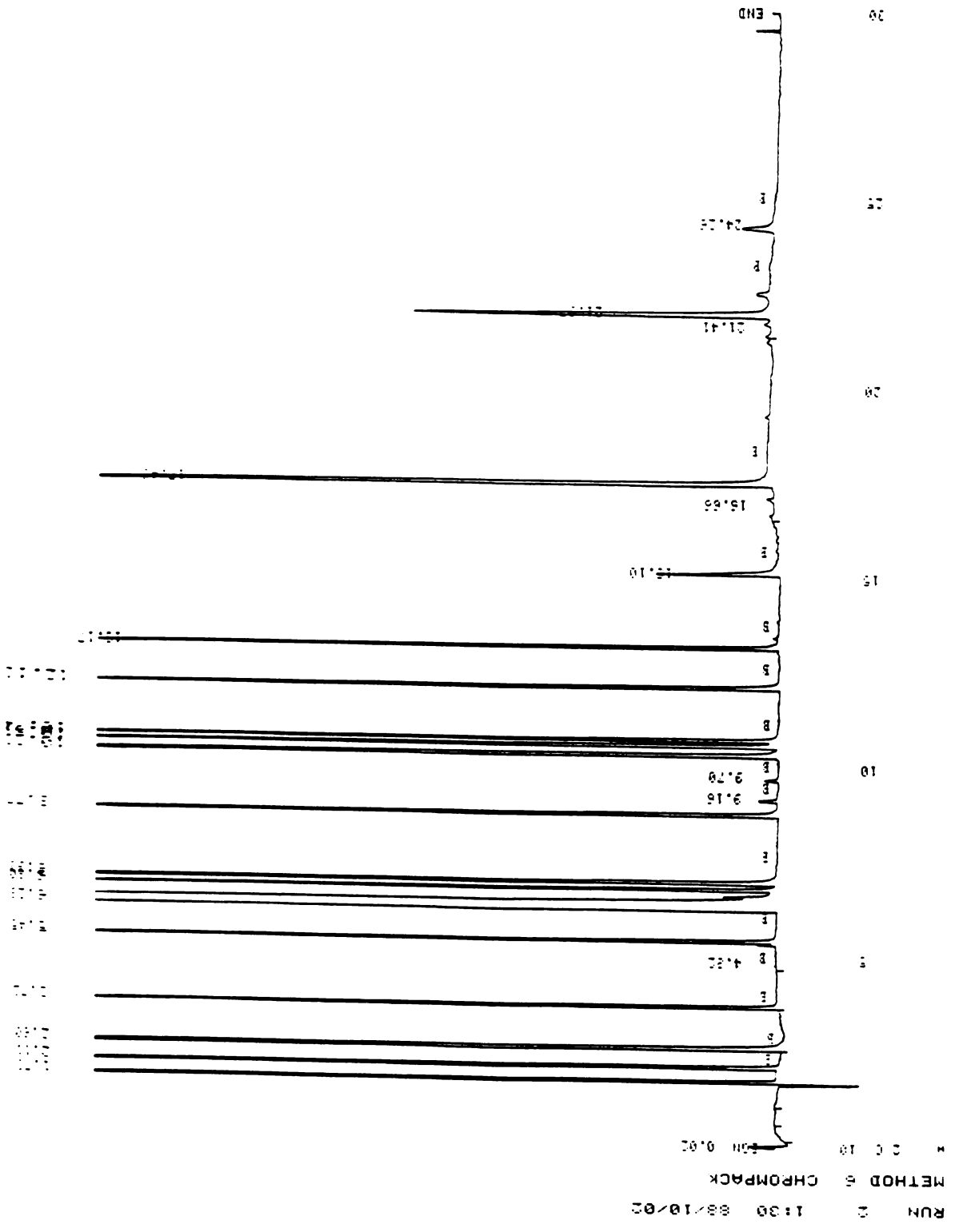

Figure 3-23 Test chromatogram for Al_2O_3/KCl column used for light hydrocarbon analysis.

3.3 Soot Field Measurements

Soot field was measured using *in-situ* optical measurement techniques. Optical measurement system was designed and built for three different measurements. The soot particle volume fraction, particle size and number density were determined by laser light scattering and extinction measurement. For measuring soot particle size, dynamic laser light scattering measurement system was used. Polycyclic aromatic hydrocarbon (PAH) also plays an important role in soot formation and oxidation in diffusion flame. And laser induced fluorescence (LIF) intensity was used as an indicator of PAH concentration. In this section, laser light scattering and extinction technique and LIF measurement methods are described. Dynamic laser light scattering measurement method is explained in Appendix C.

3.3.1 Laser Light Soot Particle Measurements

Quantitative point-wise measurements of the amount of soot produced and oxidized in the counterflow diffusion flame was at the heart of this study. Thus, considerable effort was devoted to designing instrumentation for this purpose. Two different techniques, which are classical and dynamic light scattering, based on two different physical principles were employed.

Basically, three length scales are interest for this measurement. These are: (i) the soot particle diameter (D) which varies roughly from 1 to 150 nm, (ii) light wavelength of the laser used for the measurements (λ = 514.5 nm), and (iii) the gas molecular mean free path at pressure and temperature under consideration ($l_m \simeq 50$ nm). Scattering behavior of the particle may be divided into two regimes by the first two length scales (D and λ). When $D \simeq \lambda$ (Mie regime), Mie theory predicts that intensity of light scattered by particle varies along the scattering angle. In this regime, a single extinction and two scattering measurements at different scattering angles are needed to determine the soot particle size, volume fraction, and particle number

density assuming size distribution function with given the complex refractive index of the soot particles. When $D \ll \lambda$ (Rayleigh regime), Rayleigh approximation of the Mie theory holds and the scattered light is no longer a function of the scattering angle. The width of the distribution and the volume fraction can then be obtained from extinction and a scattering measurements.

For the present study, the size of soot particles in the counterflow diffusion flame is in the range between 1 and 150 *nm* and the laser light wavelength was 514.5 *nm*. So, the parameters for soot particles were calculated basically based on the Rayleigh approximation. Apparatus and the theory for the light scattering and extinction measurement technique are described in following sections.

a. Optical measurement apparatus

A schematic of the optical apparatus is shown in Figure 3-24 and its arrangement relative to the burner and the gas chromatograph is shown in Figure 3-25. A 3 Watt Ar-ion laser (LEXEL Model 95) was used as the light source for these experiments. This laser has high stability of amplitude and frequency which are essential for light scattering measurements. This laser produces multiline laser of 6 different wavelengths such as: 514.5, 501.7, 496.5, 488.0, 476.5, and 457.9 *nm*. But for the present study, only one wavelength is requires. This is achieved by a prism wavelength selector which is installed in the laser head. 514.5 *nm* wavelength at the TEM_{00} mode was used for laser light scattering and extinction measurement. In this laser head, laser light is highly polarized in the vertical plane. So, for the present study, polarizer was not used to polarize the laser beam.

The vertically polarized laser beam was chopped by a chopper (Figure 3- 24) and lock-in detection optics was also used to measure pure light intensity scattered by soot particles without background radiation from the flame. The incident beam was then focused by a collimating lens into the center of the burner to obtain high intensity in

the scattering volume. The focal length of this lens 300 *mm* and it was determined by the burner geometry.

As shown in Figure 3-24, two simultaneous measurements were made on the detection side of the optics. These are: (i) light extinction measurements of the transmitted beam, and (ii) classical light scattering measurements at 90° scattering angle from the transmitted beam. Lock-in amplifiers (LA) were used for both the classical light scattering and extinction measurements to eliminate background radiation from the flame. Continuous analog signals from the photo-multiplier tube and photodiode were converted to digital signals by analog-to-digital converter and collected a computer.

Extinction measurements of the transmitted beam cover a wide range because of the long path length through the flame. The light intensity to be detected ranges from approximately the incident light level to several orders of magnitude smaller for the heavily sooting case. Thus, a photodiode (PD) which is linear over 11 decades together with a set of neutral density filters (NDF) was used for these measurements. Here NDF is used to reduce light intensity without significant change in chromatocity. For the present study, the optical density of NDF was 3.0 which means the light intensity reduces 1000 times of incoming light intensity.

The detection optics for classical light scattering measurements was designed with a magnification of unity, which is optimal for symmetrical bi-convex lens. The focal length of the lens was selected to maximize the solid angle for collecting the scattered signal. 150 *mm* focal length was used for the system. However, the choice was limited by the burner geometry. The solid angle is controlled by the 3 *mm* diameter aperture in front of the lens. The scattered light at 90° was polarized by a high transmittance polarizer and filtered by a narrow band line filter (centered at 514.5 *nm* and 1 *nm* band width) prior to admitting into a photomultiplier tube (PMT). The signal from this PMT was amplified by LA and collected by the computer.

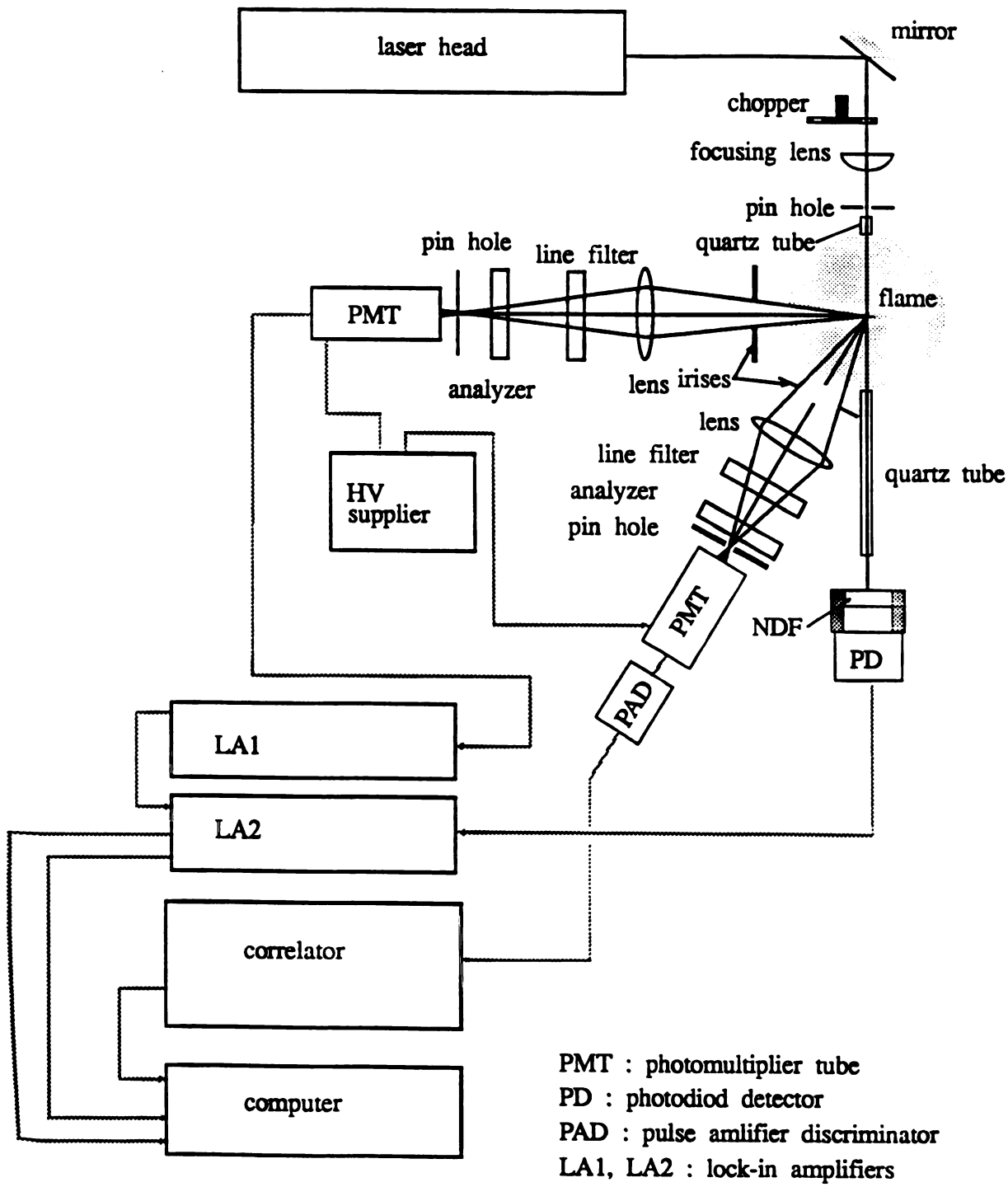

Figure 3-24 Schematic of the laser light scattering and extinction system and dynamic scattering measurement system.

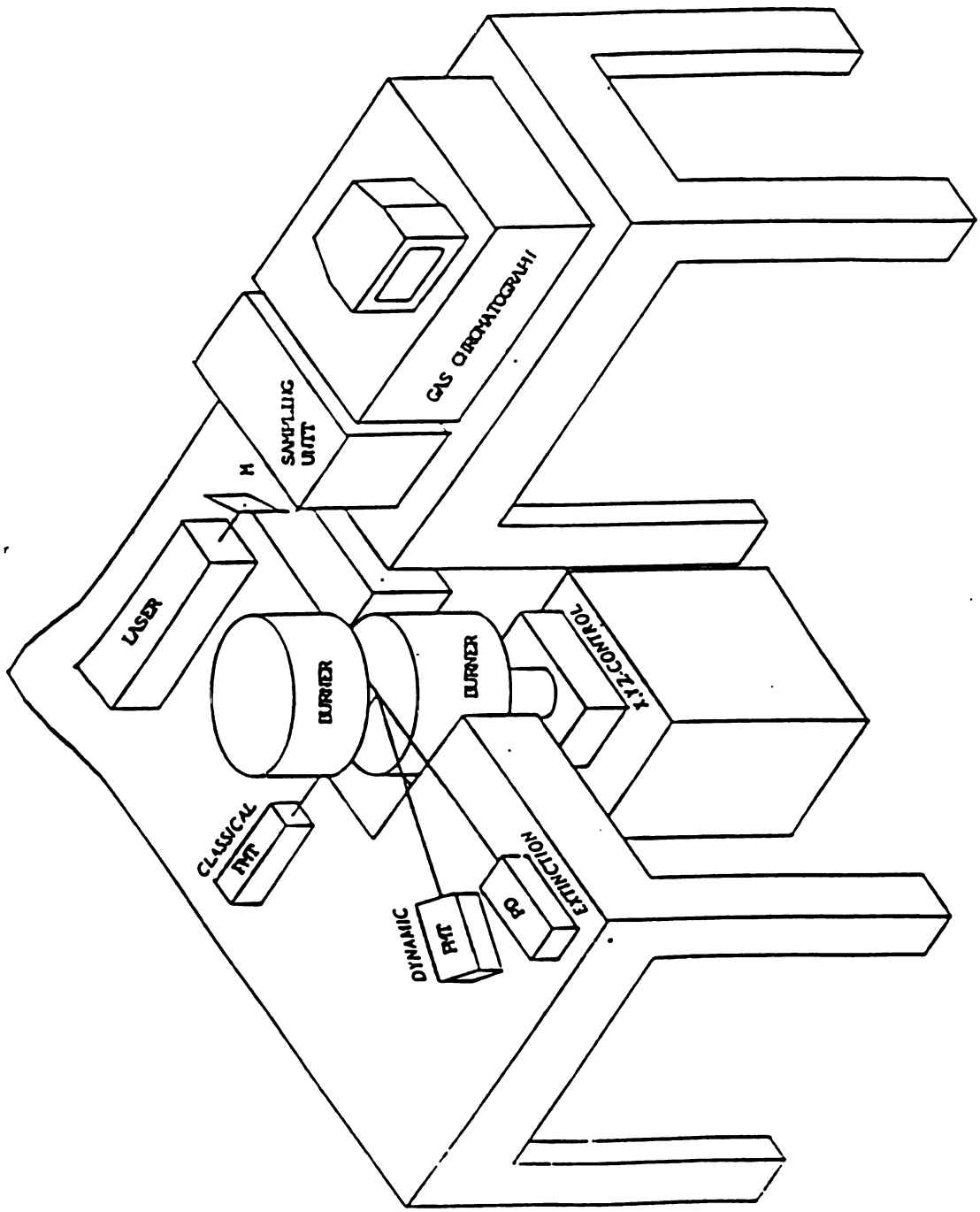

Figure 3-25 Schematic of arrangement of experimental apparatus.

b. Light Scattering and Extinction Theory

Mie Theory

The theory of light scattering and extinction is well established by Van de Hulst (1957) and Kerker (1969). It is introduced here only to an extent necessary for elucidating the evaluation procedure of the measurements. The concept of the light scattering and extinction technique is shown schematically in Figure 3-26. The incident laser light is monochromatic with a wavelength λ and intensity I_0. It is also linearly polarized. For the present study, the incident beam was vertically polarized. It means that the electric field of incident beam oscillates in a plane perpendicular to the scattering plane, which is defined by the directions of the incident and scattered beams. The measured quantity is the monochromatic energy flux of scattered light and of non-absorbed light by soot in the flame. The monochromatic energy flux $F(\theta)$ is given by

$$F(\theta) = Q\ I_0\ \Delta V\ \Delta\Omega \tag{3.8}$$

where ΔV is the scattering volume and $\Delta\Omega$ is the solid angle aperture of the detecting system. The monochromatic scattering coefficient, Q is the monochromatic energy flux scattered at an angle θ per unit solid angle from a unit volume for unit incident energy flux. This quantity Q can be obtained from the experimental data by means of a calibration procedure.

The approach from the Lorentz-Mie theory to the scattering coefficient based on the coordinate system, which is shown in the Figure 3-27, yields

$$Q = \frac{\lambda^2}{4\pi^2}\left[(i_{11} + i_{12})\sin^2\phi + (i_{21} + i_{22})\cos^2\phi\right] N \tag{3.9}$$

where ϕ is the angle measured from the vertical axis, x to the scattering detector position. i_{ij}'s are scattering functions which are derived from the squares of the amplitude functions of the scattering matrix:

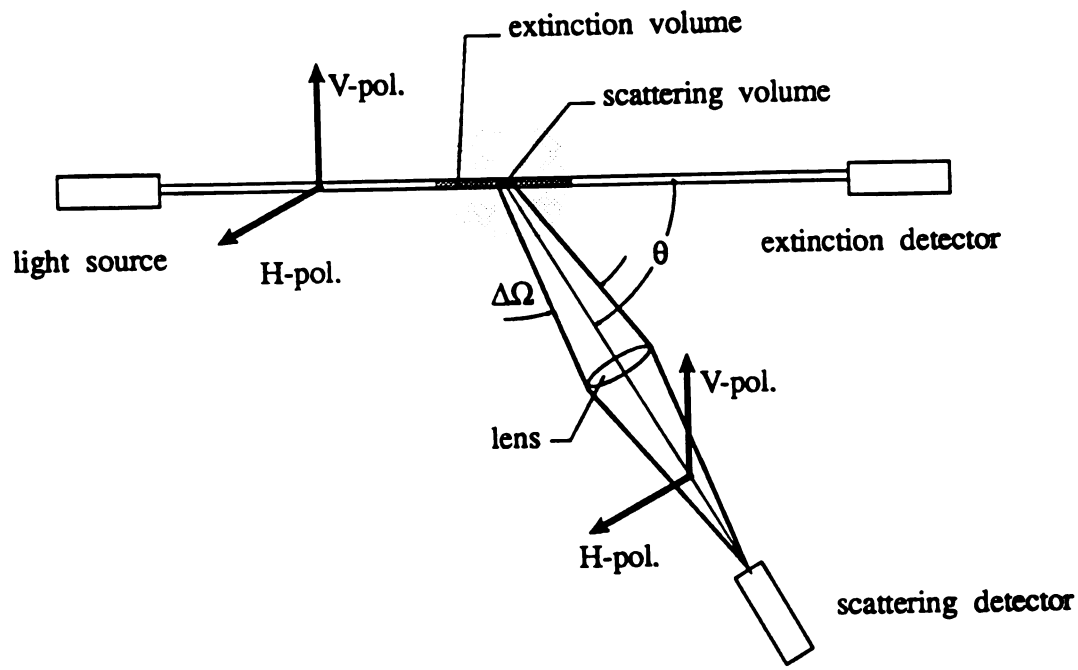

Figure 3-26 Schematic of laser light scattering measurement.

$$i_{ij} = | S_{ij}|^2 \tag{3.10}$$

The amplitude functions are expressed by infinite convergent series. For isotropic homogeneous spheres, they can be written as:

$$S_{11} = \sum_{n=1}^{\infty} \frac{2n+1}{n(n+1)} [a_n \pi_n(\cos\theta) + b_n \tau_n(\cos\theta)] (-1)^{n+1} \tag{3.11}$$

$$S_{22} = \sum_{n=1}^{\infty} \frac{2n+1}{n(n+1)} [a_n \tau_n(\cos\theta) + b_n \theta_n(\cos\theta)] (-1)^{n+1} \tag{3.12}$$

and off diagonal terms of scattering matrix, S_{12} and S_{21} are zero. For the convenience, change notations from S_{ii} to S_i. S_1 and S_2 are dimensionless, complex amplitude

functions related to the components polarized perpendicular and parallel, respectively, to the scattering plane. In Equations (3.11) and (3.12), a_n and b_n are the Mie coefficients which are solely dependent on the size parameter $\alpha = \pi D / \lambda$ and the refractive indices $m = n - ik$ of the particles. a_n and b_n are given by:

$$a_n = \frac{\psi_n(\alpha)\psi'_n(\beta) - m\psi_n(\beta)\psi'_n(\alpha)}{\zeta_n(\alpha)\psi'_n(\beta) - m\psi_n(\beta)\zeta'_n(\alpha)} \tag{3-13}$$

$$b_n = \frac{m\psi_n(\alpha)\psi'_n(\beta) - \psi_n(\beta)\psi'_n(\alpha)}{m\zeta_n(\alpha)\psi'_n(\beta) - \psi_n(\beta)\zeta'_n(\alpha)} \tag{3-14}$$

where

$$\beta = m\alpha,$$

$$\psi_n(z) = \left[\frac{\pi z}{2}\right]^{\frac{1}{2}} J_{n+\frac{1}{2}}(z)$$

$$\zeta_n(z) = \left[\frac{\pi z}{2}\right]^{\frac{1}{2}} H^{(2)}_{n+\frac{1}{2}}(z)$$

here, $J_{n+\frac{1}{2}}(z)$ is the half integral order Bessel function and $H^{(2)}_{n+\frac{1}{2}}(z)$ is the half integral order Hankel function of second kind.

Also the angular functions are given by:

$$\pi_n(\cos\theta) = \frac{P_n^{(1)}(\cos\theta)}{\sin\theta}$$

$$\tau_n(\cos\theta) = \frac{d}{d\theta}P_n^{(1)}(\cos\theta)$$

where $P_n^{(1)}(\cos\theta)$ is the associated Legendre polynomial.

These coefficients and the scattering angle dependent functions π_n and τ_n are generally computed by means of recursive formulae. Using these equations and electromagnetic theory, scattering coefficient can be determined by [Mie (1908)]:

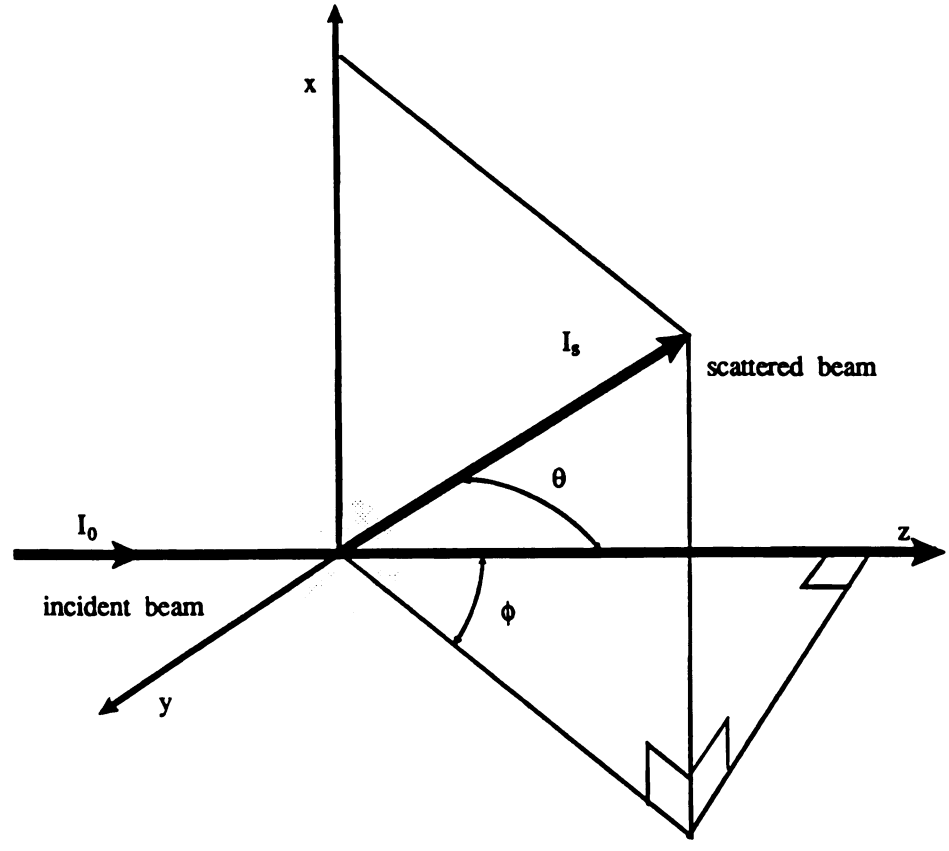

Figure 3-27 Coordinate system of laser light scattering system

$$Q_{sca} = \frac{2}{\alpha^2} \sum_{n=1}^{\infty} (2n + 1)\left[|\, a_n|^2 + |\, b_n|^2 \right] \tag{3-15}$$

Then, scattering cross section may be written as:

$$C_{sca} = \frac{\lambda^2}{2\pi} \sum_{n=1}^{\infty} (2n + 1)\left[|\, a_n|^2 + |\, b_n|^2 \right] \tag{3-16}$$

Another Quantity measured is extinction coefficient, Q_{ext} which can also be delivered from the fundamental extinction theory and Lorentz-Mie theory:

$$Q_{ext} = \frac{2}{\alpha^2} \sum_{n=1}^{\infty} (2n + 1)\mathrm{Re}(a_n + b_n) \tag{3-17}$$

The extinction cross section C_{ext} is given as:

$$C_{ext} = \frac{\lambda^2}{2\pi} \sum_{n=1}^{\infty} (2n + 1)\, \mathrm{Re}(a_n + b_n) \tag{3-18}$$

This quantity is, also, given by Lambert-Beer's law (decay law) as:

$$\frac{I}{I_0} = \exp\left\{ - \int_0^L Q_{ext}(s)ds \right\} \tag{3-19}$$

The sizes of scatterers are usually not uniform, so it is useful to use their mean values. To calculate mean values of the quantities introduced above, the relative frequency of occurrence of the various sizes in population may be expressed by the size distribution function, $P(D)$ which is defined as:

$$p(D_1 < D < D_2) = \int_{D_1}^{D_2} P(D)\, dD \tag{3-20}$$

where the left hand side represents the probability of occurrence of diameters in the range between D_1 and D_2. Undoubtedly, the best known distribution function is the normal distribution function. But a normal distribution function can not represent a distribution of particle size because it admits negative values of D. In addition, unlike the symmetrical normal distribution, naturally occurring populations are frequently positively skewed. A satisfactory representative of many such populations is the logarithmic normal distribution. A generalized logarithmic distribution function is represented by:

$$P_n(D) = \frac{1}{\sqrt{2\pi}\sigma_n} \exp\left[- \frac{\left[\ln D - \ln D_n \right]^2}{2\sigma_n^2} \right] \tag{3-21}$$

Espencsheid, Kerker, & Matijevic (1964) suggested zeroth order ($n = 0$) for works such as particle sizing with light scattering measurements. The zeroth order logarithmic distribution function, then can be derived as normalizing Equation (3-21), and can be written as :

$$P(D) = \frac{1}{\sqrt{2\pi}\,\sigma_0\,D_M\,\exp\left[\sigma_0^2/2\right]}\,\exp\left[-\frac{\left[\ln D - \ln D_M\right]^2}{2\sigma_0^2}\right] \tag{3-22}$$

It is defined by two parameters, D_M, which is the modal value of D, and σ_0, which is a measurement of the width and the skewness of the distribution. σ_0 is related to the standard deviation in a manner which will be turned the zeroth order logarithmic standard deviation.

Since soot particles in the flames are not uniform, the optical properties should be recalculated with size distribution function. As mentioned above, scattering coefficients and extinction coefficient are expressed by infinite series. For the small particles, it is useful to use Rayleigh approximation, while nonlinear regression algorithm of Mie theory is useful for larger particles.

Rayleigh Approximation

When particle sizes are small compared with the wavelength of light ($D \leq \lambda$), all terms but the first in the Mie series are small and Rayleigh approximation can be used. The mean scattering coefficient is given from Rayleigh approximation as:

$$Q_{vv} = \frac{F(m)}{4}\left[\frac{\pi}{\lambda}\right]^4 N \int_0^\infty P(D)\,D^6\,dD \tag{3-23}$$

where

$$F(m) = \left|\frac{m^2-1}{m^2+2}\right|^2$$

and

$$Q_{ext} = \frac{\pi^2}{\lambda}\,E(m)\,N \int_0^\infty P(D)\,D^3\,dD \tag{3-24}$$

where

$$E(m) = -\,\mathrm{Im}\left[\frac{m^2-1}{m^2+2}\right]$$

where the $\int_0^\infty P(D)\, D^n\, dD$ are n^{th} moments of particle size distribution $P(D)$. The subscription vv denotes the polarization direction of scattered and incident light, respectively.

A generalized mean diameter or moment ratio is useful for calculations of soot particle parameters and is defined by

$$D_{pq} = \left[\frac{\int_0^\infty P(D) D^p \, dD}{\int_0^\infty P(D) D^q \, dD} \right]^{1/(p-q)} \tag{3-25}$$

Thus, the particle volume fraction can be calculated with this generalized diameter as:

$$f_v = \frac{\pi}{6} N \, D_{30}^3 \tag{3-26}$$

or

$$f_v = \frac{\lambda Q_{ext}}{6\pi \, E(m)} \tag{3-27}$$

The particle diameter obtained from the ratio of Equations (3-23) and (3-24) is the sixth to third moment ratio D_{63}. The diameter D_{63} can then be related to the measured values of Q_{vv} and Q_{ext} as:

$$D_{63} = \lambda \left[\frac{4}{\pi^2} \frac{E(m)}{F(m)} \frac{Q_{vv}}{Q_{ext}} \right]^{1/3} \tag{3-28}$$

The particle number density can be determined from Equation (3-26) only if D_{63} can be related to D_{30}. The very high particle concentration within the flames suggest that the self-preserving particle size distribution function is applicable [Lai, Friedlander, Pich, & Hidy (1972), and Graham & Robbinson (1976)]. Using the exponential approximation of the self-preserving distribution function, the ratio $(D_{63}/D_{30})^3$ is found to be equal to 2.0 [Graham *et al.* (1976)], which also applies to logarithmic

normal distribution function of intermediate width. In this case the number density is given by:

$$N = \frac{12 f_v}{\pi D_{63}^3} \tag{3-29}$$

Note N and $P(D)$ are functions only of the axial direction in the measuring coordinate system because of the one-dimensional property of axisymmetric counterflow diffusion flames, and therefore, both Q_{vv} and Q_{ext} are position dependent.

Mie Regime

Optical properties in the Mie regime are more diverse and therefore contain greater information about the scattering field. The consequence is that both mean size and width of the distribution function can be deduced if the particle sizes lie in the Mie regime ($D \approx \lambda$).

For particles of arbitrarily large size of specified refractive index the values of D_{63} and N must be calculated from the observations. Since the quantities are expressed as ratios they are independent of particle density and are solely properties of the local D_{63} and σ_0. This can be accomplished in a trial and error manner by searching through the D_{63}-σ_0 space until suitable agreement with observed quantities is achieved. A more systematic method is afforded by the solution to the non-linear least squares problem. The Levenberg-Marquart algorithm has been found advantageous for this purpose. The soot particles generated from the counterflow diffusion flame for this research are not in this regime.

3.3.2 Laser-Induced Fluorescence Measurements

Laser-induced fluorescence (LIF) was used as non-intrusive diagnostic for polycyclic aromatic hydrocarbons (PAH) in the diffusion flames. PAH have been proposed as important intermediates in the soot formation process (Crittenden & Long, 1973;

Bittner, Howard, & Palmer, 1982; Prado *et al.*, 1984). Then, the knowledge of their concentrations in flames is important for understanding the sooting mechanism.

There are two techniques to measure PAH concentrations in diffusion flames: gas chromatograph analysis of PAH collected with a quartz-microprobe, and laser induced fluorescence measurement. Direct sampling and subsequent chemical analysis may produce primary importance but have their limitation. They are time-consuming and the results are often inaccurate, specially, for the species of which concentration is very small (smaller than 1 ppm) in the flame. It is generally assumed that the strong broadband fluorescence stimulated by the blue and green lines of the argon ion laser is due to the PAH present in the flames (Coe, Haynes and Steinfeld, 1981). Comparisons between the fluorescence emission profiles and the measured PAH concentration in the flames suggests that this class of compounds should be responsible for this effect. So, for the present study, laser induced fluorescence measurement was chosen to measure PAH concentration profile in the counterflow diffusion flames.

To obtain an LIF signal, the wavelength of the laser is tuned to match an absorption of the species of interest. Those molecules absorb the laser photons and are thus elevated to an electronically excited state. Then the molecules emit photons to come back to stable state which may be different state from previous state. These emitted photons which is fluorescence are detected by filtered photomultiplier.

The individual PAH of interest include naphthalene, pyrene, fluoranthene, phenanthrene, anthracene, benzpyrene, and others. In combustion environments many PAH will be present in varying concentrations, so that detection of an individual species requires deconvoluting the complex spectra from the multicomponent mixture. This requires a detailed knowledge of excitation and fluorescence spectra for individual species under flame conditions. Table 3.1 (Coe, Haynes & Steinfeld, 1981) lists species expected to be present in sooting flames and their fluorescence wavelengths. Comparison of these spectra with those obtained from the diffusion flame indicates that

acenapthylene is the dominant fluorescing species in this flame.

TABLE 3.1 : Major PAH and their Fluorescence Maxima

Species	Formula	Fluorescence Maxima (nm)
Benzene	C_6H_6	275
Indene	C_9H_8	323
Napthalene	$C_{10}H_8$	330
Acenapthalyene	$C_{12}H_{10}$	510
Toluene	C_7H_8	280
Stylene	C_8H_8	300
Anthracene	$C_{14}H_{10}$	400
Phenanthrene	$C_{14}H_{10}$	360
Methylnapthalene	$C_{11}H_{10}$	330
Trimethylbenzene	C_9H_{12}	290
Pyrenen	$C_{16}H_{10}$	390
Fluorene	$C_{13}H_{10}$	305
Biphenyl	$C_{12}H_{10}$	310
Fluoranthene	$C_{16}H_{10}$	460

Therefore, it is proposed that green fluorescence always has a large contribution from hot acenapthylene and will become important contributors to the total fluorescence signal. So, for the present study, 488 nm of wavelength was used as excitation wavelength while 514.5 nm is used as the detection wavelength.

The experiments were performed by using same optical measuring system which is used for laser light scattering measurements with slight modification. Figure3-28 shows the schematic of the experimental set up. The incident beam (488 *nm* wavelength) was chopped by the chopper to avoid the background intensity from the

flame, and focused by the focusing lens. The fluorescence emitted by excited PAH species was collected by the focusing lens and detected by the PMT tube after being filtered by the laser line interference filter with a 9 *nm* bandwidth with center about 514.5 *nm* wavelength. The fluorescence intensity detected by PMT is stored in computer memory.

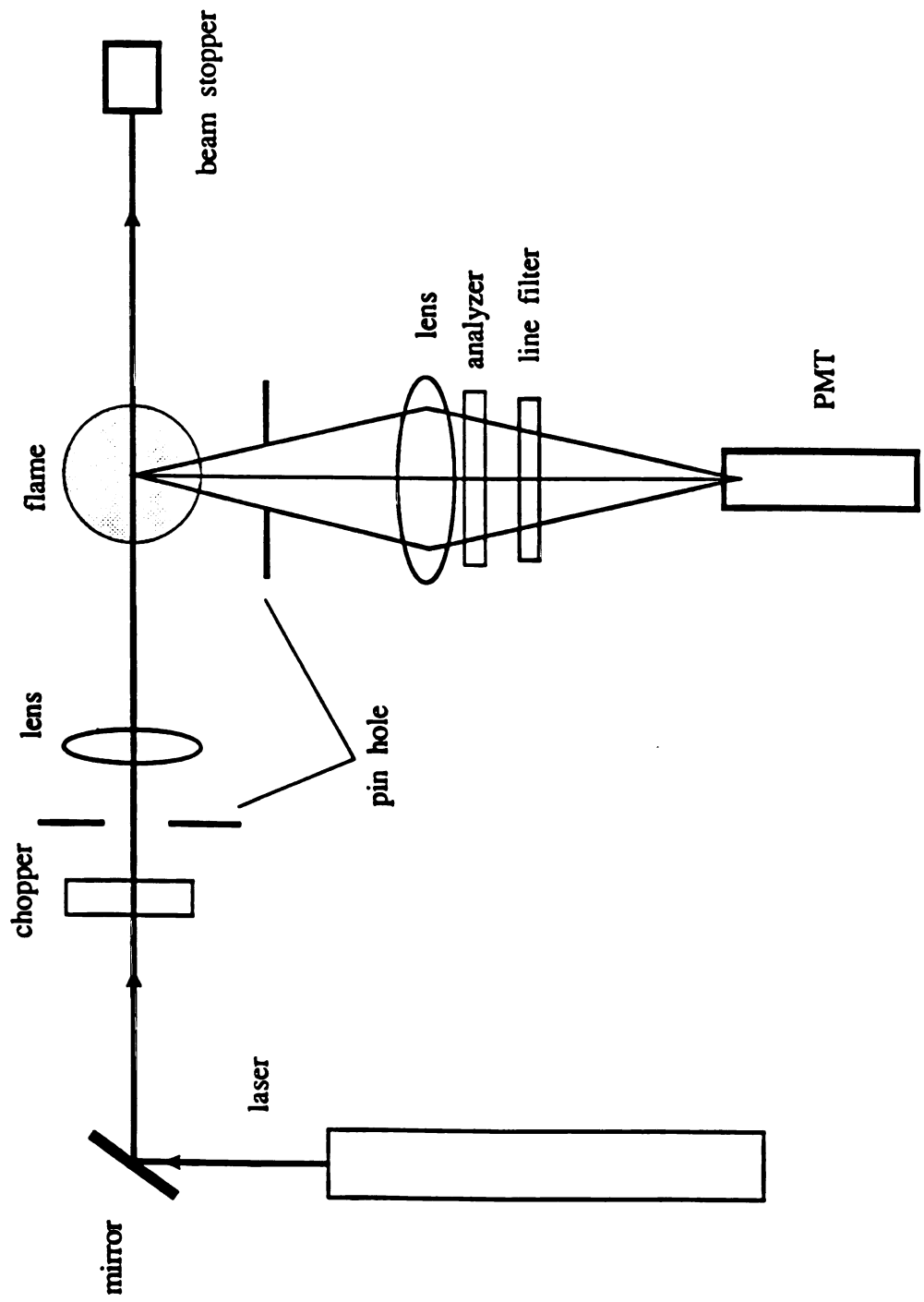

Figure 3-28 Schematic of laser induced fluorescence measurement system

Chapter 4

EXPERIMENTAL PROCEDURE AND RESULTS

Experiments were conducted for several different methane/air counterflow diffusion flames. These flames were selected to keep the methane and oxygen concentrations constant for the given pre-heat temperature. Temperature, chemical species concentrations, soot particle size, soot number density and soot volume fraction are measured for analysis of soot formation and oxidation across the counterflow diffusion flame. In this chapter, flame conditions used and experimental procedure employed for the present study are introduced and then their results are discussed.

4.1 Experimental Conditions and Procedure

As described earlier in chapters 2 and 3, the equipment is capable of independently controlling the parameters that affect the flame. These are: strain rate, pre-heat temperature, fuel and oxidizer concentrations, and additive species. Since these parameters are controlled basically in the burner system, it is necessary to examine the fuel and the oxidizer gas supply system.

4.1.1 Gas Supply System

Figure 4-1 shows the schematic of the gas supply system.[1)] Gas from the gas cylinder was filtered by a line filter of size 1.0 μm to prevent the sonic orifices from being plugged by foreign material. This filtered gas should pass through one of the two paths (Hi or Lo) for adjusting proper flow rate to establish a stable flame for a long enough period to measure all the parameters. Two different sizes of sonic orifices for

1) This gas supply system was designed and constructed by Mr. Kenneth Miller.

each gas flow were used for these two paths (Hi and Lo) to cover the whole range of gas flow rates.

When the sonic condition exists at the throat of orifice, flow rate depends on the upstream pressure and orifice area. This sonic orifice can control the flow rate very accurately and can keep the flow rate stable as far as gas cylinder pressure is high enough to deliver the desired pressure at the orifice. This system is also very useful to add gaseous additives to the flow at the downstream of the orifice without changing the flow rate of other gases. This is because the flow rate does not depend on downstream pressure.

The flow rate was calibrated with the upstream pressure for each orifice and for different gases. For the gas flow rate calibration, soap bubble flow meters were used to measure exact amount of gas flow. 50 *ml* volume of bubble flow meter was used for small gas flow rate. For large volume flow rate, larger volume of bubble flow meter was constructed using acrylic cylindrical tube (50 *mm* in diameter and 120 *cm* long). Upstream pressure was measured by a very accurate pressure gauge (PG in Figure 4-1) installed on the system. This pressure gauge can measure the range from 0 to 160 psi with 0.5 psi small scale span. The calibration curve between the gas flow rate and the upstream pressure was obtained within an error of ± 0.05 % of flow rate. This calibration curve was obtained for each orifice for each gas used for the experiments.

For additive gases (such as CO_2, H_2O and He gas), rotameters were used to measure the flow rates. The rotameter measures the flow rate based on the balance of drag force and the weight of the float. Thus, the rotameter also needs a different calibration curves for different gases. Calibration curves for the rotameters were also obtained by using the soap bubble flow meters. The calibration curve was obtained for each rotameter for the several different gases that were used. These calibration curves were obtained in ± 0.1 % error.

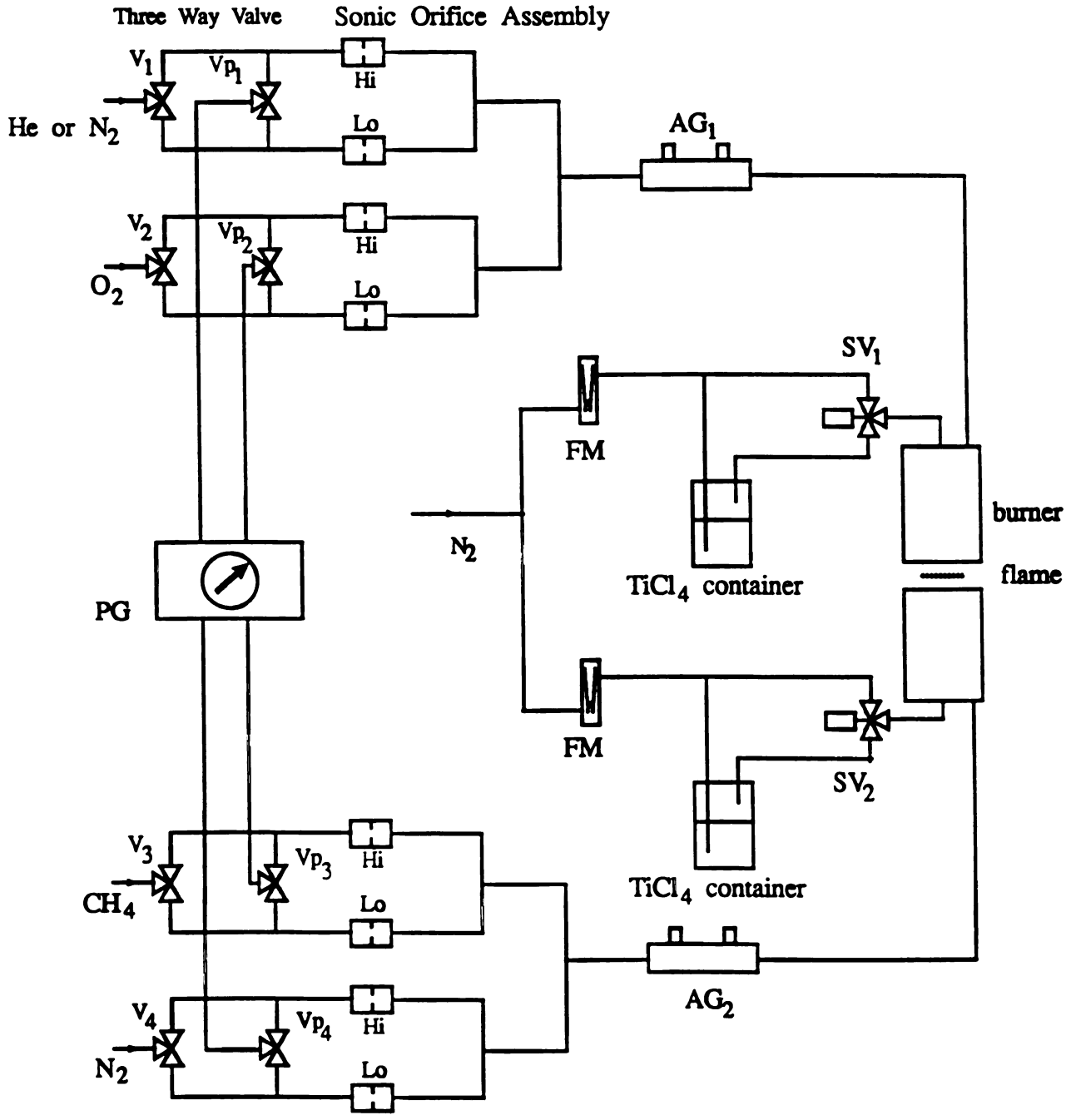

Figure 4-1 Schematic of the gas supply system and $TiCl_4$ supply system
Hi ; High flow rate sonic orifice, Lo ; Low flow rate sonic orifice,
AG_1, AG_2 ; Additive gas connectors, FM ; Flow meter
V_1,V_2,V_3,V_4 ; Three way valves for selecting high or low flow rate,
Vp_1,Vp_2,Vp_3,Vp_4 ; Three way valves for pressure gauge,
PG ; Pressure gauge, SV_1, SV_2 ; Solenoid valves for $TiCl_4$ fume.

The gases from the sonic orifices and additive gases added at additive gas connectors (AG1, AG2 in Figure 4-1) were mixed to be homogeneous mixture while they were passing through a long (about 3 *m*) 6.35 *mm* tube. This tube is composed of a high pressure polyester tube (about 2 *m* and it can be used upto 180 psi) and a flexible stainless steel tube (about 1 *m*). The flexible stainless steel tube was heated to avoid that the cold gas reaches the hot spot in the burner at high temperature pre-heat condition. These well mixed homogeneous gas mixtures after passing through the long narrow tube were delivered to the burner to establish counterflow diffusion flame in the gap between the upper and lower parts of the burner.

4.1.2 $TiCl_4$ Vapor Supply System

Flow visualization was used for both flames and non-reactive flows in the gap between the upper part and lower part of the burner. This was done by means of the TiO_2 particles generated by titanium tetra chloride ($TiCl_4$) when exposed to moisture. $TiCl_4$ is a light yellow liquid with a pungent acid smell. The liquid develops dense, white particles when brought in contact with moisture, as a consequence of the reaction:

$$TiCl_4 + 2H_2O \rightarrow TiO_2 + 4HCl \tag{4-1}$$

For visualization of the stagnation point flow, vapor should be released as short period as possible to reduce the flow disturbance by injection. In chapter 3, flow visualization was described when the one-dimensional stagnation point flow was confirmed in air flows. For the purpose of chapter 3 (see section 3.1.4 and Figure 3-9) flow disturbances was the concern and for that reason, Figure 3-9 was taken with no flame. But for the flame structure measurement, even small amount of additives may distort the diffusion flame. Therefore, it is necessary to release $TiCl_4$ vapor as short period as possible and measure it at last moment of the visualization process.

The average particle size of $TiCl_4$ vapor, as mentioned in chapter 3, is 1.1 μm. The larger sized particles (~ 15 μm) are a consequence of high concentration of TiO_2 particles in the vapor. For the spherical particles whose density is much greater than the fluid density, the particle relaxation time (Mazumder, Kirsch, 1975; Regan *et al.*, 1987) is given by;

$$\tau = \frac{\rho_p d_p^{\,2}}{18\eta} \tag{4-2}$$

where ρ_p is the particle density (= 4.17 g/cm^3), d_p is the particle diameter, and η is the average gas viscosity.

The Lagrangian macro-time scale of the turbulence can be estimated by $t = \varepsilon/v'^2$ where ε is the momentum eddy diffusivity and v'^2 is the turbulent intensity. Given Stokes law assumption for a particle, the basic parameter which determines the faithfulness of the particle following a turbulent flow is the ratio of τ to t. If $\tau/t \ll 1.0$, a particle will completely follow the turbulent fluctuations. A practical limit of $\tau/t \leq 0.02$ will ensure that the particles essentially follow the flow (Lilley, 1973). Therefore, the particle size should be selected to satisfy the following relation

$$\rho_p d_p^{\,2} \leq \frac{0.36\,\eta\,\varepsilon}{v'^2} \tag{4-3a}$$

The flow properties, for example, are calculated with $TiCl_4$ fumes in turbulent air flow whose K.E. = $\frac{2}{3} v'^2 = 4.65 \times 10^3$ cm^2/sec^2 and at $\mu = 1.42 \times 10^{-3}$ g/cm-sec. For this calculation, the size of the particle which will follow this air flow is $d_p \leq 1.157$ μm.

For the present study, the reciprocal of strain rate can be used for the time scale t. Then, Equation (4-3a) becomes for the maximum strain rate with given particle size:

$$\textit{strain rate} \leq \frac{0.36\,\eta}{\rho_p d_p^{\,2}} \tag{4-3b}$$

The maximum strain rates were calculated for two different TiO_2 particle sizes. For the average particle size (1.1 μm), the result were: the maximum strain rate are 1300 sec^{-1} for 300 K flame, 2700 sec^{-1} for 900 K flame, and 3300 sec^{-1} for 1200 K flame. The maximum strain rates were also calculated for the larger particle size (15 μm), and it showed that: the maximum strain rates are 7.1 sec^{-1} for 300 K flame, 15.0 sec^{-1} for 900 K flame, and 18.0 sec^{-1} for 1200 K flame. For these calculations, the air viscosity at each pre-heat temperature condition was used. From these calculated maximum strain rates using average particle size (1.1 μm) and larger particle size (15 μm), it was shown that $TiCl_4$ vapor and TiO_2 particles follows the low strain rate stagnation point flow.

The visualization process for the flames can be explained from Figure 4-1. $TiCl_4$ is introduced into the flame, when the solenoid valves (SV_1 and SV_2 in Figure 4-1) are open, by a dry inert gas (N_2) flowing through the $TiCl_4$ container. Then, as shown in Figure 4-1, the dry inert gas carries the $TiCl_4$ vapor to the reaction zone where $TiCl_4$ converts TiO_2. This flow visualization technique was used to verify the flow conditions in the flame and to determine the stagnation plane location.

4.1.3 Experimental Conditions and Flames

A pure diffusion flame is established in the zone of impingement of two opposed gaseous flows of the fuel and the oxidizer. A mixture of O_2 and inert gas is supplied from the upper part (oxidizer stream) and a mixture of CH_4 and inert gas is supplied from the lower part (fuel stream) (see Figure 4-1). Methane diffuses into the oxidizer side and establishes a diffusion flame on the oxidizer side of the stagnation plane. Here, it must be emphasized that this flame configuration is one-dimensional in temperature, gas concentrations, and soot fields which are all scalar variables. As mentioned in chapter 3, this is the primary reason for choosing the axisymmetric counterflow diffusion flame for the present study.

Figure 4-2 shows a typical configuration of a sooty flame. The flame is on the oxidizer side of the stagnation plane and soot particles are formed and grow between the flame and the stagnation plane. Since the oxidizer passes through the reaction zone, very small amount of oxygen exists in this sooting zone. Major species in this region are the combustion products, such as CO_2 and H_2O. Therefore, the effects of temperature and the concentrations of CO_2 and H_2O on the soot formation and oxidation were chosen as primary parameters for the present study.

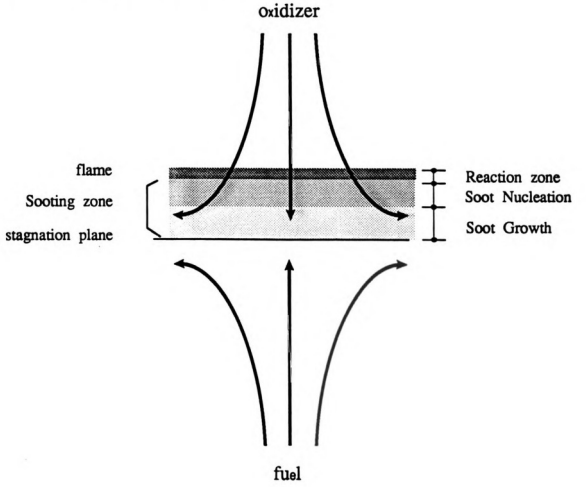

Figure 4-2 Typical sooting configuration in counterflow diffusion flame.

A series of experiments were conducted with average pre-heat temperatures of 300 K, 900 K, and 1200 K. The methane concentration in the fuel stream was held

constant at 65 % for all the experiments. The oxygen concentration was reduced as the pre-heat temperature was increased. The oxygen concentration for 300 K pre-heat temperature experiments was held at 16 %, for 900 K experiments it was 11 %, and for 1200 K experiments it was 9.7 %. The oxygen concentration was reduced primarily to approach a purely sooting flame without soot particle oxidation. This reduction of oxygen concentration helped to make it possible to measure the chemistry in the sooty flame. Increasing pre-heat temperature produces more soot in the flame and the heavy soot loading always makes the chemistry measurements difficult due to clogging of the microprobe.

The choice of diluent for methane and oxygen is an important factor in soot formation study. Basically, N_2 was chosen as a primary diluent of methane and oxygen. For 900 K and 1200 K pre-heat conditions, the temperature of oxidizer stream is higher than that of fuel stream. So, a stable diffusion flame can be established in this density profile when N_2 is used as diluent of both streams. But for 300 K experiments, if N_2 is used as diluent of both streams, reverse density profile makes the diffusion flame unstable, as mentioned in section (3.1.5). So, for the 300 K experiments helium was chosen to overcome the buoyancy problem and to establish a stable low strain rate flame. He gas flow rate was calculated to maintain the mass flow rate of oxidizer close to that of the oxidizer stream when N_2 is used as diluent. This gives the momentum of the flow and the strain rate close to those of other flames. So, the volume flow rate of oxidizer stream at 300 K pre-heat condition is bigger than that at 900 K and 1200 K pre-heat conditions. That is, the velocity at the honeycomb exit of upper part of the burner was 6.00 *cm/sec* which is slightly higher than that in the other conditions (~ 4.0 *cm/sec*) which N_2 was used as diluent of oxygen.

For experiments on the effect of combustion products on soot formation and oxidation, CO_2 or H_2O were added into the oxidizer or the fuel stream as an additive gas. When the additive gas was added, the concentrations of each components in the

mixture was calculated to maintain the same strain rate and temperature profile. This can be accomplished by maintaining the mass flow rate, volume flow rate, and thermal capacity constant.

For this purpose, the amount of the additive gas mixture was calculated based on the adiabatic flame temperature and molecular weight of the mixture. In order to have the same adiabatic flame temperature and molecular weight after adding the additive gas, the additive gas should have very close property to that of nitrogen and nitrogen should be replaced by this additive gas mixture. Since molecular weights of CO_2 and H_2O are larger than nitrogen molecular weight, the additive gas mixture can be made of CO_2 and He or H_2O and He. Adiabatic flame temperature, mass flow rate, and volume flow rate were calculated with concentrations of nitrogen, CO_2 and He. From this calculation, two additive gas mixtures were chosen as: ratios of CO_2 to He are 12 to 8 and 21 to 14.

Table 4.1 lists the conditions of the flames used in this work. This table shows the names, flow rates, and gas concentrations. The flames are named according to the following convention. The names are composed of 2 or 3 letters. The first letter stands for the additive gas and its concentration. **B** (for **B**asic) is for the flame without additive gases. **I** (for **I**ntermediate) represents that 12.0 % CO_2, while **M** (for **M**aximum) indicates 21.0 % CO_2. **W** (for **W**ater) stands for the case of 3.6 % water vapor addition. The second letter is reserved for the pre-heat temperature. **A** stands for 300 K, **B** for 900 K, and **C** for 1200 K series of experiments. The third letter identifies the stream to which the additive gas was added. Here, **O** represents the oxidizer stream and **F** represents the fuel stream.

For a given pre-heat temperature, experiments were conducted to study the effect of CO_2 by replacing a mixture of CO_2 and He to the fuel or the oxidizer stream. This series of experiments show the effect of CO_2 concentration on soot oxidation in the flame. It also showed how the effect is different if CO_2 is added to the fuel stream or

Table 4.1: Experimental flame conditions

Flame		Fuel Stream					Oxidizer Stream				
		CH4	N2	CO2	He	H2O	O2	N2	CO2	He	H2O
1. 300 K Experiments.											
BA	%	65	35	-	-	-	16	-	-	84	-
	l/min	4.687	2.524	-	-	-	1.822	-	-	9.566	-
IA	%	65	15	12	8	-	16	-	-	84	-
	l/min	4.687	1.082	0.865	0.577	-	1.822	-	-	9.566	-
MA	%	65	0	21	14	-	16	-	-	84	-
	l/min	4.687	0	1.514	1.010	-	1.822	-	-	9.566	-
WAF	%	65	31.4	-	-	3.6	16	-	-	84	-
	l/min	4.687	2.264	-	-	0.260	1.822	-	-	9.566	-
WAO	%	65	35	-	-	-	16	-	-	80.4	3.6
	l/min	4.687	2.524	-	-	-	1.822	-	-	9.156	0.410
		Q = 7.211 l/min		v = 3.79 cm/sec			Q = 11.388 l/min		v= 6.00 cm/sec		
2. 900 K Experiments											
BB	%	65	35	-	-	-	11	89	-	-	-
	l/min	4.308	2.320	-	-	-	0.798	6.225	-	-	-
IBF	%	65	15	12	8	-	11	89	-	-	-
	l/min	4.308	0.994	0.795	0.530	-	0.798	6.225	-	-	-
MBF	%	65	0	21	14	-	11	89	-	-	-
	l/min	4.308	0	1.392	0.927	-	0.798	6.225	-	-	-
IBO	%	65	35	-	-	-	11	69	12	8	-
	l/min	4.308	2.320	-	-	-	0.798	4.846	0.843	0.562	-
MBO	%	65	35	-	-	-	11	54	21	14	-
	l/min	4.308	2.320	-	-	-	0.798	3.792	1.475	0.983	-
		Q = 6.628 l/min		v = 3.5 cm/sec			Q = 7.023 l/min		v= 3.7 cm/sec		
3. 1200 K Experiments											
BC	%	65	35	-	-	-	9.7	90.3	-	-	-
	l/min	4.575	2.464	-	-	-	0.723	6.733	-	-	-
MCF	%	65	0	21	14	-	9.7	90.3	-	-	-
	l/min	4.308	0	1.479	0.985	-	0.723	6.733	-	-	-
WCF	%	65	31.4	-	-	3.6	9.7	90.3	-	-	-
	l/min	4.575	2.211	-	-	0.253	0.723	6.733	-	-	-
		Q = 7.039 l/min		v = 3.70 cm/sec			Q = 7.456 l/min		v= 3.92 cm/sec		

the oxidizer stream. This series also shows the effect of H_2O concentration which can be readily compared with the effect of CO_2 concentration.

4.1.4 Normalization of Flame Coordinate System

The location of the maximum temperature and the stagnation plane for each flame were measured. This measured maximum temperature location is used as the flame location in the present study and the thickness between the stagnation plane and the maximum temperature location is defined as the flame thickness.

The maximum temperature location was measured by a thermocouple which is carried by an accurate traversing mechanism. The temperature and the thermocouple location were recorded on the strip chart simultaneously. In order to measure the maximum temperature location, thermocouple was moved from the known reference position to the maximum temperature location relatively fast. The distance between these two points can be obtained by the record from the strip chart.

Stagnation plane location was measured by two different methods. First, it was measured by optical method. Soot particles created above the stagnation plane grow as they flow along stream lines on the oxidizer side of the stagnation plane. Then, most of soot particles leave the flame near the stagnation plane. So, the maximum scattering intensity can be used as a location of the stagnation plane of the sooting flame. To measure the maximum intensity location, scattering intensity was scanned from the known reference position to the maximum intensity location by moving the burner assembly slowly. This distance can be obtained from the scale on the traverse directly.

The second method uses flow visualization by injecting small amount of N_2 carrying $TiCl_4$. Before injecting $TiCl_4$ vapor, a location pointer was inserted into the flame to point around the stagnation plane. The tip of this location pointer was short (~ 2 *cm*) thin steel wire and this wire attached at the end of a long thin ceramic tube. This pointer was carried by a accurate traverse mechanism which was used for

measuring the maximum temperature location. After injecting the $TiCl_4$ fume, the pointer position was corrected to point exact location of stagnation plane. Then, the distance between the stagnation plane and the surface of the honeycomb of lower part of the burner can be obtained from the scale on the traverse.

These measured locations are shown in Table 4.2. The measurement was repeated 10 times for each location. The values in Table 4.2 are the average values of each measurements. Errors in this measurement are explained in section 4.5.2 and table 4.4. The stagnation plane location measured by flow visualization is always slightly higher than that by optical. The differences are in the rage of 0 to 0.32 *mm* but most of differences are within 0.2 *mm*. For the present study the location of stagnation plane by optical mean was used for calculation purpose.

In order to accurately interpret the flame structure and to compare the experimental results of different flames, the axial direction is normalized by the flame thickness. Thus, non-dimensional coordinate is defined as:

$$Z_n = \frac{Z - Z_{st}}{Z_{fl} - Z_{st}} \tag{4-4}$$

where, Z is the axial measurement which represents the distance from the surface of the honeycomb of the lower part of the burner. Z_{fl} and Z_{st} are the locations of the maximum temperature and stagnation plane from the honeycomb surface, respectively. Therefore, 0.0 presents the stagnation plane and 1.0 presents flame location in this normalized coordinate system. All the results presented in the present study are plotted against this non-dimensional coordinate system.

4.2 Temperature Measurements

Temperature is a primary factor for studying flames and is also one of the important parameters of soot formation and oxidation in diffusion flames. Measuring temperature in the flame is one of the difficult tasks in this study. Especially, for heavy

Table 4.2: Flame structures (The locations of maximum temperature and stagnation plane, and the flane thickness.)

1. 300 K Flames — unit : mm

Flames	Max. temperature	Stagnation Plane (a)	Stagnation plane (b)	Flame thickness
BA	15.00	8.74	9.01	6.27
IA	15.00	8.76	8.99	6.24
MA	15.00	8.61	8.80	6.39
WAF	14.97	8.55	8.75	6.43
WAO	15.09	8.67	8.87	6.42

2. 900 K Flames

Flames	Max. temperature	Stagnation Plane (a)	Stagnation plane (b)	Flame thickness
BB	15.62	8.33	8.51	7.29
IBF	15.80	8.33	8.55	7.47
MBF	15.35	8.20	8.45	7.15
IBO	15.48	8.20	8.52	7.28
MBO	15.53	8.74	8.74	6.79

3. 1200 K Flames

Flames	Max. temperature	Stagnation Plane (a)	Stagnation plane (b)	Flame thickness
BC	16.00	8.19	8.37	7.81
MCF	15.50	8.43	8.61	7.07
WCF	15.60	8.55	8.74	7.05

* Max. temperature : flame location.
* Stagantion plane (a) : stagnation plane location by optical measurement.
* Stagnation plane (b) : stagnation plane location by flow visualization.
* Flame thickness : distance between stagnation plane (a) and max. temperature location.

sooting flames (Farrow, Luch, Flower & Palmer, 1984; Eisner & Rosener, 1984; Ang, Pagni, Matagle, & Lyon, 1988). Among the suggested several methods, the most common method is measuring by thermocouple probe.

For the present study, temperatures were measured with 0.0762 mm Pt/Pt-10 % Rh thermocouple probe. These thermocouple wires can be used in the range of 300 K ~ 1800 K without melting in the flames. Because of the radiative heat loss, thermocouple temperature is lower than the surrounding gas temperature. So, it was safe up to 2000 K.

Platinum is also a good conductor of heat transfer. Very often the errors from the conduction from the thermocouple bead to the thermocouple leads occur. Especially, two or three dimensional temperature profiles are suffered from this kind of errors. For the axisymmetric counterflow diffusion flames which have one dimensional temperature property, this effect can be eliminated by using triangle shape thermocouple. Figure 4-3 shows the schematic of thermocouple used for the present study.

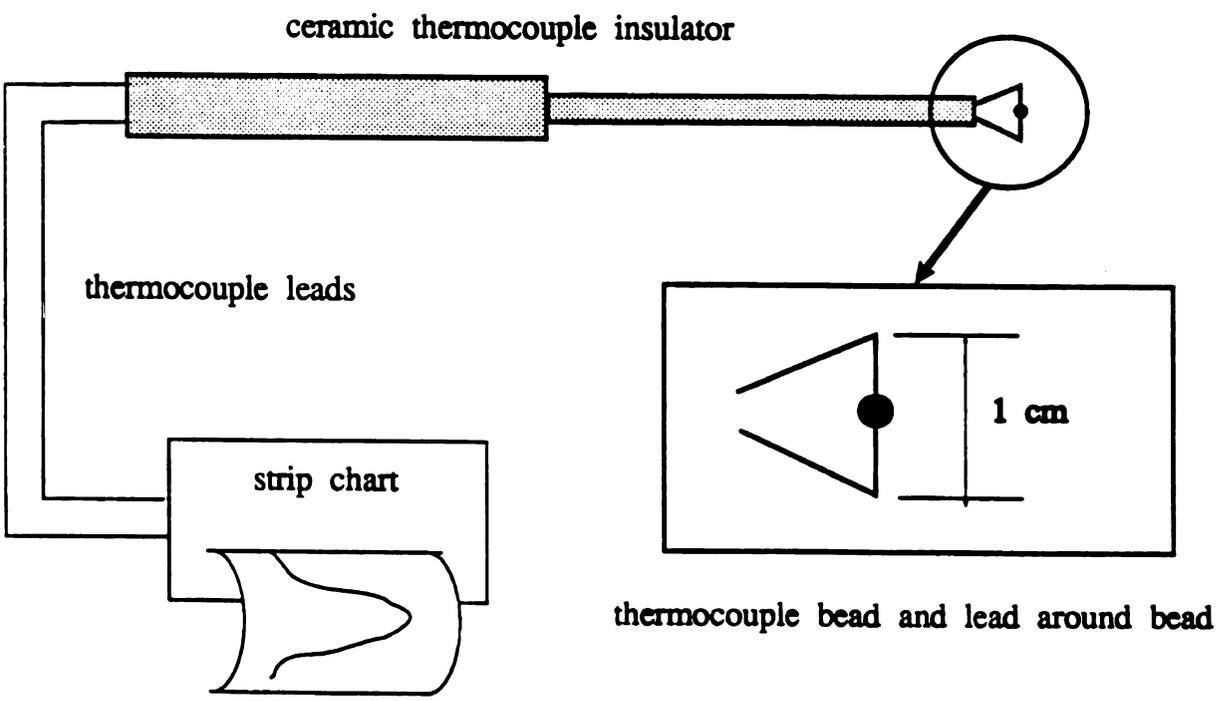

Figure 4-3 Schematic of thermocouple used for measuring temperature in flame.

The thermocouple is coated with silicon dioxide (SiO_2) to prevent reaction from occurring on the catalytic platinum surface. After coated the thermocouple was examined under microscope to check coating thickness and quality. Thermocouple thickness

was measured along the number of coating layers. The best result obtained when the thermocouple coated once and the coated surface uniform. This shows that thermocouple thickness is very important for temperature correction due to radiative loss.

It is well known, for example, that soot deposits on the thermocouple bead, makes it difficult to measure temperature correctly. The presence of soot on the thermocouple bead substantially reduces the measured temperature. Since the bead has a finite response time, it should take enough time to respond the local gas temperature. But longer time gives more possibility to deposit soot on the thermocouple surface. For the present study, a traverse speed of about 0.64 mm/sec was found to be best of reduction of soot deposition on the thermocouple bead. When the thermocouple traveled along the axial direction through the sooting zone, it was also found that the travel direction also affects the soot deposition on thermocouple bead. The direction from the reaction zone toward stagnation plane obtained less soot deposition than the reverse direction.

Temperatures were measured along the axial direction. Temperature measured by thermocouple is lower than the gas temperature because of the radiative heat loss from the bead to the surrounding. This correction for the radiation can be obtained by assuming that a steady state exists between convective heat transfer to and radiative heat loss from the thermocouple. This approach neglects conduction effects along the thermocouple leads. The shape factors, F_{b-i} were determined by using a model of a sphere over a circular plate for upper and lower honeycomb. Here, subscription b stands for the thermocouple bead and i stands for the surface which radiative heat transfer takes place from and to the thermocouple bead. Emissivity of honeycomb is nearly 1.0 because it is assumed as a hole on black body which is burner.

In order to properly characterize the radiative heat loss, the emissivity of thermocouple coated by SiO_2 as a function of measured temperature was investigated. Detail can be found elsewhere (Miller, 1991). The radiative heat loss from the thermocouple

bead to the surroundings using the optically thin approximation can be written as:

$$q_{rad} = \sigma A_b \varepsilon_b \sum_i F_{b-i} \left[T_b^4 - T_{sur\ i}^4 \right] \qquad i = 1, 2, 3 \qquad (4\text{-}4)$$

where i = 1, 2 are for the upper and the lower honeycomb surfaces, and i = 3 is for the surrounding wall which can be seen by thermocouple through the gap between the upper and lower parts of the burner.

And heat gain from the combustion gas to the thermocouple by convection can be written as:

$$q_{conv} = hA_b \left[T_{gas} - T_b \right] \qquad (4\text{-}5)$$

where, σ is the Stephen-Boltzmann constant, ε_b is the thermocouple emissivity, A_b is the thermocouple surface area, T_b is the measured thermocouple temperature, T_{sur} is the surrounding temperature, and T_{gas} is the gas temperature. From the balance of Equations (4-4) and (4-5), temperature correction, ΔT can be obtained as:

$$\Delta T = \frac{\sigma \varepsilon_b d}{Nu_d k} \sum_i F_{b-i} \left[T_b^4 - T_{sur\ i}^4 \right] \qquad (4\text{-}6)$$

where, thermocouple emissivity,

$$\varepsilon_b = 0.8650987 - 2.746295 \times 10^{-4} T_b,$$

thermal conductivity of air which is curve fitted by a third-order polynomial (Ang, Pagni, Matagle & Lyon, 1988),

$$k = 0.0037 + 8.6818 \times 10^{-5} T - 3.595 \times 10^{-8} T^2 + 1.3054 \times 10^{-11} T^3,$$

and $Nu_d = 2.0$ for the range of present flames. The measured upper and lower honeycomb temperatures were used as the surrounding temperatures.

Tables 4.3 shows the typical temperature profiles of measured temperatures ($T_{uncorr.}$), corrected temperatures ($T_{corr.}$), and their differences in Kelvin along the normalized coordinate between the stagnation plane and the maximum temperature

location. For the 300 K flames the correction temperature at stagnation plane is about 90 K and at maximum temperature location is about 180 K. For higher pre-heat conditions, the correction temperatures are much smaller than those for the 300 K flame because the honeycombs temperatures are higher and hence reduces the heat loss to the honeycomb surfaces significantly.

Figures 4-4a, 4-4b, and 4-4c show that corrected temperature profiles for 300 K, 900 K, and 1200 K flames, respectively. All the temperature profiles are almost identical with ± 50 ° C range for given pre-heat temperature. Therefore, if there exists difference in soot formation and oxidation in the flames of different conditions for given pre-heat temperature, it is easily recognized that it is not due to the temperature difference. Instead, it should be due to the difference of chemistry of the fuel and the oxidizer streams.

The maximum temperatures (flame temperatures) were different between 300 K and 900 K flames. This temperature difference was a result of significant reduction of oxygen concentration (5.0 %) in oxidizer stream. Flame temperatures of 1200 K flames was higher than those of 900 K flames. The oxygen concentration difference of these pre-heat conditions was only 1.3 %. The oxygen concentration of 1200 K flame is 1.3 % lower than that in 900 K flames. This temperature increment may be explained by the preheating the gas stream rather than reduction of oxygen concentration. The flame temperature difference was close to the temperature difference at the inlet of the fuel and the oxidizer streams. The temperature profiles (Figures 4-4a, 4-4b, 4-4c) indicated that the temperatures in sooting zone ($0.0 \leq Z_n \leq 0.7$) have similar trend in any pre-heat conditions. The temperatures in this zone for all the flames is in the range of 1200 K to 1700 K. This temperature range for the sooting zone agreed with literatures.

Table 4.3: The comparison of temperatures corrected and measured by thermocouple for BA-flame in the sooting zone. (Zn = 0.0 ; stagnation plane, Zn = 1.0 Flame location.)

unit : Kelvin

Zn	T(corr.)	T(uncorr.)	Diff.
0.000	1,309.3	1,220.1	89.2
0.016	1,320.1	1,229.3	90.8
0.032	1,331.0	1,238.6	92.4
0.048	1,341.9	1,247.9	94.0
0.065	1,353.1	1,257.4	95.7
0.081	1,364.4	1,267.0	97.4
0.097	1,375.8	1,276.7	99.1
0.113	1,387.4	1,286.5	100.9
0.129	1,398.7	1,296.2	102.6
0.145	1,410.0	1,305.7	104.3
0.161	1,420.8	1,314.9	105.9
0.177	1,431.2	1,323.7	107.5
0.194	1,441.4	1,332.4	109.0
0.210	1,451.5	1,340.9	110.6
0.226	1,461.7	1,349.6	112.1
0.242	1,472.0	1,358.3	113.7
0.258	1,482.5	1,367.2	115.3
0.274	1,493.1	1,376.2	116.9
0.290	1,504.0	1,385.5	118.6
0.306	1,515.3	1,395.0	120.3
0.323	1,526.9	1,404.9	122.0
0.339	1,538.8	1,415.0	123.8
0.355	1,550.6	1,424.9	125.6
0.371	1,562.3	1,434.9	127.4
0.387	1,573.5	1,444.4	129.1
0.403	1,585.5	1,454.6	130.9
0.419	1,597.6	1,464.9	132.7
0.435	1,610.4	1,475.7	134.6
0.452	1,622.8	1,486.3	136.5
0.468	1,634.9	1,496.6	138.3
0.484	1,646.4	1,506.4	140.0
0.500	1,657.0	1,515.5	141.5
0.516	1,667.0	1,524.0	143.0
0.532	1,676.8	1,532.3	144.4
0.548	1,687.2	1,541.3	145.9
0.565	1,699.2	1,551.5	147.7
0.581	1,712.2	1,562.6	149.5
0.597	1,726.5	1,574.9	151.6
0.613	1,740.3	1,586.7	153.5
0.629	1,753.9	1,598.5	155.4
0.645	1,766.1	1,609.0	157.1
0.661	1,777.4	1,618.7	158.7
0.677	1,787.6	1,627.5	160.1
0.694	1,797.0	1,635.6	161.4
0.710	1,806.3	1,643.7	162.6

Table 4.3 : Continued

Zn	T(corr.)	T(uncorr.)	Diff.
0.726	1,815.8	1,651.8	163.9
0.742	1,825.5	1,660.3	165.2
0.758	1,835.2	1,668.7	166.5
0.774	1,845.3	1,677.4	167.8
0.790	1,855.7	1,686.5	169.2
0.806	1,867.0	1,696.4	170.6
0.823	1,878.3	1,706.2	172.1
0.839	1,889.0	1,715.6	173.4
0.855	1,899.5	1,724.8	174.7
0.871	1,908.1	1,732.3	175.8
0.887	1,918.1	1,741.1	177.0
0.903	1,930.5	1,752.0	178.5
0.919	1,955.7	1,774.3	181.4
0.935	1,960.5	1,778.6	182.0
0.952	1,962.9	1,780.7	182.2
0.968	1,969.4	1,786.4	183.0
0.984	1,973.7	1,790.2	183.5
1.000	1,974.9	1,791.3	183.6

4.3 Chemical Species Measurements

The species concentrations in the flame were measured by a direct-sampling quartz microprobe and a Perkin Elmer Gas Chromatograph. Samples were drawn from the flame at a flow rate at which no visual distortion was caused in the flame (refer 3.2.1). The quartz microprobe was mounted on the traverse and gas samples were withdrawn from the flames. The location of the sampling position was measured by a distance from the stagnation plane which was measured by optical mean. Errors involved in probe positioning were estimated to be within ± 4 % of one span of the traverse (0.635 *mm*).

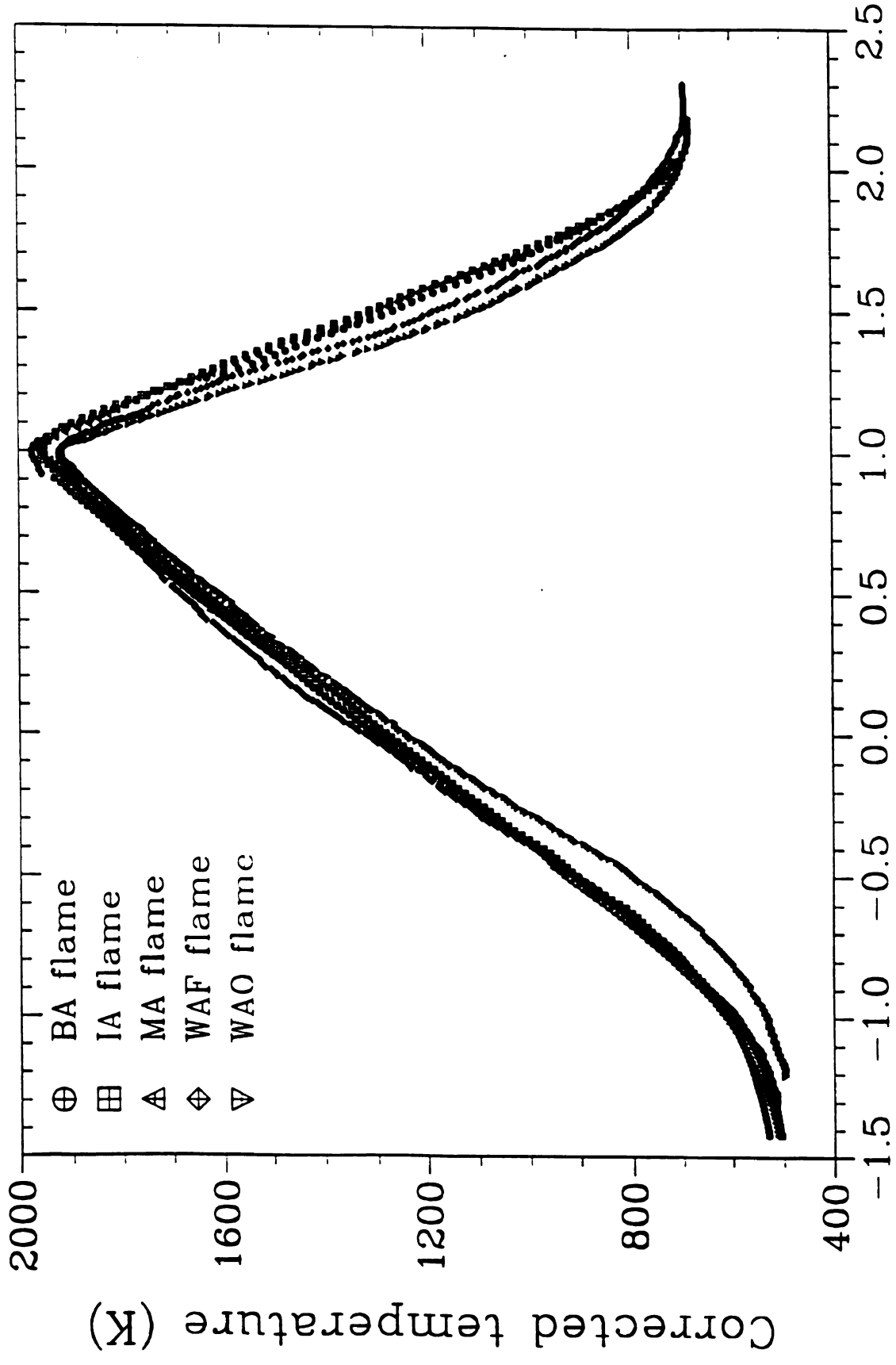

Figure 4-4a Corrected temperature profiles versus normalized coordinate for BA-, IA-, MA-, WAF- and WAO-flame (300 K flames)

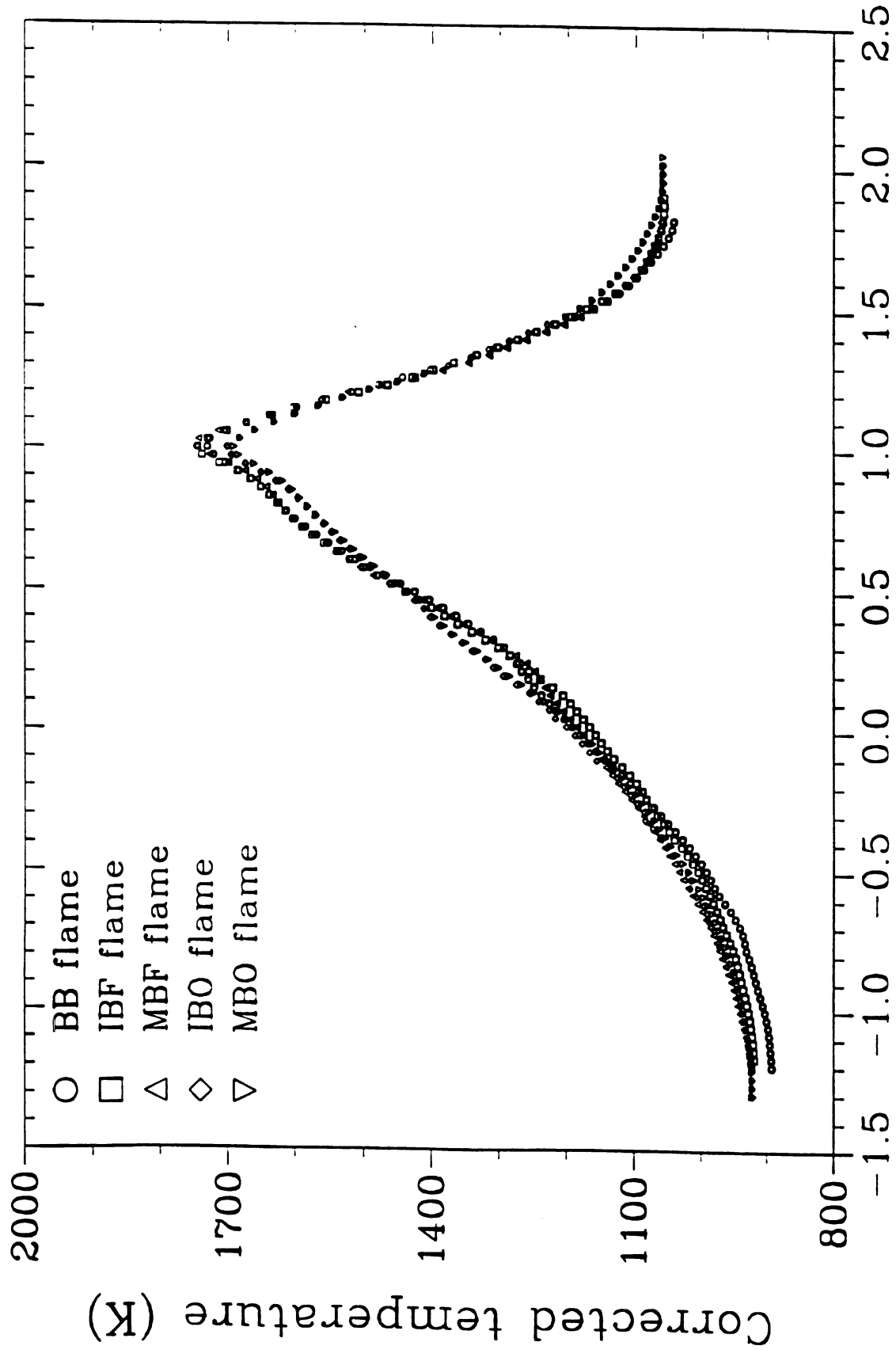

Figure 4-4b Corrected temperature profiles versus normalized coordinate for BB-, IBF-, IBO- MBF- and MBO-flame (900 K flames)

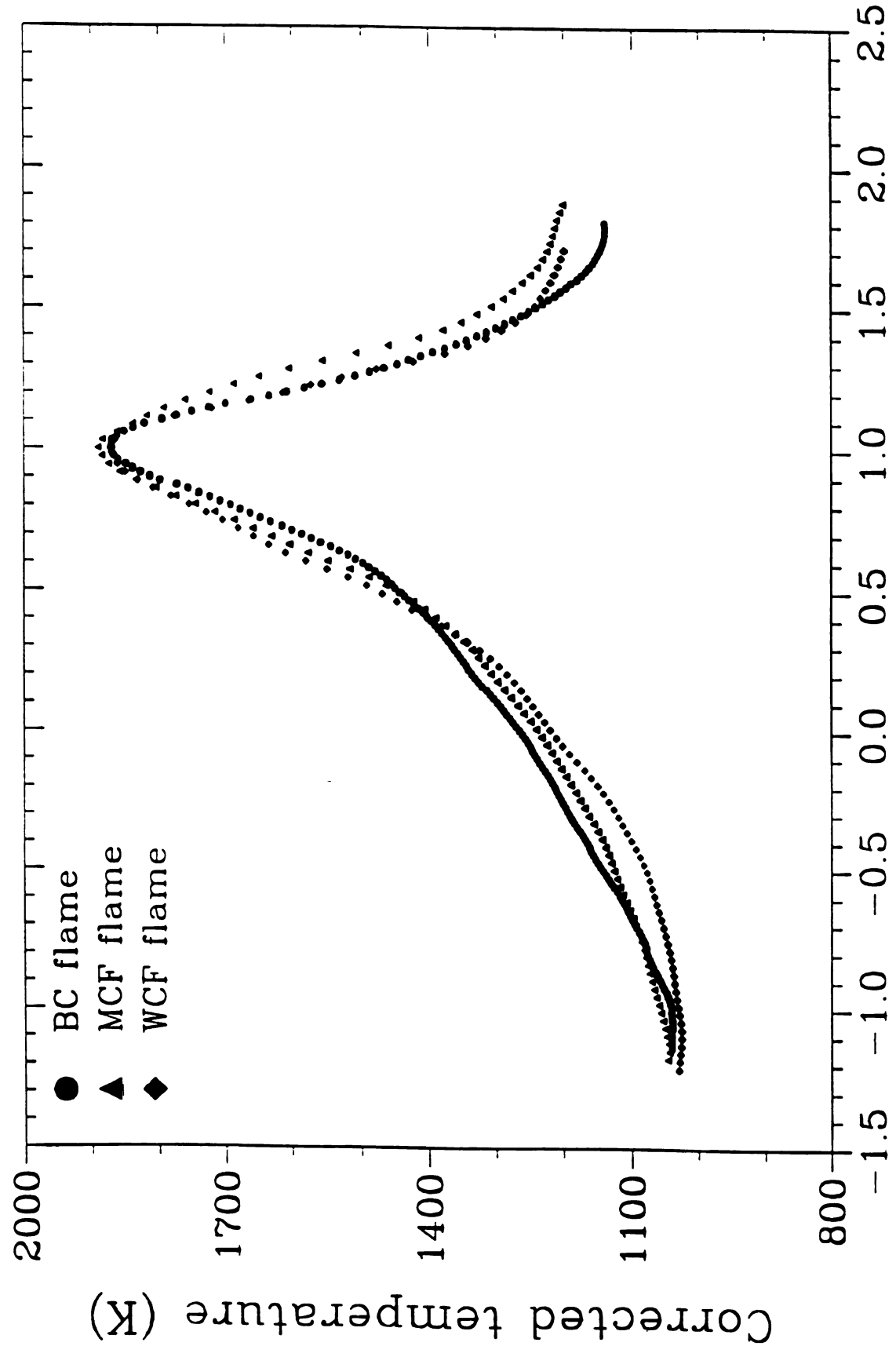

Figure 4-4c Corrected temperature profiles versus normalized coordinate for BC-, MCF- and WCF-flame (1200 K flames)

The gas sample was analyzed based on two different groups of species which are stable species and light hydrocarbons for the present study. Stable gases, which are H_2, CO_2, O_2, N_2, CH_4, CO, H_2O, and He, are composed of the main supplied gases and combustion products. So, these gas concentrations were measured in percent and the summation of these gas concentrations should be close to the unity. The concentrations of light hydrocarbons (C_2 to C_7) were also measured. The concentrations of the hydrocarbons are very small when compared with those of stable species. These hydrocarbon concentrations were measured in the unit of parts per million (ppm).

Figures 4-5 through 4-16 show the concentration profiles of stable gases and hydrocarbons. These two different groups of species are shown on the same normalized coordinate on x-axis. Figures 4-10, 4-14 and 4-16 show the concentration profiles of the BB-, BC- and WCF-flames which does not have Helium gas in the fuel and the oxidizer streams. The column used for analyzing stable species is not capable of measuring the He gas concentration, because He gas was used as a carrier gas. From the summation of the stable species concentrations in each of these three flames, it was found that the good agreement with the ideal mass balance is within ± 10 % throughout the flames, which yields confidence in these results. Therefore, He gas concentration can be obtained by subtraction the summation of the measured concentrations from 100.0 % for the flames which were established by the fuel and the oxidizer streams with He gas.

The methane concentration decreases toward the oxidizer side and disappears almost completely before it reaches the lower edge (Z_n ~ 0.7) of the flame zone. The oxygen concentration decreases sharply toward the flame from the oxidizer side. Carbon dioxide, water vapor, and carbon monoxide (CO_2, H_2O, CO) have their peak concentration in and around the flame zone which corresponds to the sharp disappearance of O_2. It therefore seems that O_2 has been consumed by CO and H_2 to produce H_2O and CO_2 which have their peaks in this region. The inert gases, nitrogen and helium,

change monotonically toward the flame from both the fuel and the oxidizer side.

CO_2 profile in the flames, to which CO_2 is added, has different characteristic in the profile. It reduces slowly from the added side until it is produced from the chemical reaction, then increased until reaches local peak concentration. Finally, the CO_2 concentration decreases to zero. This CO_2 profile in these flames is not similar to the CO_2 profile in the flames without adding CO_2. When the CO_2 gas is added in the fuel or the oxidizer stream, CO_2 profile has a superimposed image of the profile of conserved gas, like N_2, and that of CO_2 gas generated in the flame.

H_2O profile should have same trend that CO_2 showed. But in this case, the mole fraction added into the stream was quite small compared with the amount generated in the flame. So, the superimpose image of H_2O was not shown clearly in the profiles (Figures 4-8, 4-9, 4-16).

Mole fraction of light hydrocarbons were illustrated in the same figures. In this study, light hydrocarbons have been analyzed up to the toluene (C_7H_8). However, only those hydrocarbons with concentrations exceeding 50 ppm were plotted.

The width of hydrocarbon profiles are narrower than those of the stable species. Most of hydrocarbons are formed at around the stagnation plane, increased quickly up to its peak and depleted quickly before the flame zone. The C_2H_2 concentration is highest value among the measured hydrocarbons. This species has the simplest structure with C and H atoms. It may be said that C_2H_2 is basic species of the soot particles.

Adding additive gas reduces hydrocarbon concentration significantly. Especially, C_2H_2. For the given pre-heat temperature, the peak value of C_2H_2 concentration reduced when the CO_2 or H_2O concentration increased in the inlet stream. The location of peak C_2H_2 concentration was also moved toward fuel side, even up to below the stagnation plane.

It was also found that the reduction of concentrations was depend upon to which inlet stream the additive gas was added. The more hydrocarbons were reduced when CO_2 or H_2O was added into the oxidizer stream. This may be explained. When the additive gas is introduced into the oxidizer stream, it should pass the reaction zone where the temperature is about 2000 K. When it pass the high temperature zone, the more CO or OH can be generated and it will diffuse toward fuel side. This slightly higher radical concentration will react with more hydrocarbon molecules. So, it may be more effective to reduce soot particles or hydrocarbons to add CO_2 or H_2O into the oxidizer stream when the flame is in the oxidizer side of stagnation plane.

The C_2H_2 profile was narrower but higher concentration in higher pre-heat condition than that in lower pre-heat condition. The C_2H_2 molecules in BA-flame (Figure 4-8) were distributed between Z_n = -0.5 and 1.0 and its peak value was about slightly lower than 800 ppm. In BB-flame (Figure 4-9), they were between Z_n = -0.5 and 0.8 and its peak was about 1350 ppm. In BC-flame (Figure 4-10), they were between Z_n = 1.0 and 0.8 and its peak value was about 1600 ppm. It indicates that preheat generates more hydrocarbon in narrower zone and it is depleted faster along the streamline.

Another important measurements of species was the concentration of PAH. PAH concentration was measured by the laser light induced fluorescence measurement. This gives the relative concentration profiles for each flame. The measured intensity of blue-green fluorescence is plotted against the normalized coordinate in Figures 4-17, 4-18, and 4-19 for the series of 300 K, 900 K, and 1200 K experiments, respectively. Fluorescence intensity is assumed to be related to the PAH concentration. Thus, fluorescence intensities were used as a tracer of the PAH concentrations (Prado, Garo, Ko, & Sarofim, 1984) for the present study.

The PAH concentration begins to rise around $Z_n \sim 0.7$, and passes through a maximum just before the stagnation plane ($Z_n \sim 0.05$). The PAH concentration then decreases to a small value on the fuel side of the stagnation plane ($Z_n < 0.0$).

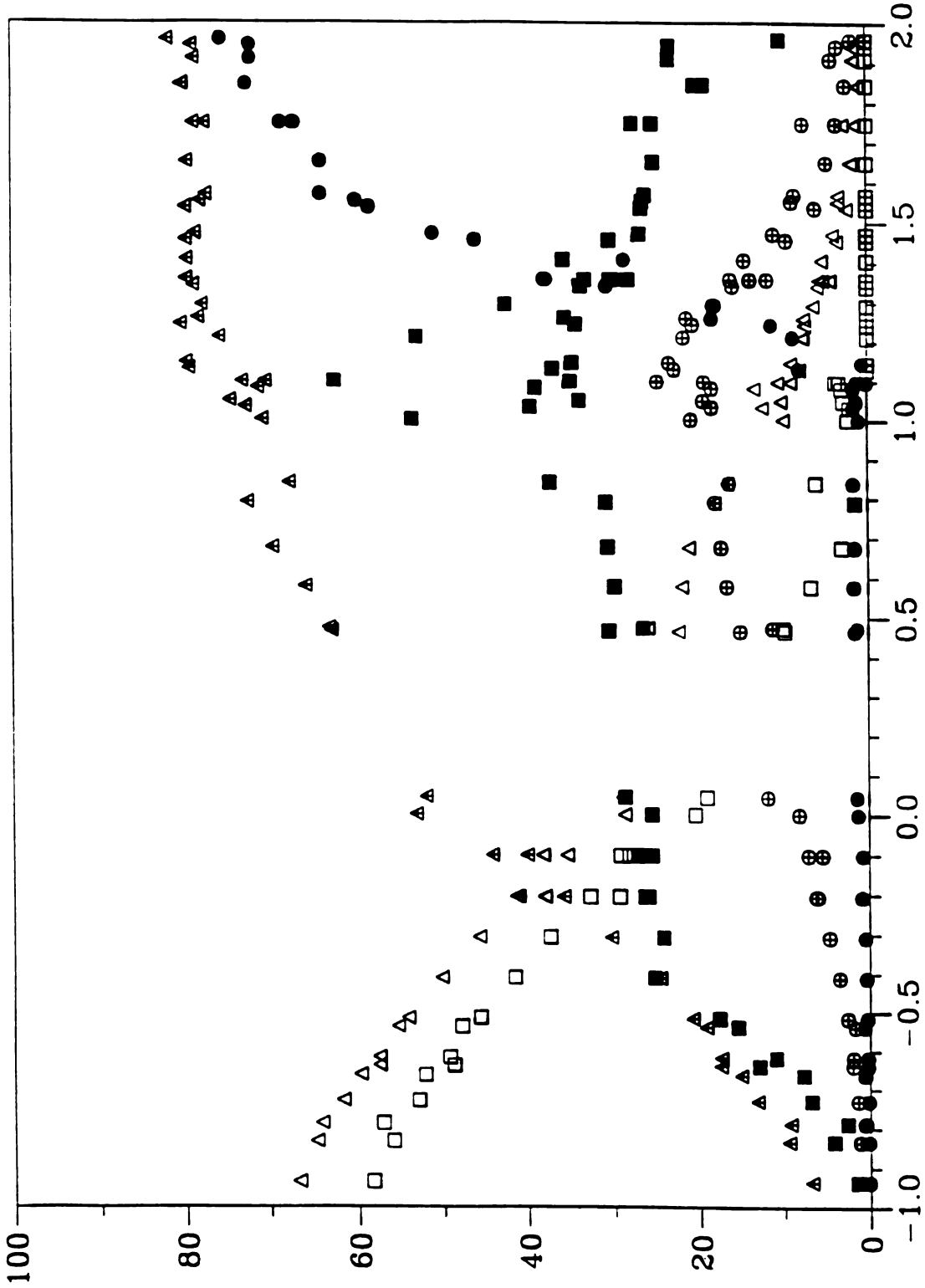

Figure 4-5a BA-flame stable species concentration profiles

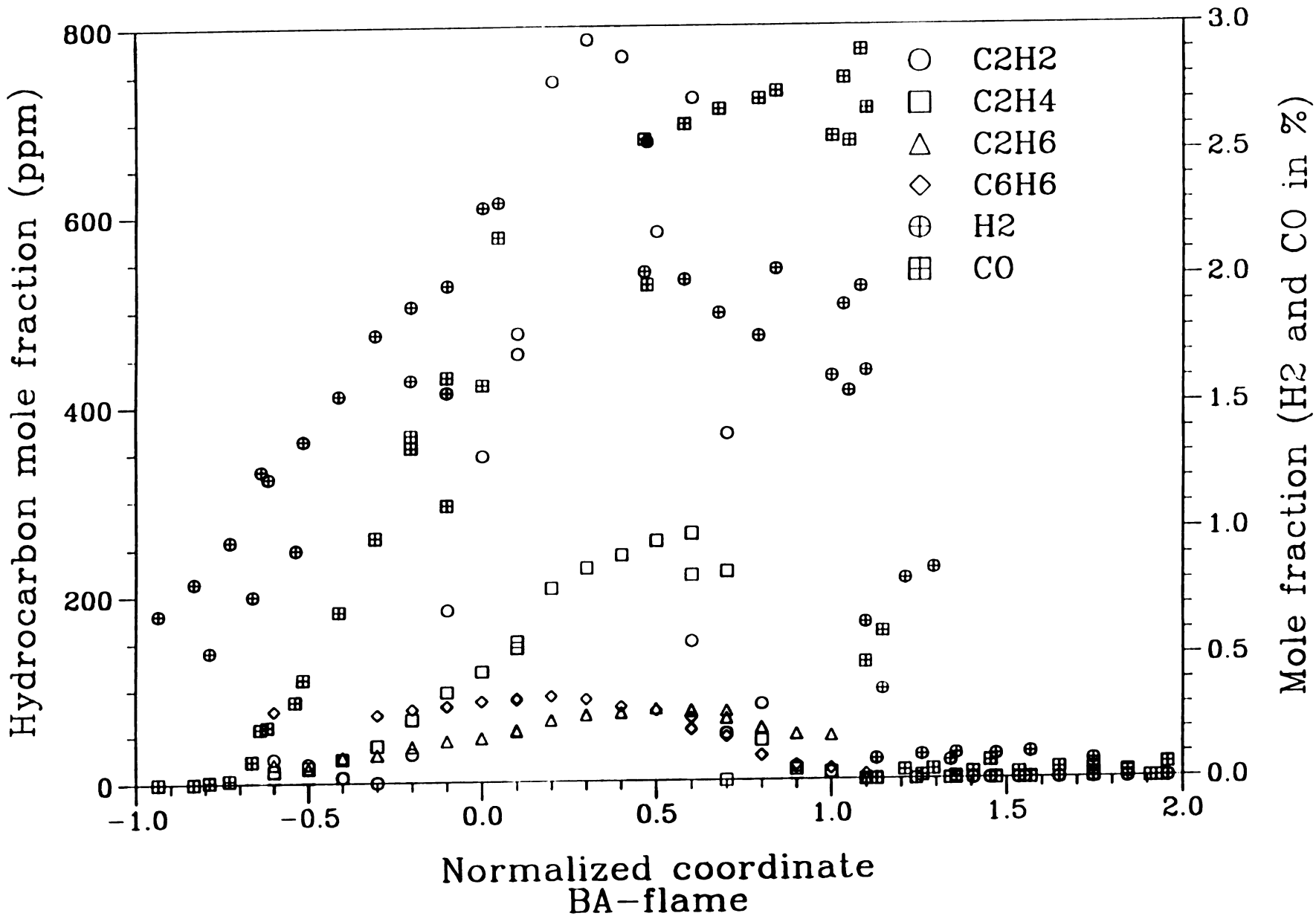

Figure 4-5b BA-flame hydrocarbon concentration profiles

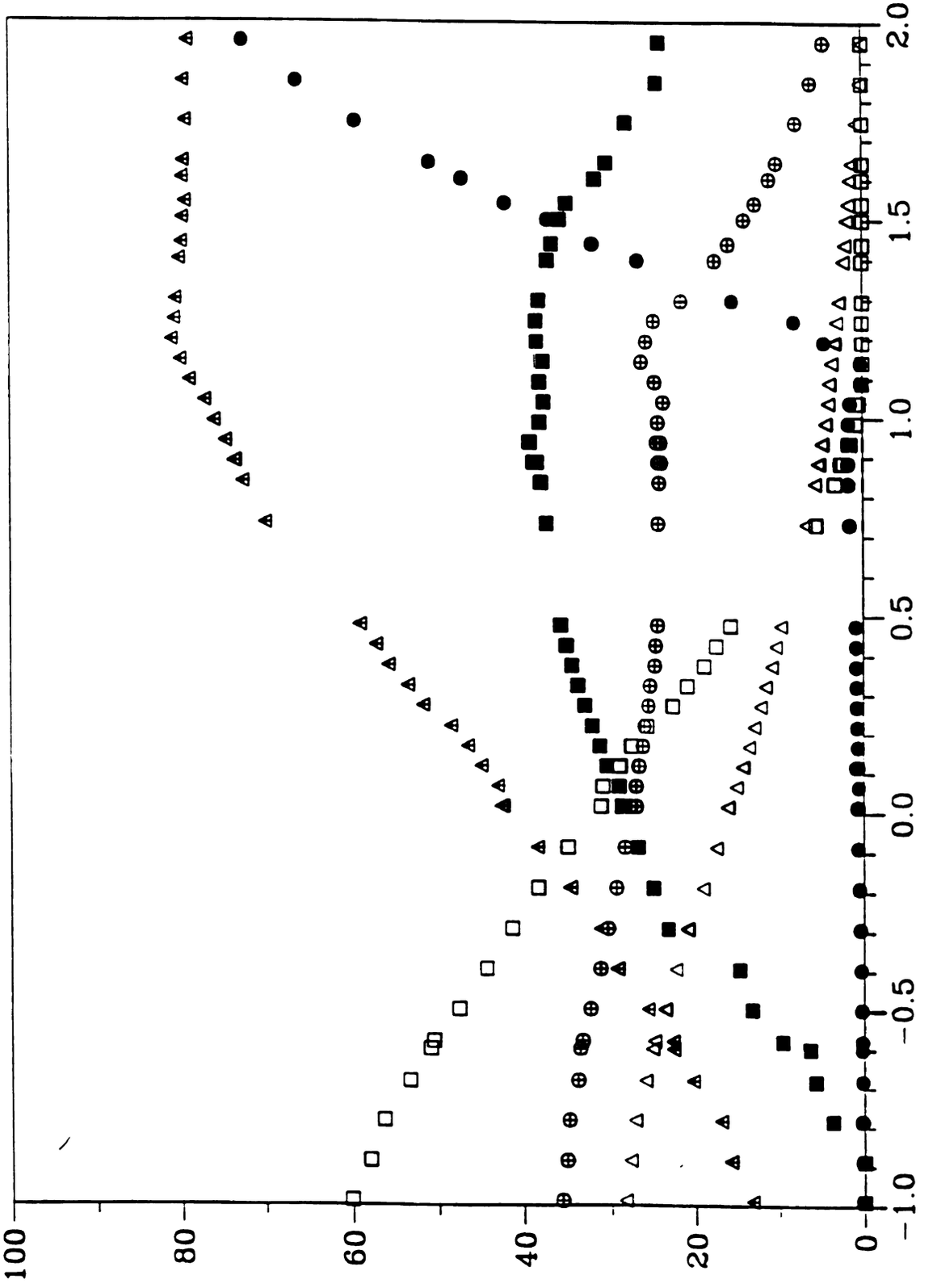

Figure 4-6a IA-flame stable species concentration profiles

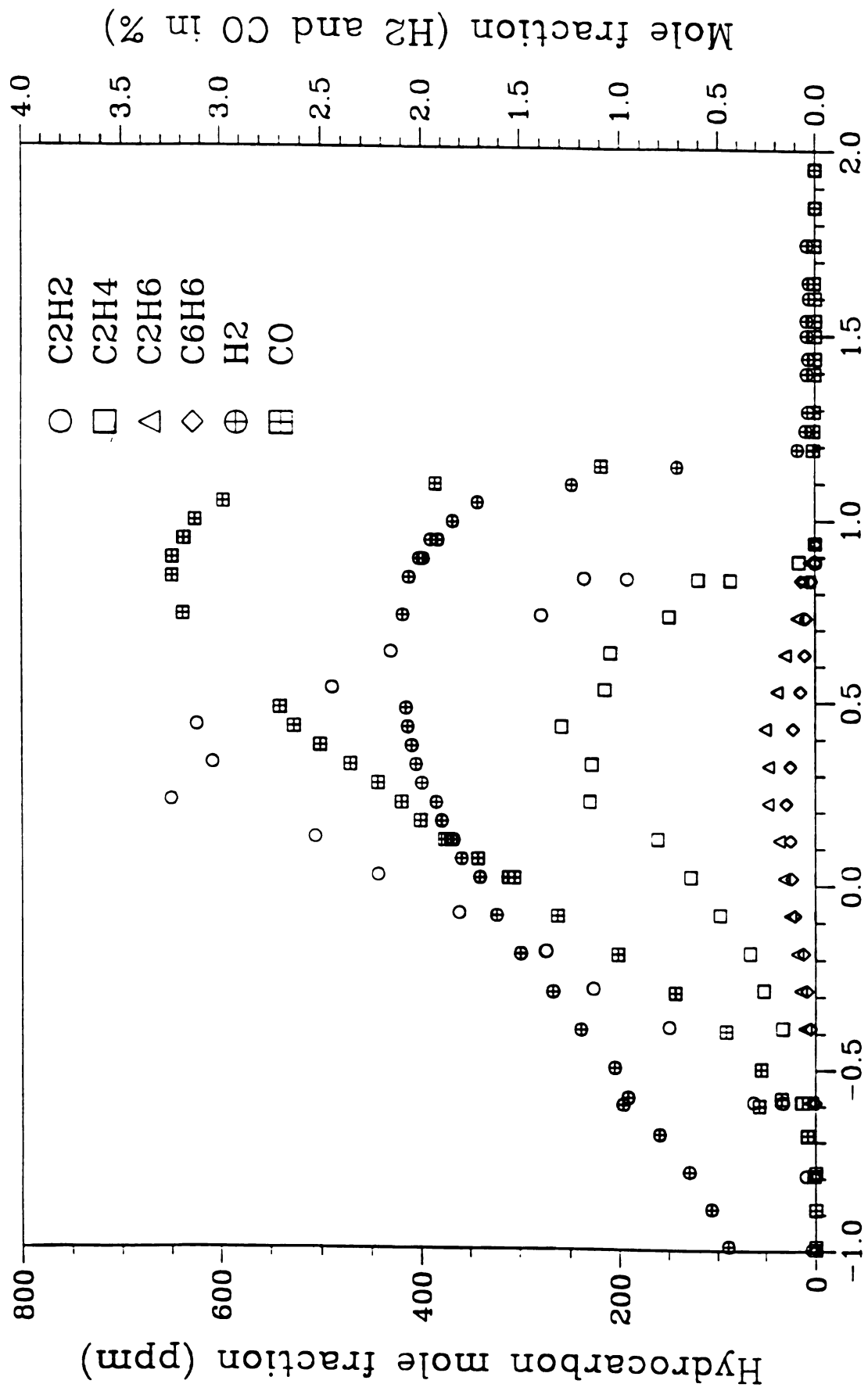

Figure 4-6b IA-flame hydrocarbon concentration profiles

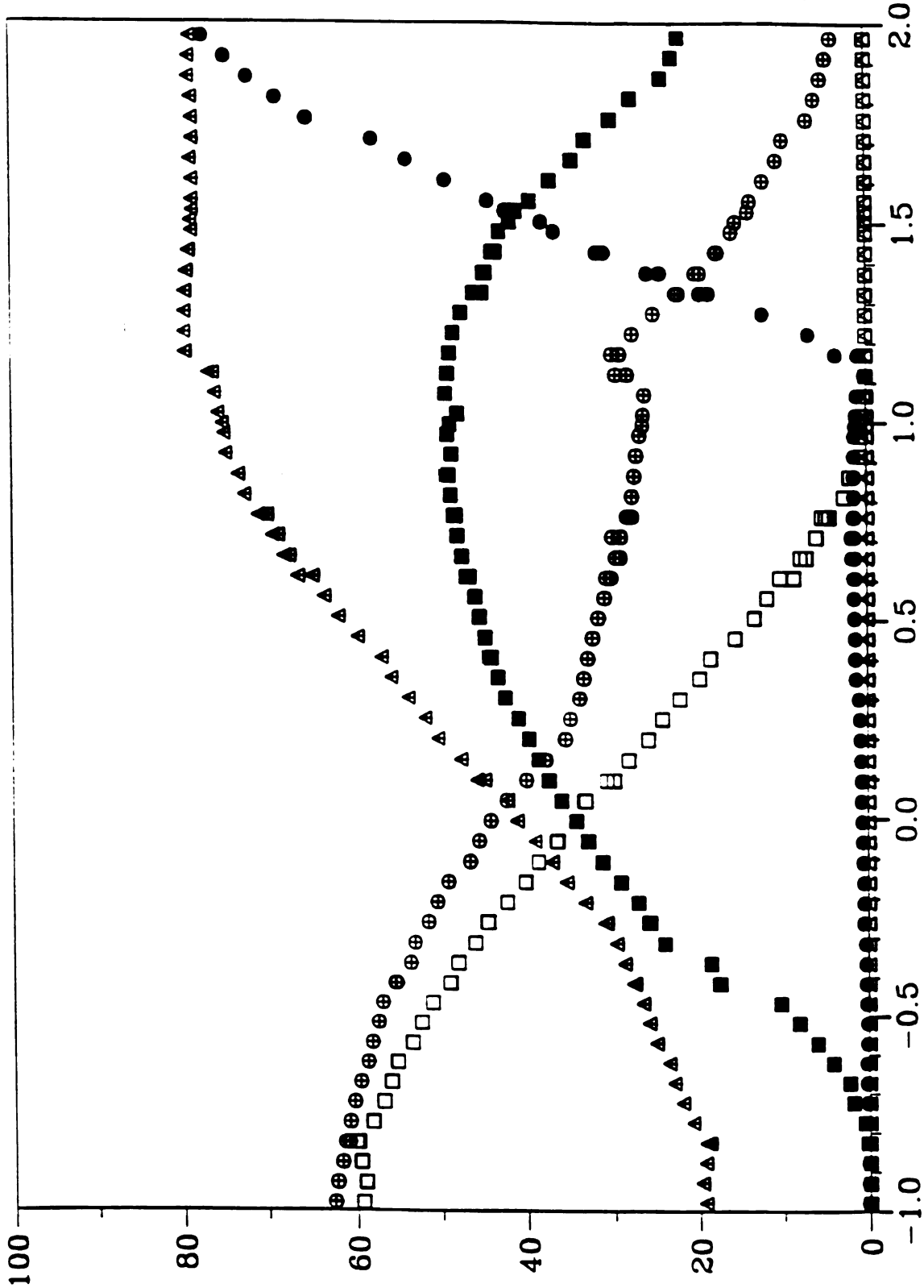

Figure 4-7a MA-flame stable species concentration profiles

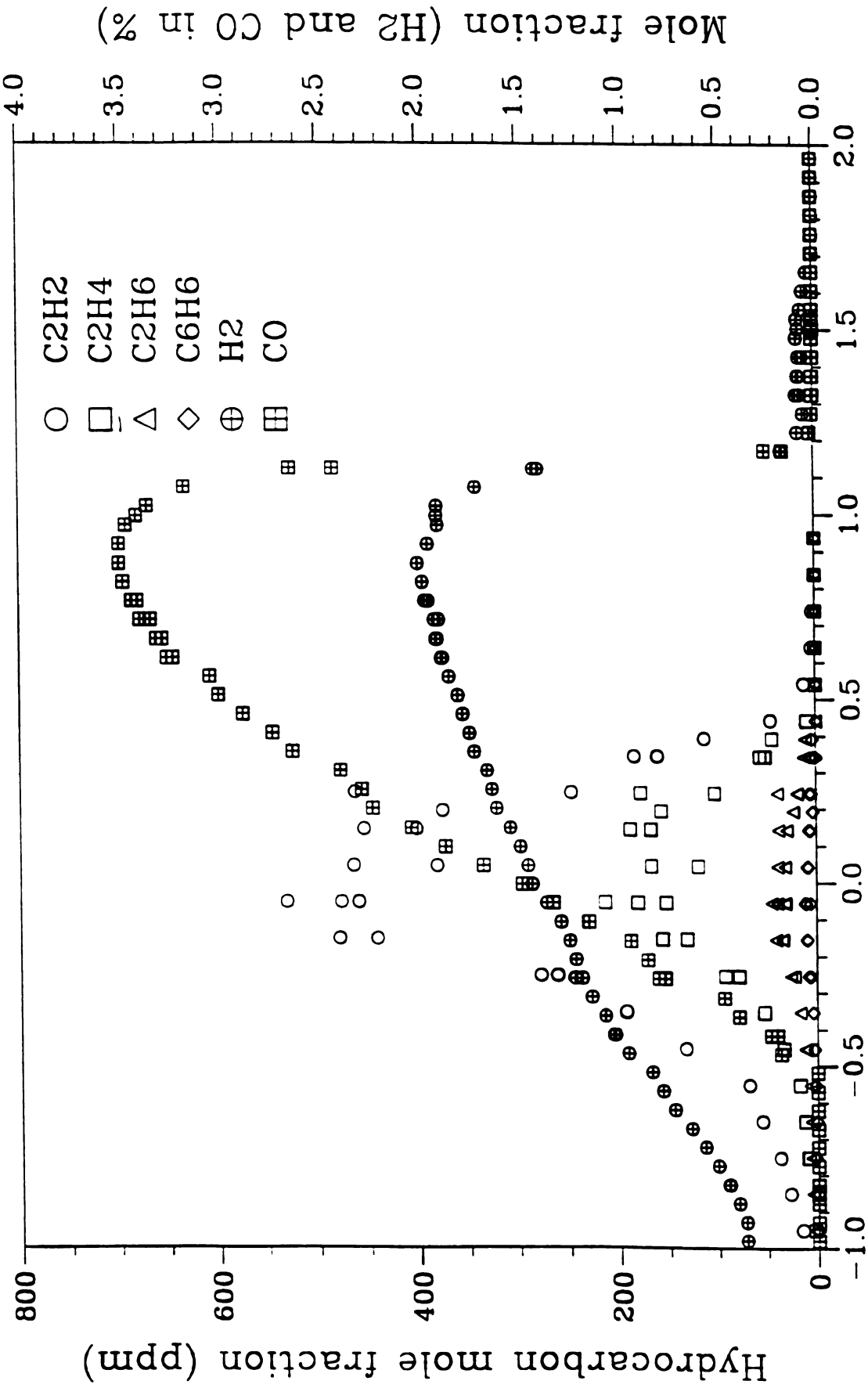

Figure 4-7b MA-flame hydrocarbon concentration profiles

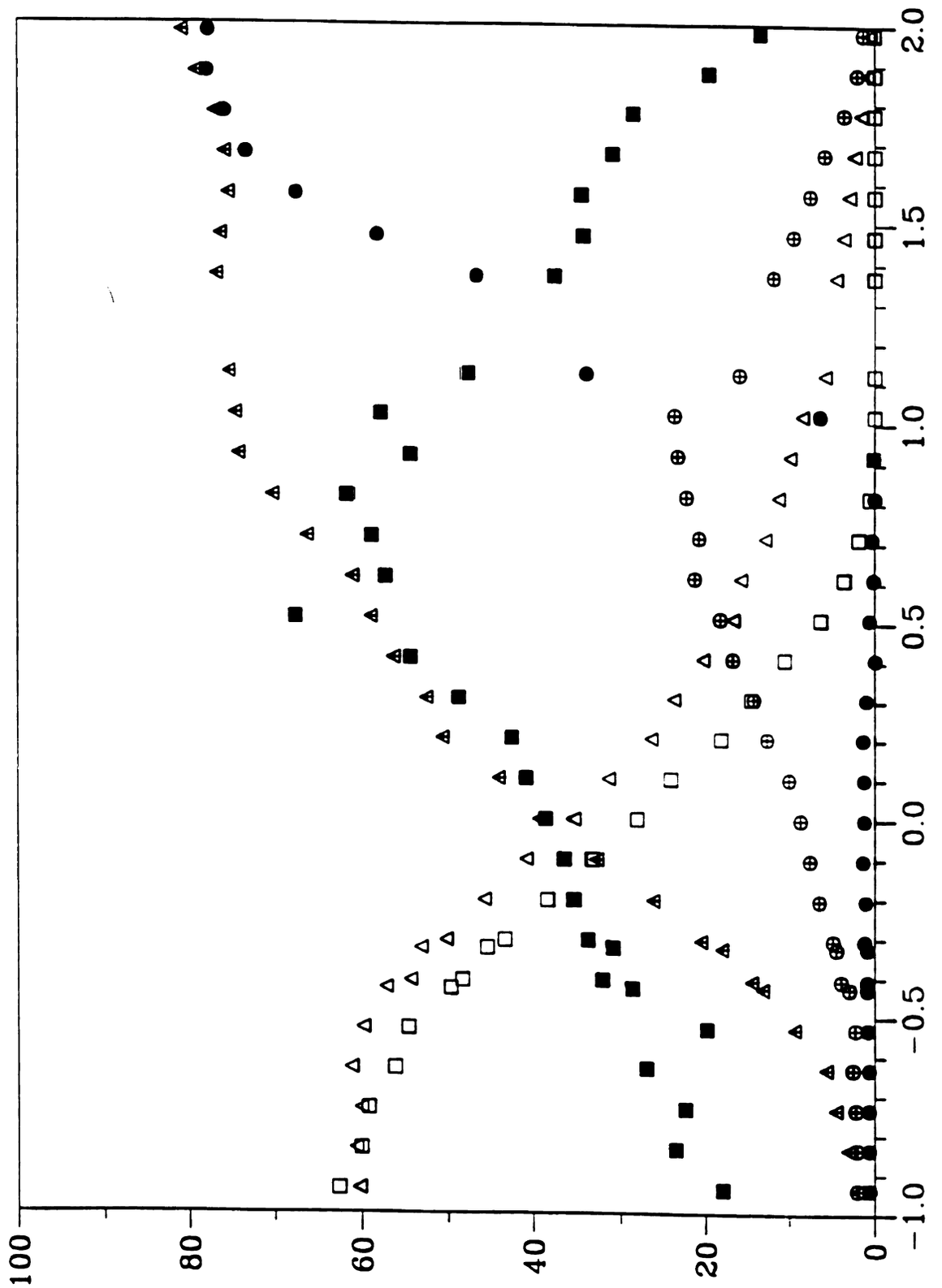

Figure 4-8a WAF-flame stable species concentration profiles

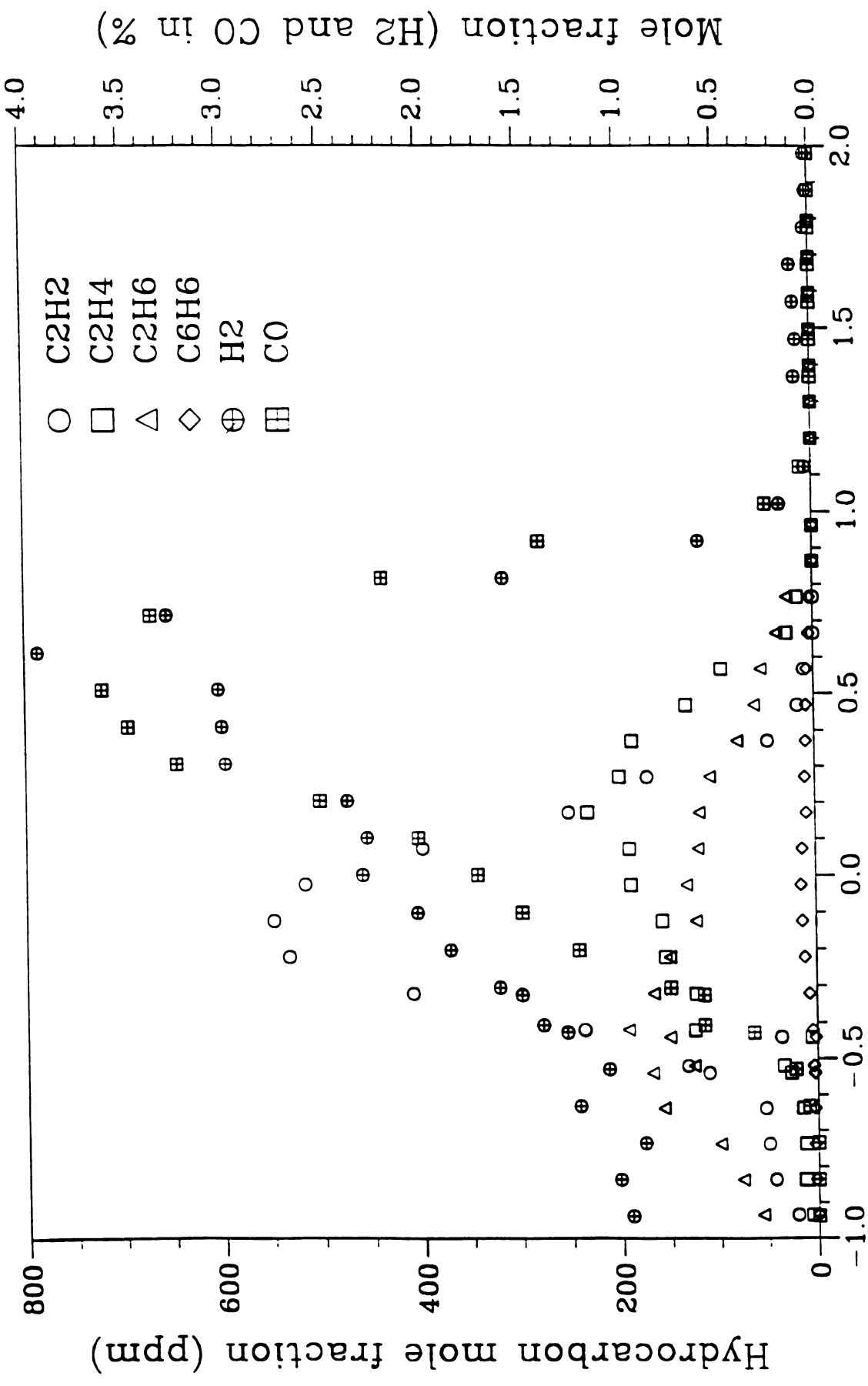

Figure 4-8b WAF-flame hydrocarbon concentration profiles

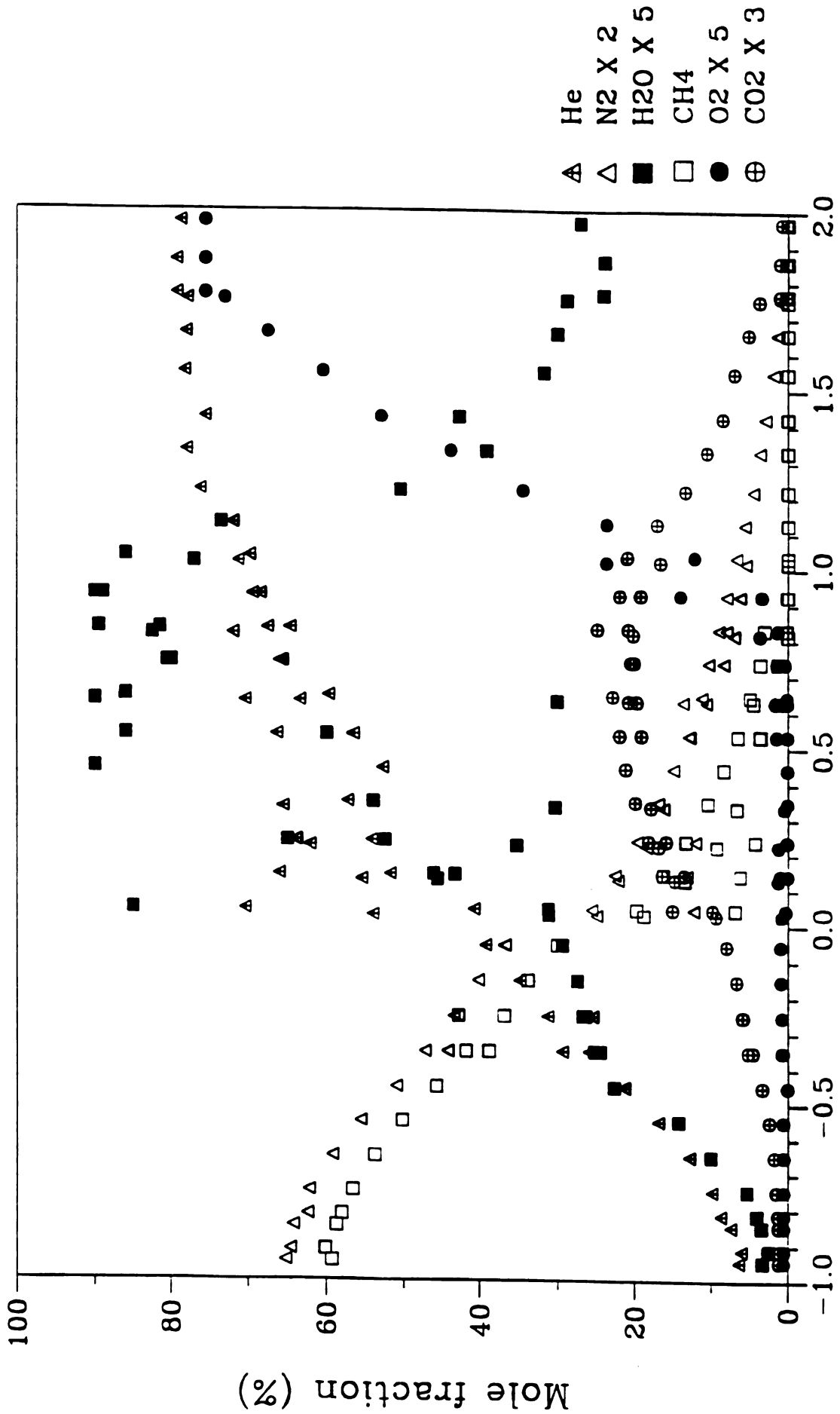

Figure 4-9a WAO-flame stable species concentration profiles

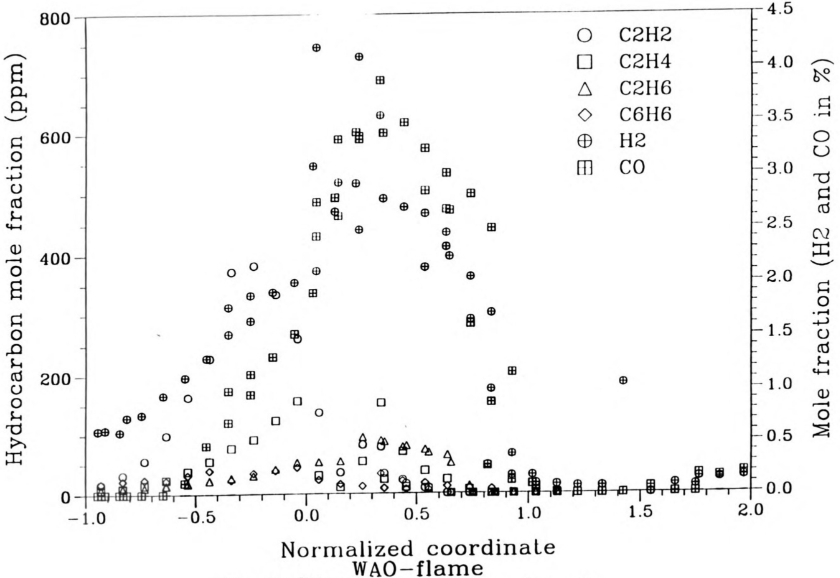

Figure 4-9b WAO-flame hydrocarbon concentration profiles

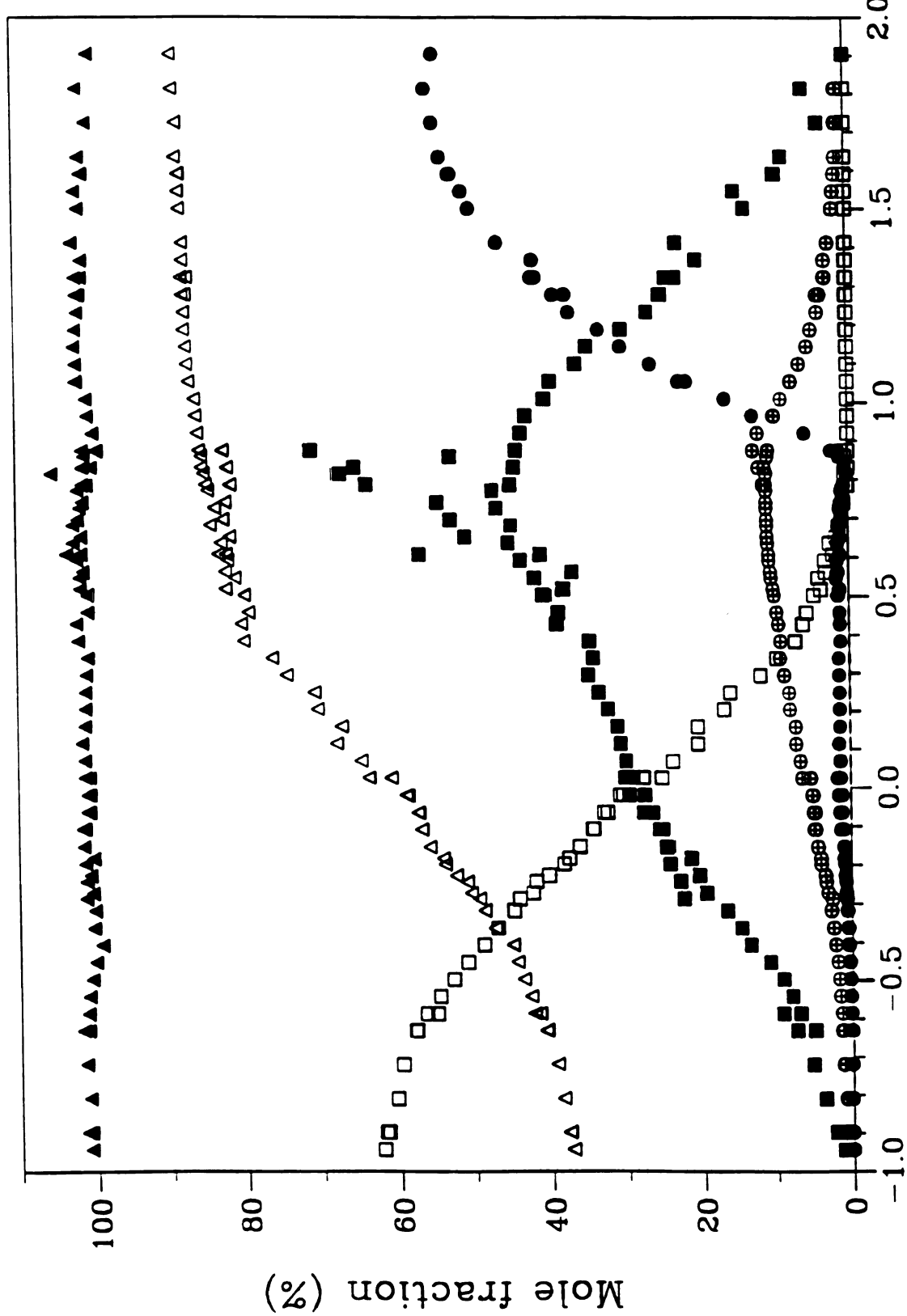

Figure 4-10a BB-flame stable species concentration profiles

Figure 4-10b BB-flame hydrocarbon concentration profiles

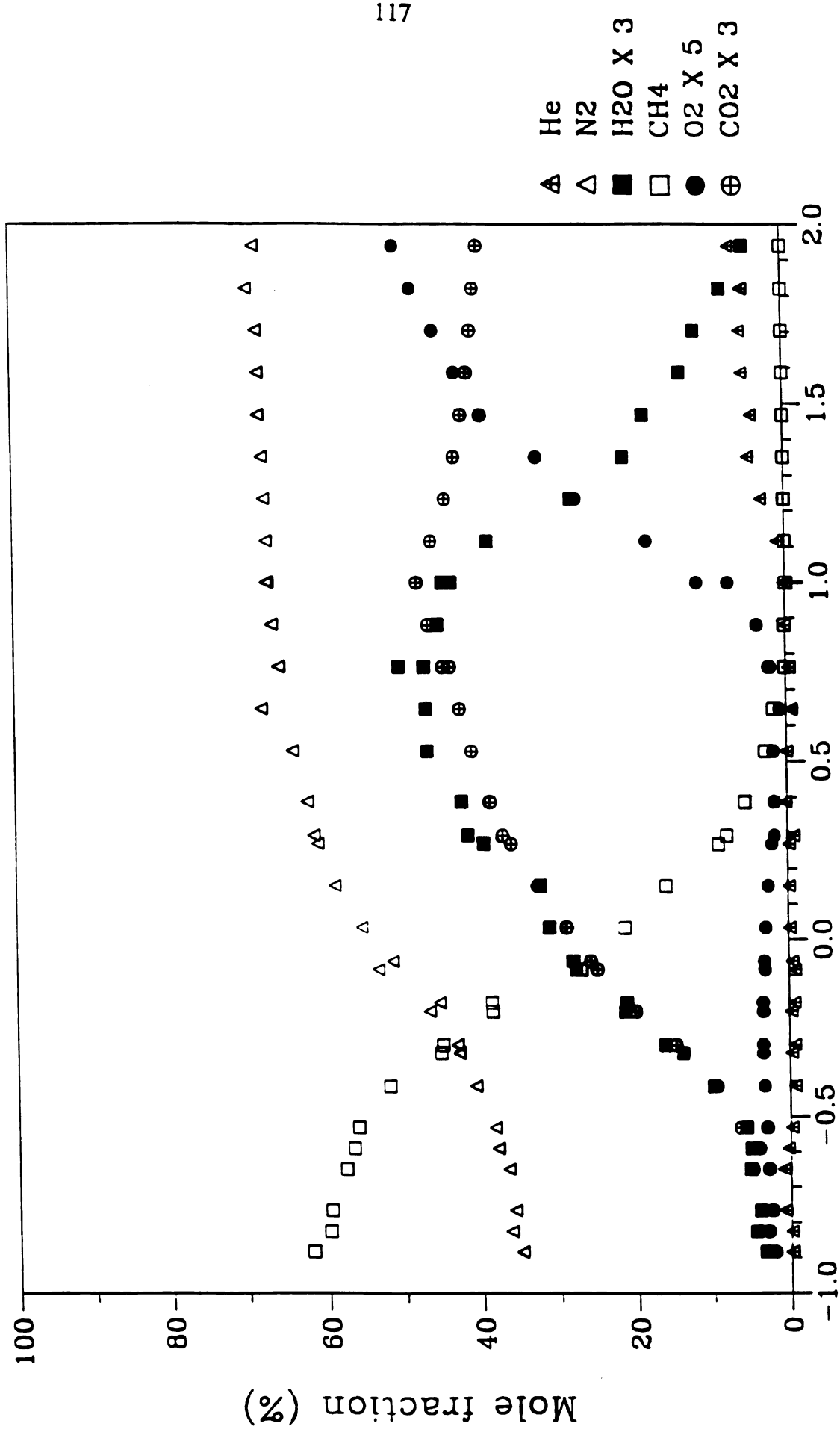

Figure 4-11a IBO-flame stable species concentration profiles

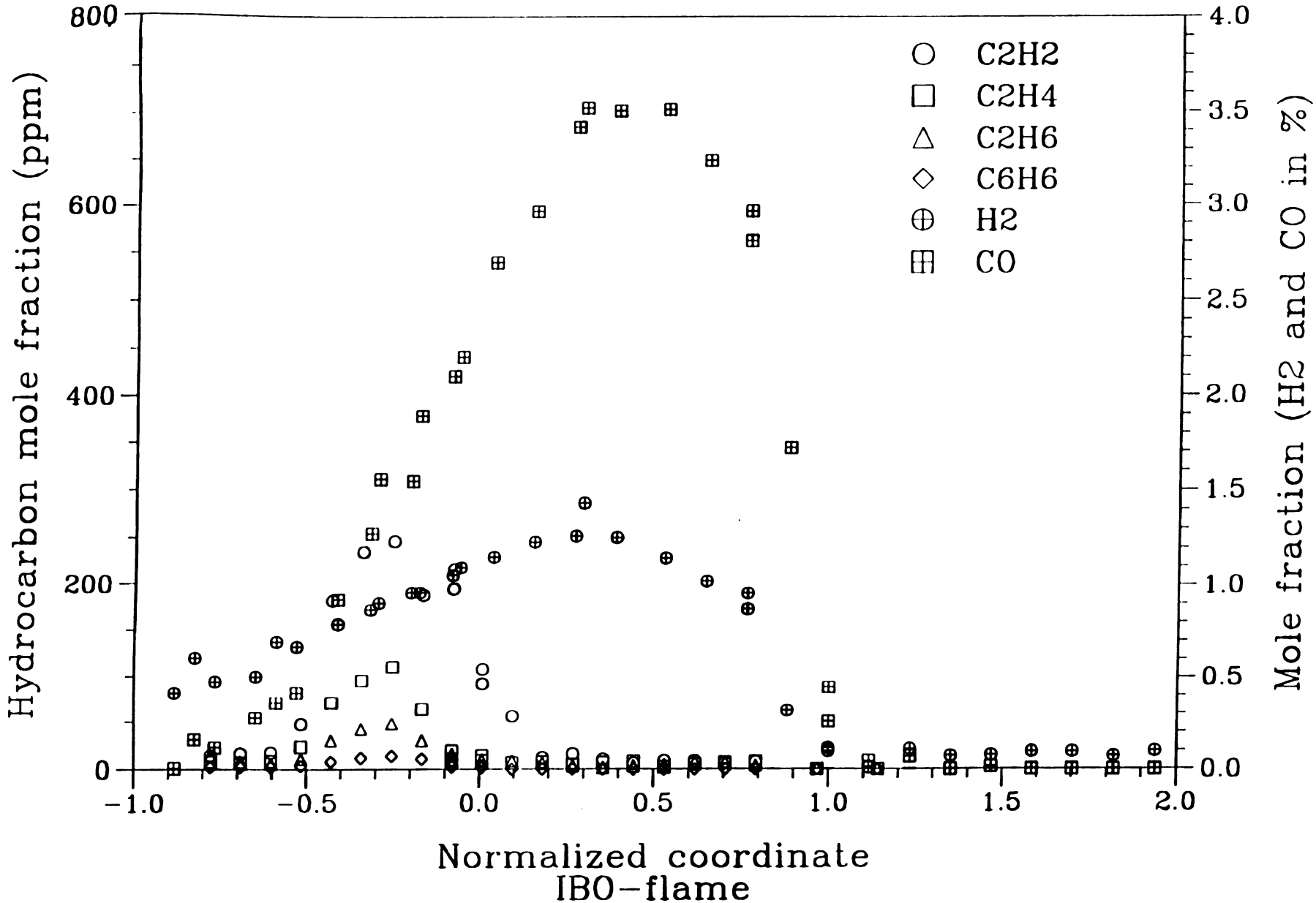

Figure 4-11b IBO-flame hydrocarbon concentration profiles

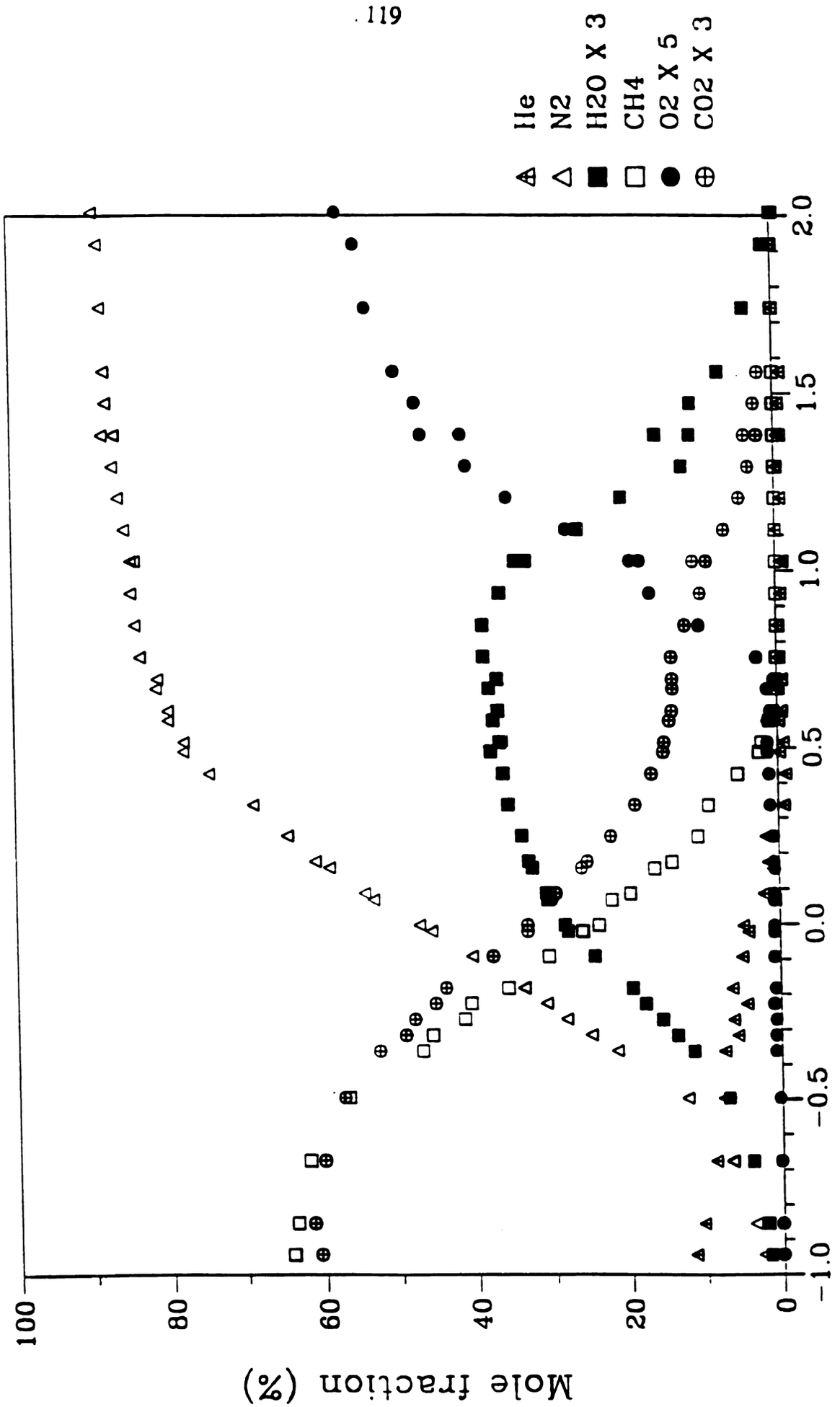

Figure 4-12a MBF-flame stable species concentration profiles

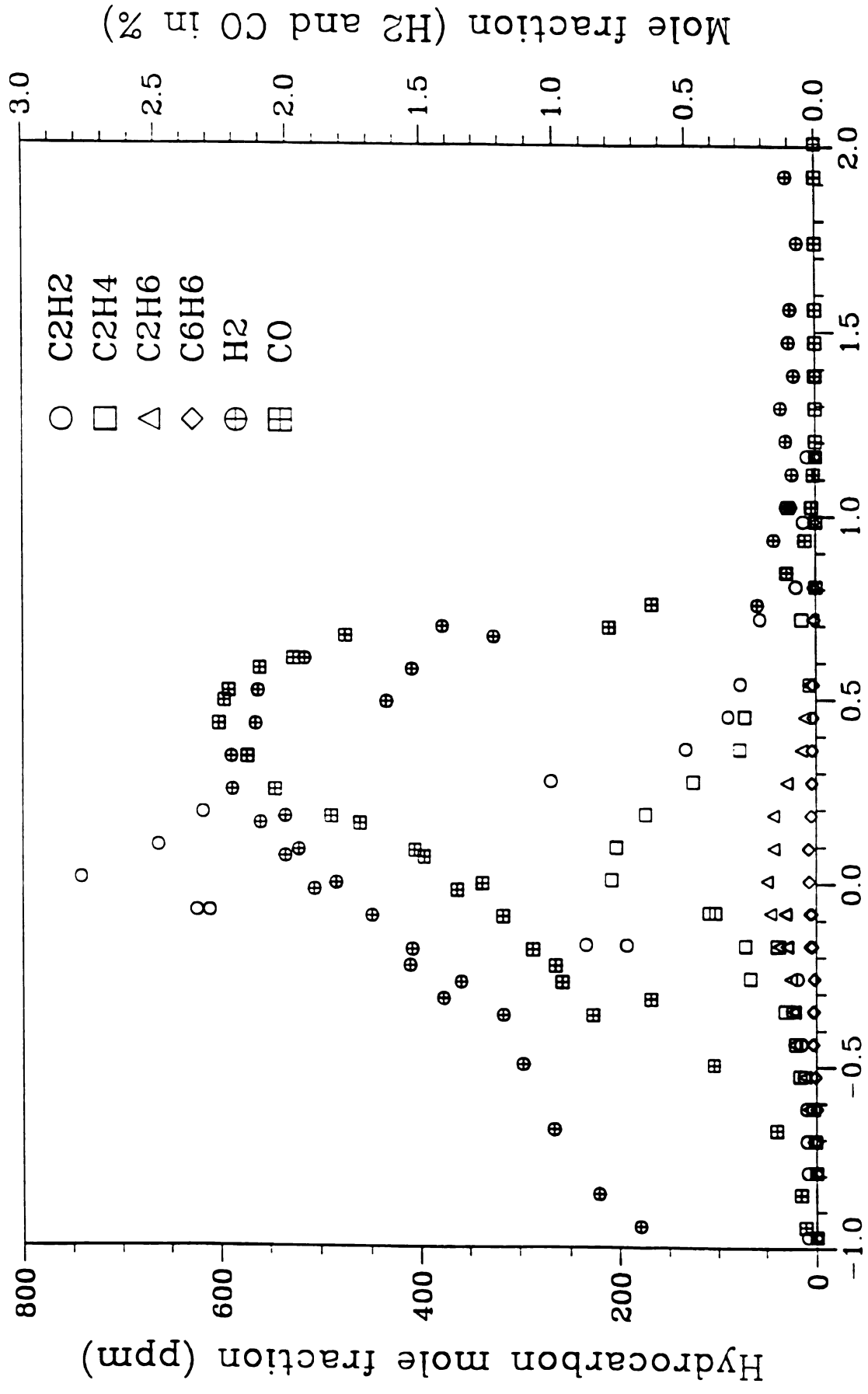

Figure 4-12b MBF-flame hydrocarbon concentration profiles

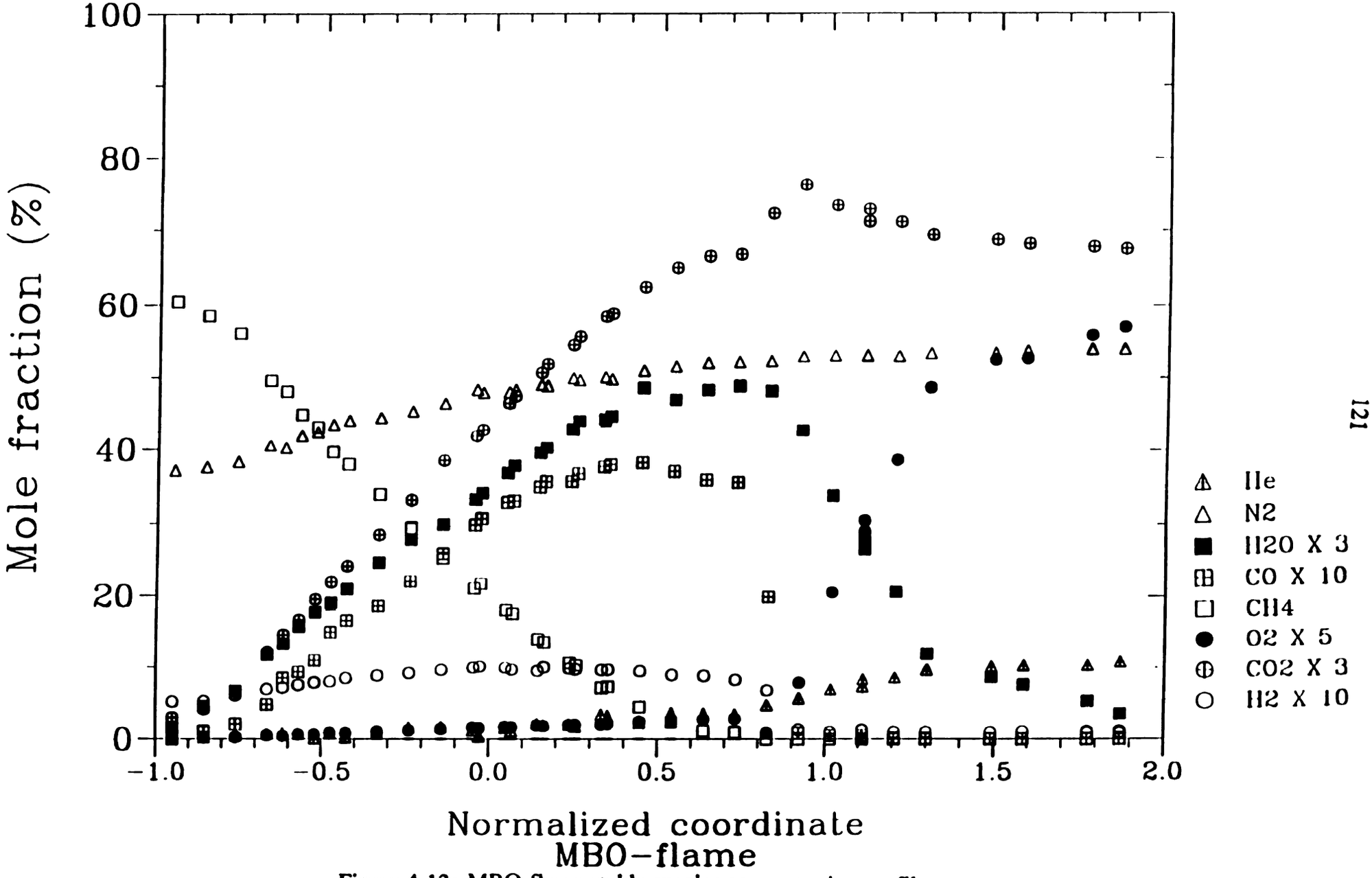

Figure 4-13a MBO-flame stable species concentration profiles

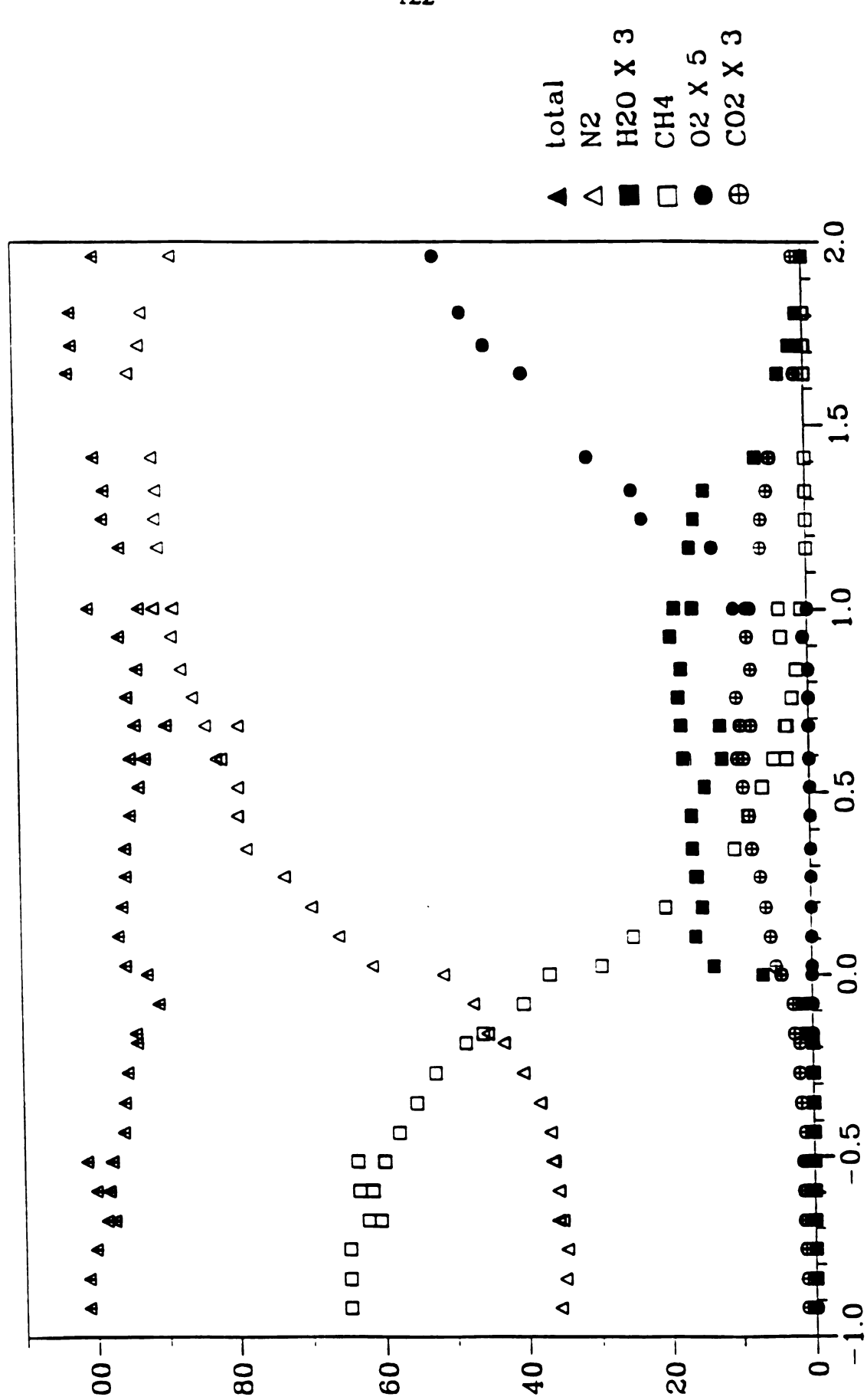

Figure 4-14a BC-flame stable species concentration profiles

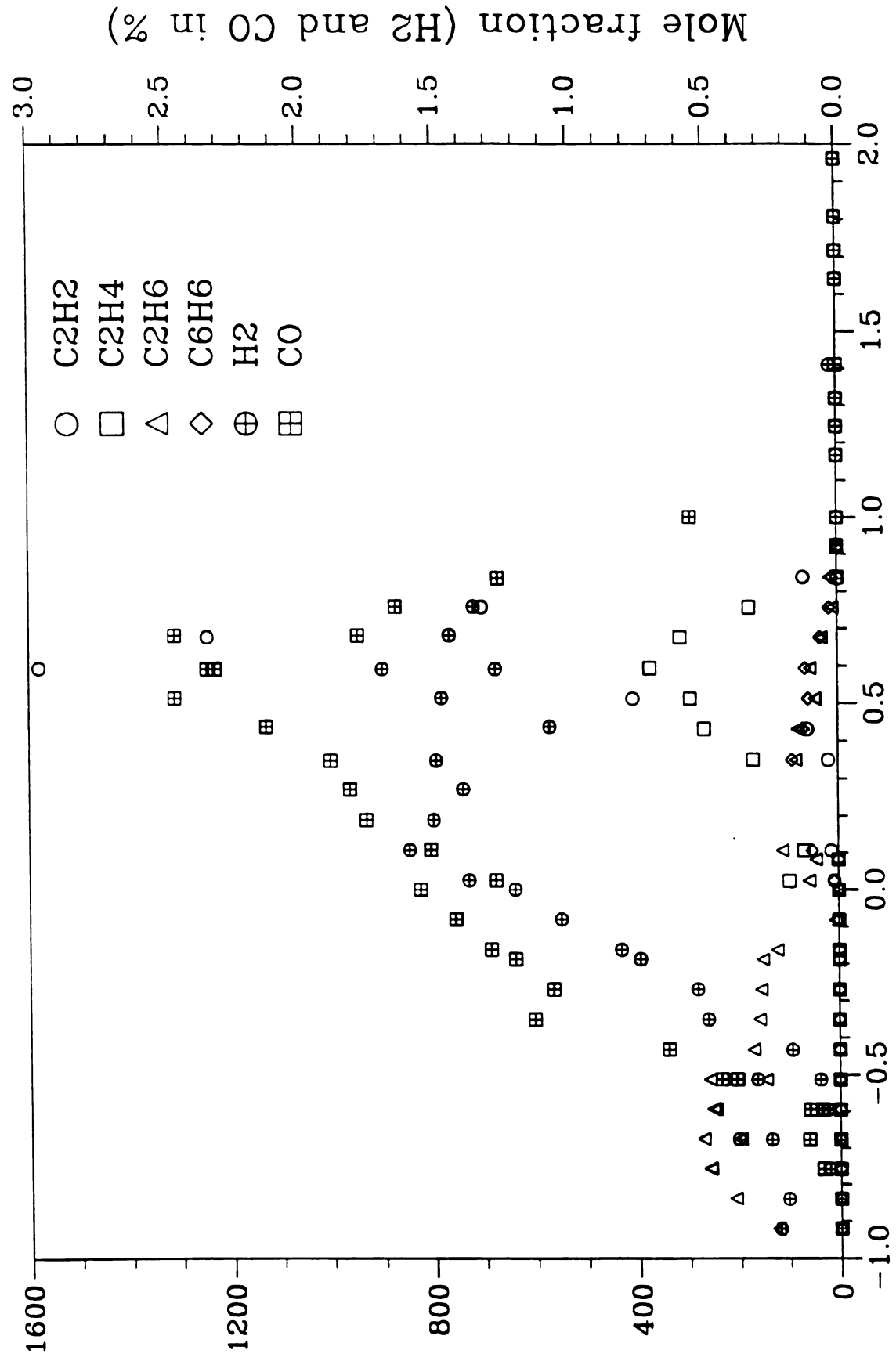

Figure 4-14b BC-flame hydrocarbon concentration profiles

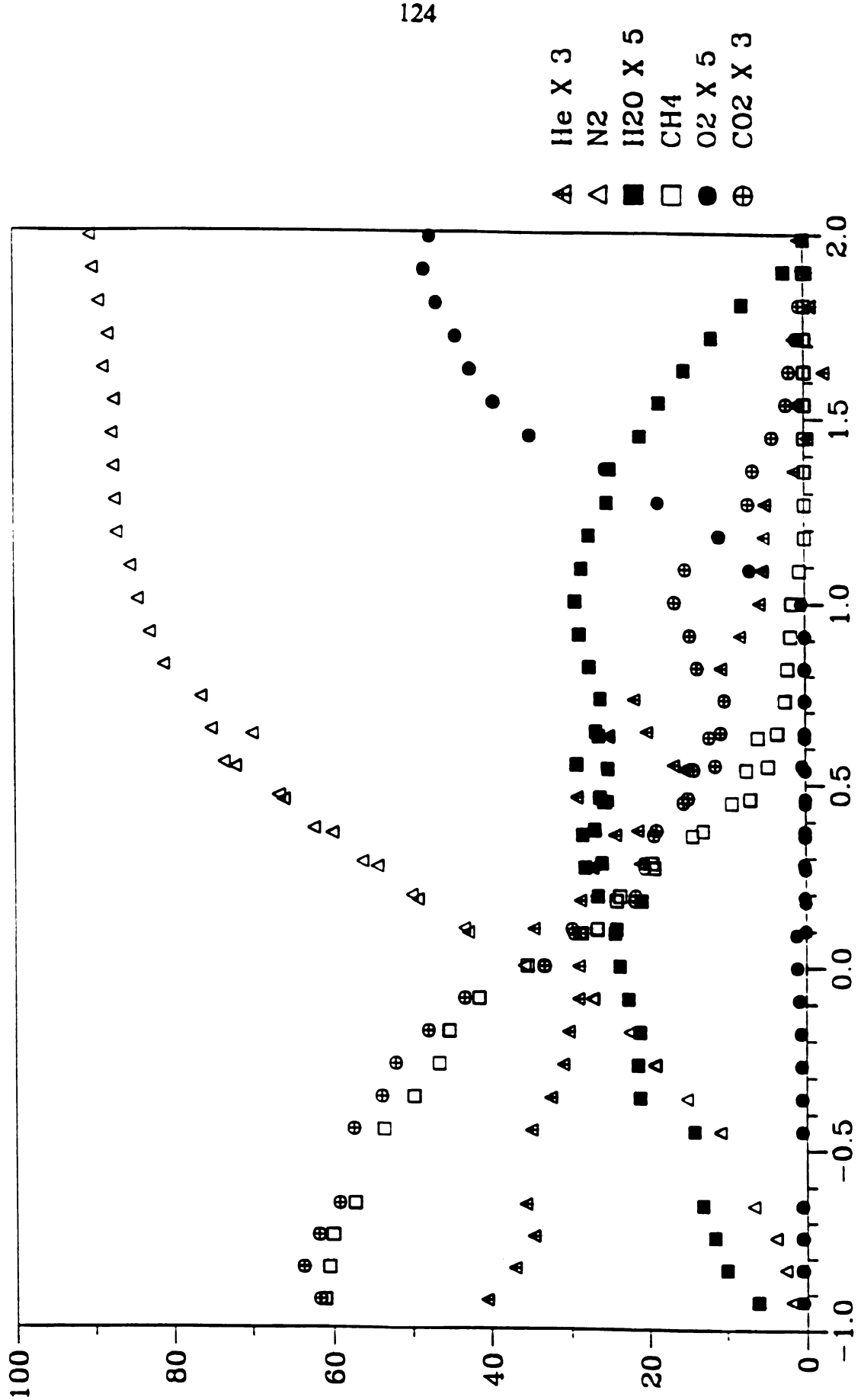

Figure 4-15a MCF-flame stable species concentration profiles

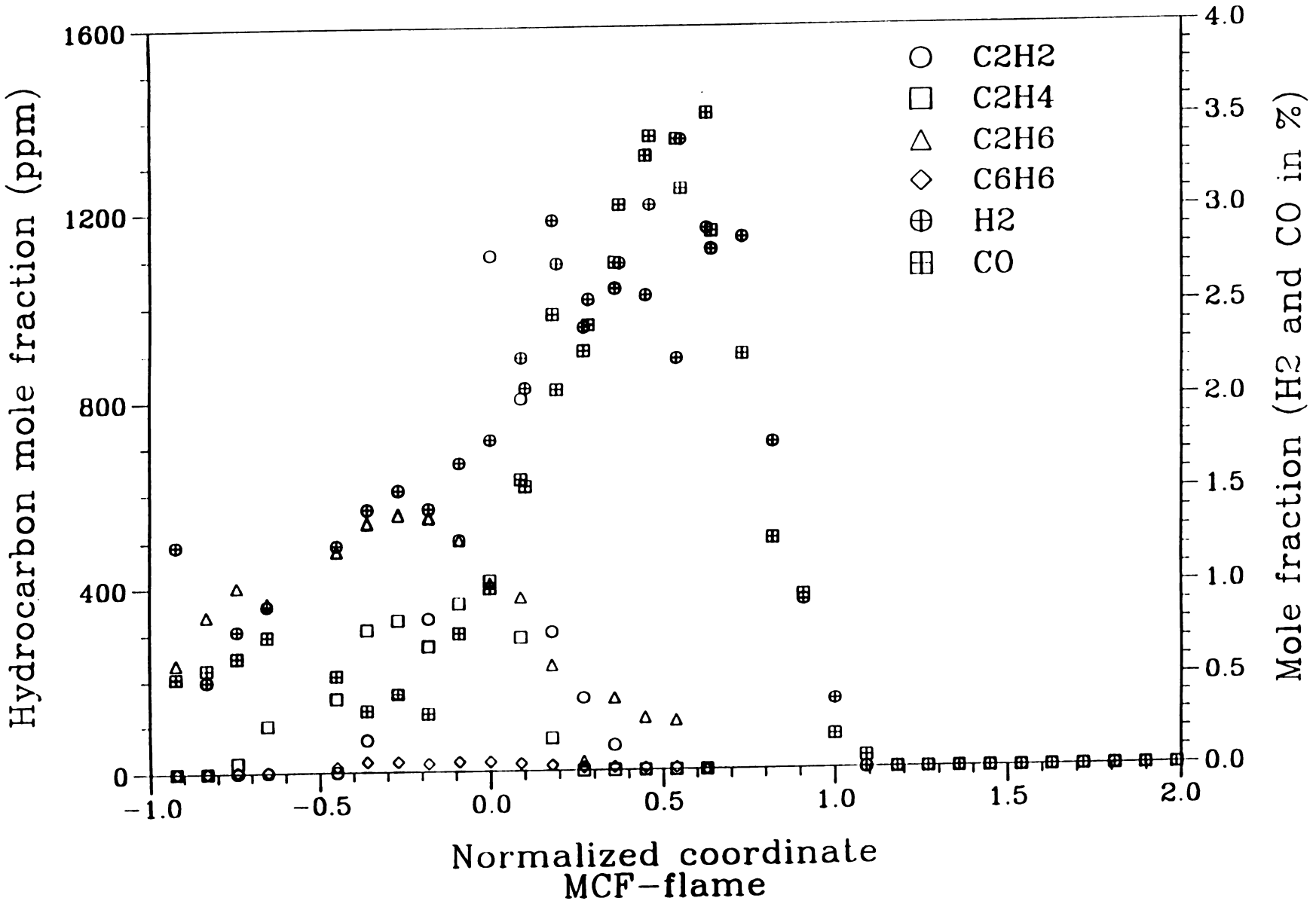

Figure 4-15b MCF-flame hydrocarbon concentration profiles

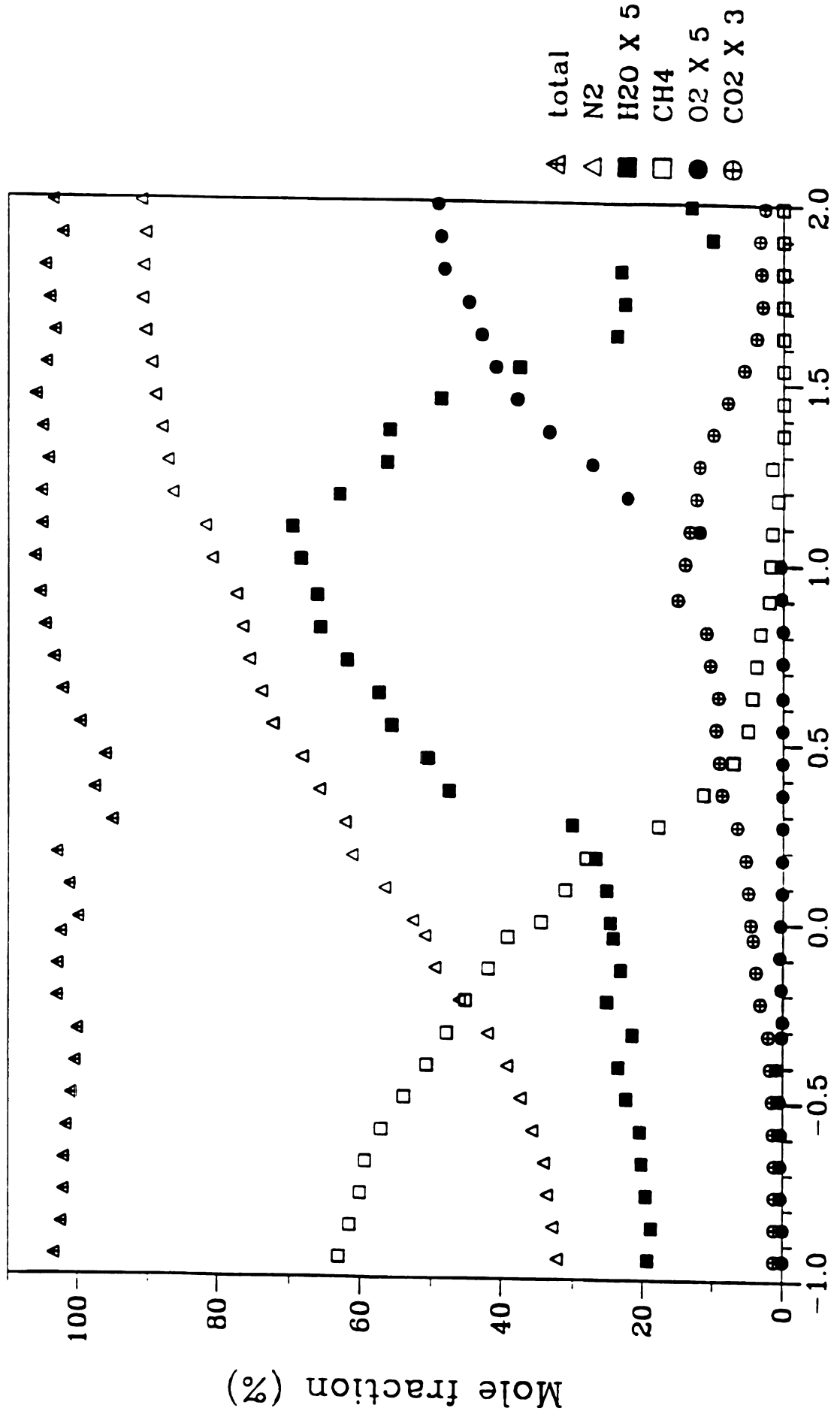

Figure 4-16a WCF-flame stable species concentration profiles

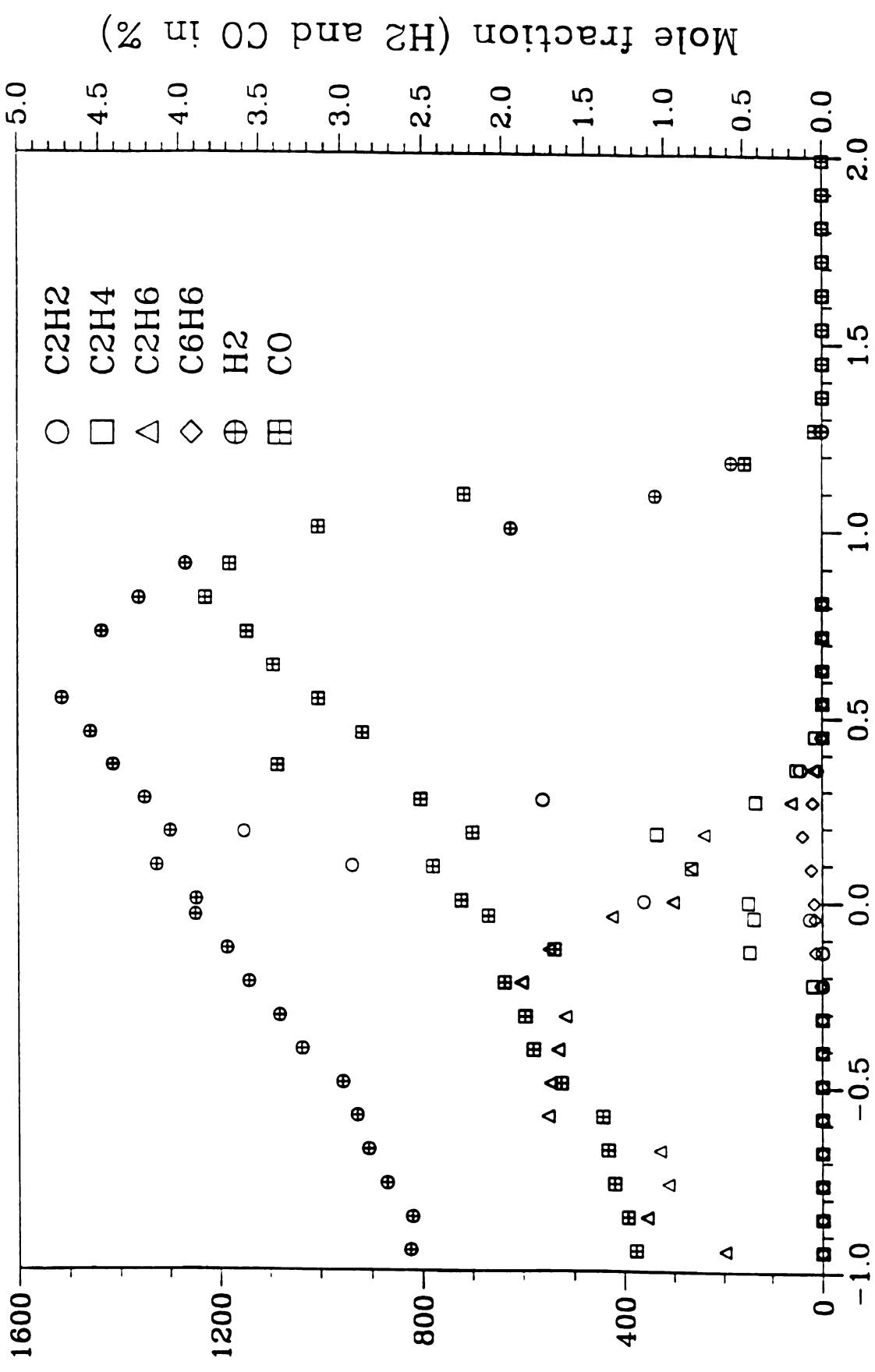

Figure 4-16b WCF-flame hydrocarbon concentration profiles

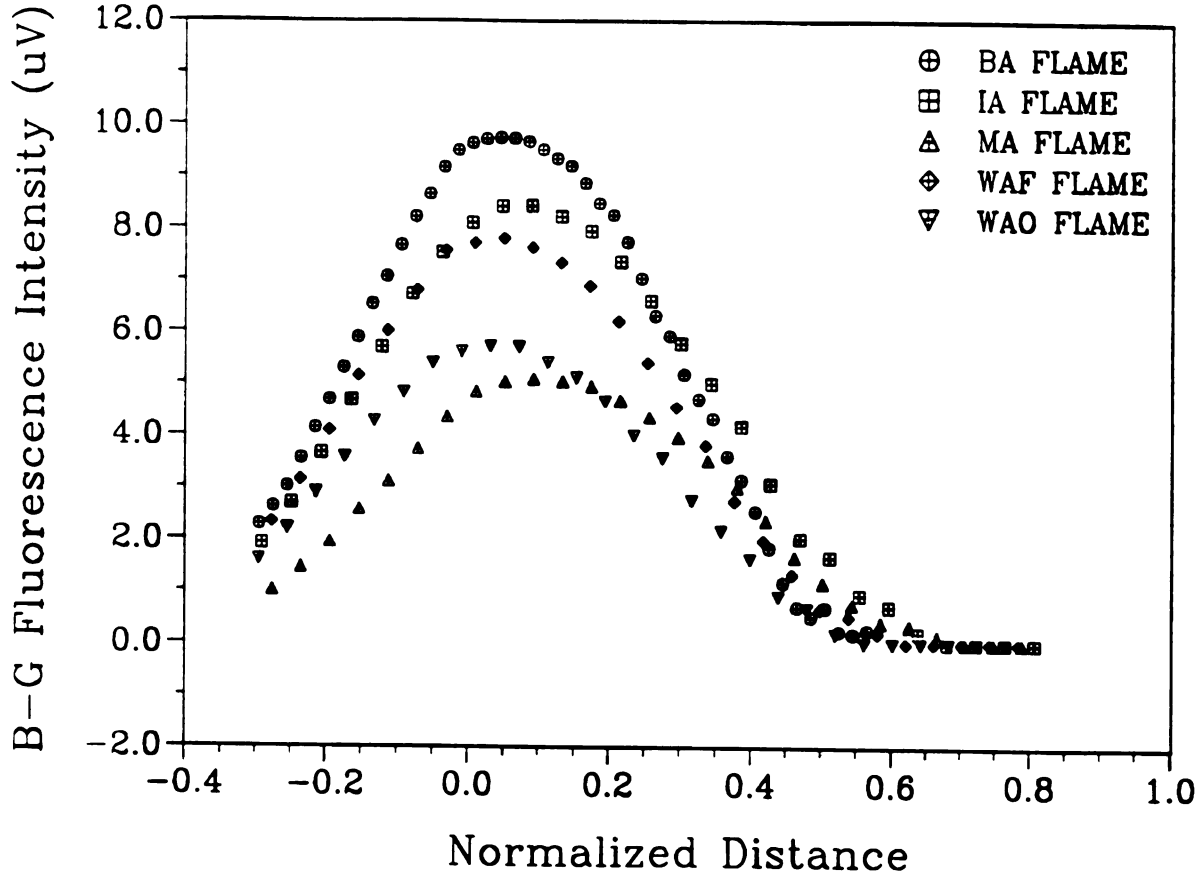

Figure 4-17 Measured intensity of blue-green fluorescence for 300 K flames.

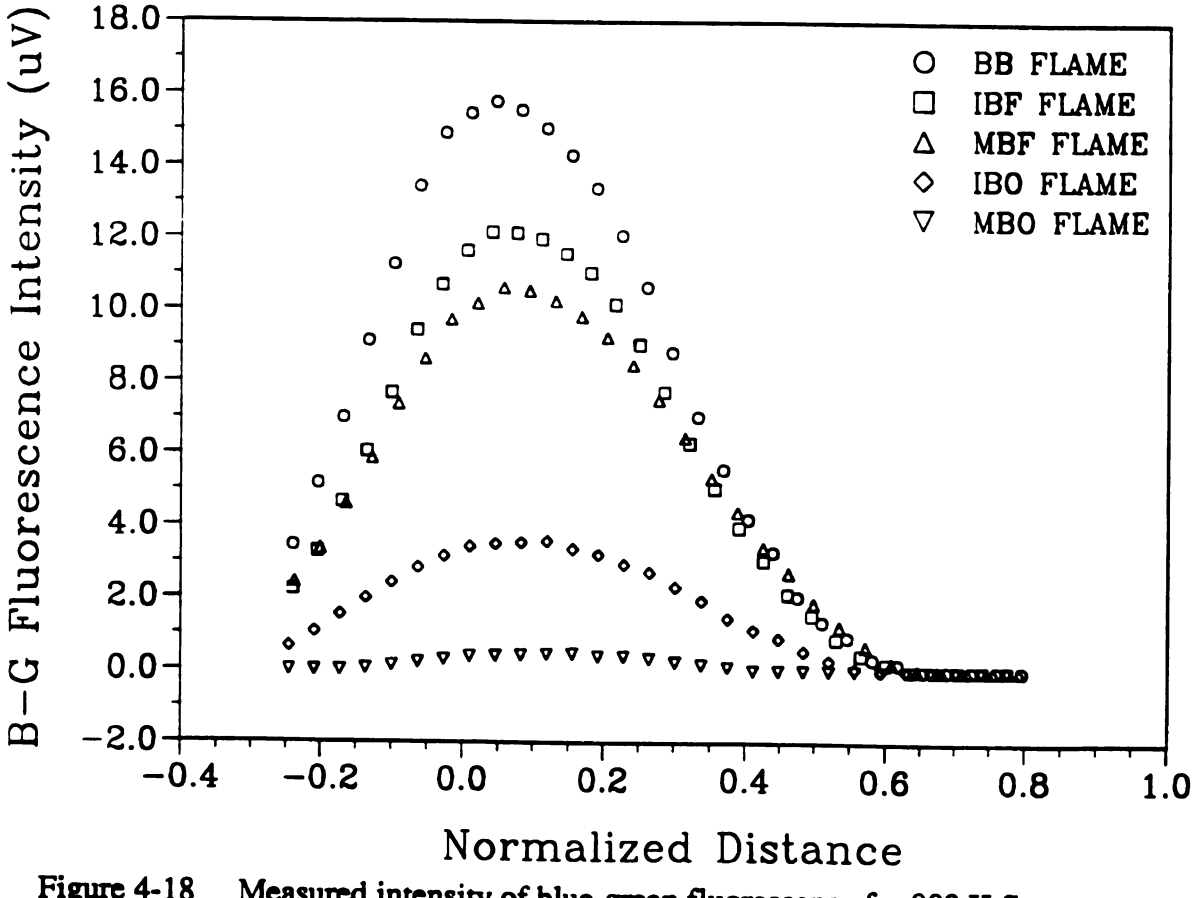

Figure 4-18 Measured intensity of blue-green fluorescence for 900 K flames.

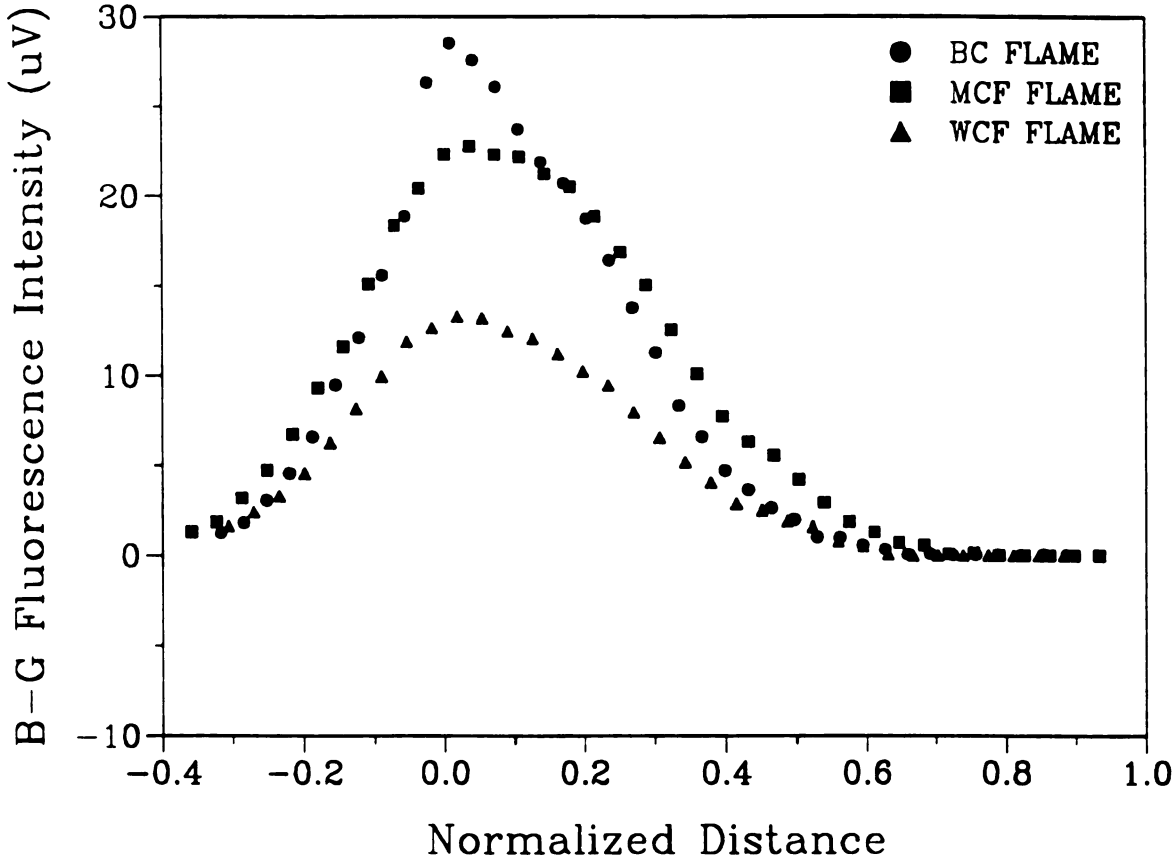

Figure 4-19 Measured intensity of blue-green fluorescence for 1200 K flames.

It was observed that increasing CO_2 or H_2O concentration reduces the PAH concentration just like hydrocarbons. For 300 K experiments, 12 % CO_2 (IA-flame) in the input fuel stream reduces the PAH concentration by 15.8 % when compared with 0 % CO_2 (BA-flame). Further increases in CO_2 concentration to 21 % (MA-flame) reduces the PAH by 52.6 %. Similarly, for 900 K experiments, the PAH in IBF-flame (12 % CO_2) and MBF-flame (21 % of CO_2) show reduction of 24.5 % and 34.4 %, respectively when compared 0 % of CO_2 (BB-flame).

In 900 K experiments, a comparison of the PAH concentrations in the IBO-flame (CO_2 introduced into the oxidizer side) with that in the IBF-flame (CO_2 introduced

into the fuel side) shows a larger reduction of the PAH concentration when CO_2 was introduced into the oxidizer side. This is presumed to be because of large CO_2 concentration in the higher temperature zone which exists on the oxidizer side. In 1200 K experiments, adding 21 % CO_2 reduced PAH about 24.2 %. The percentage of reduction of PAH when 21 % CO_2 introduced into fuel stream decreases along rising pre-heat temperature, 52.6 % at 300 K, 34.4 % at 900 K, 24.2 % at 1200 K. Adding water vapor was found similar effects on PAH reduction.

Pre-heat temperature also affects the PAH concentration in the flame. The PAH concentrations in the BA, IA, MA flames are smaller by 60.5 %, 68.4 %, and 43.7 % than those in BB, IBF, and MBF, respectively. Also, in 1200 K experiments, even more PAH was observed.

4.4 Soot Particle Measurements

4.4.1 Calibration for Optical Measurement

By using a gas with a known scattering cross section, σ_o, the optical measurements can be calibrated and then used to determine the soot particle size, number density, and volume fraction. The scattering cross section is defined as the apparent projected area of a particle relative to its ability to scatter radiation. This scattering cross section may depend on the particle size, the shape and material of the scattering body. It may also depend on wavelength, polarization and coherence of incident beam.

Rudder and Bach (1968) determined the Rayleigh scattering cross section of N_2 and other gases by using ruby-laser light (λ = 694.3 *nm*). Let's consider a small control volume, dV, at the focus of incident beam (Figure 4-20). The ratio of the scattered portion I_s of the incident intensity to the intensity I of the incident beam is equal to the ratio of the apparent projected scattering area dA_s occupied by all scattering particles to the cross sectional area of the incident beam dA:

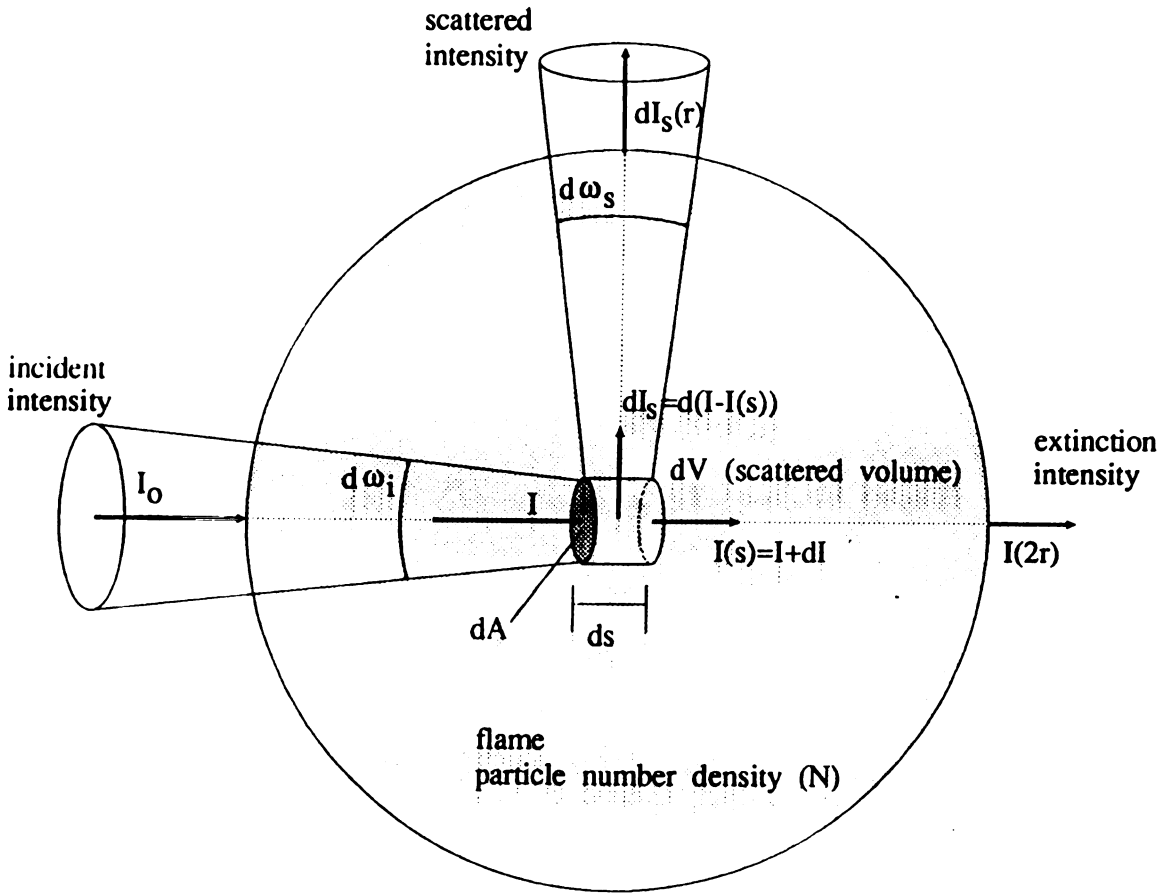

Figure 4-20 Laser light scattering from soot particles in the flame as measured perpendicular to incident light and its polarization.

For a b

mediur

present

volume

particle

The ch

For a

(4-9)

The p

Here,

This i

presen

scatteri

scatteri

$$\frac{I_s}{I} = \frac{dA_s}{dA} \tag{4-7}$$

For a beam of a particular wavelength, λ, traveling a differential distance, ds, within a medium in which it encounters the scattering area, dA_s, the apparent scattering area presented by a group of the scattering particles of number density, N, in control volume, dV, is related to the average scattering cross section, σ_s, of the individual particles by:

$$dA_s = \sigma_s \, N \, dV = \sigma_s \, N \, dA \, ds \tag{4-8}$$

The change dI of the intensity as a result of the scattering from the incident beam:

$$-\frac{dI}{I} = \frac{I_s}{I} = \frac{\sigma_s N dA ds}{dA} = \sigma_s N ds \tag{4-9}$$

For a finite, cylindrical control volume of length s (Figure 4-21), integrating Equation (4-9) over the path, the intensity at s can be written as:

$$I(s) = I \, \exp\left[-\int_0^s \sigma_s \, N \, ds' \right] \tag{4-10}$$

The portion of the incident intensity that was scattered away along the path is thus:

$$I - I(s) = I \left[1 - \exp\left[-\int_0^s \sigma_s \, N \, ds' \right] \right] \tag{4-11}$$

Here, by the definition of scattering coefficient, $Q_{sct} = \sigma_s N$, Equation (4-10) becomes:

$$I(s) = I \, \exp\left[-\int_0^s Q_{sct}(s') \, ds' \right] \tag{4-12}$$

This is the pure scattering form of Bouguor's law (Siegel & Howell, 1981). For the present study, incident beam was polarized vertically and only vertically polarized scattering intensity was detected. So, for the present study, Q_{vv} will be used for scattering coefficient of soot particles, and rewrite Equation (4-12). Then,

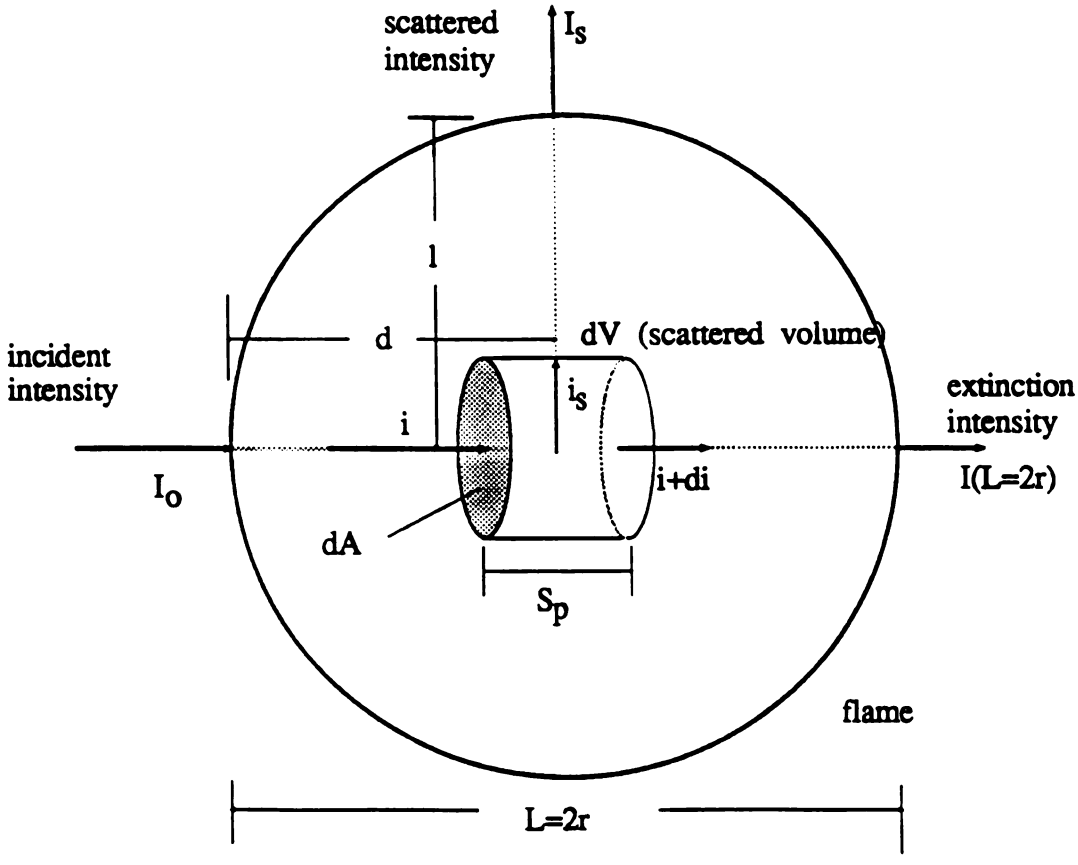

Figure 4-21 Laser light intensity calibration configuration in diffusion flame.

$$I(s) = I \exp\left[-\int_0^s Q_{vv}(s')\, ds' \right] \tag{4-13}$$

There are also losses due to absorption as well as scattering as the beam travels along a pathlength s. From the Beer's law and the attenuation, the extinction coefficient K_{ext} can be defined as:

$$\frac{I(s)}{I_o} = \exp\left[-K_{ext}\ s \right]$$

It is important to point out that the incident beam is also absorbed by the gas which exists in the flame as well as soot particles. This absorption by this gas is, of course, very small to compare with the attenuation by the soot particles. But it was found that the effect was big enough to be concerned at the edge of the sooting zone. So, it is necessary to avoid the effect on the laser intensity by the gas in the flame.

Therefore, the extinction intensity by the gas in the non-sooty flame was measured. The measured intensity attenuated by the gas of blue or yellow flame (non-sooty flame) varied along the axial direction. This may come from the density difference from the temperature gradient in the flame. Because, the gas temperature in the observed region was in the range between 1200 K and 2000 K. So, the gas density could be two or three times smaller than the gas density at room temperature.

This problem can be avoided if these two attenuations can be separated. Consider I_m be a measured intensity after passing through sooty flame. Then it can be written as:

$$\begin{aligned} I_m &= I \exp\left[-\int K_{ext}\, dl \right] \\ &= I \exp\left[-\int (K_{ext,\,gas} + K_{ext,\,soot})\, dl \right] \\ &= I \exp\left[-K_{ext,\,gas}\, l_{gas} \right] \exp\left[-K_{ext,\,soot}\, l_{soot} \right] \\ &= I_{gas} \exp\left[-K_{ext,\,soot}\, l_{soot} \right] \end{aligned}$$

where, $K_{ext,\,gas}$, $K_{ext,\,soot}$ are extinction coefficients of gas and soot particles, respectively. l_{gas}, l_{soot} are laser pathlength through gas and soot particles, respectively. And I_{gas} is defined the laser extinction intensity only by gas.

From above investigation, if I_{gas} is used as a incident laser intensity, then the extinction intensity only by soot particles can be separated. So, it is very important to find a flame of which physical and chemical properties are exactly same as those of the sooty flame except soot existence. Then the measured intensity attenuated purely by the gas instead of soot particle can be used as reference incident intensity for the calculation. Figure 4-22 shows the difference between the extinction intensities path through the sooting flame and reference flame. This ideal reference flame does not exist in nature. Therefore, the reference flame was chosen to be very close to the each sooty flame. To define the reference flame, maximum scattering intensity, temperature, and stagnation plane location were measured, while increasing fuel concentration in fuel stream and decreasing oxygen concentrations in oxidizer stream. Maximum scattering intensity was selected for the reference flame to be less than 0.5 % of that of sooty flame. Temperature profile and stagnation plane location were selected to be very close to the sooty flame, so that the density profile can be close to that of sooty flame. To obtain the best reference flame, the process was repeated until all the conditions were satisfied.

Based on the reference incident intensity, I_r, instead of the incident beam intensity, I_o, of laser light, the extinction coefficient of soot particles in the flame can be redefined as:

$$K_{ext} = -\frac{1}{l} \ln \left[\frac{I(l)}{I_r} \right] \tag{4-14}$$

For the soot particles in the flame on the Figure 4-21, incident beam is attenuated along the path d and the scattered intensity is attenuated along the path l. For these two pathlength, I_s and i can be expressed using the extinction coefficient, K_{ext}:

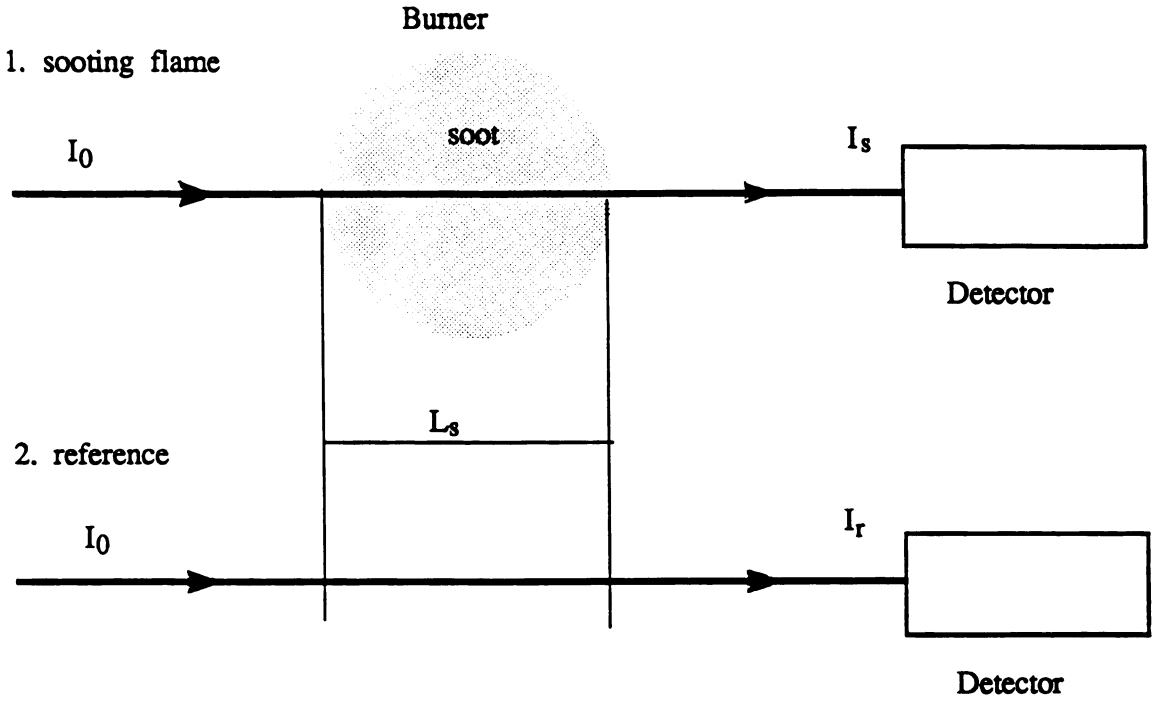

Figure 4-22 Conceptual schematic of extinction intensities of sooting flame and reference flame.

$$\frac{i}{I_o} = \exp\left[- K_{ext}\ d \right] \tag{4-15}$$

$$\frac{I_s}{i_s} = \exp\left[- K_{ext}\ l \right] \tag{4-16}$$

Also from Equation (4-13), and for the one-dimensional soot field in which Q_{vv} is not function of the position, the scattering intensity can be written as:

$$\frac{i_s}{i} = C_1 \left[1 - \exp\left[- Q_{vv}\ S_p \right] \right] \tag{4-17}$$

where C_1 is due to the solid angle of measured scattering intensity.

Equations (4-15), (4-16), and (4-17) can be used to determine the ratio of the measured scattering intensity to the incident intensity as:

$$\frac{I_s}{I_o} = C_2 \frac{I_s}{i_s} \frac{i}{I_o} \frac{i_s}{i}$$

or

$$\frac{I_s}{I_o} = C_o \exp\left[- K_{ext}\ d \right] ext\left[- K_{ext}\ l \right] \left[1 - \exp\left[- Q_{vv}\ S_p \right]\right] \qquad (4\text{-}18)$$

where, I_o is incident intensity of laser light, I_s is scattered intensity after pass flame from the scattered volume, i is incident intensity just before scattered volume (attenuated by flame gas and soot), and i_s is scattered intensity by soot at the scattered volume. Here, C_2 and C_o are the calibration constant with the phase functions. The calibration constant can be determined by measuring the scattering intensity from a gas with known scattering cross section. For the present study, nitrogen gas was used as a calibration gas. Rudder and Bach (1968) measured the scattering cross section of nitrogen experimentally. It was found $\sigma_{N_2} = 2.12 \times 10^{-28}\ cm^2$ for the incident beam wavelength 694.3 nm. It can be converted for the laser beam wavelength 514.5 nm:

$$\sigma_{N_2} = 2.12 \times 10^{-28} \left[\frac{694.3}{514.5} \right]^4 = 7.03 \times 10^{-28}\ cm^2$$

Then, for the nitrogen gas with assuming negligible extinction, the Equation (4-18) becomes:

$$I_{s,N_2} = C_o\ I_o \left[1 - \exp\left[- Q_{vv,N_2}\ S_p \right]\right] \qquad (4\text{-}19)$$

For the soot particles in the flame with assumption of using the same optical system, so that the calibration constant, C_o remains the same, Equation (4-18) becomes:

$$I_{s,soot} = C_o\ I_o \left[1 - \exp\left[- Q_{vv,soot}\ S_p \right]\right] \exp\left[- K_{ext}\ (l+d) \right] \qquad (4\text{-}20)$$

For the small value of x, exponential function can be approximated, $\exp(x) = 1 + x$,

with reasonable accuracy. Taking this approximation and dividing Equation (4-20) by Equation (4-19) becomes:

$$\frac{I_{s,\,soot}}{I_{s,\,N_2}} = \frac{\left[1-\left[1-Q_{vv,\,soot}\,S_p\right]\right]}{\left[1-\left[1-Q_{vv,\,N_2}\,S_p\right]\right]}\exp\left[-K_{ext}(l+d)\right] \tag{4-21}$$

Solving for $Q_{vv,\,soot}$ with extinction coefficient (Equation 4-14) gives:

$$Q_{vv,\,soot} = Q_{vv,\,N_2}\frac{I_{s,\,soot}}{I_{s,\,N_2}}\left[\frac{I(L)}{I_r}\right]^{-(l+d)/L} \tag{4-22}$$

Here, since the control volume is located at the center of circular shape of flame, l = d = L/2. So the exponent can be simplified to -1.

4.4.2 Soot Particle Measurement Results

By using Equations (4-14) and (4-22), the extinction and the scattering coefficients were calculated from the measured scattering and extinction intensities. The physical properties of soot particles can be derived from these extinction and scattering coefficients with Rayleigh approximation. Recall Equations (3-33), (3-35), and (3-36) and rewrite with measured soot optical properties for soot volume fraction, soot particle diameter, and soot number density that are already explained in detail in chapter 3:

$$f_v = \frac{\lambda\,K_{ext}}{6\pi\,E(m)}, \tag{4-23}$$

$$D = \lambda\left[\frac{4}{\pi^2}\,\frac{E(m)}{F(m)}\,\frac{Q_{vv,soot}}{K_{ext}}\right]^{\frac{1}{3}}, \tag{4-24}$$

and

$$N = \frac{12\,f_v}{\pi\,D^3}. \tag{4-25}$$

where

$$F(m) = \left| \frac{m^2-1}{m^2+2} \right|^2$$

$$E(m) = -\,\mathrm{Im}\left[\frac{m^2-1}{m^2+2}\right]$$

For the present study, refractive index $m = 1.57 - i\ 0.56$ is used.

The measured scattering and extinction intensities are shown in Figures 4-23 through 4-34 for each flame. Scattering intensity is zero below the stagnation plane. The scattering intensity sharply increases at stagnation plane. This indicates that the soot particles are big enough to follow the streamlines instead of to diffuse into below the stagnation plane. This maximum scattering intensity decays exponentially cross the sooting zone.

Extinction intensity is integrated quantity, so, it depends not only on the optical properties of the medium but also on its pathlength. The lowest value was measured at the longest pathlength through soot particles just above the stagnation plane ($Z_n \sim 0.1$). The extinction intensity measured below the stagnation plane was always lower than that around the flame location. In these locations, the scattering intensities were almost zero. This showed these attenuation is taken only by gas and this difference may come from the gas density and the deflection of beam due to the density gradient. Fortunately, the extinction intensities of reference flame are close enough to those in the sooty flame at the places where soot does not exist.

Extinction coefficient, K_{ext}, scattering coefficient, Q_{vv}, soot particle diameter, D, and soot particles number density, N were plotted against normalized coordinate system with the pre-heat temperatures. Soot particle total surface area is also known as an important factor of soot growth rate (Harris, 1990). This was also plotted against normalized coordinate. These are shown in Figures 4-35 through 4-43.

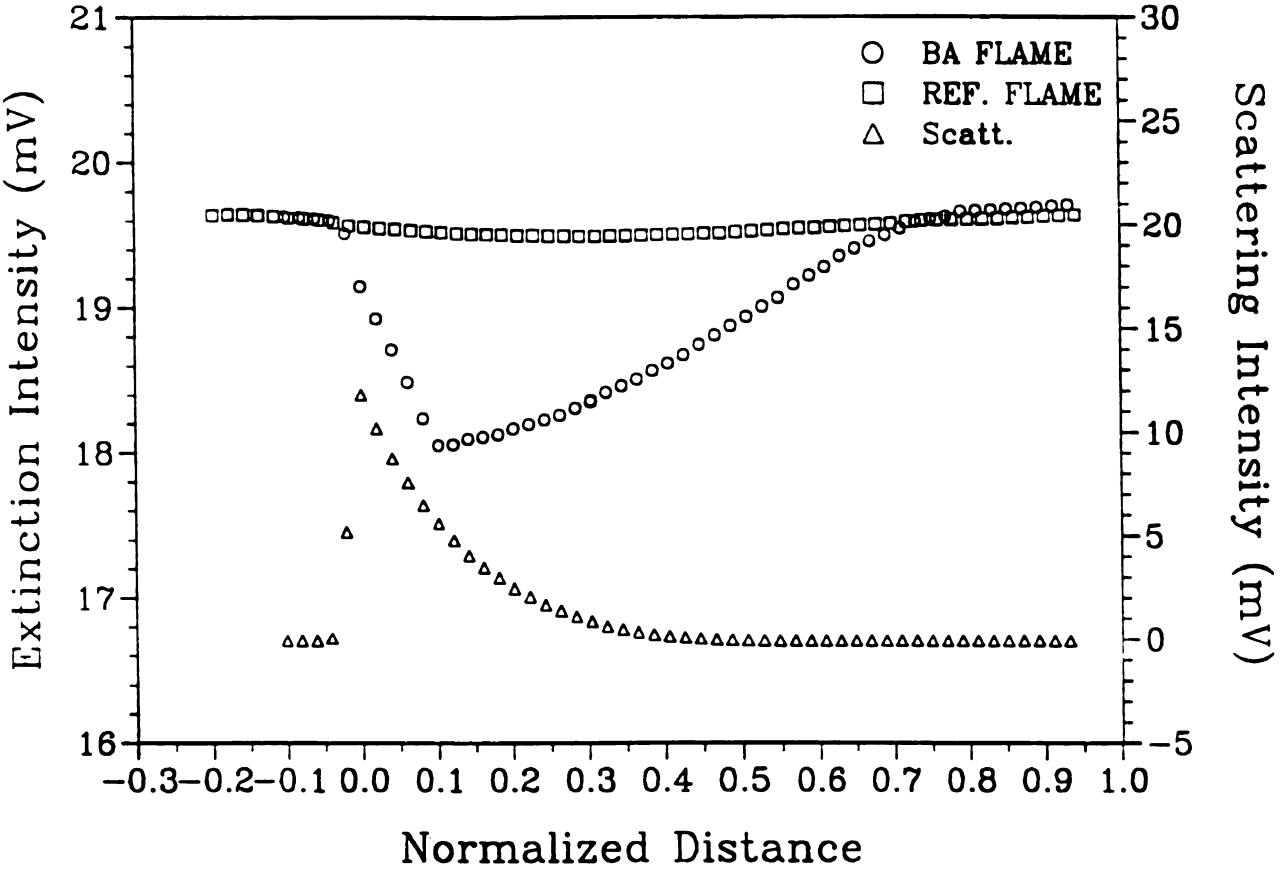

Figure 4-23 Measured scattering and extinction intensities of BA-flame and its reference flame.

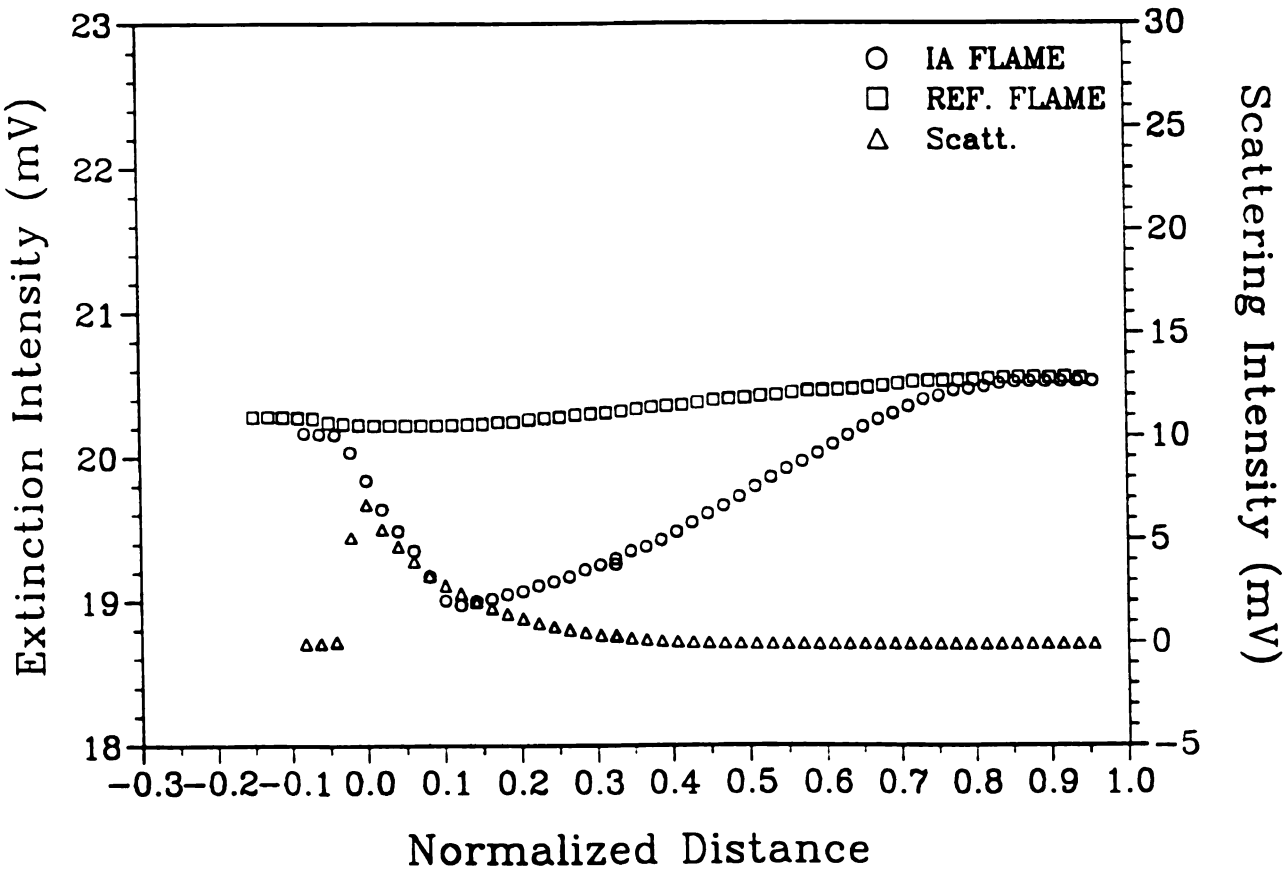

Figure 4-24 Measured scattering and extinction intensities of IA-flame and its reference flame.

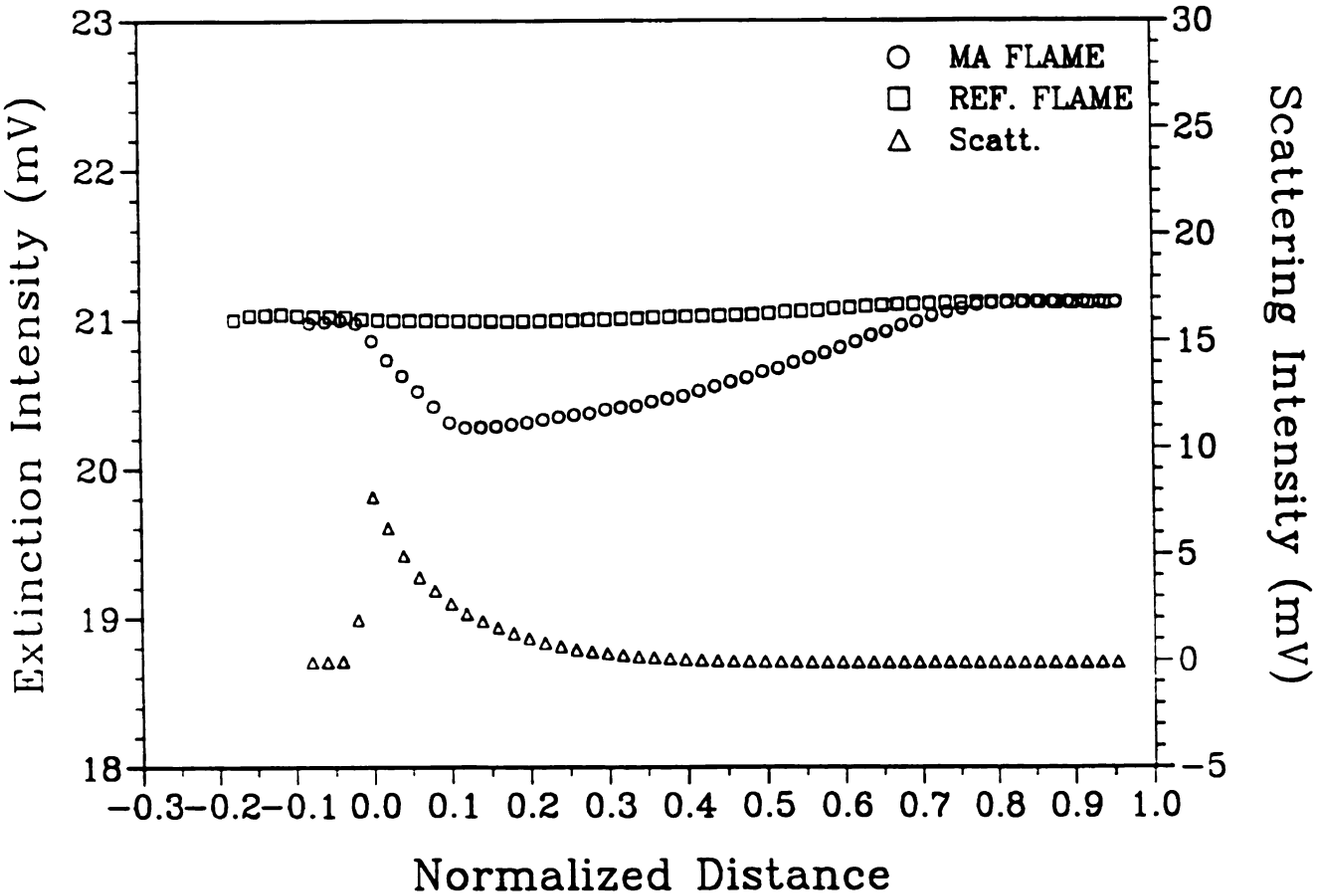

Figure 4-25 Measured scattering and extinction intensities of MA-flame and its reference flame.

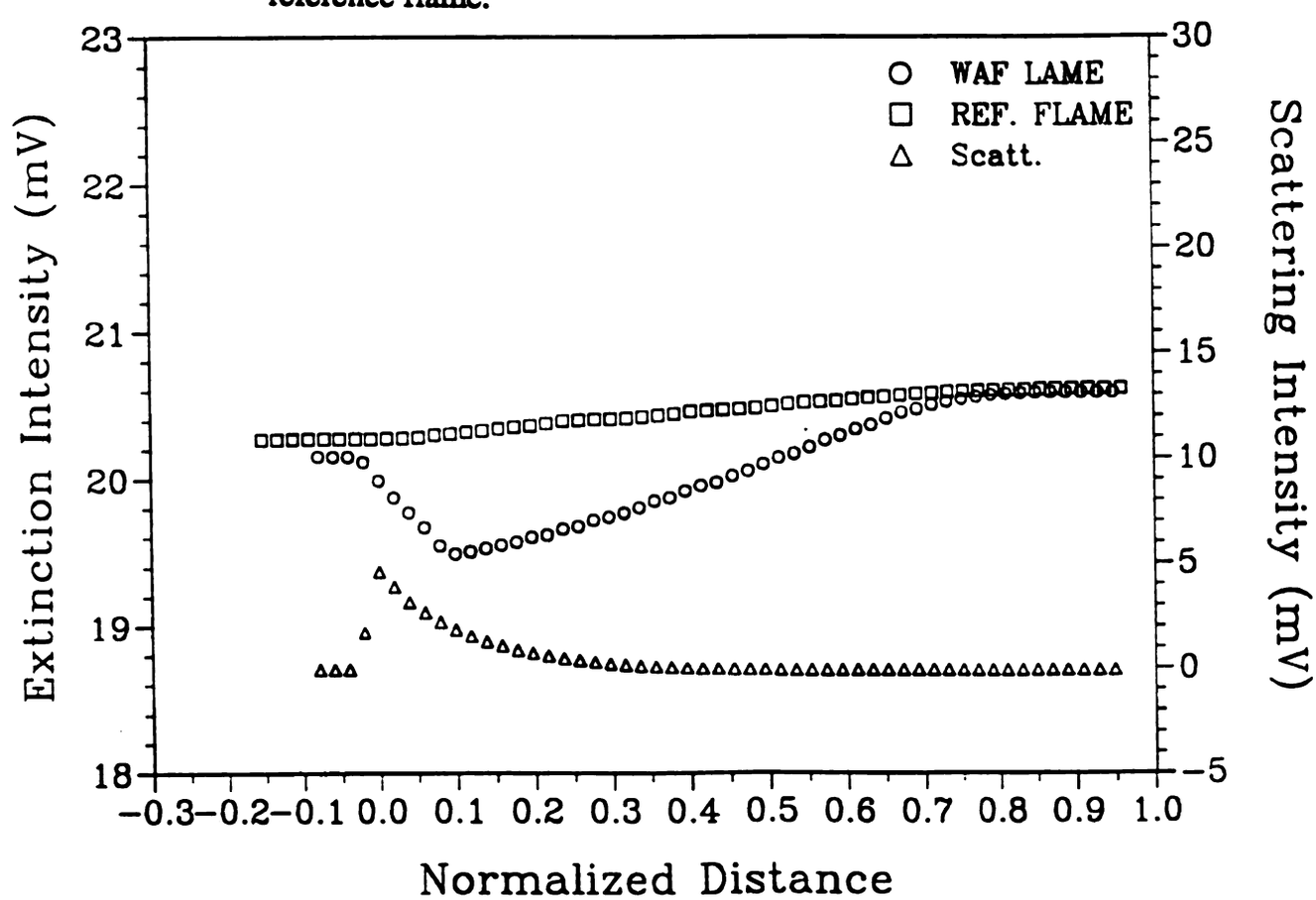

Figure 4-26 Measured scattering and extinction intensities of WAF-flame and its reference flame.

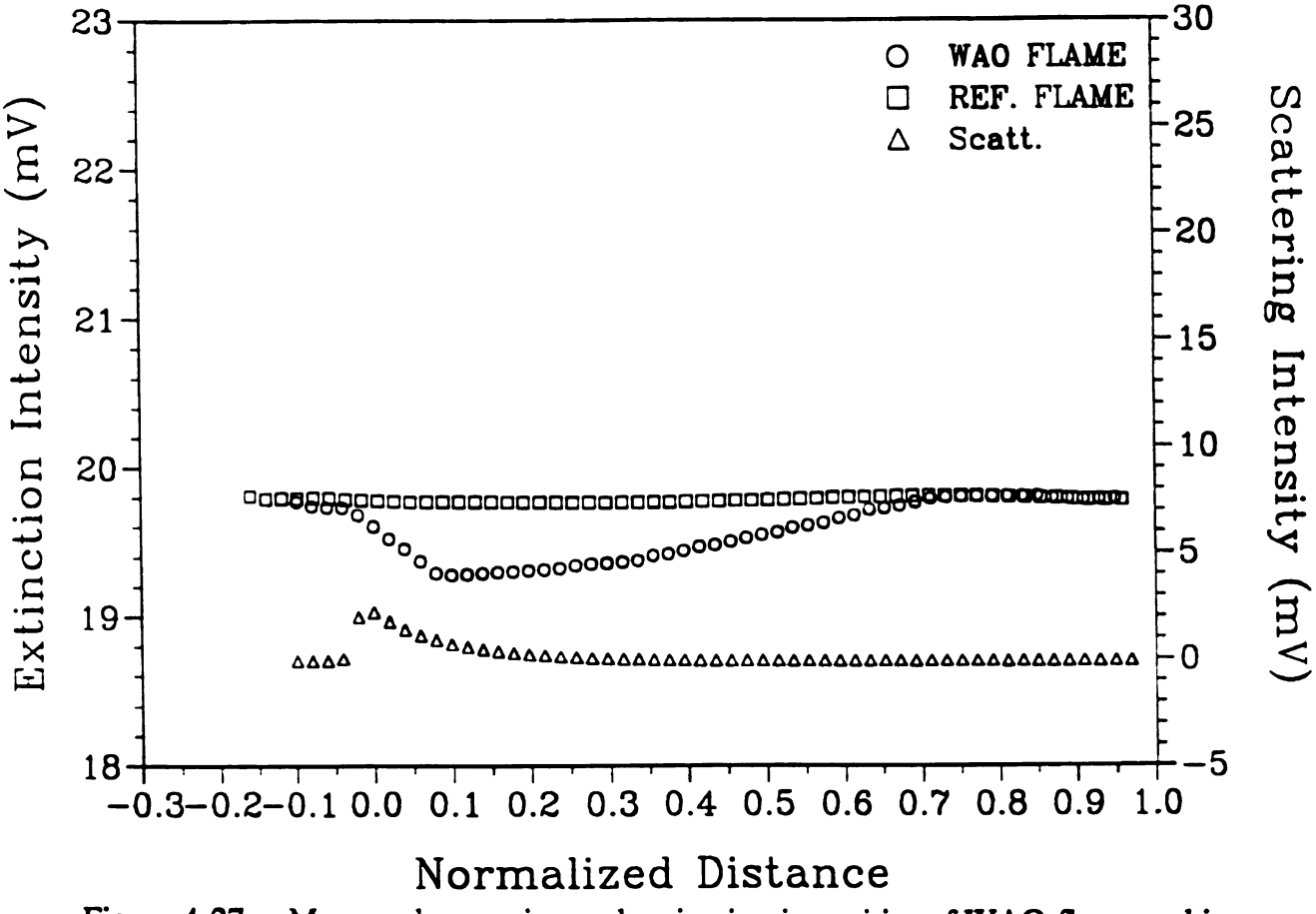

Figure 4-27 Measured scattering and extinction intensities of WAO-flame and its reference flame.

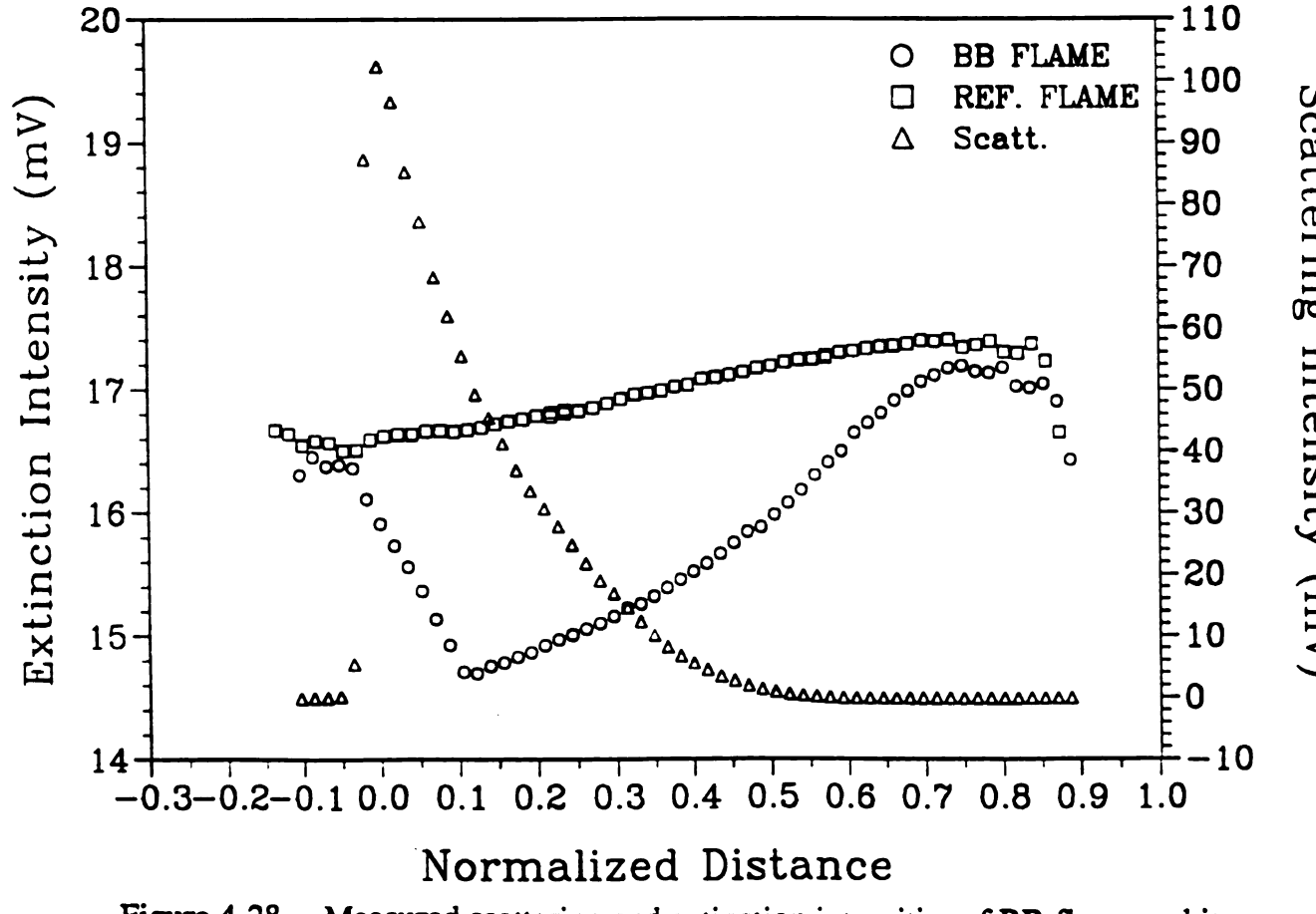

Figure 4-28 Measured scattering and extinction intensities of BB-flame and its reference flame.

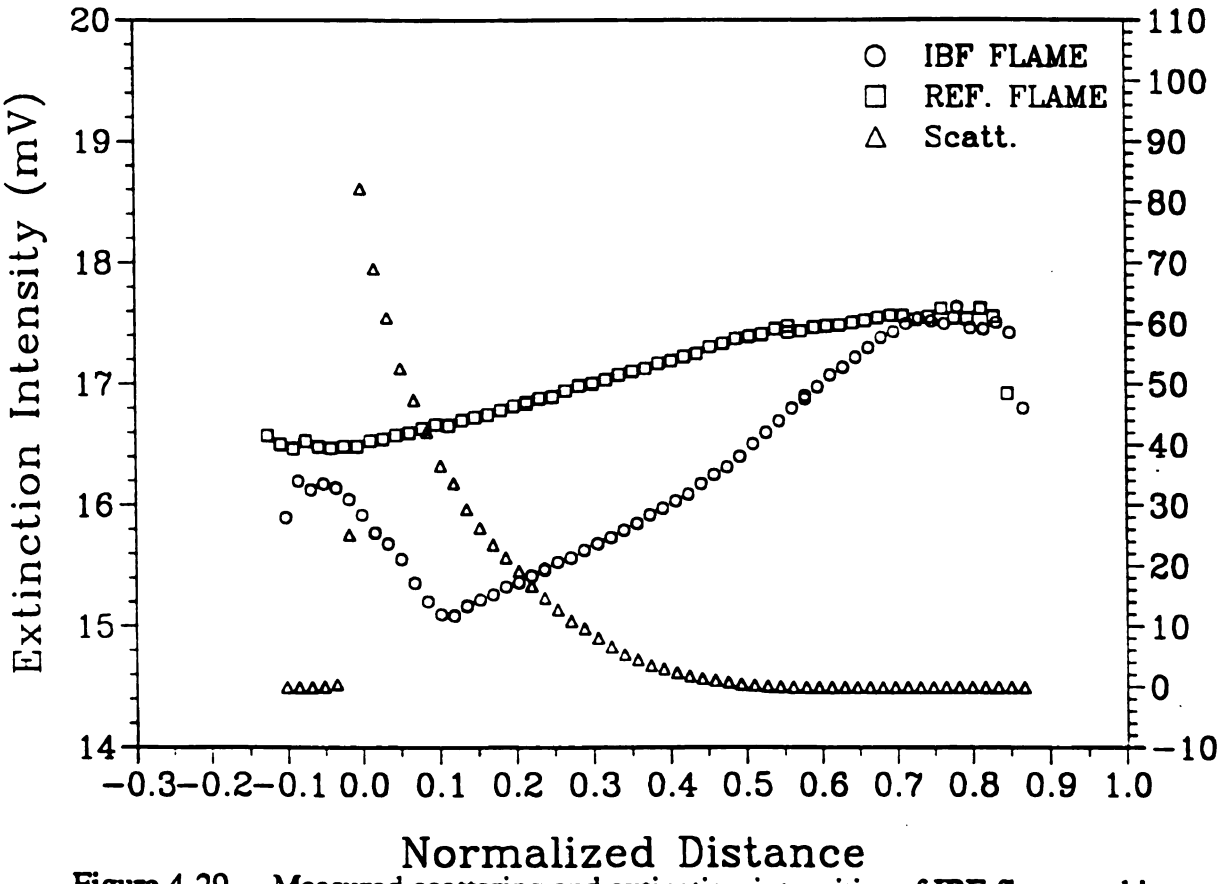

Figure 4-29 Measured scattering and extinction intensities of IBF-flame and its reference flame.

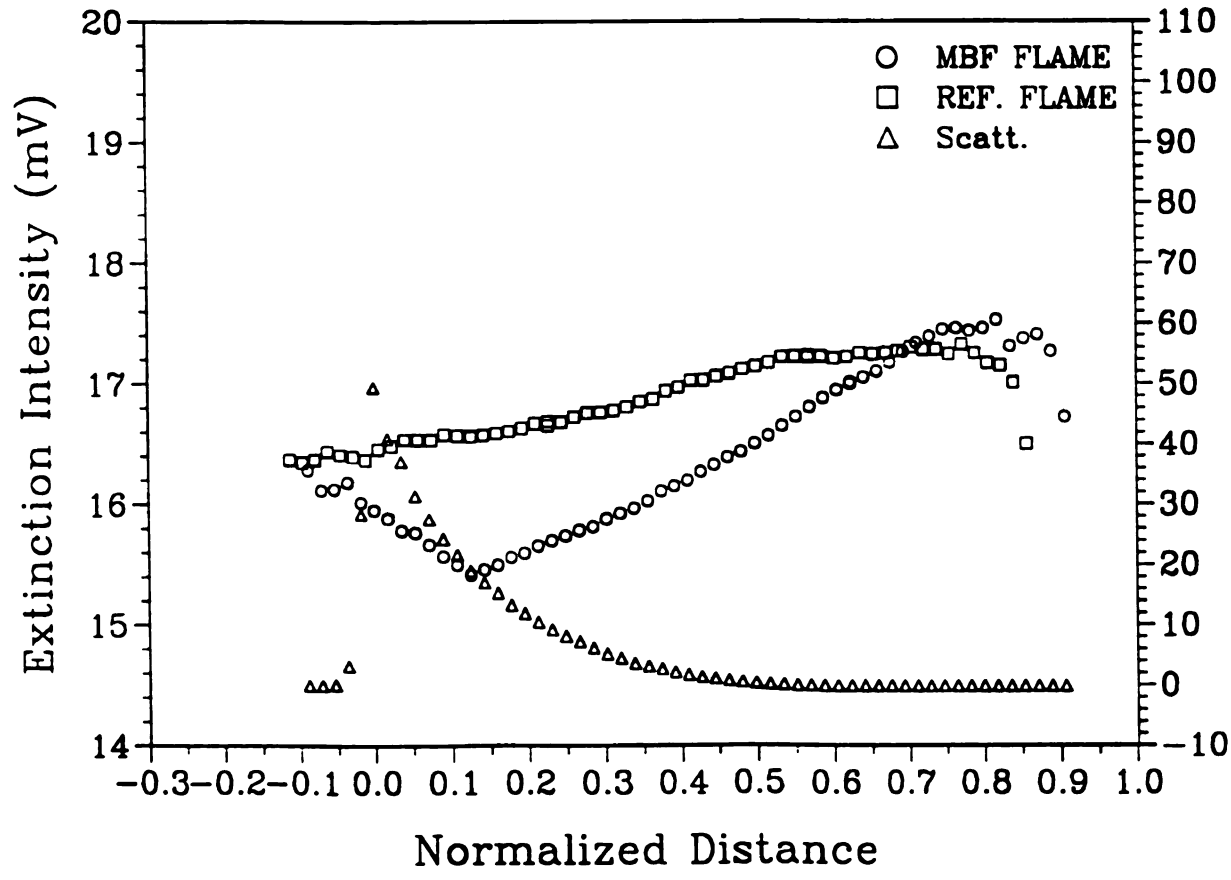

Figure 4-30 Measured scattering and extinction intensities of MBF-flame and its reference flame.

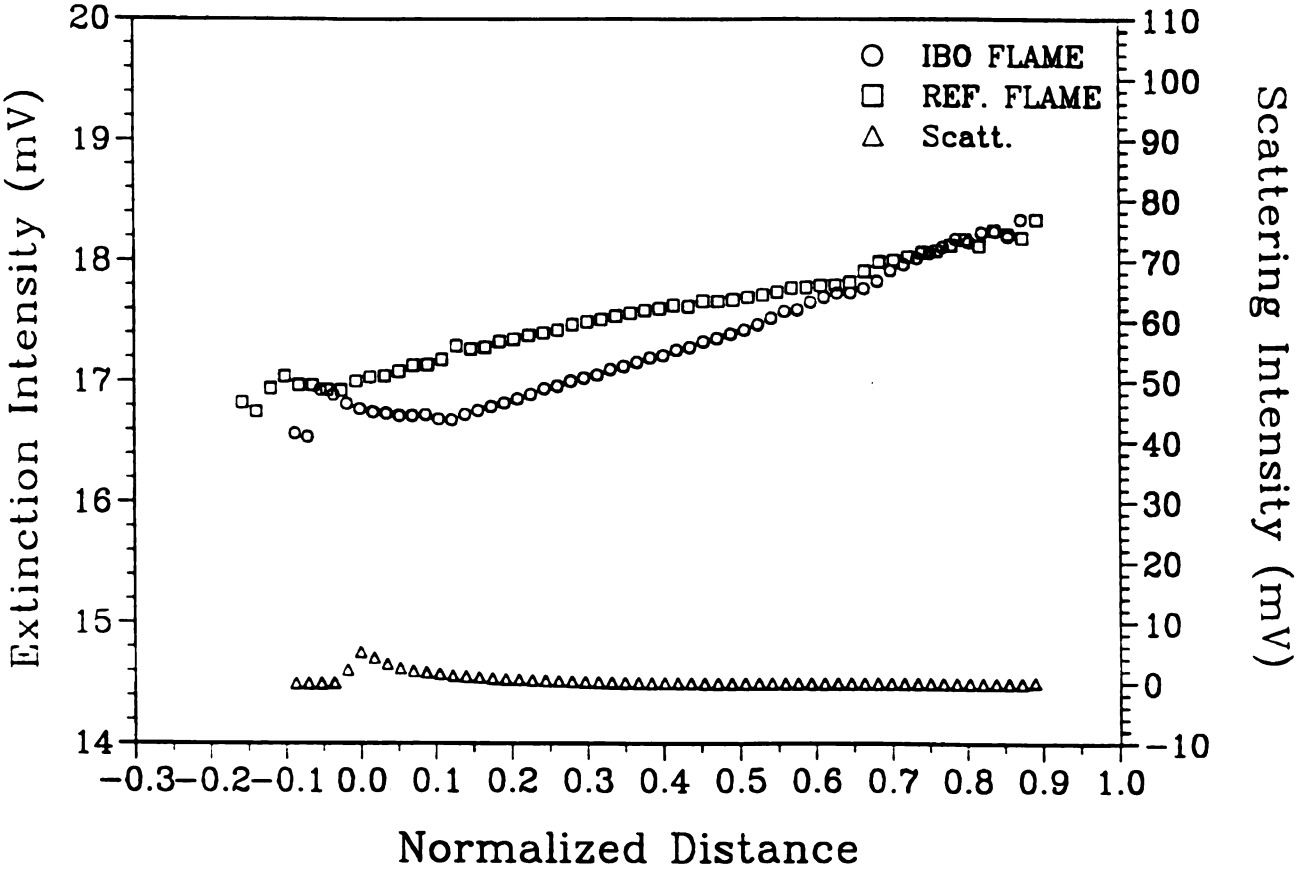

Figure 4-31 Measured scattering and extinction intensities of IBO-flame and its reference flame.

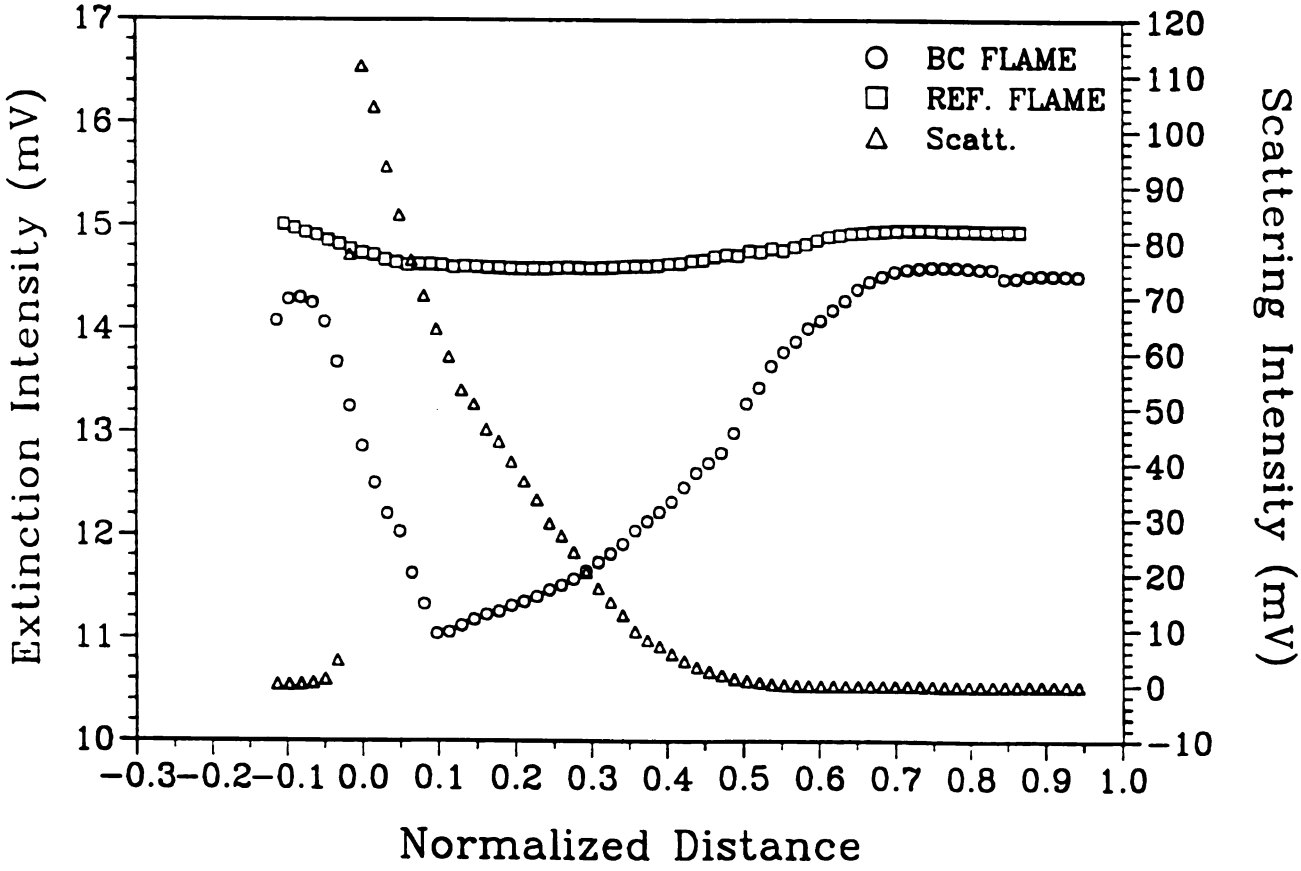

Figure 4-32 Measured scattering and extinction intensities of BC-flame and its reference flame.

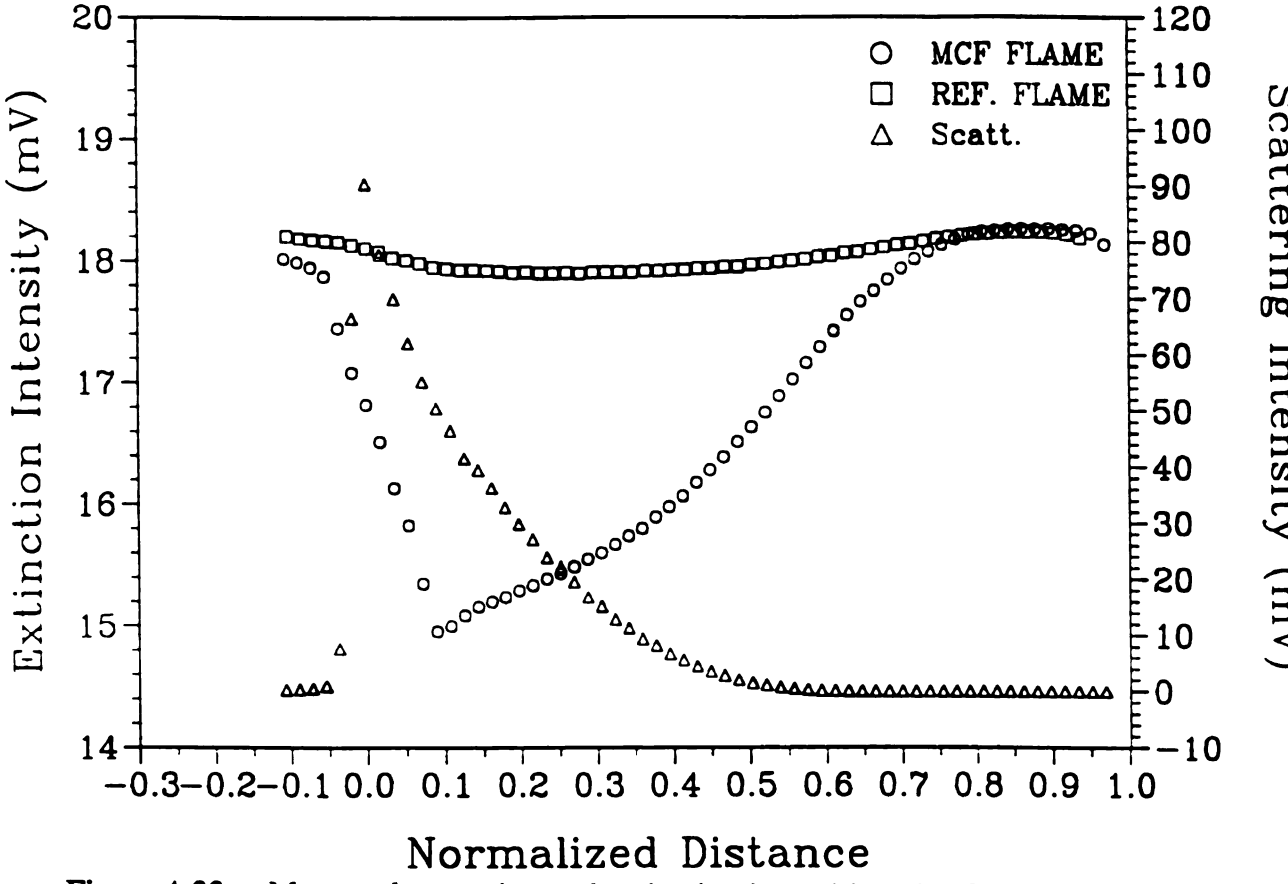

Figure 4-33 Measured scattering and extinction intensities of MCF-flame and its reference flame.

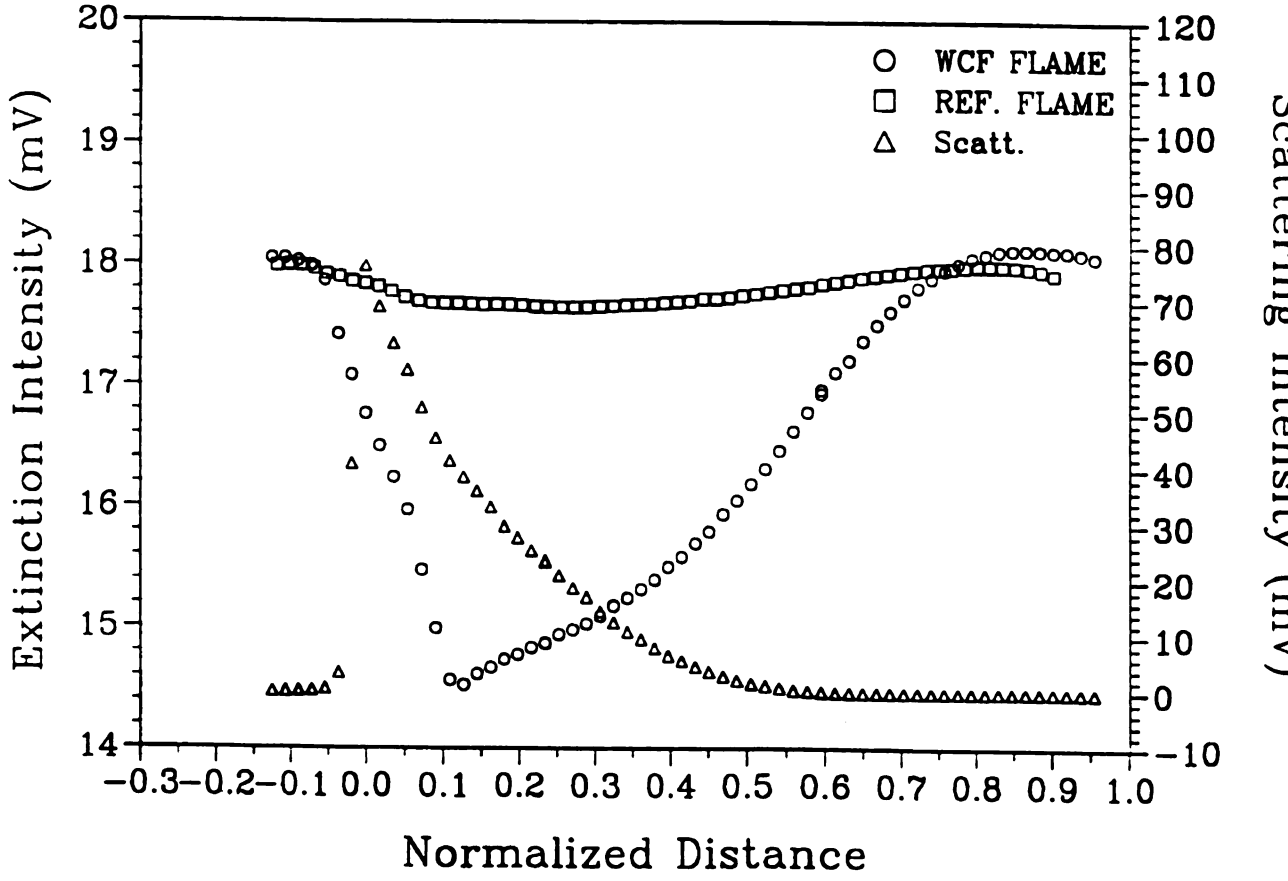

Figure 4-34 Measured scattering and extinction intensities of WCF-flame and its reference flame.

The scattering and extinction coefficients are shown in Figures 4-35, 4-38, and 4-41 for 300 K, 900K and 1200 K flames, respectively. These extinction coefficients, in general, has peak values at the stagnation plane and decreases slowly along the axial direction until the soot particle size becomes about an order of 1 *nm*. Then it decreases little faster, then slowly approach to zero value. The scattering coefficient, also in general, decreases almost linearly in log scale until the soot particle size about an order of 1 *nm*. Beyond that it was out of scale of the scattering measurements. At the sensitivity of the lock-in amplifier set for measuring the peak value of scattering intensity, the scattering intensity beyond that point could not be detected.

Figures 4-36(a), 4-39(a), and 4-42(a) show soot particle number density profiles for 300 K, 900 K, and 1200 K flames. Soot number density decreases very sharply from the huge number and then the slope of the curve decreases from the nucleation zone. Soot particles number density is always order of about 1.0×10^9 for all flames at the stagnation plane. Based on this soot number density profile and particle size, the zone in where the number density is larger then 1.0×10^{12}, can be called soot inception zone. In this zone soot particle size is subnanometer. So, it can be called big molecule instead of particle. When it becomes a particle, coagulation dominates the particle nucleation. After turning to the particle from the molecule, particle grows by coagulation or agglomeration and surface growth.

Soot particle size profiles are shown in Figures 4-36(b), 4-39(b), and 4-42(b). Particle size increases almost linearly along the normalized coordinate. This shows that soot particles which passed longer pathlength are bigger in size. So, the smaller particles are created at lower position and larger particles are created earlier (closer to the flame zone).

For the 300 K experiments, Figures 4-35 (a) and (b), Figures 4-36 (a) and (b), and Figures 4-37 (a) and (b) show the scattering coefficient, extinction coefficient, number density, soot particle diameter, soot particles total surface area, and volume

frac

diti

Ad

the

sho

soc

par

tio

hig

(b)

K

fla

an

tha

are

Fi

are

tho

(a)

tha

12

abo

20

den

1.0

fraction, respectively. BA flame, which is the most sooty flame at 300 K pre-heat condition, has the highest value of scattering and extinction coefficients in all range. Adding CO_2 in the fuel stream reduces these coefficients. This reduction comes from the decreasing of soot volume fraction and particle size. Figures 4-36 (b) and 4-37 (b) show the decreasing of soot volume fraction and particle diameter. In WAO flame, soot particles are created later and hence the soot particle sizes are the smallest. Soot particle number densities are almost the same at 1.0×10^9 particles/cm^3 at the stagnation plane. And surface area varies from about 0.3 to 0.1 cm^2/cm^3.

For the 900 K experiments, the scattering and extinction coefficients are much higher than those in 300 K experiments, except the IBO flame (Figures 4-38 (a) and (b)). The scattering coefficient in 300 K flames are in the order of 10^{-5}, while in 900 K flames they are in the order of 10^{-4}. Extinction coefficients of BB, IBF, and MBF flames in 900 K experiments increase between 1.4 and 2.0 times of those in BA, IA, and MA flames in 300 K experiments. Soot particle sizes also increase about 1.5 times than those in 300 K flames. At the stagnation plane the soot particle number densities are also 1.0×10^9 which is same value in 300 K flames, except that in IBO flame. Figure 4-40 (a) shows the soot particles total surface area. In 900 K flames, the surface area varies about 0.4 to 0.2 cm^2/cm^3. The surfaces area increased about 30 % than those in 300 K flames.

The results of 1200 K experiments are shown in Figures 4-41 (a) and (b), 4-42 (a) and (b), and 4-43 (a) and (b). Scattering and extinction coefficient are much larger than those in 900 K. In 900 K, scattering coefficient are in the order of 10^{-4} but in 1200 K flames they are in the order of 10^{-3}. The extinction coefficients are increased about twice than those in 900 K flames. Soot particle sizes are increased about 10 to 20 % from those in 900 K flames. Even in 1200 K flames the soot particle number densities are the same as the other conditions. At the stagnation plane, they are about 1.0×10^9 particles/cm^3. Volume fractions are increased about twice than those in 900

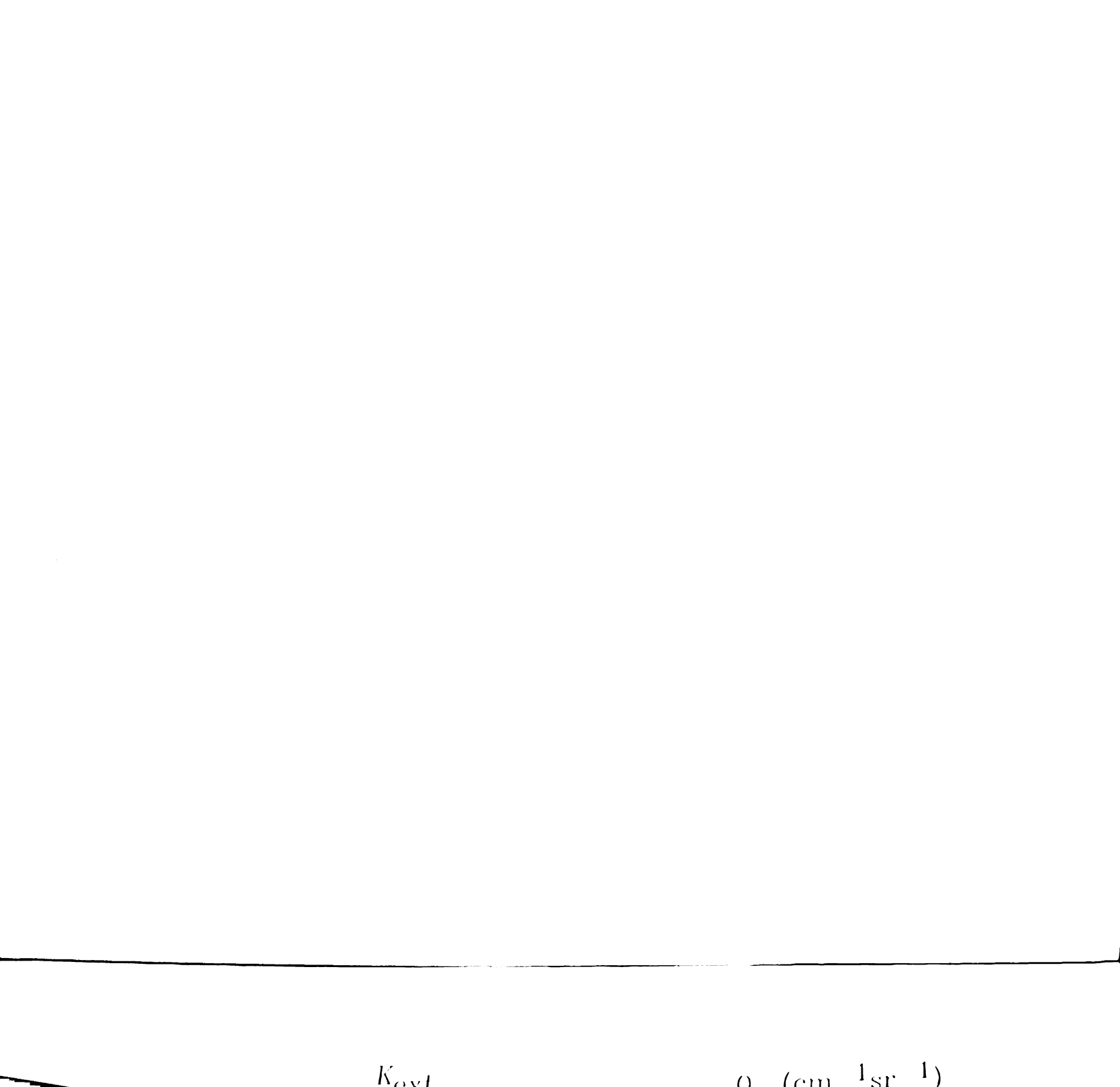
K_{ext}
() (cm ^{1}sr ^{1})

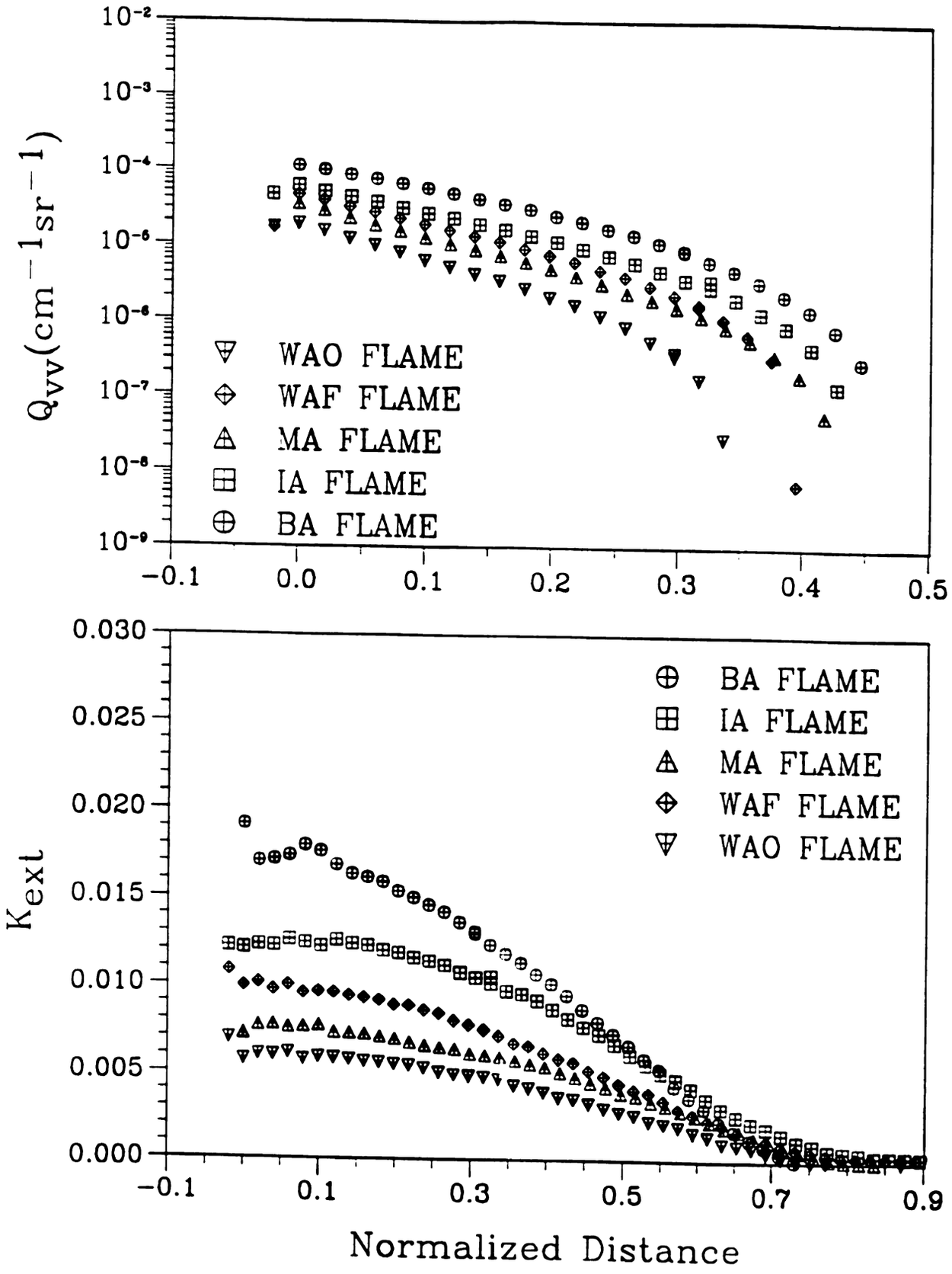

Figure 4-35 Extinction and scattering coefficient between stagnation plane and flame location, for 300 K flames
a) Scattering coefficient, Q_{vv} in cm^{-1} sr^{-1}
b) Extinction coefficient, K_{ext} in cm^{-1}

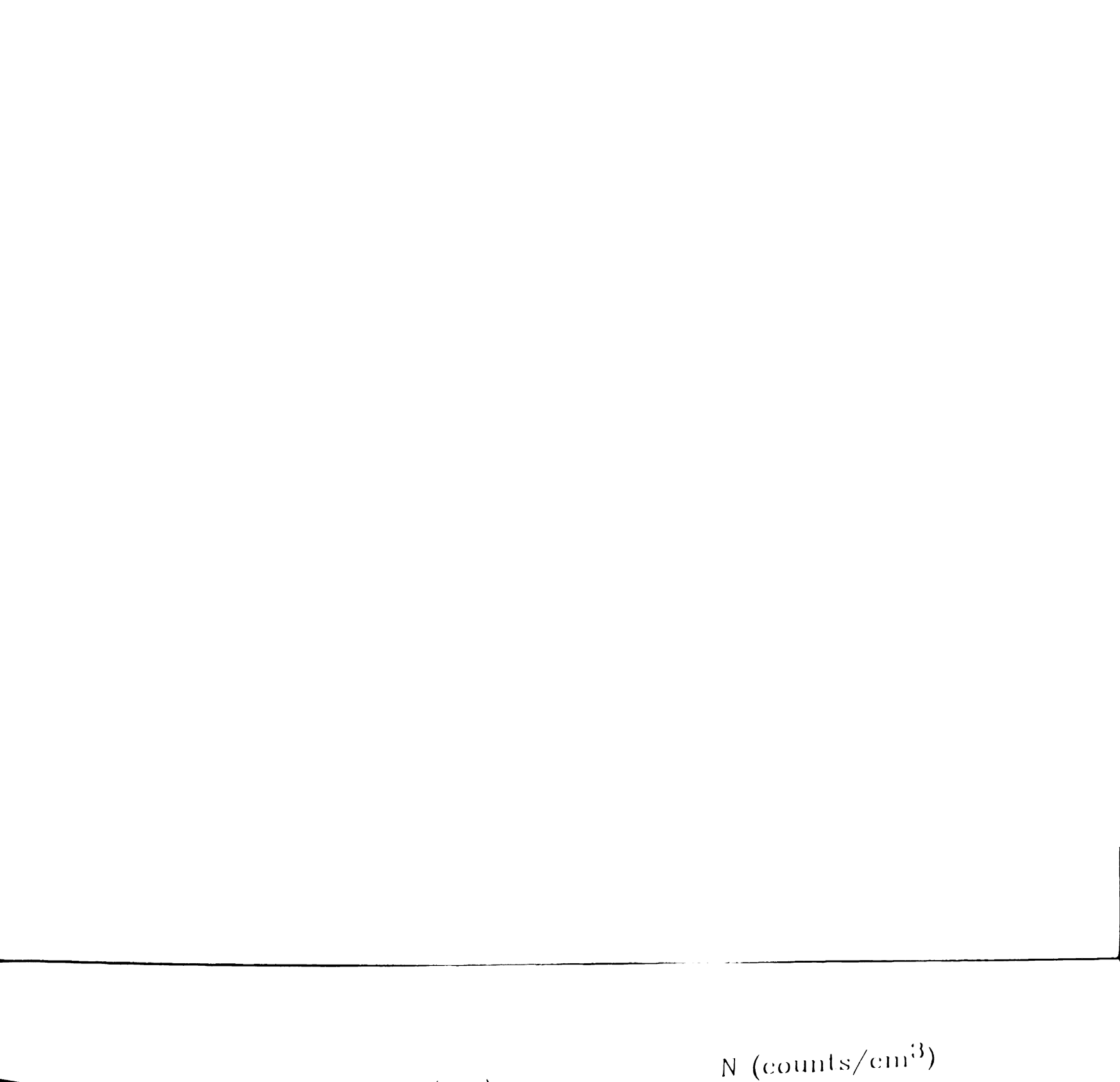
N (counts/cm^3)

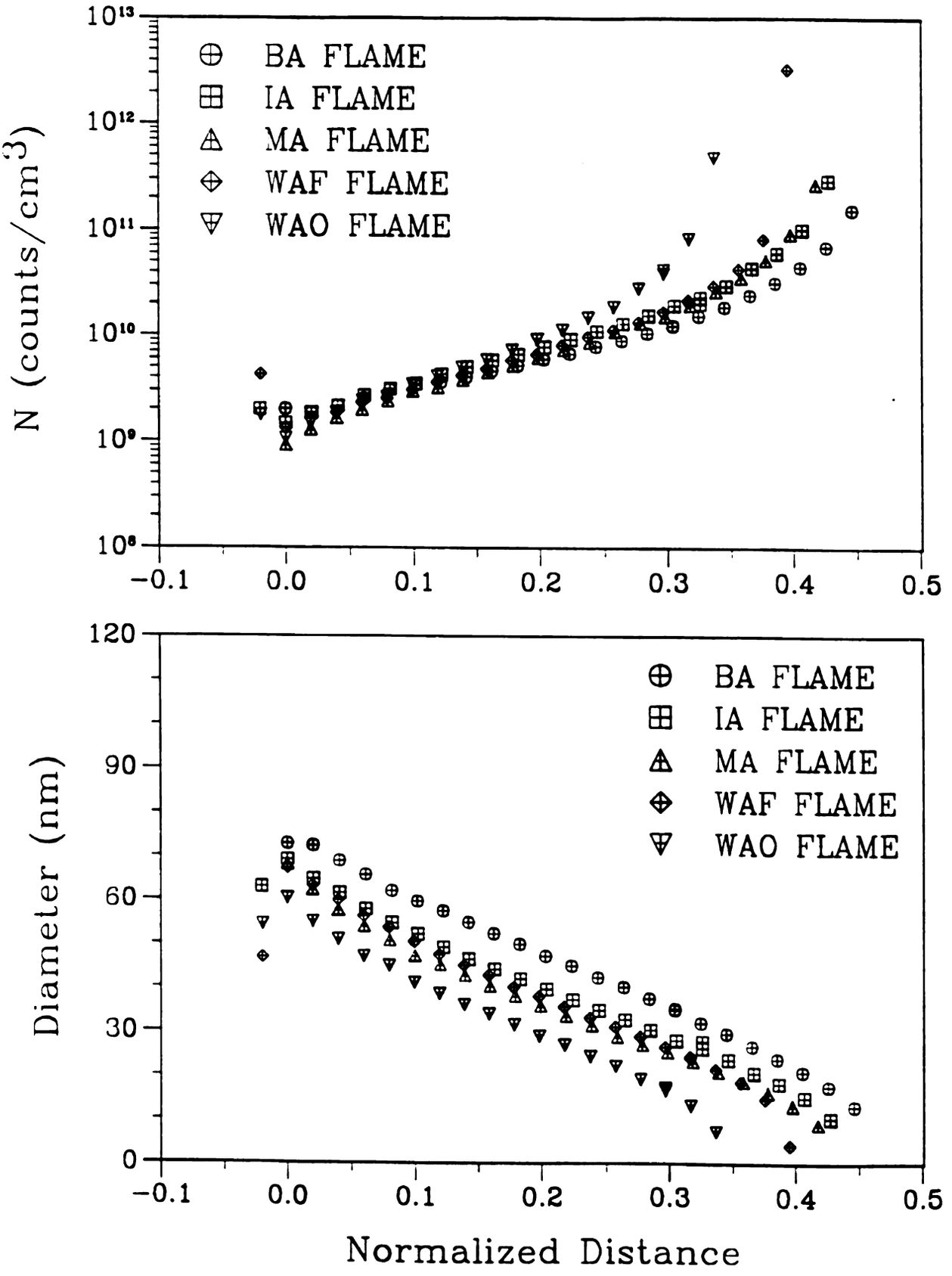

Figure 4-36 Soot particle number density and particle size for 300 K flame
a) Soot particle number density in counts/cm^3
b) Soot particle diameter in nm

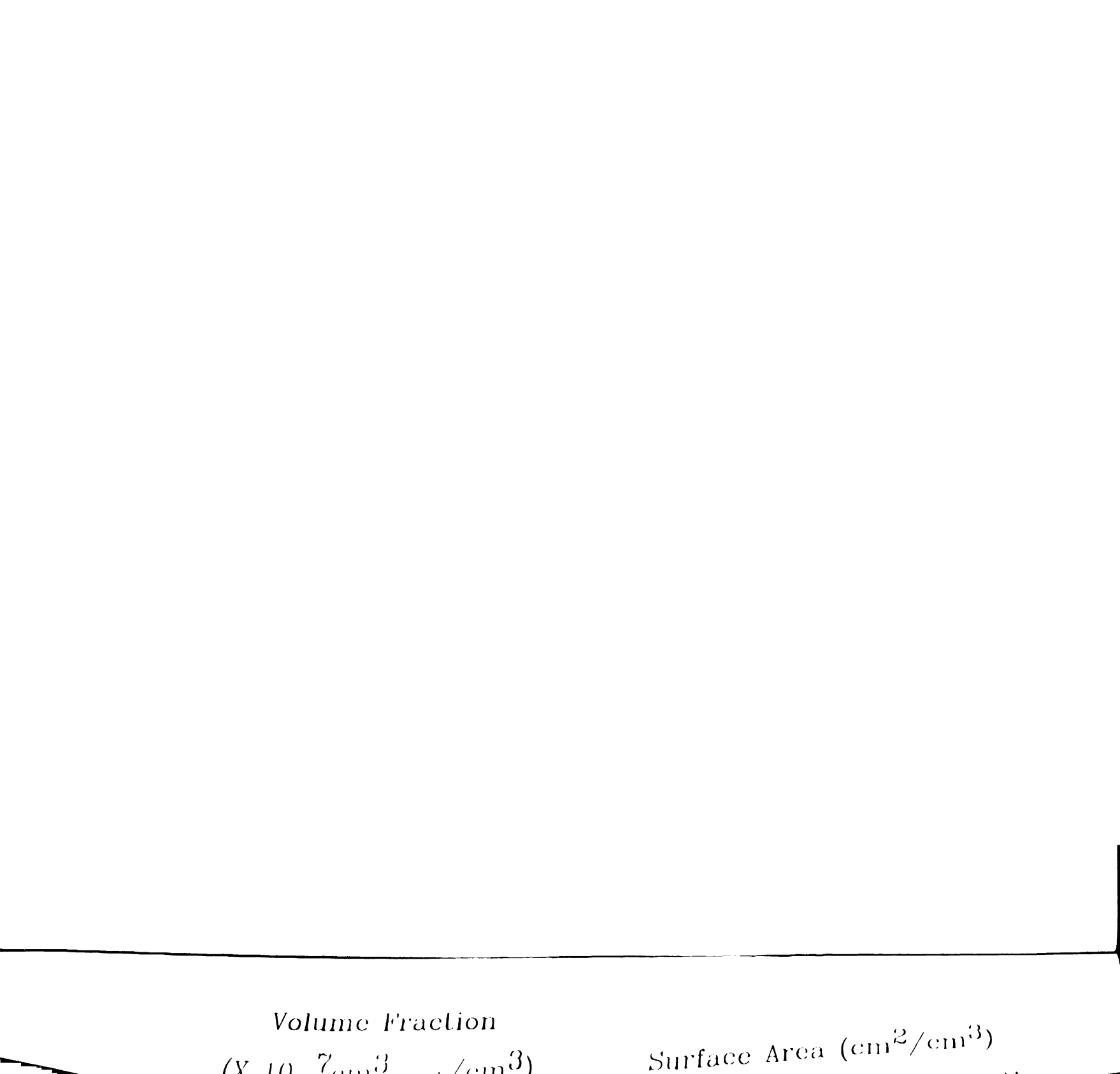
Volume Fraction
Surface Area (cm2/cm3)

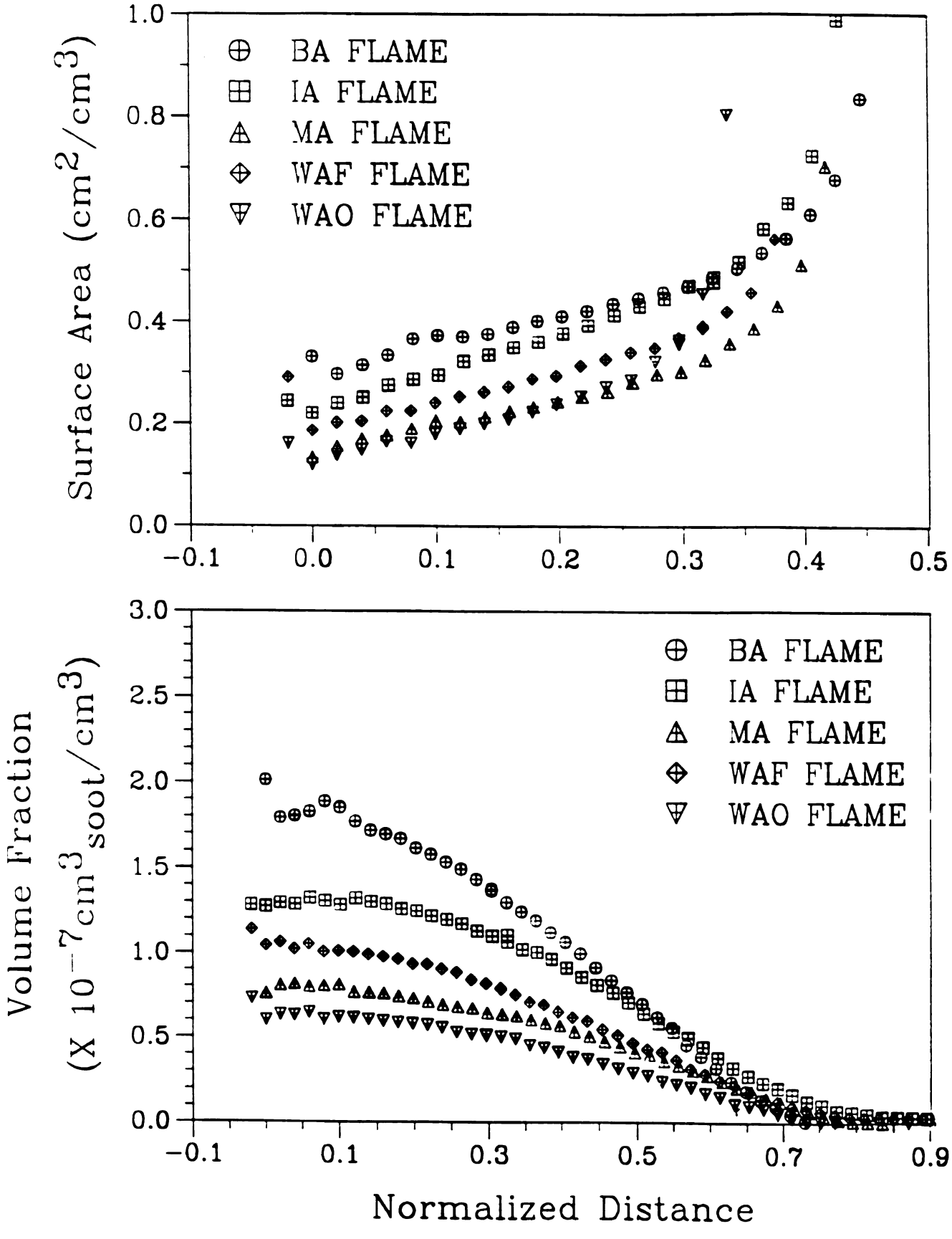

Figure 4-37 Soot particle total surface area and volume fraction for 300 K flame
a) Soot particle total surface area in cm^2_{soot}/cm^3_{space}
b) Soot particle volume fraction in cm^3_{soot}/cm^3_{space}

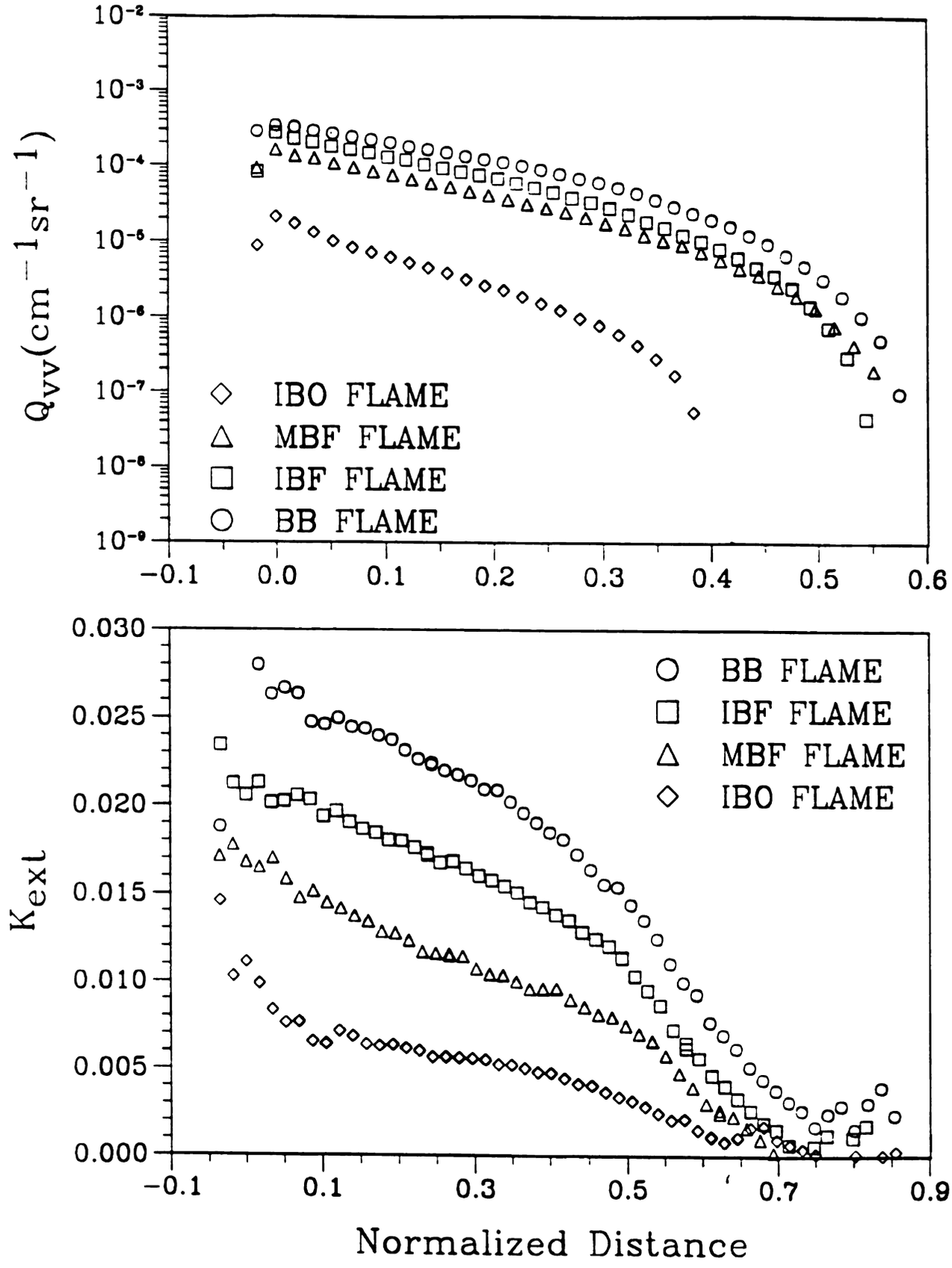

Figure 4-38 Extinction and scattering coefficient between stagnation plane and flame location, for 900 K flame
a) Scattering coefficient, Q_{vv} in cm^{-1} sr^{-1}
b) Extinction coefficient, K_{ext} in cm^{-1}

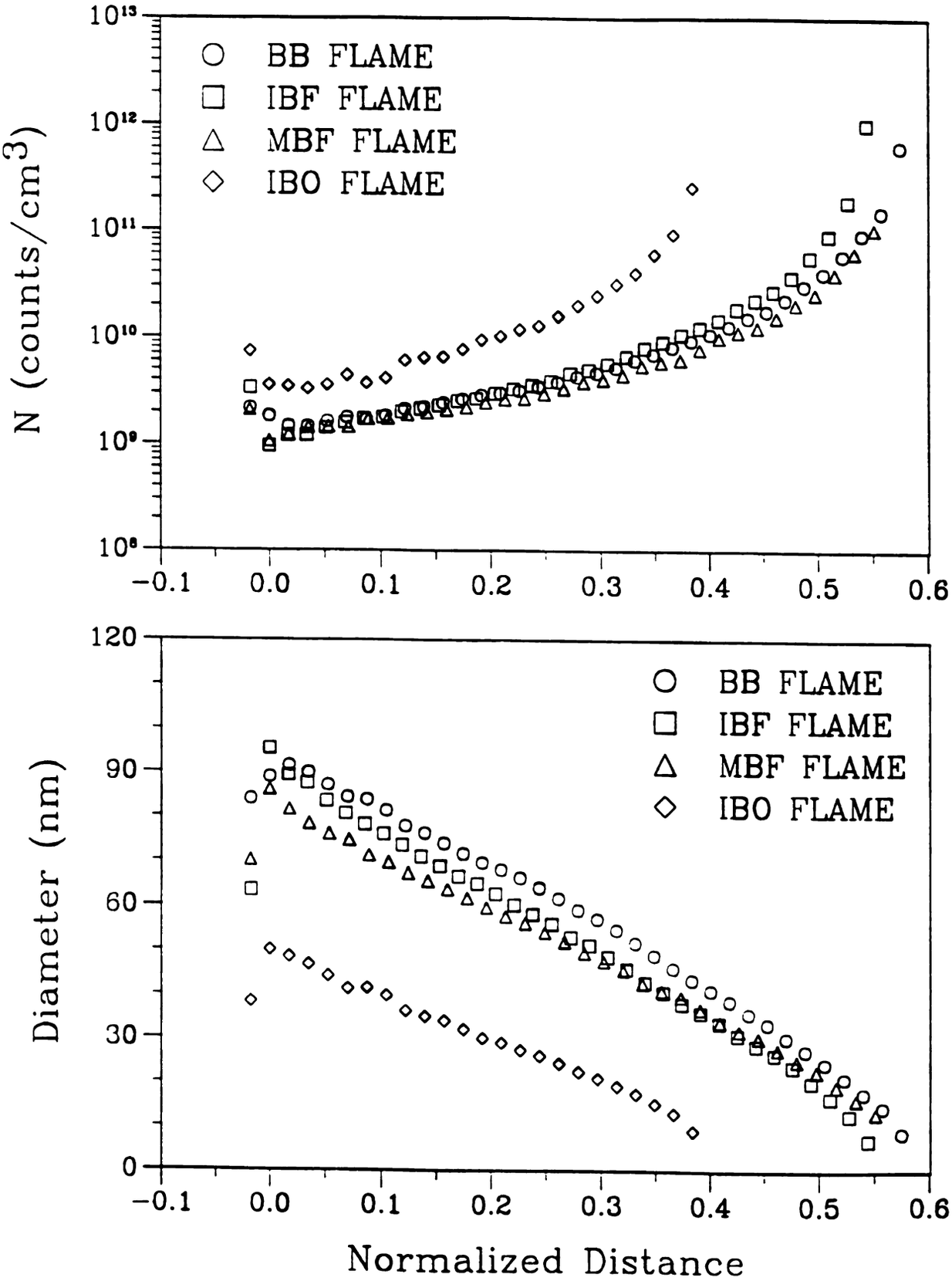

Figure 4-39 Soot particle number density and particle size for 900 K flame
a) Soot particle number density in counts/cm^3
b) Soot particle diameter in nm

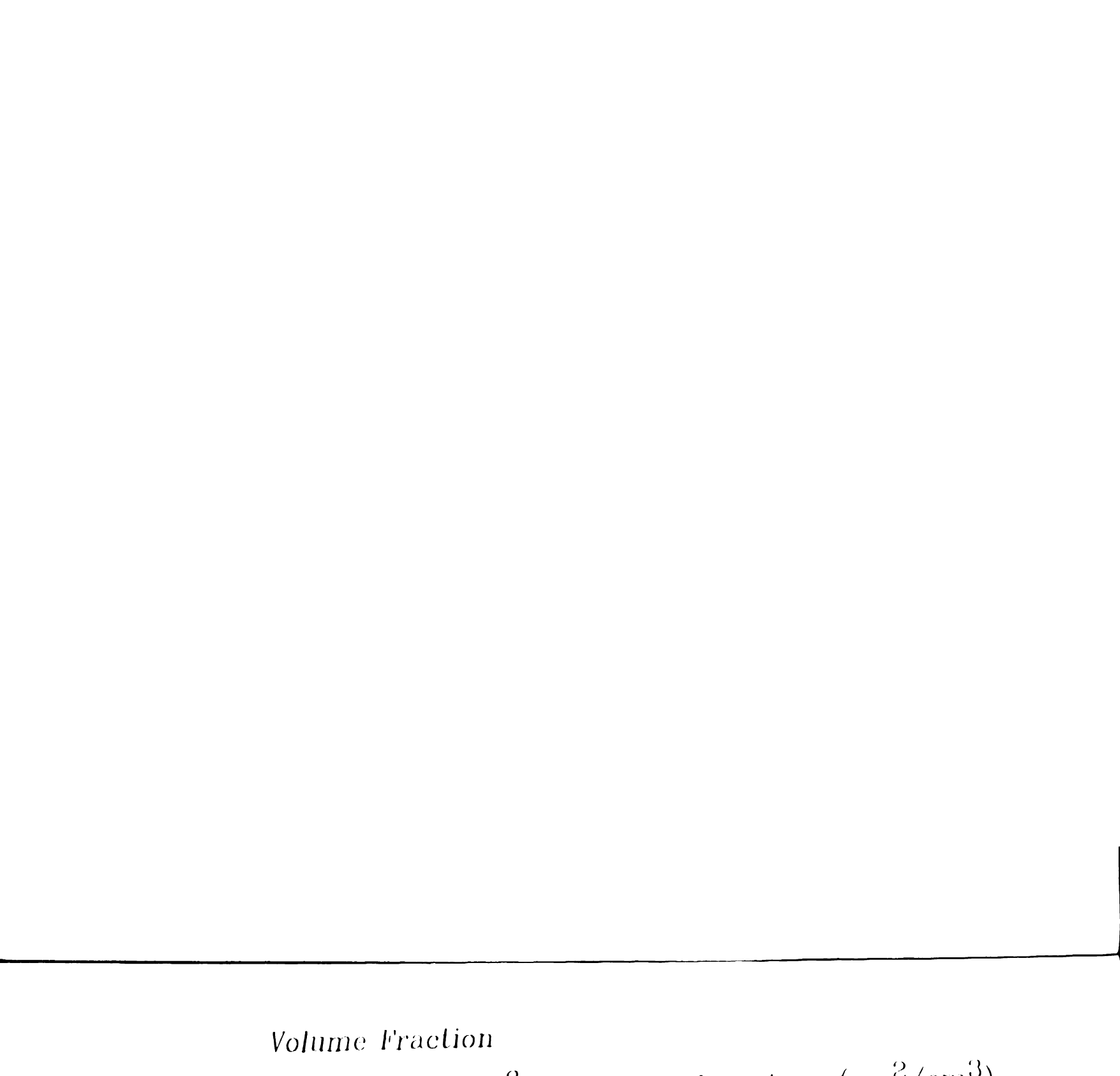
Volume Fraction

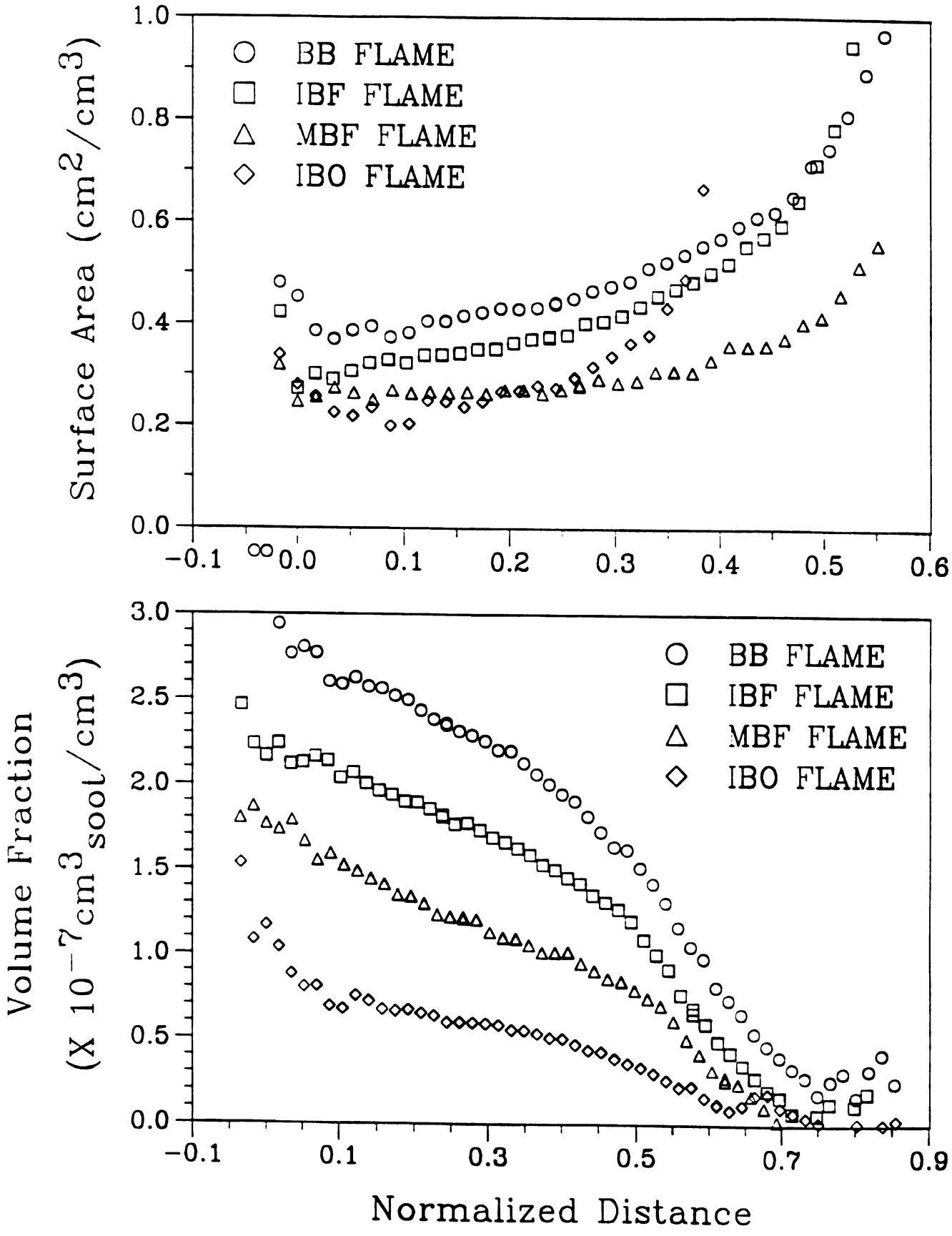

Figure 4-40 Soot particle total surface area and volume fraction for 900 K flame
a) Soot particle total surface area in cm^2_{soot}/cm^3_{space}
b) Soot particle volume fraction in cm^3_{soot}/cm^3_{space}

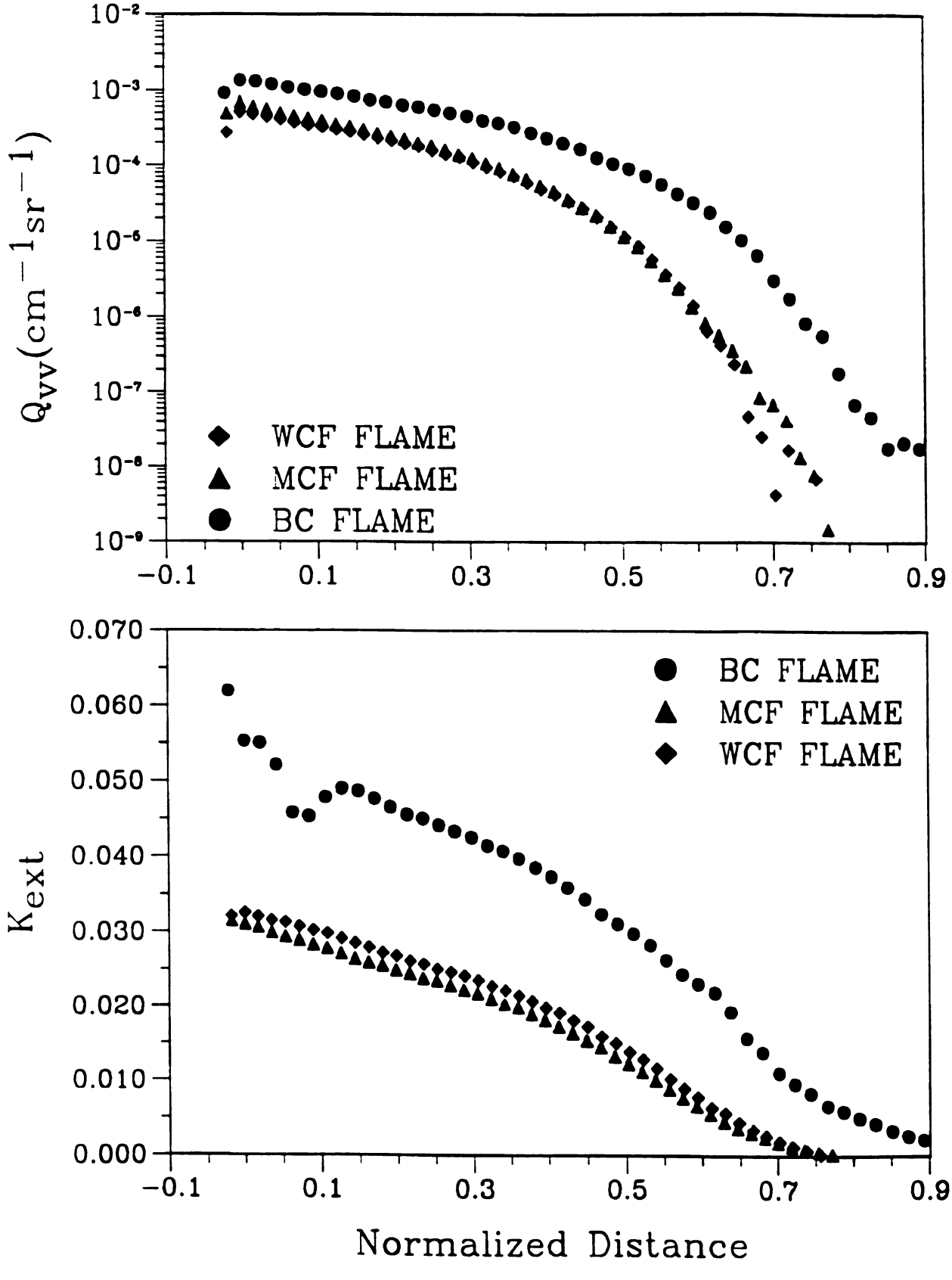

Figure 4-41 Extinction and scattering coefficient between stagnation plane and flame location, for 1200 K flame
a) Scattering coefficient, Q_{vv} in cm^{-1} sr^{-1}
b) Extinction coefficient, K_{ext} in cm^{-1}

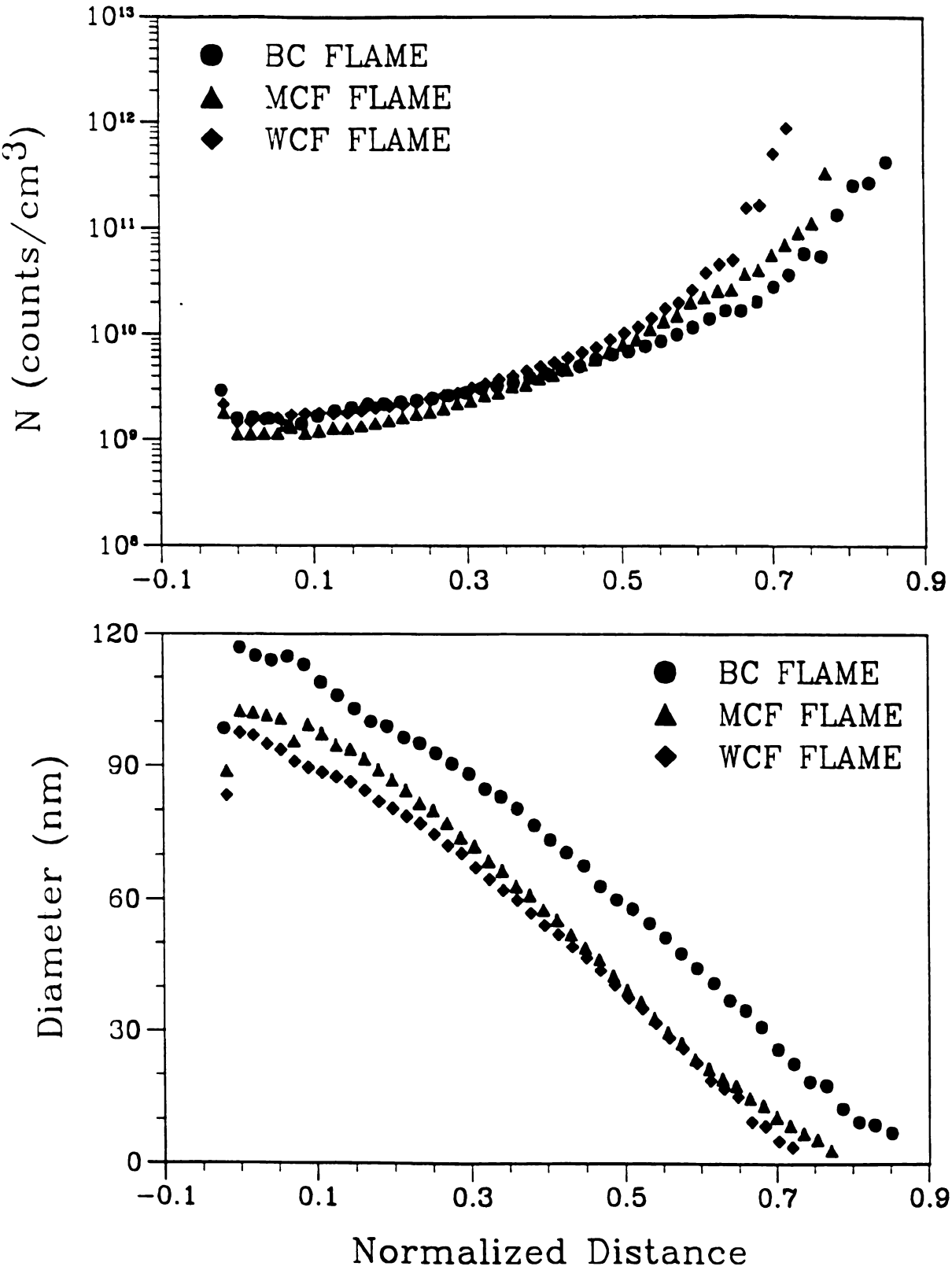

Figure 4-42 Soot particle number density and particle size for 1200 K flame
a) Soot particle number density in counts/cm^3
b) Soot particle diameter in nm

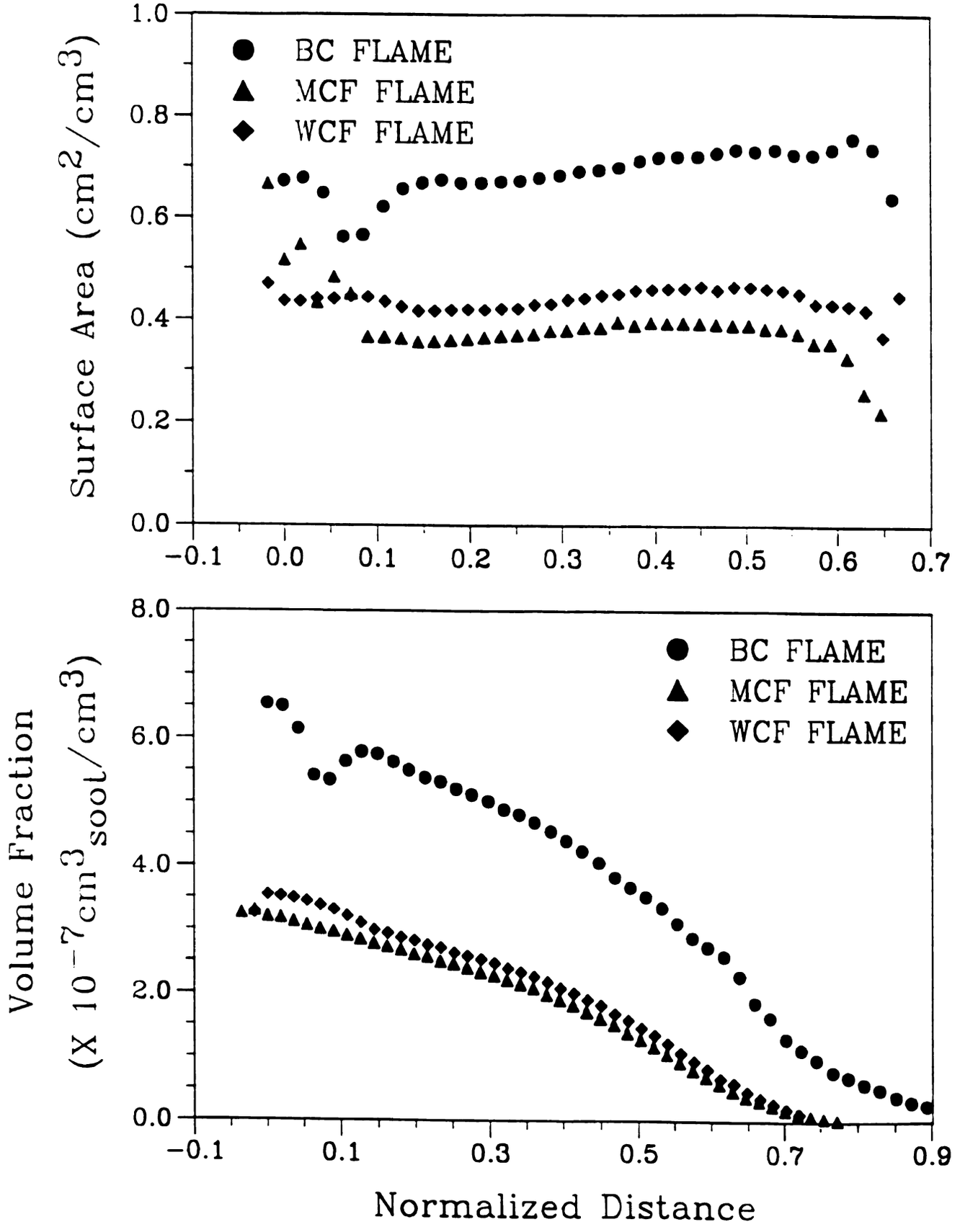

Figure 4-43 Soot particle total surface area and volume fraction for 1200 K flame
a) Soot particle total surface area in cm^2_{soot}/cm^3_{space}
b) Soot particle volume fraction in cm^3_{soot}/cm^3_{space}

K flames. Surface areas are between 0.7 and 0.4.

In any pre-heat condition, adding CO_2 in fuel stream reduced soot particles volume fraction and particle sizes. Comparison of the IBF flame (adding 12 %) to the MBF flame (adding 21 %) showed that adding more CO_2 in fuel stream reduced more soot particle volume fraction and particle size in diffusion flame. This showed that adding CO_2 in fuel stream reduced the surface growth rate. This can be expected from the reduction of PAH concentration in the soot particle path.

In the experiment of IBO-flame, it was also shown that adding CO_2 in oxidizer stream reduced soot particles even more in the diffusion flame. Adding CO_2 in oxidizer stream also increased the soot particle number density at the stagnation plane. Some coagulated particles can be oxidized from the surface. Those oxidized ones may loose their linkages and then separate into two or more small particles. This increases the soot particle number density and reduces the particle size much more than the particles in the MBF or IBF flames.

The experimental results showed that H_2O is more effective species than the CO_2 to reduce soot volume fraction in the diffusion flame. Comparisons of WAF to MA and of WCF to MCF showed that the reductions of soot volume fractions were almost identical to each other. It might also show the other optical and physical soot particles properties are very close to each other. From this observation one can say that adding 3.6 % of H_2O in fuel stream can reduce the soot particle volume fraction as much as the adding 21 % of CO_2 in the fuel stream can do. From the comparison of WAF and WAO, adding into oxidizer stream is much effective than adding into the fuel stream just like CO_2 case.

From the observation of results of the present study, soot reduction may not occur at last stage of the sooting mechanism in counterflow diffusion flame. When adding the CO_2 or H_2O into the fuel or the oxidizer stream, soot loading was reduced in whole range of observation. This showed that the reduction process is not independent

process from the soot formation, and growth process. So, the soot reduction process occurs in any stage of sooting process in diffusion flames.

This section can be concluded with the following summaries.

(i) Pre-heating temperature is very effective to increase the soot formation. Increasing pre-heat temperature produced more soot volume fraction and bigger particles.

(ii) Adding CO_2 or H_2O in fuel stream reduced the PAH concentration, the soot volume fraction and soot particle size. This showed that adding these species reduced the soot surface growth rate.

(iii) H_2O was more effective species to oxidize soot and related species, and hence soot particles volume fraction and their sizes.

(iv) Adding CO_2 or H_2O into the oxidizer stream was more effective than adding them into fuel stream. This can be explained. When the added species across the high temperature zone (~ 2000 K) more radicals such as OH or CO produces in high temperature zone and diffuses into the zone to oxidize (or react with) the soot and related species.

(v) soot particle size increased linearly along the nondimensional coordinate. The increasing rate was almost constant for all conditions.

(vi) Soot reduction occurred in any stage of sooting process in diffusion flame.

4.5 Error analysis

4.5.1 Statistical Formulation for Experimental Error Analysis

Consider a quantity, q such as $q = f(x_1, x_2, x_3, ..., x_n)$. Here $x_1, x_2, x_3, ..., x_n$ are independent variables. Then the fractional uncertainty is given by:

$$\left[\frac{\Delta q}{q}\right]^2 = \left[\frac{\delta f}{\delta x_1}\frac{\Delta x_1}{q}\right]^2 + \left[\frac{\delta f}{\delta x_2}\frac{\Delta x_2}{q}\right]^2 + ... + \left[\frac{\delta f}{\delta x_n}\frac{\Delta x_n}{q}\right]^2 \qquad (4\text{-}26)$$

Where, Δq, Δx_1, Δx_2, and Δx_n, are the differences between the measured values and true values (possible errors) in quantity q, variable x_1, variable x_2, and variable x_n, respectively.

For i^{th} variable, the difference between the measured value and the true value (possible error), which is called confidence interval, can be calculated from the average, $\bar{x}_i$, standard deviation, σ_i, and total number of data points, n_i, with normal distribution. The confidence interval, Δx_i is defined as:

$$\Delta x_i = c\,\frac{\sigma_i}{\sqrt{n_i - 1}} \qquad (4\text{-}27)$$

Where, c is a constant that stands for percentage of data points in the confidence interval between $\bar{x}_i - \Delta x_i$ and $\bar{x}_i + \Delta x_i$. For the present study, c = 2 was used for the optical experimental data. The corresponding percentage in normal distribution is above 95 %.

4.5.2 Error Analysis in Flame Structure Measurement

Flame location and stagnation plane location were measured for normalize the axial distance based on the length between these two locations. The methods how to measure the locations are described in section 4.1.4 in detail. So, in this section, errors involved in the location measurement are analyzed.

Each location was measured for 10 times and based on these measured data errors were analyzed. Table 4-4 shows the average locations and their confidence interval for 95 % of normal distribution. In Table 4-4, Max. Temp. is for maximum temperature location. St. Plane(a) stands for the stagnation plane measured by optical method and St. Plane(b) stands for the stagnation plane measured by flow visualization.

Table 4-4: Error analysis for the location measurement.

1. 300 K Flames — unit : mm

Flames	Max. Temp	Dxi	St. Plane (a)	Dxi	St. Palne (b)	Dxi
BA	15.00	0.062	8.74	0.040	9.01	0.064
IA	15.00	0.087	8.76	0.051	8.99	0.065
MA	15.00	0.088	8.61	0.037	8.80	0.063
WAO	15.09	0.096	8.67	0.054	8.87	0.069

2. 900 K Flames

Flames	Max. Temp	Dxi	St. Plane (a)	Dxi	St. Palne (b)	Dxi
BB	15.62	0.060	8.33	0.056	8.51	0.073
MBF	15.35	0.066	8.20	0.047	8.45	0.073
IBO	15.48	0.080	8.20	0.074	8.52	0.086
MBO	15.53	0.083	8.74	0.064	8.74	0.091

3. 1200 K Flames

Flames	Max. Temp	Dxi	St. Plane (a)	Dxi	St. Palne (b)	Dxi
MCF	15.50	0.074	8.43	0.055	8.61	0.067
WCF	15.60	0.082	8.55	0.059	8.74	0.088

1) Dxi : confidence interval for 95 % of normal distribution.
2) Max. Temp. : maximum temperature location.
3) St. Plane (a) : stagnation plane location measured by optical
4) St. Plane (b) : stagnation plane location measured by flow visualization.

All the confidence intervals (denoted by Dxi in Table 4-4) are within the range of $\pm$ 0.1 *mm* from the average value. These locations were measured traversing mechanisms of which smallest scale is 0.0254 *mm*. The confidential intervals are within 4 small scales of the used traverse mechanisms. But when locating the measuring probe

at the reference position, the locations were decided by eyes. That might be the reason of the large confidential interval compare to the traverse scale.

4.5.3 Error Analysis in Optical Measurement

Errors in optical measurements were analyzed based on the fractional uncertainty with extinction and scattering coefficients. From Equation (4-14) and fractional uncertainty (Equation (4-26)), the error in K_{ext} may be written as:

$$\frac{\Delta K_{ext}}{K_{ext}} = \left[\left(\frac{\Delta I}{I \ln \frac{I}{I_r}} \right)^2 + \left(\frac{\Delta I_r}{I_r \ln \frac{I}{I_r}} \right)^2 + \left(\frac{\Delta L}{L} \right)^2 \right]^{\frac{1}{2}} \tag{4-28}$$

Where, I is the extinction intensity measured by photodiode after pass the sooty flame, I_r is also the extinction intensity measured by the photodiode after pass the reference flame, and L is beam pathlength in sooty flame.

For scattering coefficient, the uncertainty can also be derived from Equation (4-22) and (4-25) as:

$$\frac{\Delta Q_{vv,soot}}{Q_{vv,soot}} = \left[\left(\frac{\Delta I_{s,soot}}{I_{s,soot}} \right)^2 + \left(\frac{\Delta I_{s,N_2}}{I_{s,N_2}} \right)^2 + \left(\frac{\Delta I}{I} \right)^2 + \left(\frac{\Delta I_r}{I_r} \right)^2 \right]^{\frac{1}{2}} \tag{4-29}$$

Where, $I_{s,soot}$, I_{s,N_2} are the light intensities scattered by soot particles and N_2 molecules, respectively. I and I_r are the same intensities in Equation (4-28).

For the present study, the ratio between errors in detected intensities can be expressed by the recorded voltage by lock-in amplifiers. Figures (4-44), (4-45) and (4-46) show the graphs of the typical raw data from the lock-in amplifier for light intensities scattered by N_2 molecules and soot particles, and extinction intensity for sooty and reference flames, respectively. The graphs show only one fifth of total number of data points for plotting. But for the calculation purpose, all data points were used.

These raw data were plotted against the time to take the data. The data for the flames were taken for 20 seconds at one location. The X, Y, Z traverse traveled by 0.127 mm in every 20 second. So, this x-axis can show the location of the measurement. For the nitrogen calibration, it took 50 second for each incident beam intensity. Three laser power, 100 *mw*, 200 *mw*, and 300 *mw*, were used to calibrate scattered intensity from N_2 molecules. For optical measurements for the flame, 100 *mw* incident beam power was used.

From these data, the average values were calculated for each location. The confidential intervals, $\Delta I_{s,soot}$, $\Delta I_{s,N_2}$, ΔI, and ΔI_r were obtained based on the statistics and Equation (4-27). Figures (4-47), (4-48) and (4-49) show the average value at the each measured location and its confidential interval.

Using the ratio confidential intervals and local values, and Equations (4-28) and (4-29), the errors in K_{ext} and $Q_{vv,soot}$ were calculated. The results are shown in Figures (4-50) and (4-51). The maximum error was always occurred just below the stagnation plane.

Using Equation (4-28), the errors in volume fraction can be obtained. From the relation between soot volume fraction and extinction coefficient, the errors in soot volume fraction can be obtained from:

$$\frac{\Delta f_v}{f_v} = \frac{\Delta K_{ext}}{K_{ext}} \tag{4-30}$$

To calculate the errors in soot particle diameter and number density, the errors in ratio of soot particle scattering and extinction coefficients are needed. Let us define the ratio of soot particle scattering and extinction ratio as:

$$F = \frac{Q_{vv,soot}}{K_{ext}} \tag{4-31}$$

Then, the error in this quantity can be obtained as:

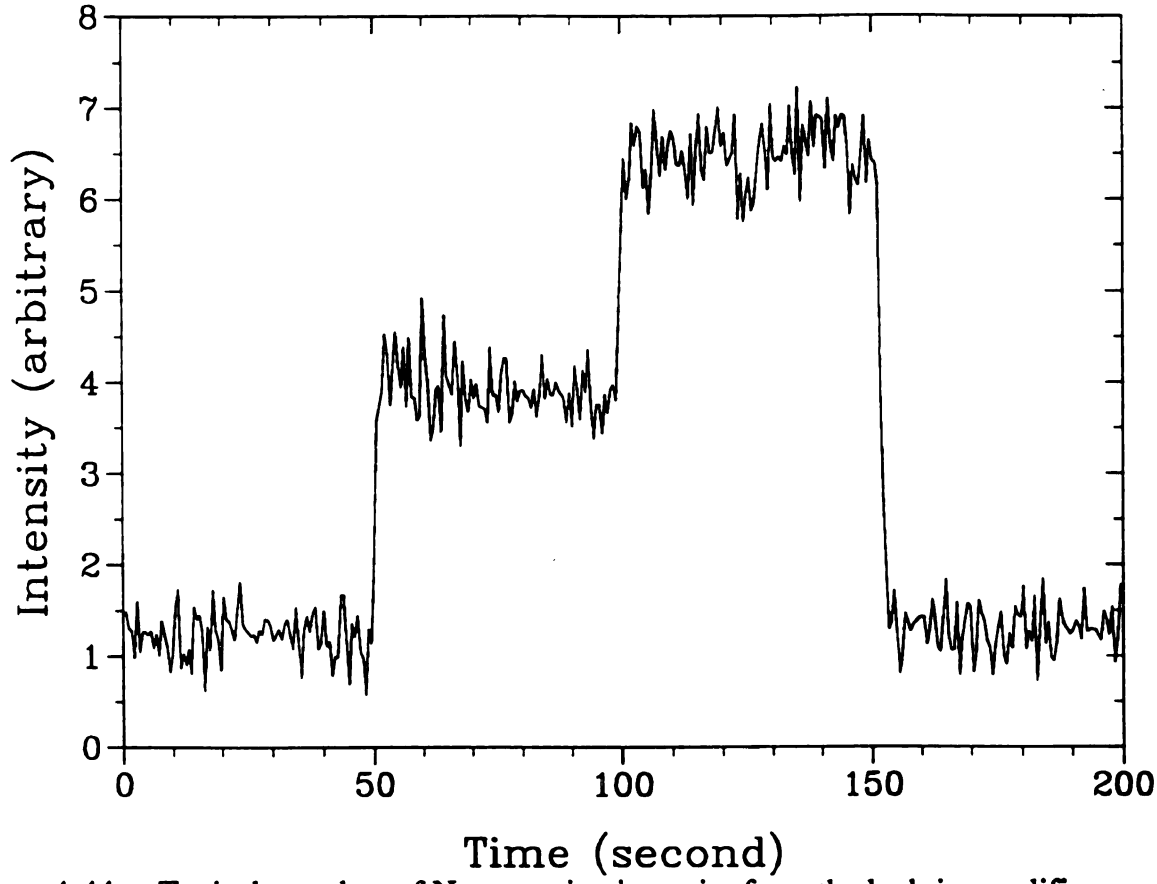

Figure 4-44 Typical raw data of N_2 scattering intensity from the lock-in amplifier. Used laser power were 100 mw, 200 mw, and 300 mw. For plotting the data, number of data point was reduced by 1/5.

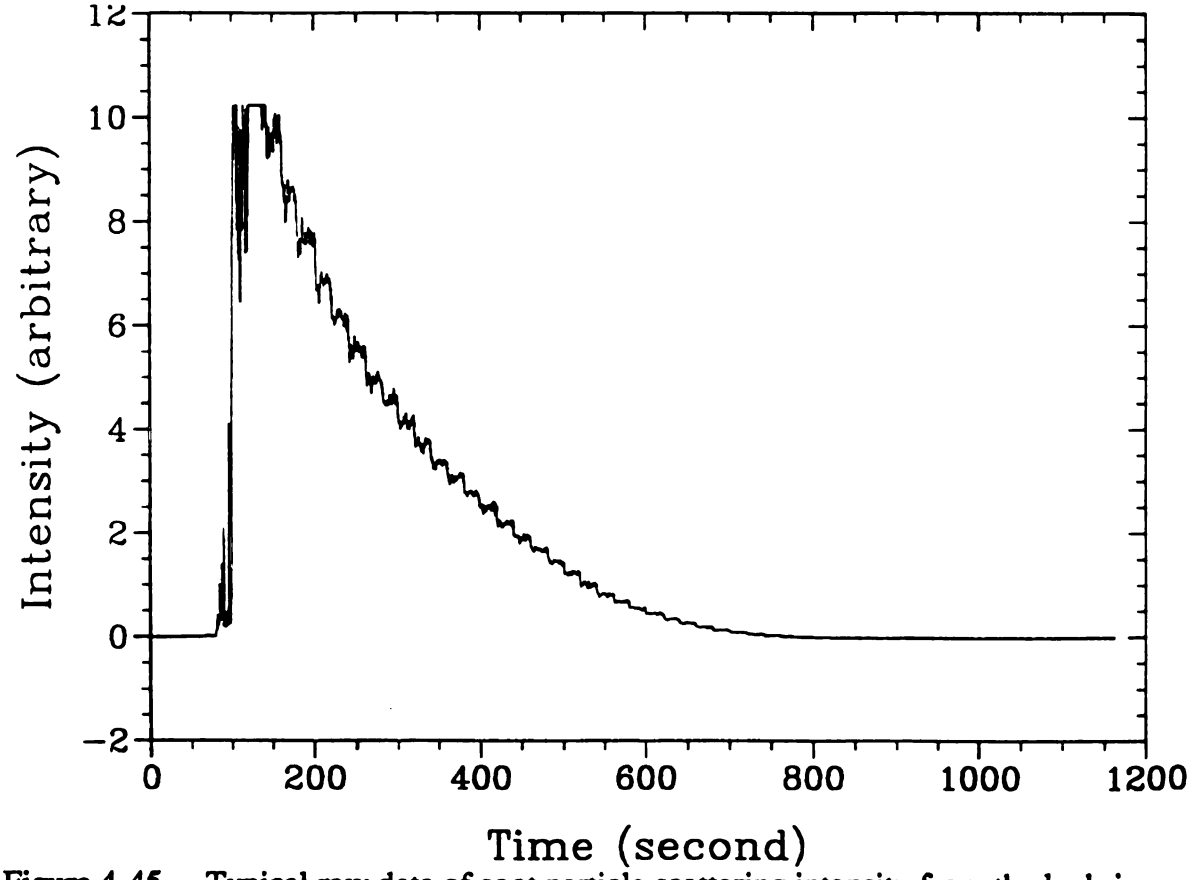

Figure 4-45 Typical raw data of soot particle scattering intensity from the lock-in amplifier. For plotting the data, number of data point was reduced by 1/5.

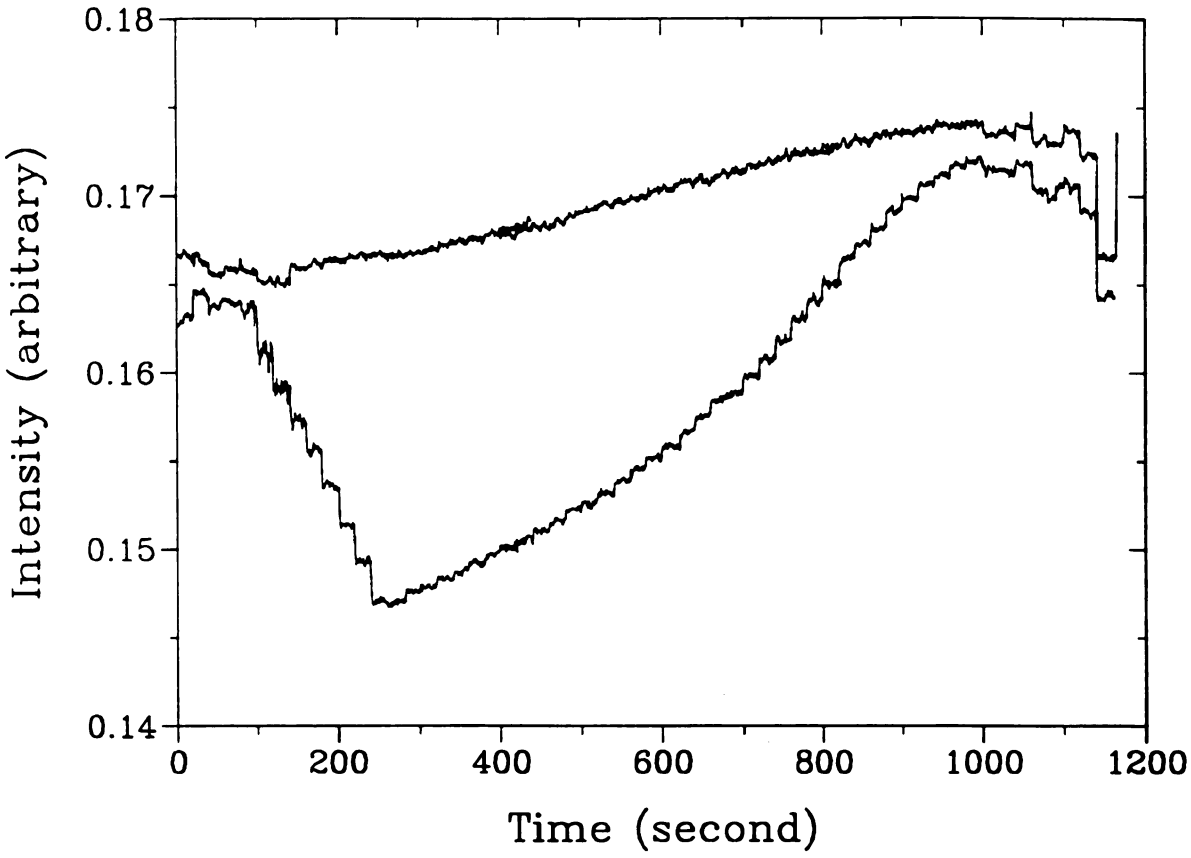

Figure 4-46 Typical raw data of extinction intensities of sooty flam and reference flame from the lock-in amplifier. For plotting the data, number of data point was reduced.

$$\frac{\Delta F}{F} = \left[\left[\frac{\Delta Q_{vv,soot}}{Q_{vv,soot}} \right]^2 + \left[\frac{\Delta K_{ext}}{K_{ext}} \right]^2 \right]^{\frac{1}{2}} \tag{4-32}$$

Then, the errors in the soot particle diameter and number density can be expressed using Equation (4-32) by:

$$\frac{\Delta D}{D} = \frac{1}{3} \frac{\Delta F}{F} \tag{4-33}$$

and

$$\frac{\Delta N}{N} = \left[\left[\frac{\Delta K_{ext}}{K_{ext}} \right]^2 + \left[\frac{\Delta F}{F} \right]^2 \right]^{\frac{1}{2}} \tag{4-34}$$

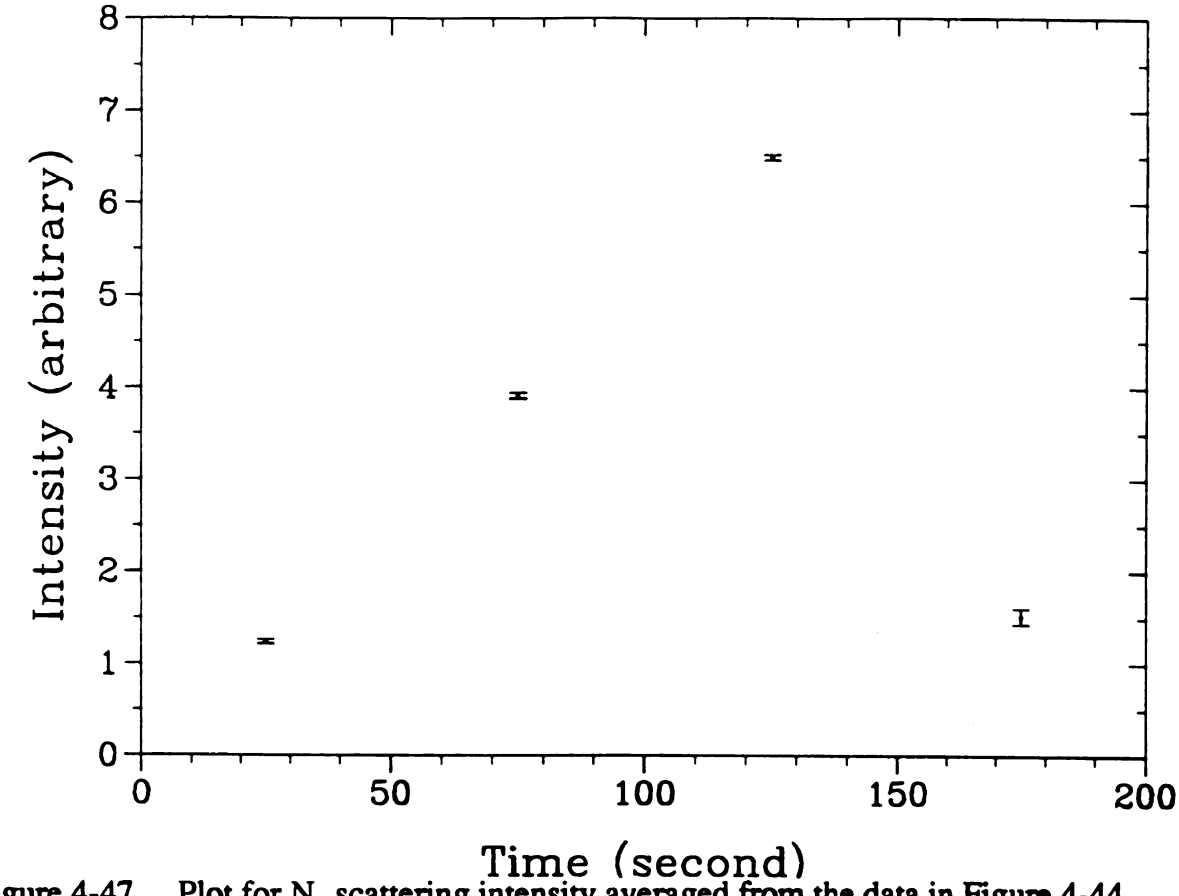

Figure 4-47 Plot for N_2 scattering intensity averaged from the data in Figure 4-44 versus normalized coordinated converted from the time in Figure 4-44. Error bar stands for the confidence interval from the average values.

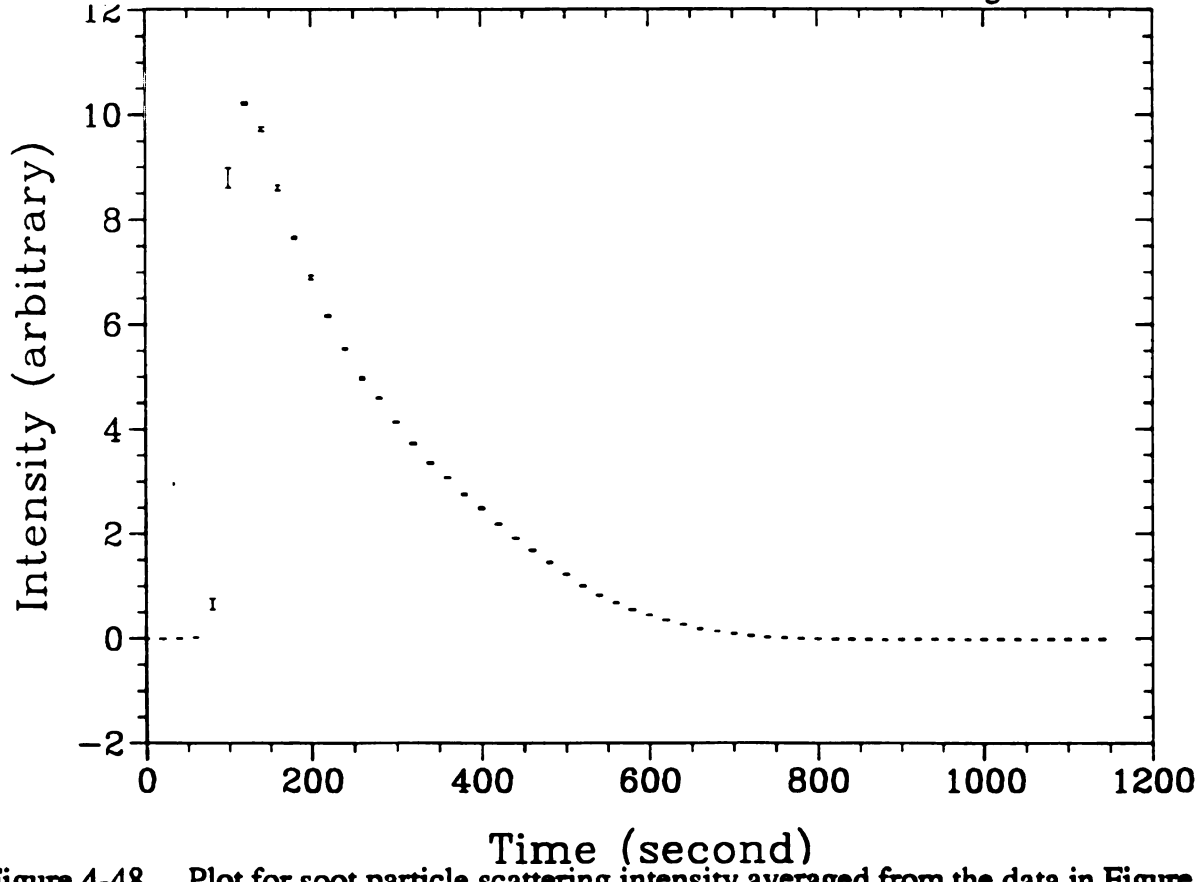

Figure 4-48 Plot for soot particle scattering intensity averaged from the data in Figure 4-45 versus normalized coordinated converted from the time in Figure 4-45. Error bar stands for the confidence interval from the average values.

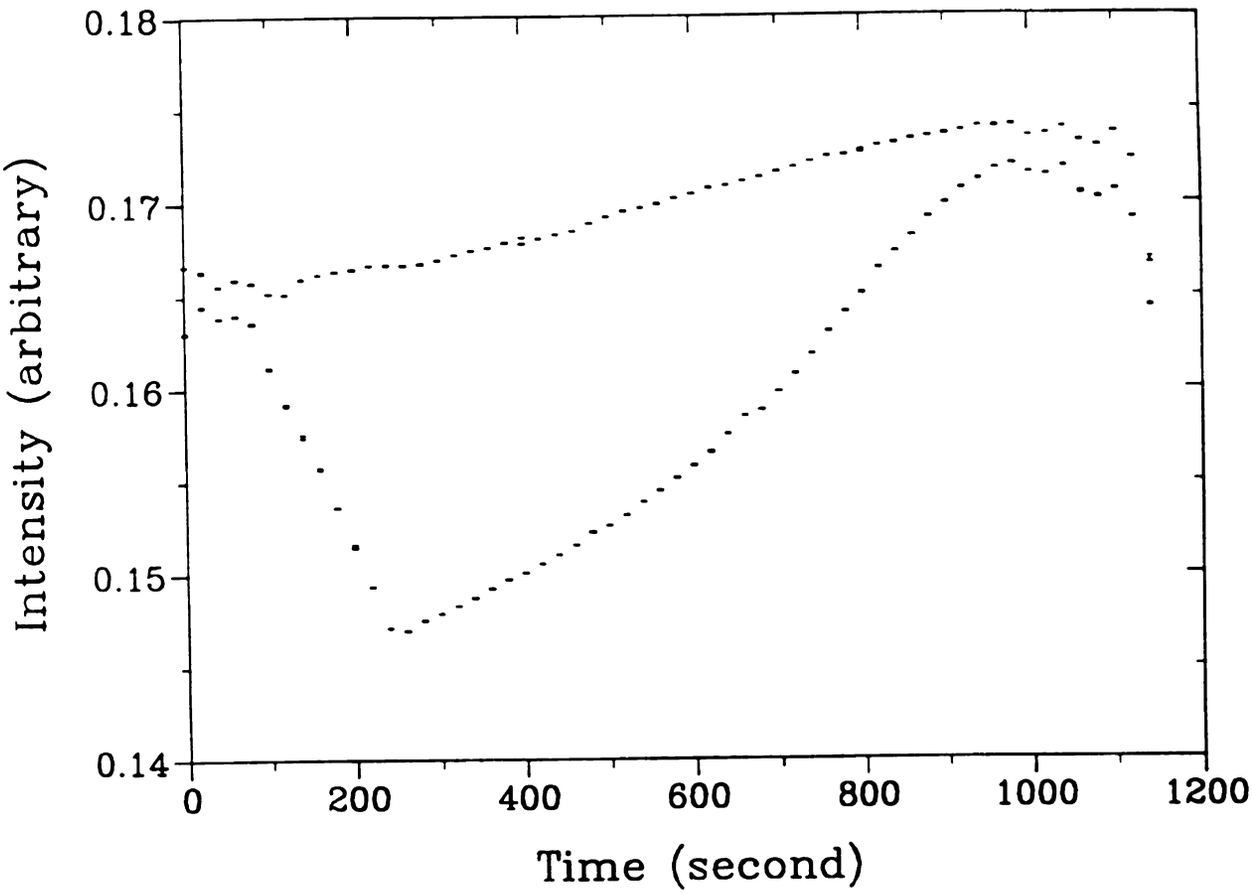

Figure 4-49 Plot for extinction intensities of sooty flame and reference flame. These extinction intensities were averaged from the data in Figure 4-46 versus normalized coordinated converted from the time in Figure 4-46. Error bar stands for the confidence interval from the average values.

Errors in soot particle size, volume fraction, and number density were calculated and are shown in Figures 4-52, 4-53, and 4-54, respectively. Just below the stagnation plane, the maximum error always occur. For the present study, below the stagnation plane was not main area to measure soot particles. In any calculation, the error is less than 2.0 % with above 95 % confidence in normal distribution. Therefore, the optical measurement for the present study has the accuracy with less than 2.0 % error.

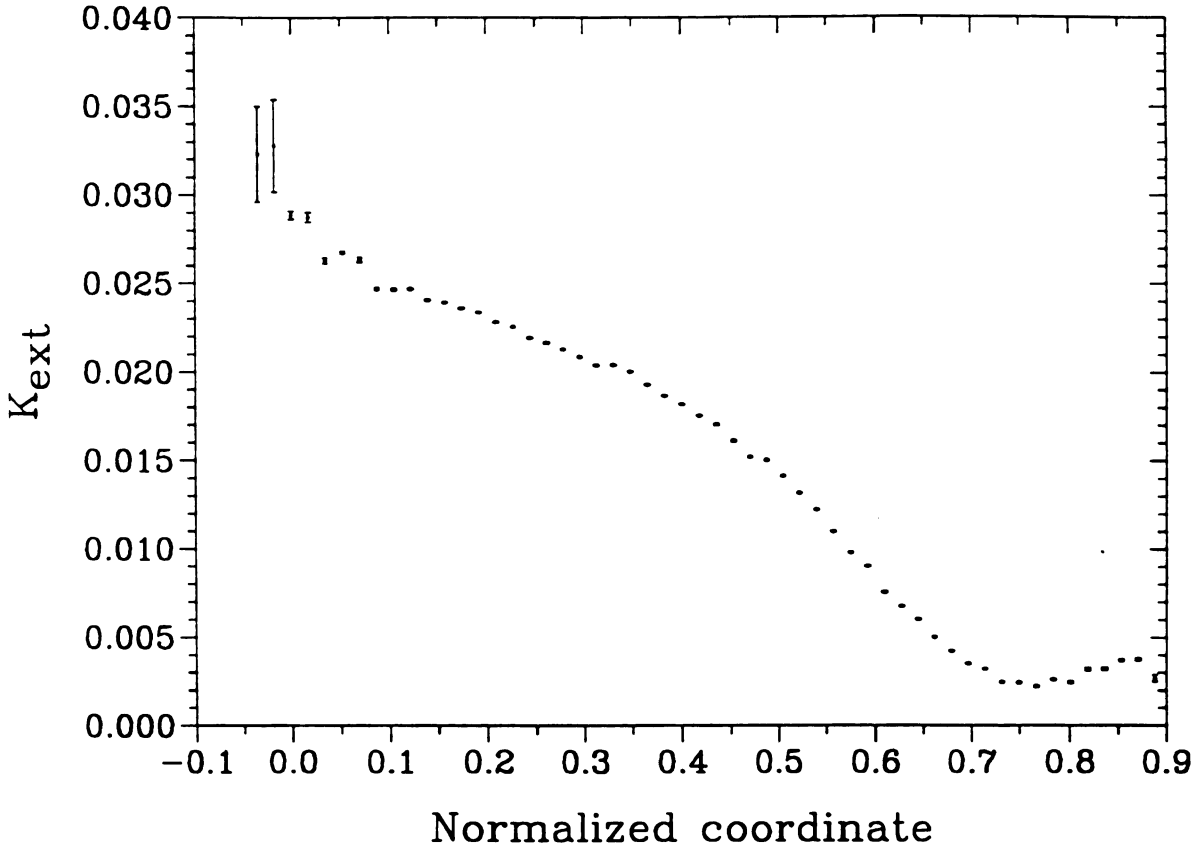

Figure 4-50 Calculated errors in extinction coefficient (K_{ext}) in typical flame.

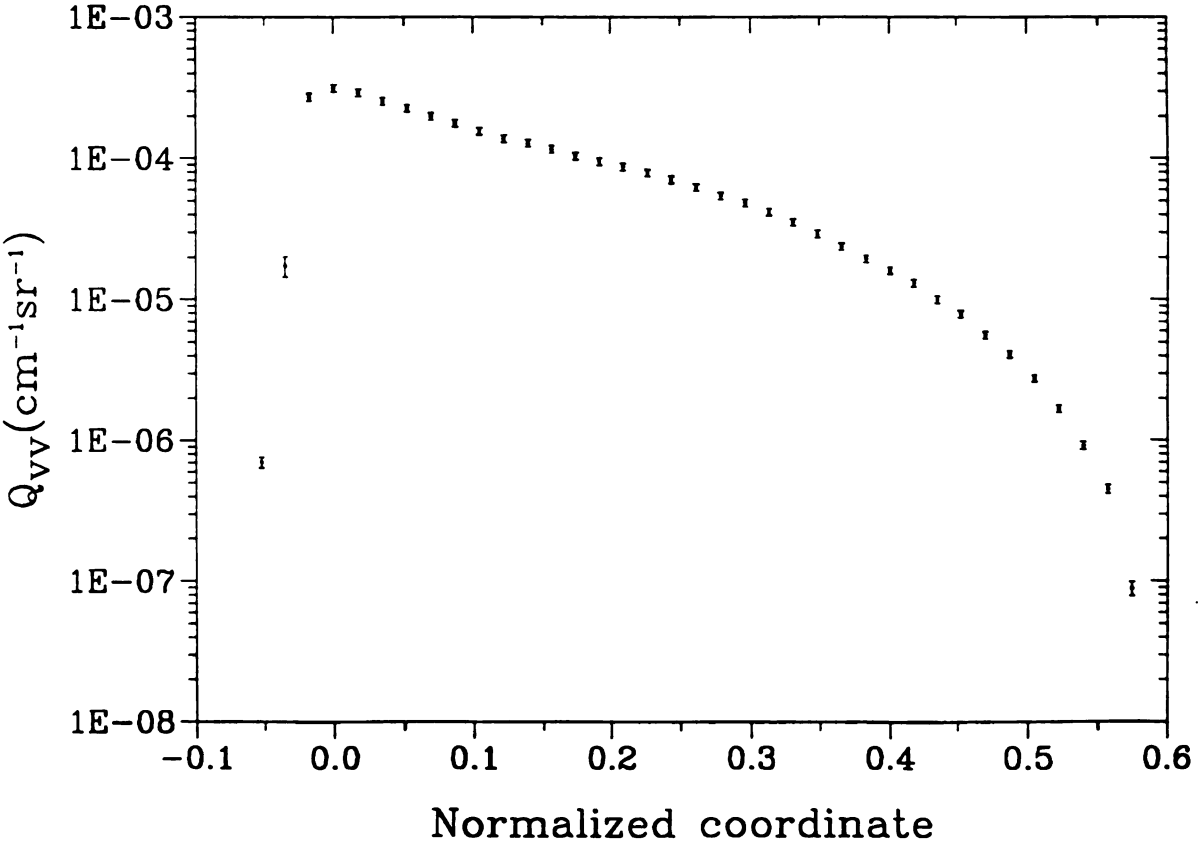

Figure 4-51 Calculated errors in scattering coefficient of soot particles ($Q_{vv,soot}$) in typical flame.

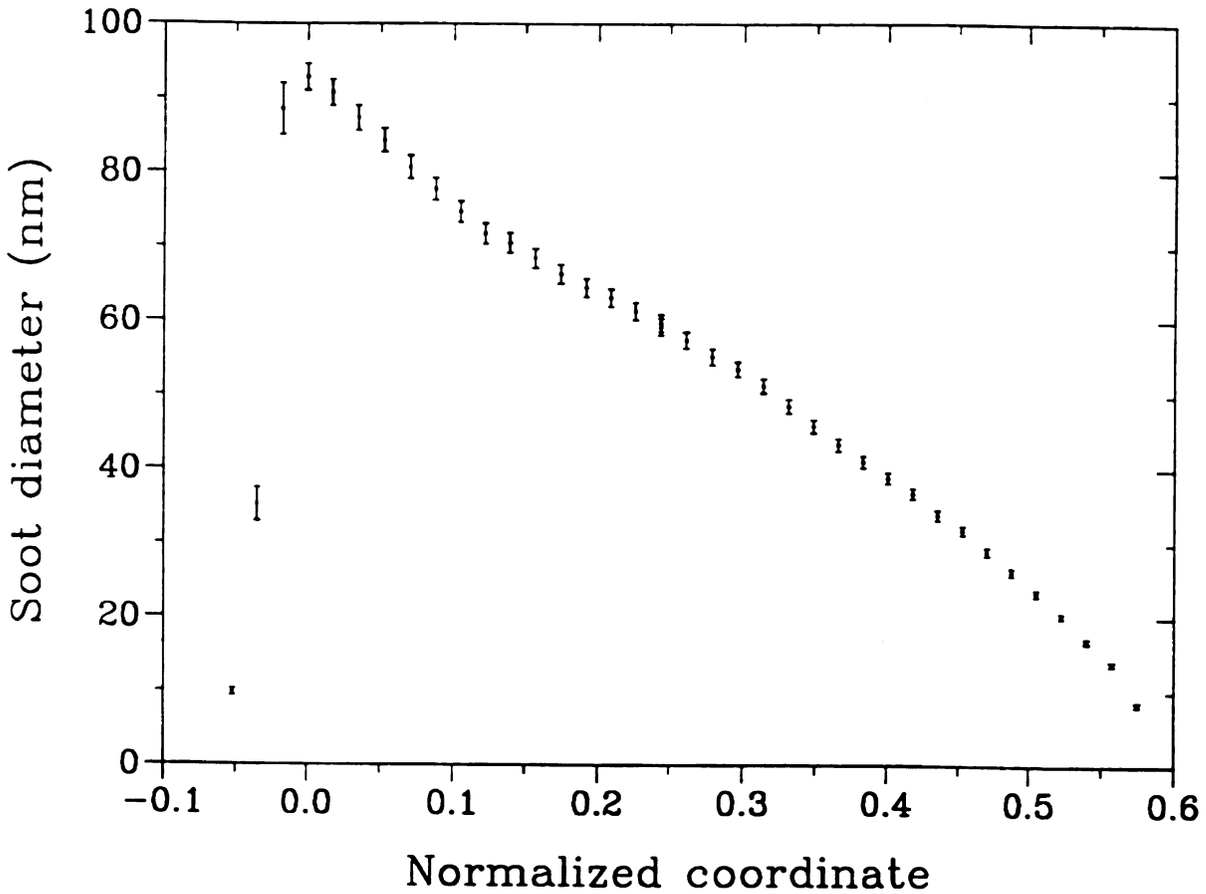

Figure 4-52 Calculated errors in soot particle size (Diameter in nm) in typical flame.

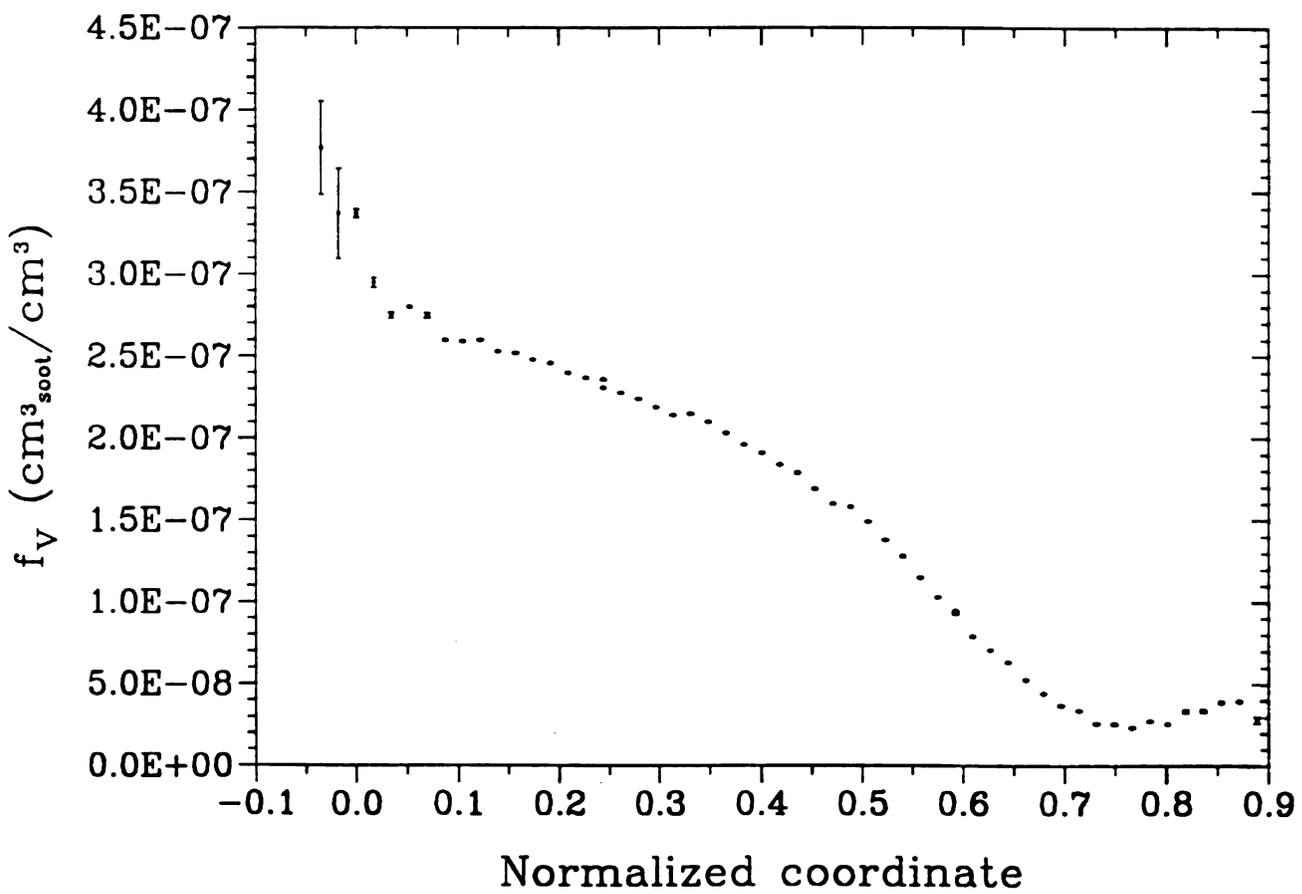

Figure 4-53 Calculated errors in soot volume fraction in typical flame.

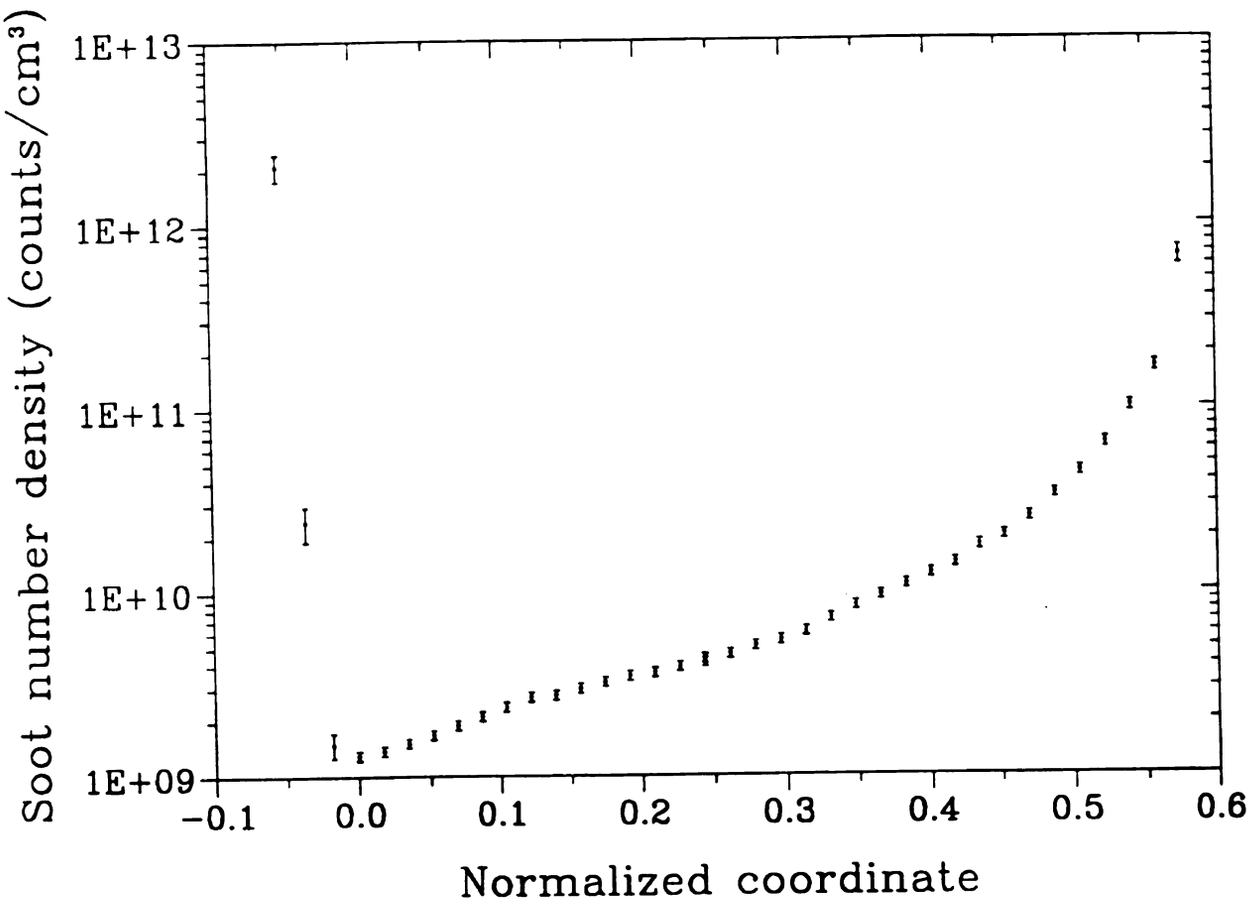

Figure 4-54 Calculated errors in soot particle number density in typical flame.

4.5.4 Experimental Repeatability

Another important aspect of error analysis is repeatability of experiments. Two sets of data were taken for the same flame in different days. Figures (4-55) and (4-56) show two sets of data for the same flames. Figure (4-55) shows the scattering and extinction intensities for IA flame. Figure (4-56) shows the same quantities for BB flame.

The scattering intensity profiles are almost identical while the extinction intensity profiles are very similar in shapes of profiles but different intensities. In extinction measurement, the angle of detector to the laser beam was very sensitive. The

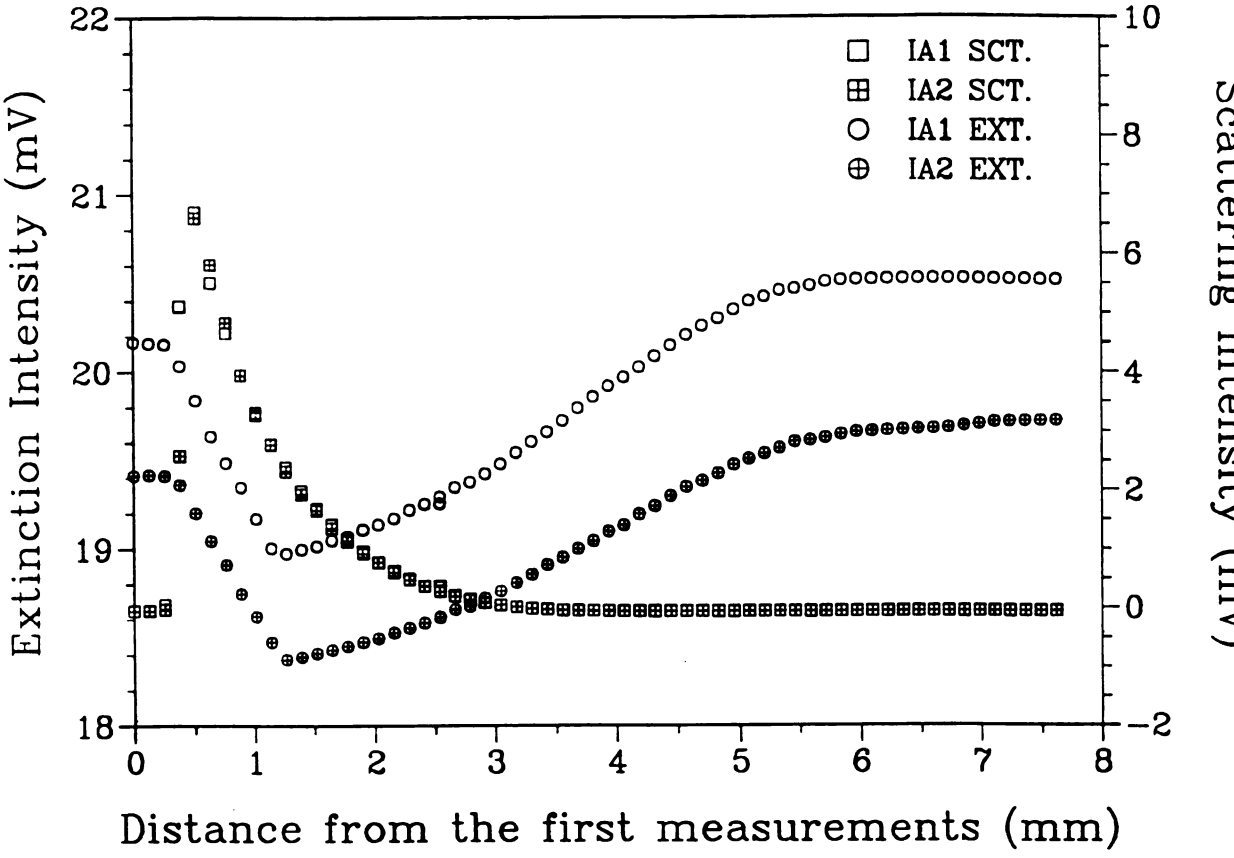

Figure 4-55 Scattering and extinction intensities of IA-flame measured in two different days.

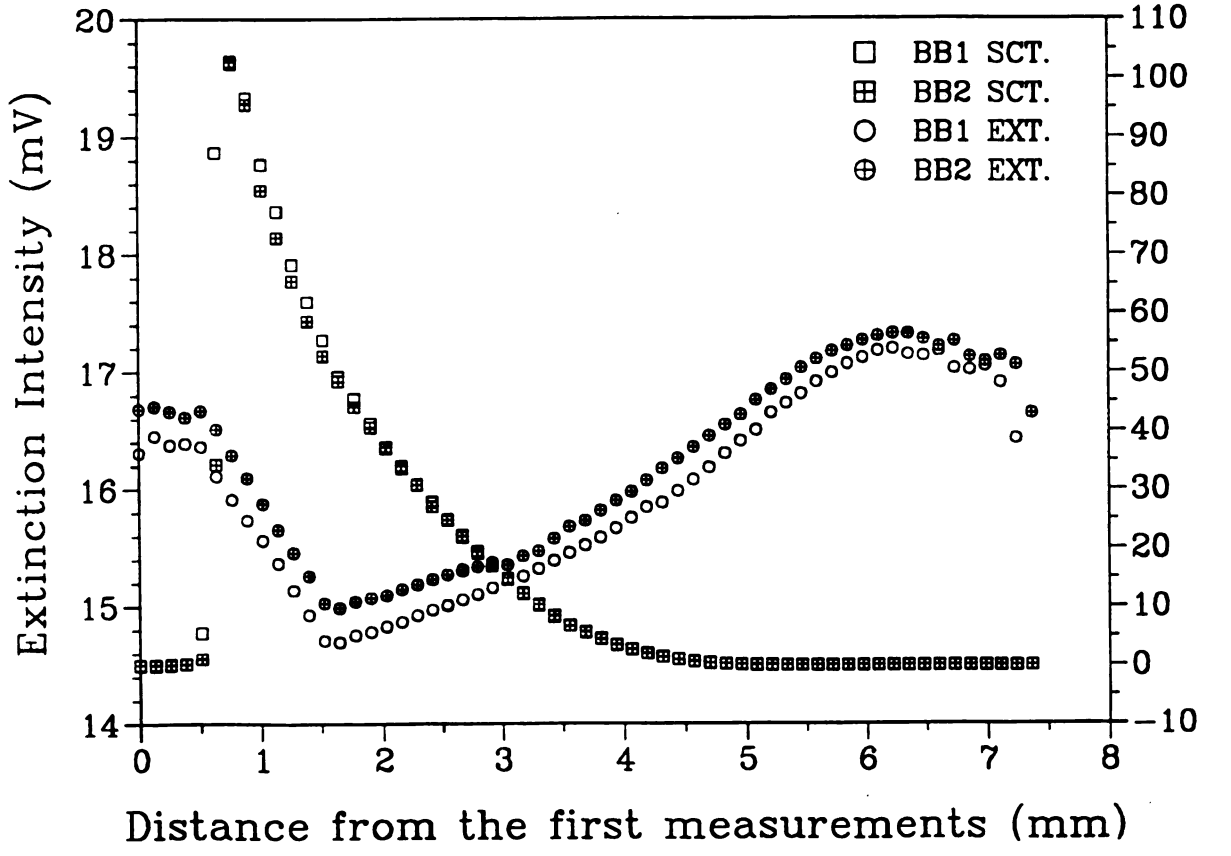

Figure 4-56 Scattering and extinction intensities of BB-flame measured in two different days.

difference of the extinction intensities in two measurements for the same flame may come from the angle of detector to the laser beam. Because before start optical measurement, the detector for the extinction measurement was adjusted to obtain best result for every measurement. But after setting, the detector was not adjusted while the experimental data were being taken.

This difference does not affect the calculation of particle properties. Because actual intensity attenuated by soot is difference between the extinction intensities of sooty flame and reference flame. In extinction intensity profile, as far as the shapes of the profiles are congruent, the intensities attenuated should be same each other.

Therefore, these two sets of comparisons show that the measurements with the experimental equipments and instrumentation are repeatable. They also show that the same flame conditions can be obtained correctly with the sonic orifices and rotameters.

AN EXPERIMENTAL STUDY OF SOOT FORMATION AND OXIDATION IN AXISYMMETRIC COUNTERFLOW DIFFUSION FLAMES

By

Keunchul Lee

A DISSERTATION

VOLUME II

Submitted to
Michigan State University
in partial fulfillment of the requirements
for the degree of

DOCTOR OF PHILOSOPHY

Department of Mechanical Engineering

1991

chapter 5

ANALYSIS OF RESULTS

5.1 Theoretical Formulation

Theoretical formulation for the present study is following the model which was developed by Dr. Arvind Atreya. As shown in Figure 5-1, an axisymmetric counterflow diffusion flame is established between two impinging streams. Let r and z denote the independent spatial coordinates in the radial and the axial directions, respectively. The origin is the stagnation point where $u = v = 0.0$. The fuel is supplied at $z = -\infty$, and the oxidizer is supplied at $z = \infty$. The flow is assumed to be laminar axisymmetric stagnation-point flow. The fundamental equations governing the conservation of mass, momentum, species and energy are then written in the following boundary-layer-flow forms (Smook, Seshadri, & Puri, 1988; Puri, Seshadri, Smook, & Keyes, 1987; Hahn & Wendt, 1981a,b):

$$\textit{Continuity}: \qquad \frac{d}{dz}\left[\rho v\right] + 2\varepsilon_0 \rho \psi = 0 \tag{5-1}$$

$$\textit{Momentum}: \qquad \frac{d}{dz}\left[\mu \frac{d\psi}{dz}\right] - \rho v \frac{d\psi}{dz} + \varepsilon_0\left[\rho_\infty - \rho\psi^2\right] = 0 \tag{5-2}$$

$$\textit{Species}: \qquad R_i = \frac{1}{W_i}\left\{\frac{d}{dz}\left[\rho y_i\left[v + v_{di}\right]\right] + 2\varepsilon_0 \psi y_i \rho\right\} \tag{5-3}$$

$$\textit{Energy}: \qquad Q = \rho \frac{dT}{dz} \sum_{i=1}^{n} C_{pi} y_i \left[v + v_{di}\right] - \frac{d}{dz}\left[\lambda \frac{dT}{dz}\right] \tag{5-4}$$

Where :

$$v_{di} = -\frac{1 - x_i}{\left[\sum_{j \neq i}^{n} \frac{x_j}{D_{ij}}\right]} \frac{1}{x_i} \frac{dx_i}{dz} \tag{5-5}$$

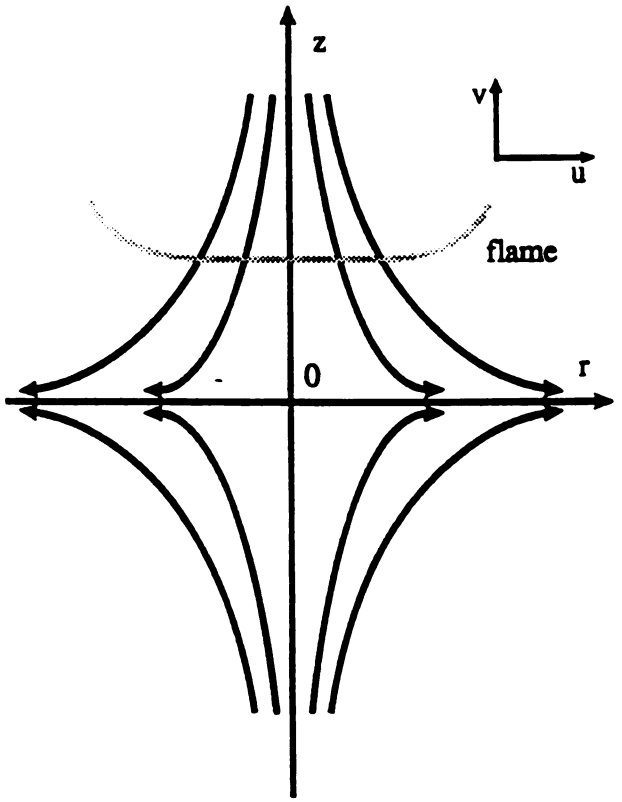

Figure 5-1 Schematic of axisymmetric countrflow diffusion flame, streamlines and its coordinate system

and perfect gas law

$$\rho = \frac{P\ W}{R\ T} \tag{5-6}$$

To complete the specification of the problem, boundary conditions must be imposed on both sides, at $z = -\infty$:

$$v = v_{-\infty} \tag{5-7}$$

$$\psi = \sqrt{\frac{\rho_{\infty}}{\rho_{-\infty}}} \tag{5-8}$$

$$y_i = y_{i-\infty} \tag{5-9}$$

$$T = T_{-\infty} \tag{5-10}$$

And at z=∞ :

$$v = v_{\infty} \tag{5-11}$$

$$\psi = 1 \tag{5-12}$$

$$y_i = y_{i\infty} \tag{5-13}$$

$$T = T_{\infty} \tag{5-14}$$

In these equations, T denotes the temperature; y_i and x_i, the mass and mole fraction; W_i, the molecular weight of the i^{th} species; v, the velocity; ε_0, the constant strain rate; ψ, similarity function; ρ, density of the gas mixture; R, the universal gas constant; λ, the thermal conductivity; C_{pi}, the specific heat at constant pressure of i^{th} species; R_i, the molecular reaction rate of i^{th} species per unit volume; μ, the viscosity; v_{di}, the diffusion velocity; D_{ij}, the binary diffusion coefficient; and Q, the heat release rate.

For soot production and oxidation, consider an arbitrary control volume in the reaction zone. Then an atomic mass fraction can be defined as:

$$\xi_j = \sum_{i=1}^{n} \left[\frac{M_j \, \nu_i^j}{W_i} \right] y_i \tag{5-15}$$

Here, W_i denotes the molecular weight of species i. M_j denotes atomic weight of atom j and ν_i^j denotes the number of atoms of j in species i. Assuming that the only atomic constituents in flames are C, H, N, O and He. And soot particle is assumed a particle which is composed only of carbon and hydrogen atoms, for the present study. Then, the summation of atomic mass fractions along with soot mass fraction yields:

$$\xi_C + A_C \left[\frac{\rho_s f_v}{\rho} \right] + \xi_H + A_H \left[\frac{\rho_s f_v}{\rho} \right] + \xi_O + \xi_N + \xi_{He} = 1 \tag{5-16}$$

Here,

$$y_{soot} = \frac{\rho_s f_v}{\rho} \tag{5-17}$$

Where, A_C and A_H are the atomic mass fraction of carbon and hydrogen atoms in soot particle. ρ_s is the soot particle density which is taken as $1.86 g/cm^3$. Since methane is used as fuel, mass fraction of fuel can be written as a summation of mass fractions of carbon and hydrogen atoms as :

$$\xi_F = \xi_C + \xi_H \tag{5-18}$$

By the definition, $A_C + A_H = 1$. Then, a new quantity, a summation of fuel mass fraction, ξ_F and soot mass fraction, y_{soot} will be conserved. This new quantity is total mass fraction of carbon and hydrogen atoms and will be denoted by ξ_T. Also, since none of the atoms can be created or destroyed in the flame, mass fractions of oxygen, nitrogen and helium atoms should be conserved in the flame.

Here, let's define normalized fuel and oxygen mass fraction as:

$$Z_F \equiv \frac{\xi_F}{\xi_{F_\infty}} \quad \text{and} \quad Z_O \equiv \frac{\xi_O}{\xi_{O_\infty}}, \tag{5-19}$$

where, the subscripts O_∞ and F_∞ represent the inlet conditions on the oxidizer and the fuel side, respectively.

Then, the total mass fraction of carbon and hydrogen atoms, ξ_T and the mass fraction of oxygen atom can be written by conservation equations in terms of normalized fuel and oxygen mass fraction, and soot volume fraction. In general, these conservation equations are:

$$\xi_{F_\infty}\left\{ \rho\vec{V}\cdot\vec{\nabla}Z_F - \vec{\nabla}\cdot\left[\rho D_F \vec{\nabla}Z_F\right]\right\} + \rho_s\left\{ \rho\vec{V}\cdot\vec{\nabla}\left[\frac{f_v}{\rho}\right] - \vec{\nabla}\cdot\left[\rho D_{Th} f_v \vec{\nabla}T\right]\right\} = 0 \tag{5-20}$$

and

$$\rho\vec{V}\cdot\vec{\nabla}Z_O - \vec{\nabla}\cdot\left[\rho D_O \vec{\nabla}Z_O\right] = 0 \tag{5-21}$$

Where, D_F and D_O are the diffusion coefficients of fuel mixture and oxygen, respectively. D_{Th} is thermophoretic diffusion coefficients of soot particles which can be defined (Kent & Honnery, 1990) as:

$$D_{Th} \equiv \frac{3\,\nu}{4\,(1+\pi/8)\,\rho\,T} \tag{5-22}$$

In chapter 4, the experimental results showed that soot formation and oxidation processes occur simultaneously in sooting zone of the counterflow diffusion flame. That is, soot production in the flame indicates the net soot production is a result of the soot production and soot oxidation. Let $\dot{m}_{NT}'''$, $\dot{m}_{SP}'''$ and $\dot{m}_{SO}'''$ denote the net soot production rate, the pure soot production rate and the pure soot oxidation rate. Then, the net soot production rate is:

$$\dot{m}_{NT}''' = \dot{m}_{SP}''' - \dot{m}_{SO}'''$$

Equation (5-20) can be divided into two groups which are for fuel and for soot particle. First and second terms of the equation are related to the C- and H- atoms in fuel while third and forth terms are related to the C- and H- atoms in soot particles. These third and forth terms can then be expressed as an source of soot particles. That means these terms are the net soot production rate. So, the soot terms (third and forth terms) of Equation (5-20) and net soot production rate can be equated as:

$$\rho\vec{V}\cdot\vec{\nabla}\left[\frac{f_v}{\rho}\right] - \vec{\nabla}\cdot\left[\rho D_{Th} f_v \vec{\nabla}T\right] = \frac{1}{\rho_s}\left[\dot{m}_{SP}''' - \dot{m}_{SO}'''\right] \tag{5-23}$$

Then, Equation (5-20) becomes:

$$\rho\vec{V}\cdot\vec{\nabla}Z_F - \vec{\nabla}\cdot\left[\rho D_F \vec{\nabla}Z_F\right] = -\frac{1}{\xi_{F_\infty}}\left[\dot{m}_{SP}''' - \dot{m}_{SO}'''\right] \tag{5-24}$$

From Equation (5-23), the soot particle number density, N can be induced as same form as:

$$\rho\vec{V}\cdot\vec{\nabla}\left[\frac{N}{\rho}\right] - \vec{\nabla}\cdot\left[\rho D_{Th} N \vec{\nabla} T\right] = \dot{N}_{Nu} - \dot{N}_{Co} \tag{5-25}$$

where $\dot{N}_{Nu}$ stands for the number of soot particles nucleated per unit time per unit volume (nucleation rate) and $\dot{N}_{Co}$ is the number of soot particles coagulated per unit time per unit volume (coagulation rate).

From these vector form equations, soot equations for the one-dimensional counterflow diffusion flame can be derived as:

$$\rho v \frac{d\left[\frac{f_v}{\rho}\right]}{dz} - \frac{d}{dz}\left[\rho D_{Th} f_v \frac{dT}{dz}\right] = \frac{1}{\rho_s}\left[\dot{m}_{SP}''' - \dot{m}_{so}'''\right] \tag{5-26}$$

$$\rho v \frac{dZ_F}{dz} - \frac{d}{dz}\left[\rho D_F \frac{dZ_F}{dz}\right] = -\frac{1}{y_{F_-}}\left[\dot{m}_{SP}''' - \dot{m}_{so}'''\right] \tag{5-27}$$

$$\rho v \frac{dZ_O}{dz} - \frac{d}{dz}\left[\rho D_O \frac{dZ_O}{dz}\right] = 0 \tag{5-28}$$

$$\rho v \frac{d\left[\frac{N}{\rho}\right]}{dz} - \frac{d}{dz}\left[\rho D_{Th} N \frac{dT}{dz}\right] = \dot{N}_{Nu} - \dot{N}_{Co} \tag{5-29}$$

A significant fraction of the observed particle growth is due to coagulation whereby particles collide and fuse, thus reducing their overall number density while increasing the average size of the particles. Soot particle coagulation rate has been investigated by many researchers. From these researches (Graham & Homer, 1973; Graham & Robinson, 1976; Hidy & Brock, 1970; Haynes & Wagner, 1981) coagulation rate were led to:

$$\dot{N}_{Co} = -\frac{6}{5} k_{th} f_v^{1/6} N^{11/6} \tag{5-30}$$

where

$$k_{th} = \frac{5}{12}\left[\frac{3}{4\pi}\right]^{\frac{1}{6}}\left[\frac{6kT}{\rho_s}\right]^{\frac{1}{2}} G\ \alpha$$

and G is a factor to take account of the interparticle dispersion forces and can be expected to have a value of about 2 for spherical particles (Graham & Hommer, 1973; Hayns & Wagner, 1981). α is a weak function of the particle size distribution. For a monodisperse system $\alpha = 4\sqrt{2}$.

The soot nucleation rate, $\dot{N}_{Nu}$ can be obtained From the Equation (5-29) with known $\dot{N}_{Co}$. The right hand side of Equation (5-29) can be calculated with measured values of number density and temperature profile.

For the present study, soot production and oxidation rates were assumed as:

$$\dot{m}'''_{SP} = A_P\ \xi_{F-}\ Z_F\ N^{1/3}\ f_v^{2/3} \exp\left[-\frac{E_P}{RT}\right] \tag{5-31}$$

$$\dot{m}'''_{SO} = A_O\ \xi_{O-}\ Z_O\ N^{1/3}\ f_v^{2/3} \exp\left[-\frac{E_O}{RT}\right] \tag{5-32}$$

Where A_P and A_O are the pre-exponential constants and E_O and E_P are the activation energies of soot production and oxidation, respectively.

To solve soot production rate, it is necessary to know soot oxidation rate which is given by Equation (5-32). This equation can be solved with measured values of N, f_v, and T, if A_O, E_O, and Z_O are known.

To obtain Z_O, Equation (5-21) non-dimensionalized by using:

$$z^* = \frac{z - z_{st}}{z_{fl} - z_{st}}, \quad v^* = \frac{v}{(z_{fl} - z_{st})\,\varepsilon}$$

$$\rho^* = \frac{\rho}{\sqrt{\rho_\infty \rho_{-\infty}}}, \quad D_O^* = \frac{D_O}{(z_{fl} - z_{st})^2\,\varepsilon}$$

Then, Equation (5-21) becomes:

$$\rho^* v^* \frac{dZ_O}{dz^*} - \frac{d}{dz^*}\left[\rho^* D_O^* \frac{dZ_O}{dz^*}\right] = 0 \tag{5-33}$$

Furthermore, it is useful to change variable from the non-dimensionalized axial coordinate z, to the normalized velocity defined by $V^* = \rho^* v^*$. Then, the equation becomes simple form as:

$$V^* \frac{dZ_O}{dV^*} + \frac{d}{dV^*}\left[2\rho^{*2} D^* \psi \frac{dZ_O}{dV^*}\right] = 0 \tag{5-34}$$

From the experimental results and numerical solutions, ψ and $\rho^{*2} D_O^*$ were assumed to be constant. Since $\rho^{*2} D_O^*$ is assumed constant, it is convenient to use known values for the ρ^* and D_O^*. So, the values at $z = \infty$, $\rho_\infty^* \rho_{-\infty}^* D_{O_-}^*$ was used for the convenience.

Let

$$\tilde{V} = \frac{V^*}{2\sqrt{\rho_\infty^* \rho_{-\infty}^* \psi D_{O_-}^*}}$$

Finally, simple homogeneous ordinary second order differential equation for the Z_O was derived:

$$\frac{d}{d\tilde{V}}\left[\frac{dZ_O}{d\tilde{V}}\right] + 2\tilde{V}\frac{dZ_O}{d\tilde{V}} = 0 \tag{5-35}$$

The solution is given as :

$$Z_O = C_1\, erfc(\tilde{V}) + C_2\, erfc(-\tilde{V}) \tag{5-36}$$

With boundary conditions at $z = \infty$ and $z = -\infty$, integration constants C_1 and C_2 were determined. The solution Z_O to the conserved scalar equation is:

$$Z_O = \frac{erf(\tilde{V}_{F_-}) - erf(\tilde{V})}{erf(\tilde{V}_{F_-}) - erf(\tilde{V}_{O_-})} \tag{5-37}$$

where

$$\tilde{V} = \frac{\rho v}{\sqrt{4\,\varepsilon_0 \bar{\psi} D_{O_-}\,\rho_{F_-}\rho_{O_-}}} \tag{5-38}$$

Here, $\bar{\psi}$ is an average value of similarity function. $\tilde{V}_{F_-}$ and $\tilde{V}_{O_-}$ are the $\tilde{V}$ values at $z = -\infty$ and $z = \infty$, respectively.

Libby and Blake (1981) suggested that for the soot oxidation due to CO_2 and H_2O, A_O is 1194.5 (g/cm^2 sec) and E_O is 41.9 (Kcal/mol). Using these values and non-dimensionalized conserved scalar quantity of oxygen, Z_O, soot production rate was calculated.

Equations (5-1) through (5-4) are a set of ordinary non-linear, two-point boundary value differential equations. A one-dimensional computer code was developed to calculate the velocity distribution. An ODE integration package obtained from Lehigh University was employed for the present calculations. This ODE integration package was modified and the equations were calculated numerically by Dr. Zhang. For the measured species profiles, it is necessary to smooth them to calculate their first and second derivatives. Thus, numerical smoothing method (Atreya, 1983) was used to process the mole fraction profiles. Smooth curves were drawn through 30 to 50 original data points to take for each species profile by HP digitizer. These curves were used in the computer program to calculate the net reaction rate after smooth by the code.

After solving a set of second order ordinary differential Equations (5-1) and (5-2) for v and ψ with measured quantities (temperature and species concentration profiles), species reaction rate and heat release rate were obtained by Equations (5-3) and (5-4). Normalized conserved scalar quantity of oxygen, Z_O was given by Equation (5-36) with calculated values of ε and ψ. Soot production rate, $\dot{m}'''_{SP}$ and soot particle nucleation rate, $\dot{N}_{Nu}$ were obtained by Equation (5-26) or (5-27), and Equation (5-29), respectively. The soot production rate was plotted in Arrhenius form (Equation (5-31)) to find A_P and soot production activation energy, E_P. The results of analysis are

shown in the following sections.

5.2 Velocity Distribution

Velocities, in general, can be measured by intrusive and non-intrusive methods. None of these methods can measure the velocities without disturbing the flame. For example, Laser Doppler Velocimetry (LDV) can measure the velocity of fluid without inserting any physical probe in the flame. But it needs particles as a scatterer in the fluid. The size of the particles are comparable to that of soot particles in the sooty flame. And the introducing the particles, even very small amount, can disturb the flame condition. Soot particles themselves might be suggested to be scatterer particles for this measuring method. Soot particles in the flame are created, grow, and are oxidized along their path. So, it is hard to measure the flow velocity by LDV measurement without disturbing flames. Therefore, for the present study, velocity was calculated based on the measured quantities which are species concentration and temperature profiles, using governing equations (Equations (5-1) through (5-4)).

Figures 5-2, 5-3 and 5-4 show the calculated normal velocity distributions for 300 K, 900 K, and 1200 K flames. Near the peak flame temperature (z_n = 1.0), a small double hump is seen. For the counterflow diffusion flames, this double hump is always exist, because in the vicinity of the flame, density changes rapidly. This is consistent with the literature [Smook *et al.*, 1988; Puri *et al.*, 1987; Hahn *et al.*, 1981).

From the velocity profiles, the fuel inlet velocity of 300 K flame is about 65 mm/sec, for 900 K about 120 mm/sec and for 1200 K about 130 mm/sec. Similarly, for the oxidizer flow, the velocity at the end of honeycomb of the upper part of the burner was increased as pre-heat temperature. According to the temperature profiles (Figure 4-4), temperature difference among 300 K, 900 K and 1200 K pre-heat temperatures were almost same on each side.

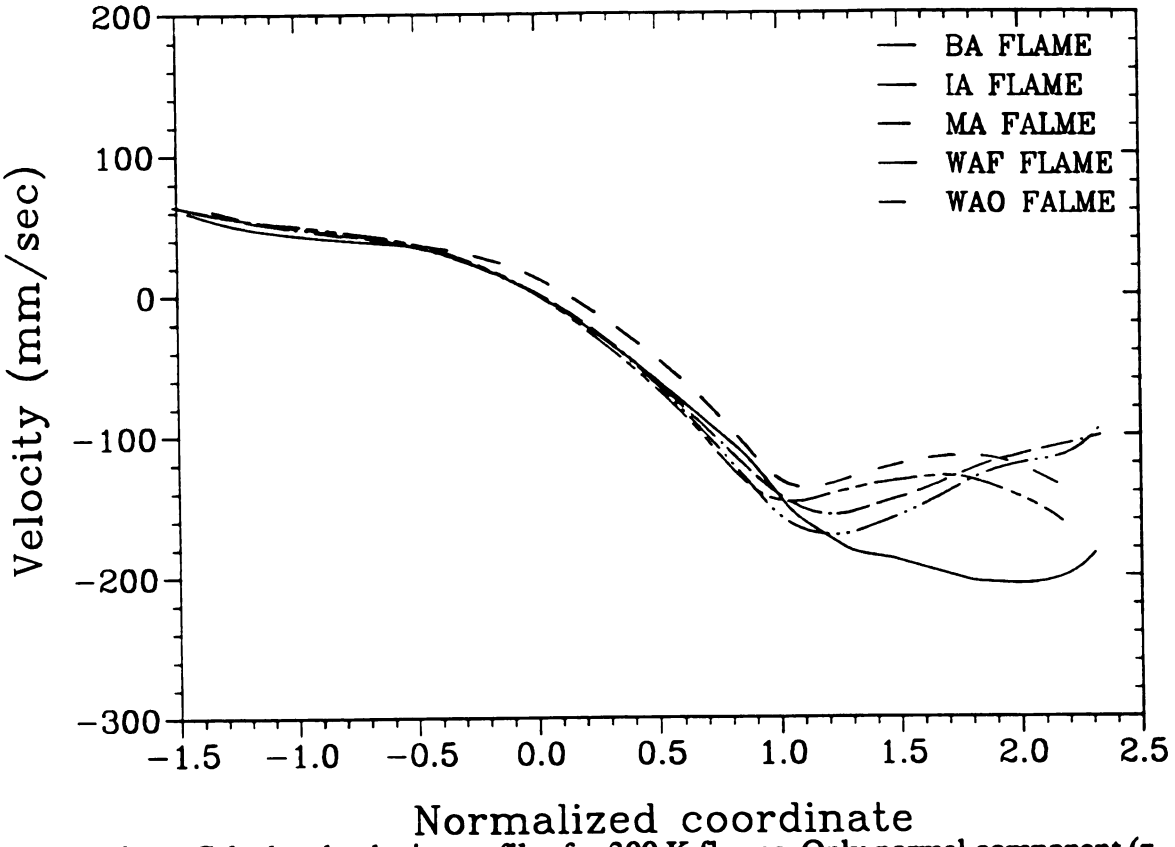

Figure 5-2 Calculated velocity profiles for 300 K flames. Only normal component (z-component) of velocities were plotted.

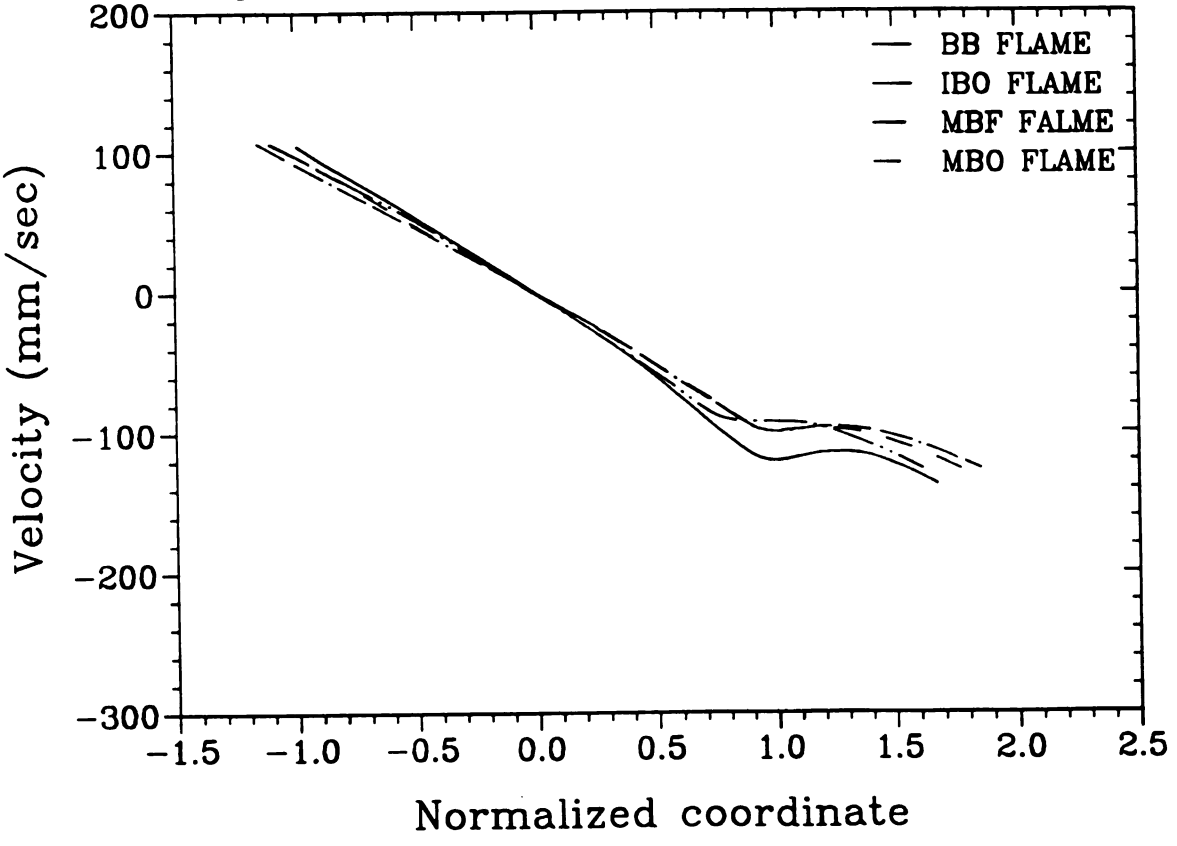

Figure 5-3 Calculated velocity profiles for 900 K flames. Only normal component (z-component) of velocities were plotted.

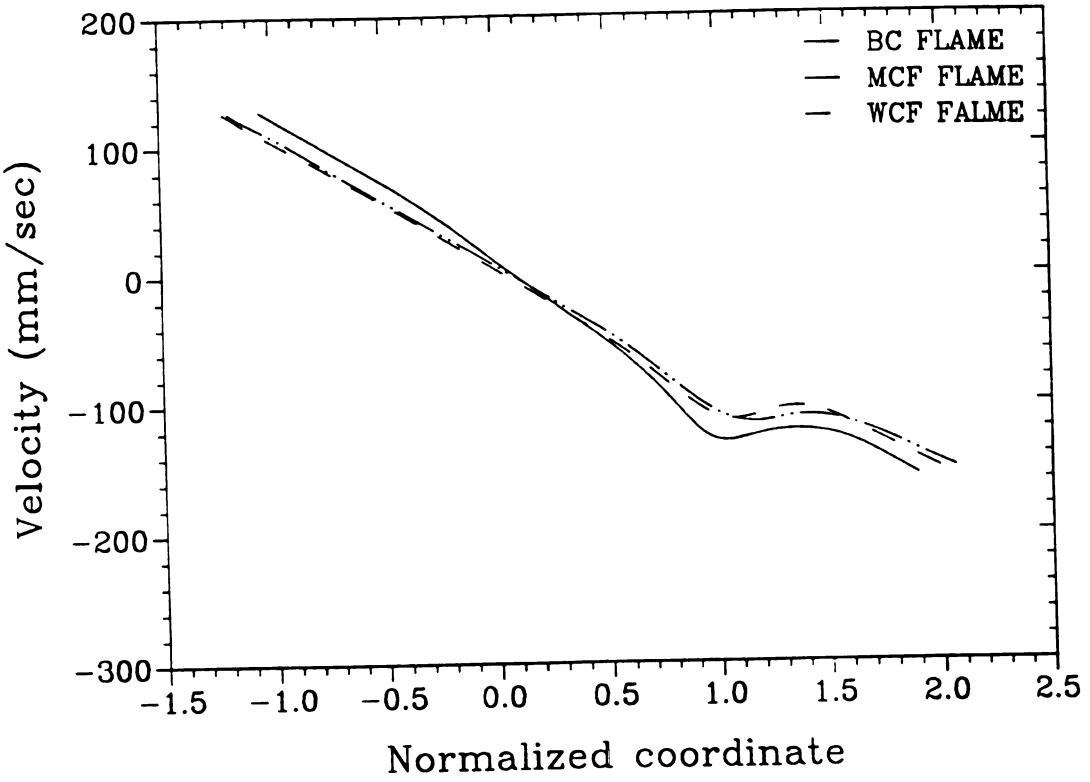

Figure 5-4 Calculated velocity profiles for 1200 K flames. Only normal component (z-component) of velocities were plotted.

For the given pre-heat temperature, velocity profiles were almost identical each other. This indicates that momentum of flow was not changed significantly when N_2 was replaced by the mixture of CO_2 or H_2O and He. It also showed that strain rates were maintained as constant value for given pre-heat temperature.

5.3 Net Chemical Reaction Rate

The net chemical reaction rates were calculated from experimental data for the major species (H_2, CO_2, O_2, CH_4, CO, H_2O) and major hydrocarbons. Figures 5-5 and 5-6 show the typical chemical reaction rate of major species. Figure 5-7 and 5-8

show the typical chemical reaction rate of hydrocarbons.

Figures 5-5 and 5-6 showed that most of CH_4 was depleted in the zone $0.5 < Z_n < 1.0$ and O_2 was depleted in $0.9 < Z_n < 1.4$. CO and H_2 were generated mostly just below the blue flame and were depleted the oxidizer side of the flame. Most of CO_2 and H_2O were produced at around the blue flame. For these species, the peak production rates were located at the same place where most CO and H_2 existed.

Figures 5-7 and 5-8 showed that most of hydrocarbons were produced between stagnation plane and flame. Just above the flame which is oxidizer side of the flame, all the hydrocarbons were depleted in very short range ($0.9 < Z_n < 1.2$). These figures also showed that positive hydrocarbon production rate exists only in the zone soot particles present. The width of range of producing hydrocarbon may depend on the size of molecules. C_2H_2 had widest range of positive production rate and C_3H_4 had narrowest range.

It is clear that the flame can be conveniently divided into two zones. The first zone extends from the fuel to the lower edge of blue flame ($Z_n < 0.8$) in which methane totally disappears and light hydrocarbons are produced. This is the soot formation zone and is confirmed by the optical measurements discussed in section 4.4. The second zone is the main reaction zone ($0.8 < Z_n < 1.5$) where the primary combustion products such as H_2O and CO_2 are formed and O_2 is consumed. Also in this main reaction zone H_2 and CO are first produced and then converted to CO_2 and H_2O.

Examining the detailed net reaction rate profiles for chemical species along with the soot particle profiles, one notes how complex the process of soot formation and oxidation is. CH_4 was converted predominantly into C_2 hydrocarbons and benzene(C_6H_6) and that negligible amount of C_3, C_4 and C_5 hydrocarbons were presented. Most of hydrocarbons were produced in the sooting zone ($0 < Z_n < 0.8$). The hydrocarbons were depleted around the flame. Optical results also showed that

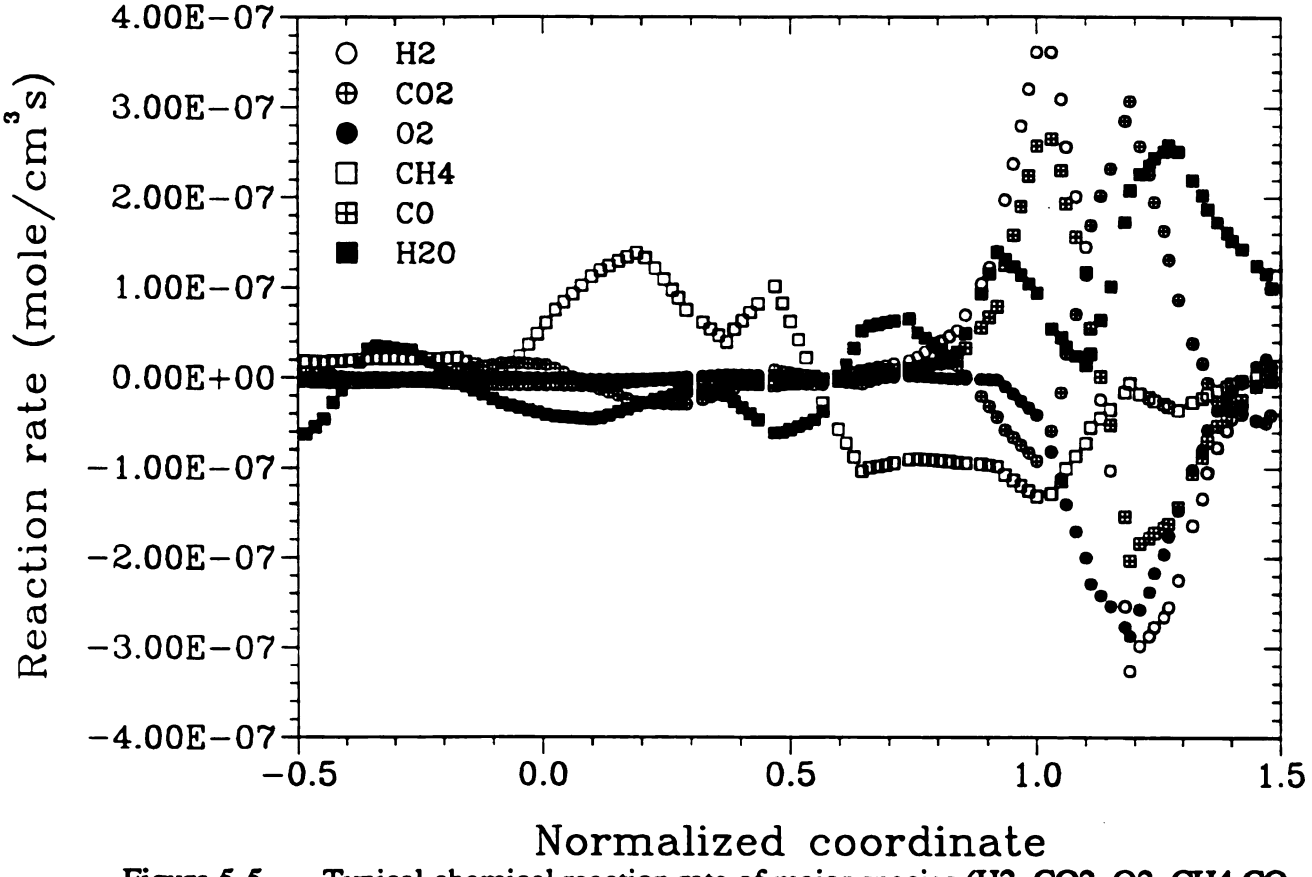

Figure 5-5 Typical chemical reaction rate of major species (H2, CO2, O2, CH4,CO, and H2O) were plotted against moralized coordinate.

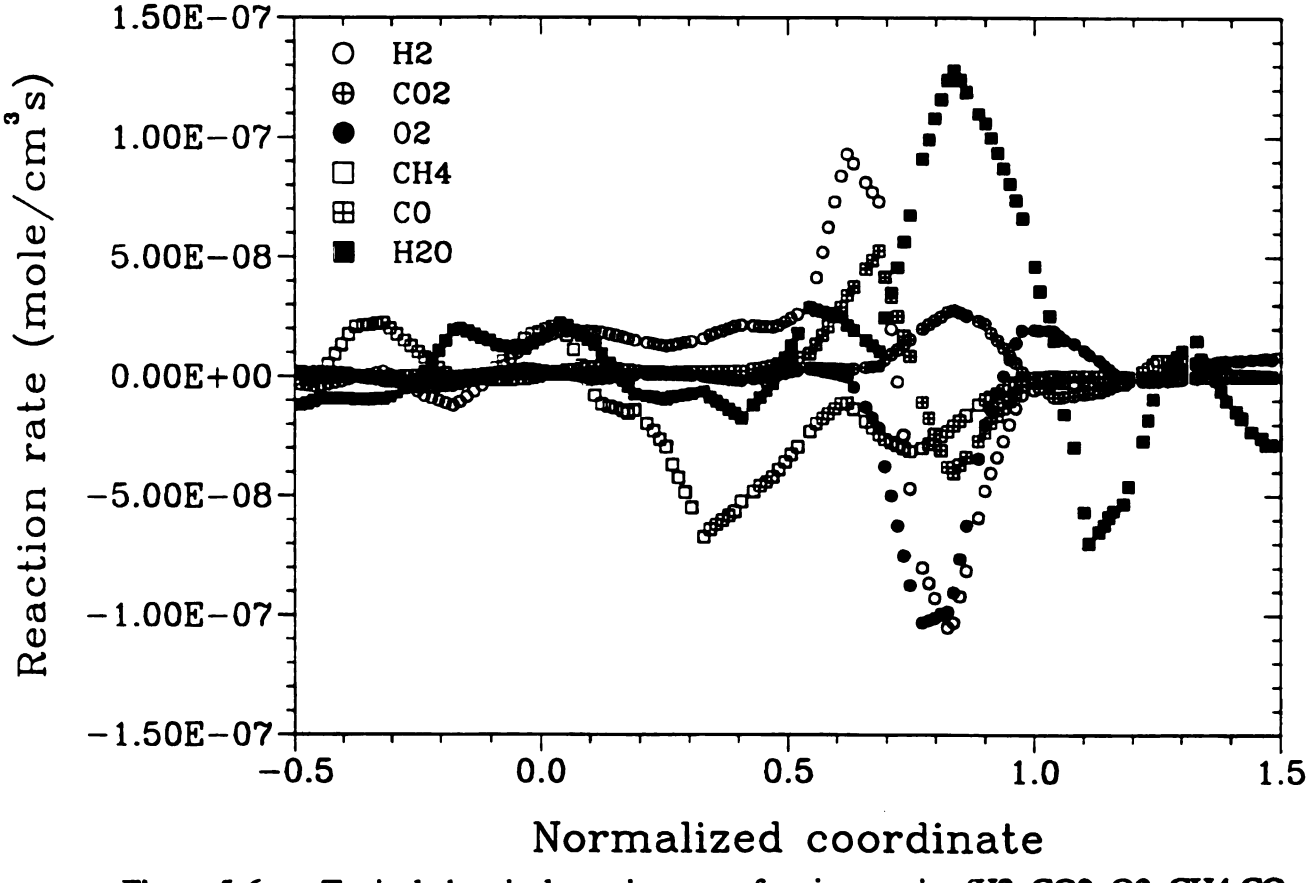

Figure 5-6 Typical chemical reaction rate of major species (H2, CO2, O2, CH4,CO, and H2O) were plotted against moralized coordinate.

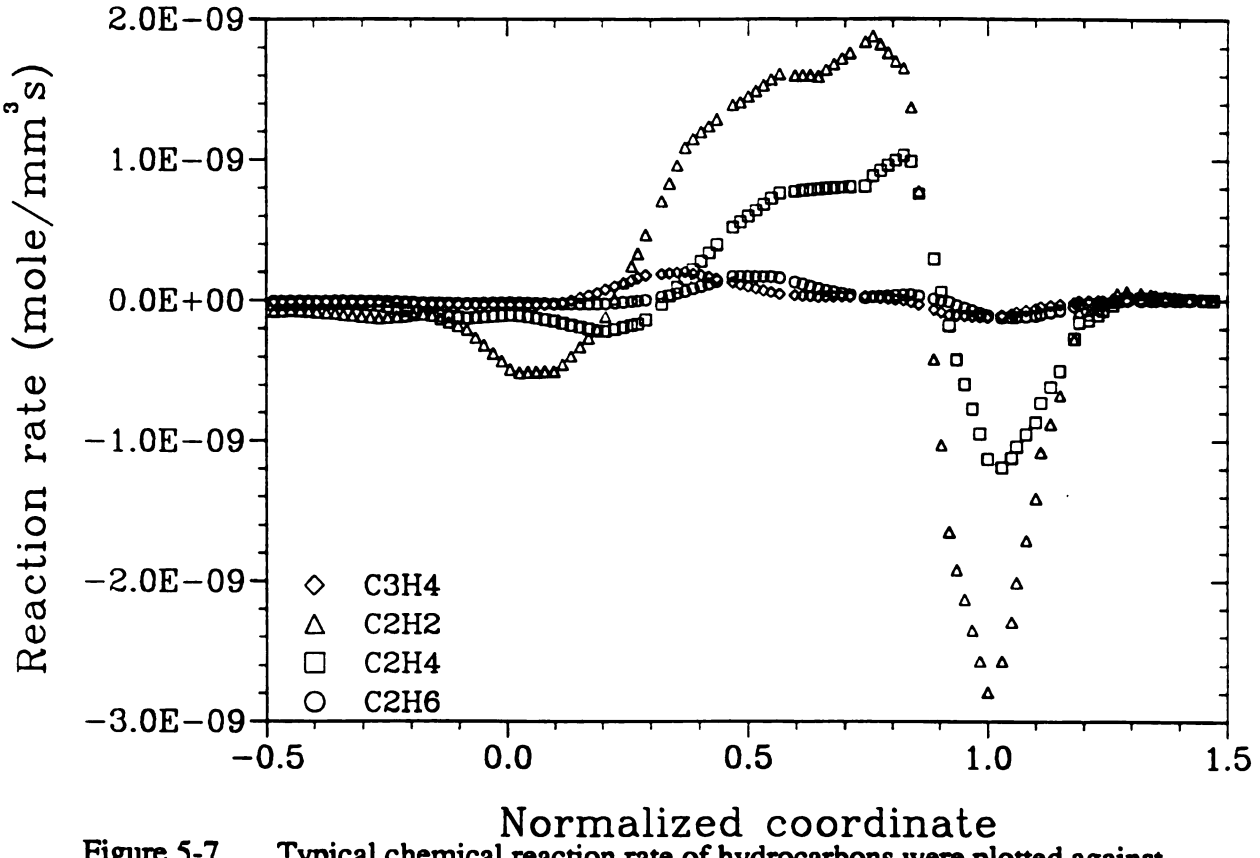

Figure 5-7 Typical chemical reaction rate of hydrocarbons were plotted against moralized coordinate.

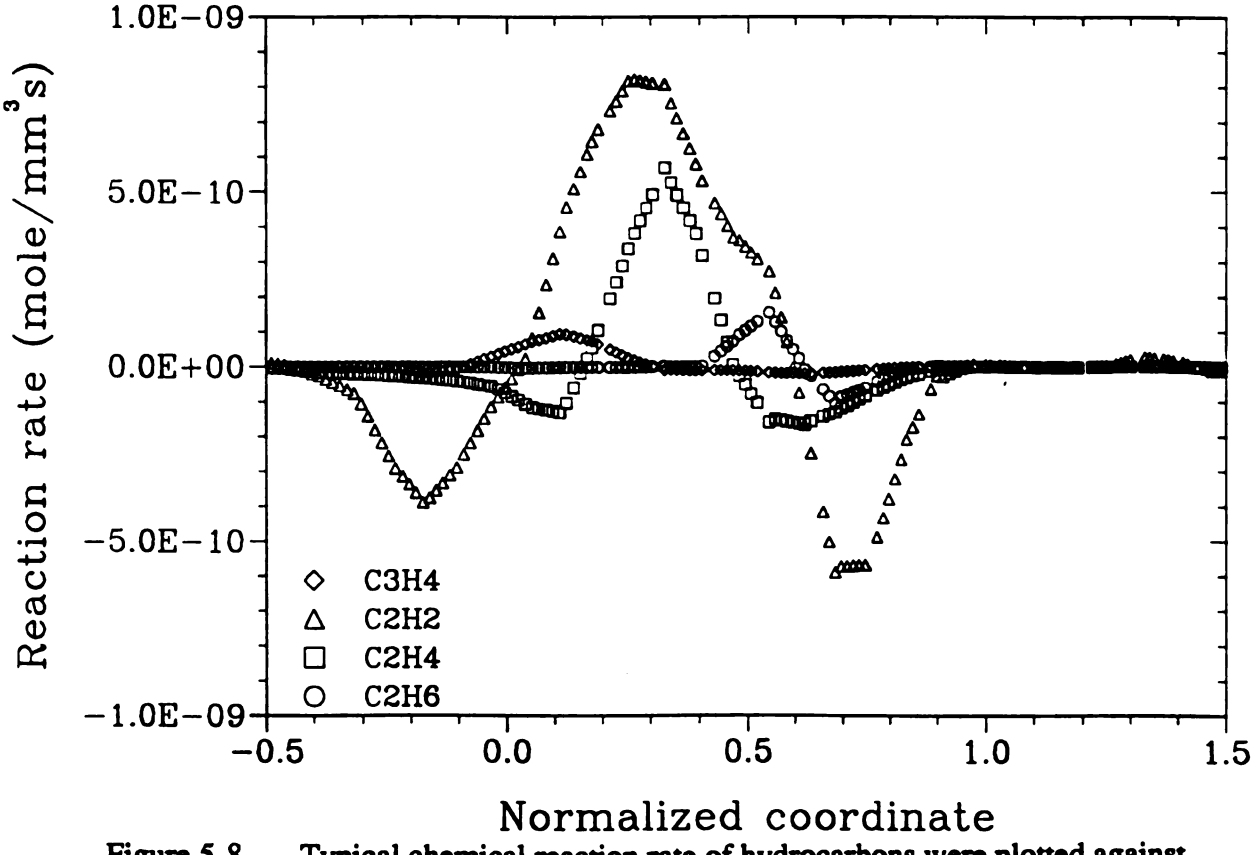

Figure 5-8 Typical chemical reaction rate of hydrocarbons were plotted against moralized coordinate.

soot was produced all through this zone and temperature measurements showed that this zone corresponds to a temperature of 1200 K to 1700K.

5.4 Heat Release Rate

Figures 5-9, 5-10 and 5-11 show the heat release profiles calculated for 300 K, 900 K and 1200 K flames using the measured temperature and Equation (5-4). Heat release rates for given pre-heat temperature are almost same. This can be expected from the temperature profiles because the heat release rate is dominated mostly by temperature. The heat release rate shows a maximum in the flame zone (Z_n = 1.0) and a valley (negative value) for Z_n < 1.0. This endothermic effect can be related to soot formation and the resulting flame radiation.

In Figures 5-12 and 5-13, contributions of mass diffusion, gas mixture convection and thermal conduction to the total heat release rate were examined. From the figures, it was easily observed that the dominant heat release mode is thermal conduction. Heat release by convection and diffusion contribute less than 20 % together.

Since temperature is the most dominant physical characteristic that affects soot formation, the appearance of negative heat release rate in the sooting zone is an interesting result. It is not clear whether the negative heat release rate implies energy consumed in the soot formation process or it is a consequence of flame radiation.

5.5 soot nucleation and formation rate

Soot nucleation rates for all the flames are shown in Figures 5-14. Soot nucleation mostly takes place in the zone of particle size (soot particle diameter) below order of 1 *nm*. The curves show that in sooty flames soot particles are nucleated before the less sooty flames. The nucleation rate decreases quickly and then slowly toward the fuel side. Finally, at around stagnation plane, the nucleation rate is almost constant with value of around 1.0×10^{11} particles/cm^3 sec. Vicinity of stagnation plane, more

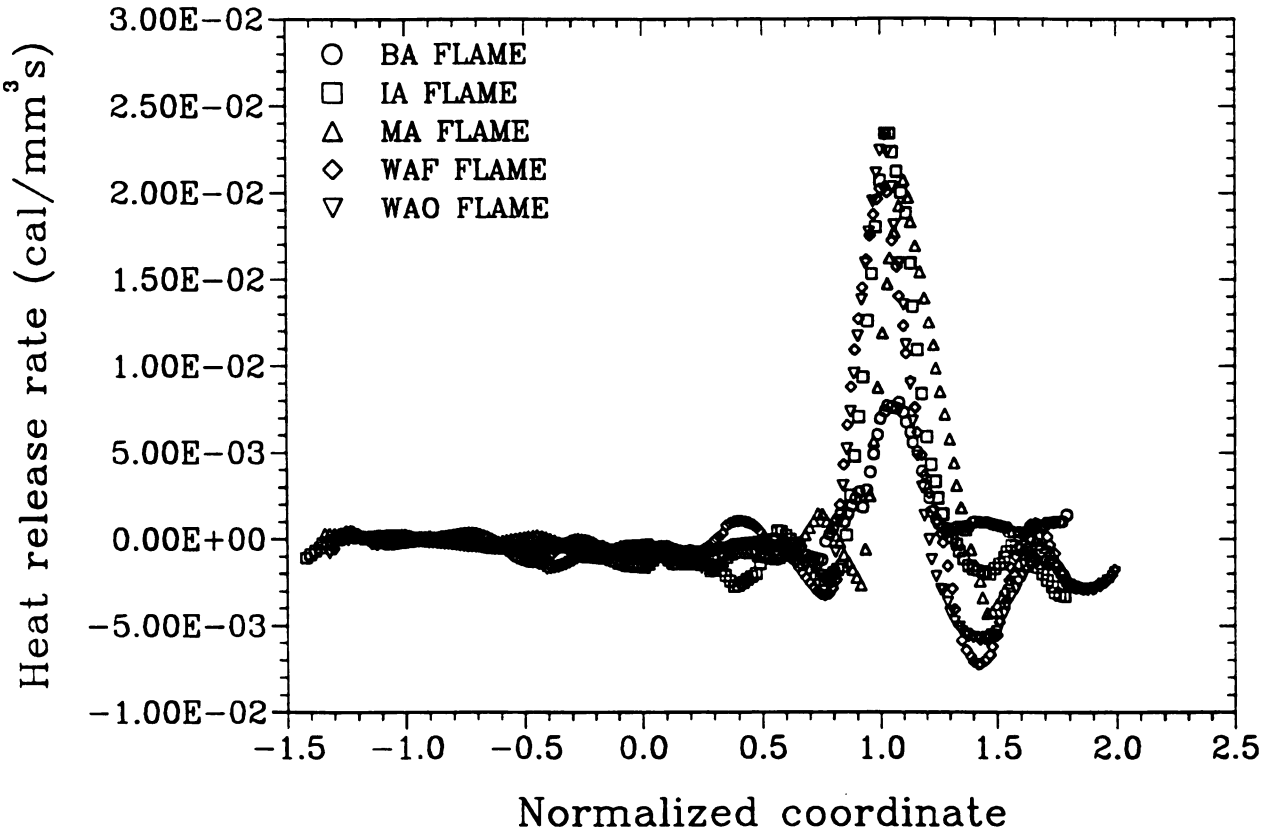

Figure 5-9 Calculated heat release rate from 300 K flames were plotted against normalized coordinate.

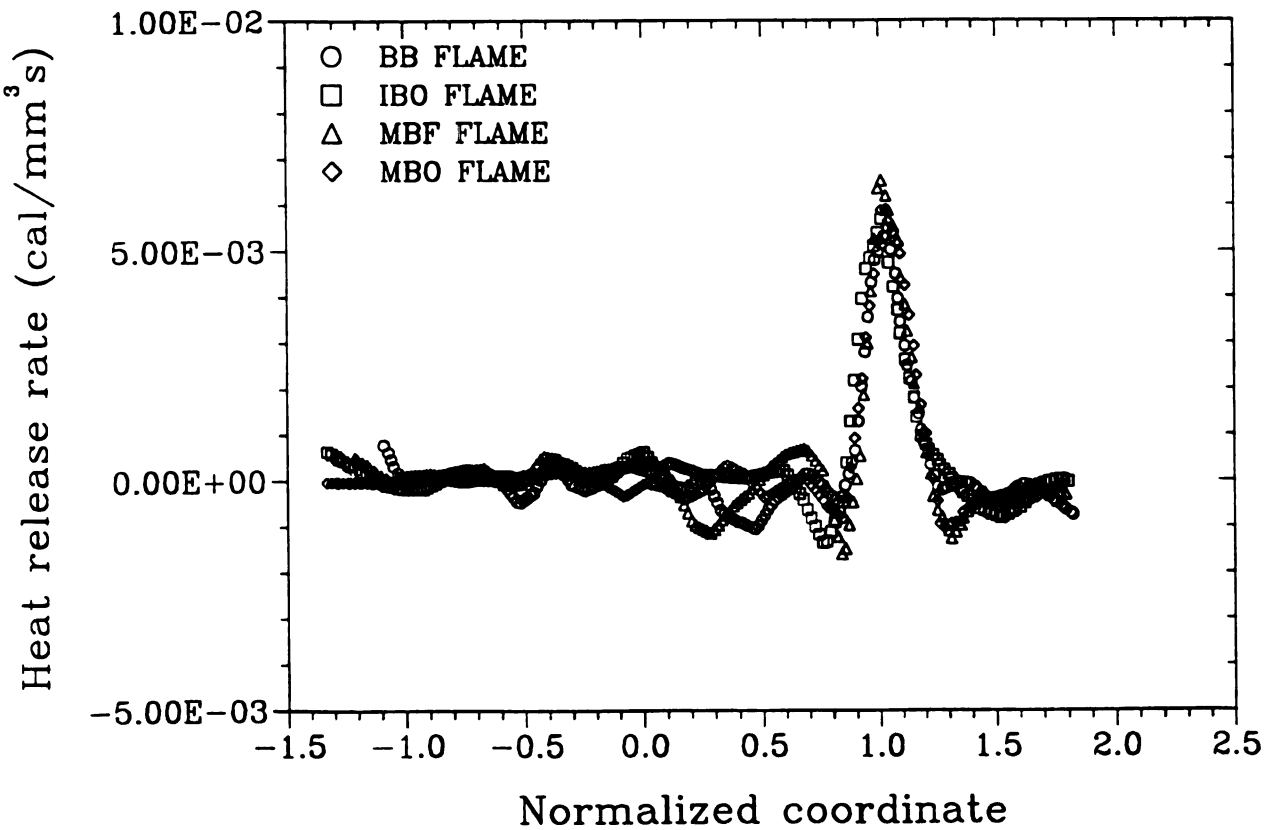

Figure 5-10 Calculated heat release rate from 900 K flames were plotted against normalized coordinate.

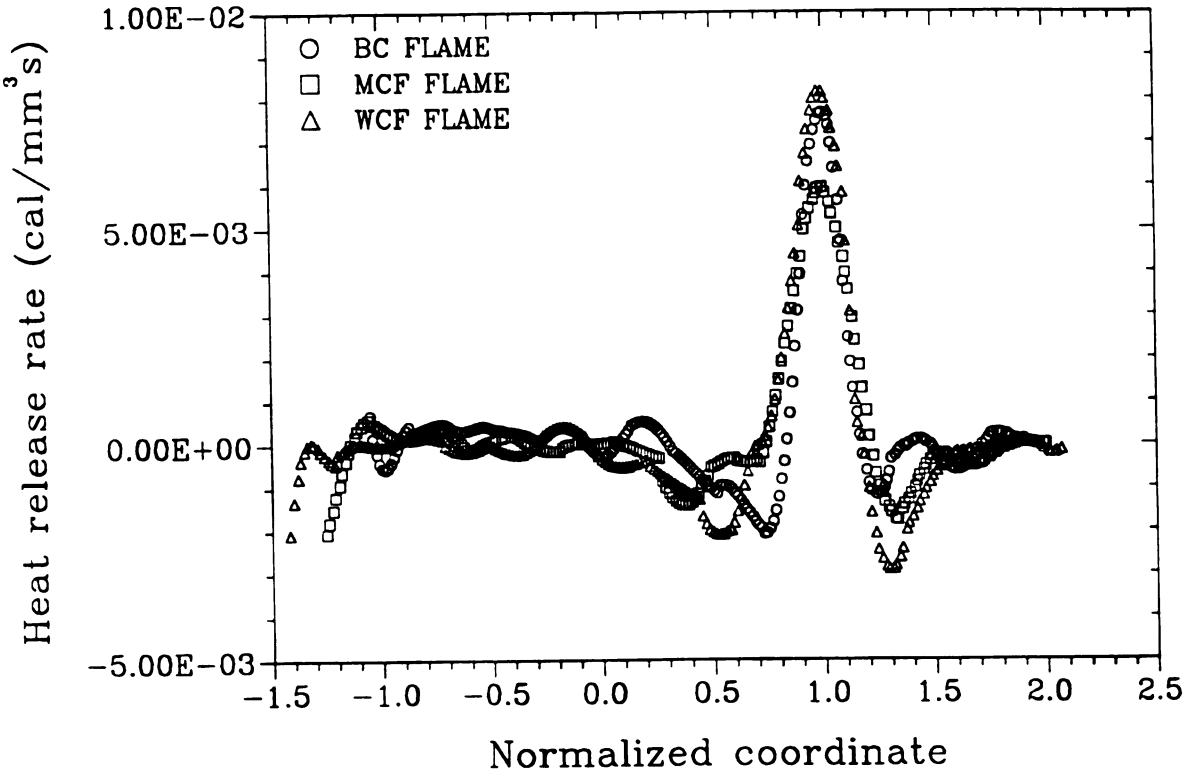

Figure 5-11 Calculated heat release rate from 1200 K flames were plotted against normalized coordinate.

amount of available species may be attached on the soot particles to increase particle size and less species may be used to create new soot particles.

The pure soot formation rates ($\dot{m}'''_{SP} = \dot{m}'''_{NT} + \dot{m}'''_{SO}$) for the flames were calculated. The result were plotted on the Arrhenius plot for the temperature range 1200 K to 1700 K at which the soot particles are produced, grow, and are oxidized. In this calculation, soot formation rate was modified by $\xi_F Z_F N^{\frac{1}{3}} f_v^{\frac{2}{3}}$ to fit Arrhenius form. The results are shown in Figure 5-15. This figure show that the modified soot formation rates from all experiments, approximately, fell into one linear equation. Thus, one can say that the soot formation rate correlates as a straight line on the Arrehnius plot. This

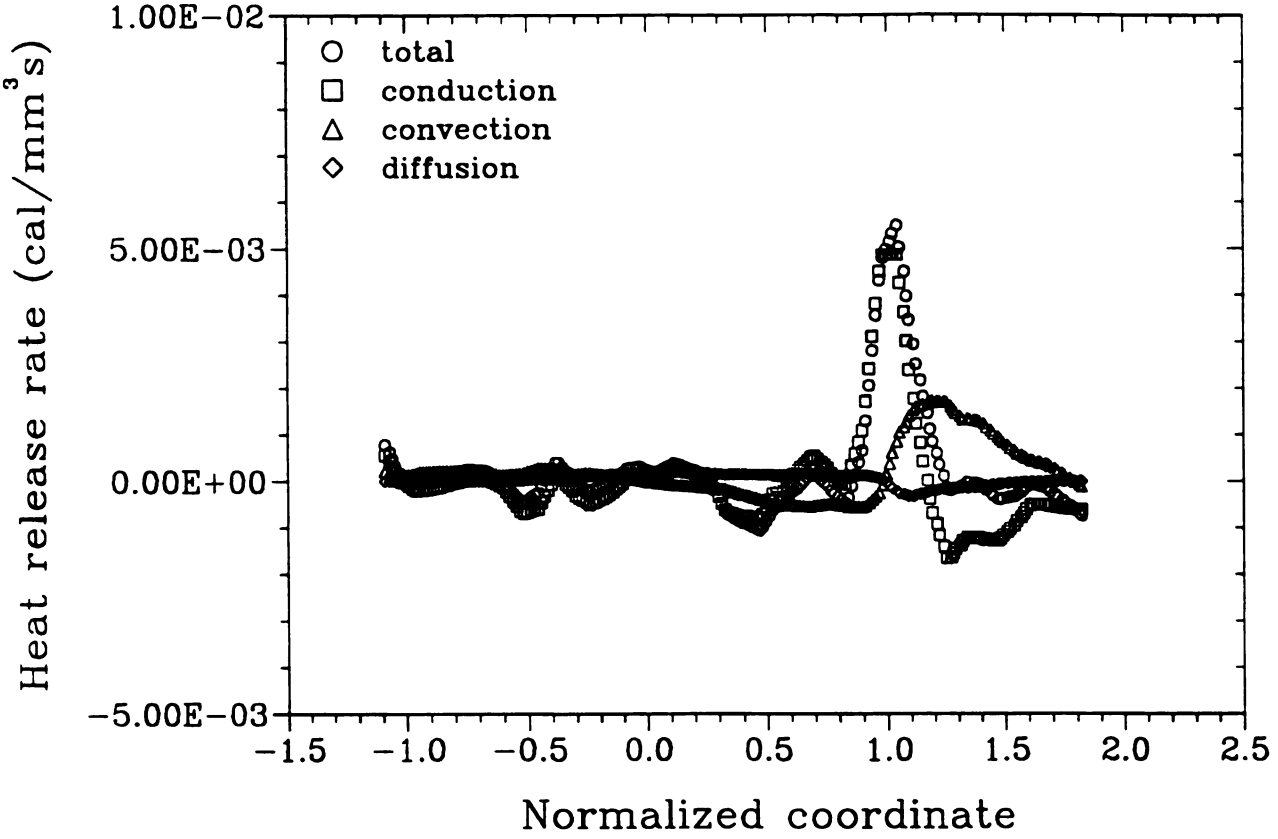

Figure 5-12 Comparison of heat release rates by mass diffusion, by convection, and by thermal conduction in counterflow diffusion flames.

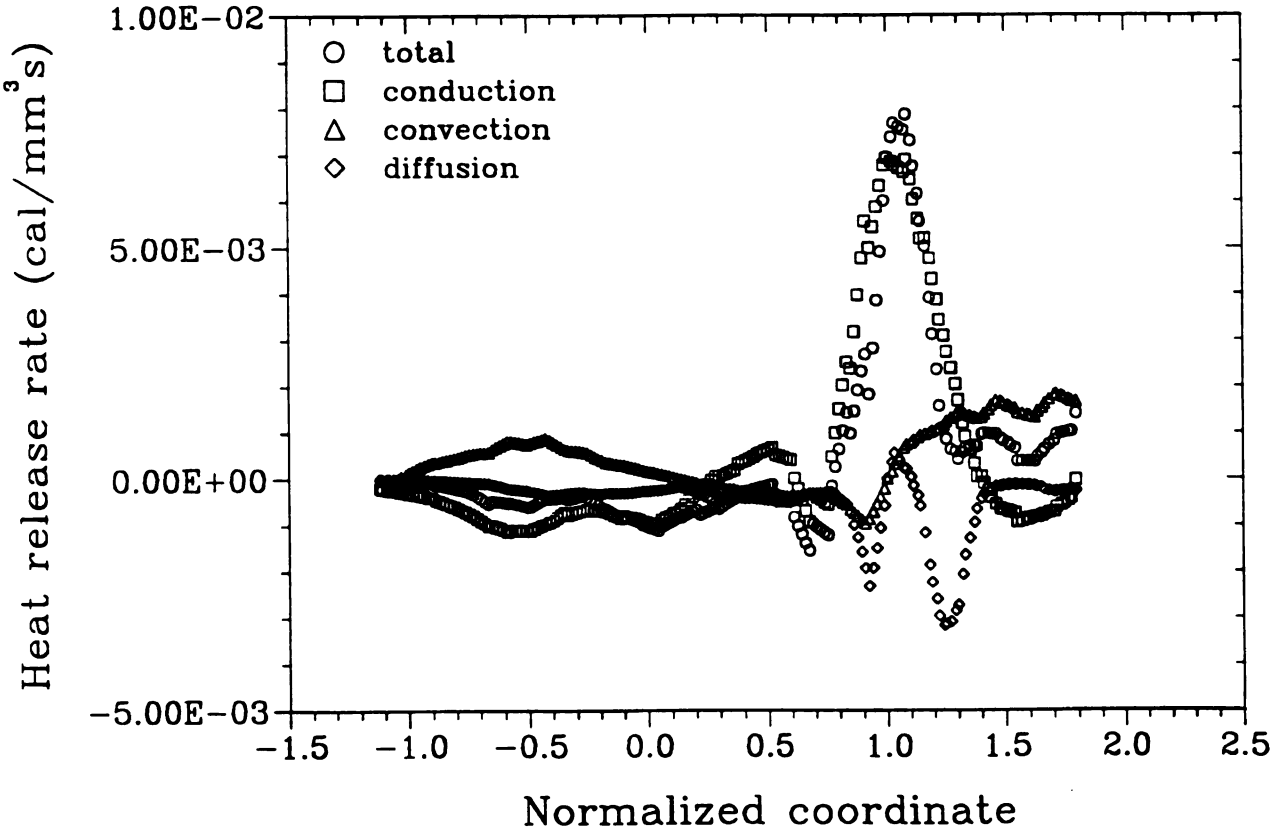

Figure 5-13 Comparison of heat release rates by mass diffusion, byconvection, and by thermal conduction in counterflow diffusion flames.

implies that soot formation rate may be represented by a single pure production rate. From this analysis, the activation energy of the pure soot formation, E_P determined from the plot is about 36 ± 3 Kcal/mole. The pre-exponential constant of the pure soot formation, A_P obtained as 213 g/cm^2sec (ln A_p = 5.4 ± 0.9).

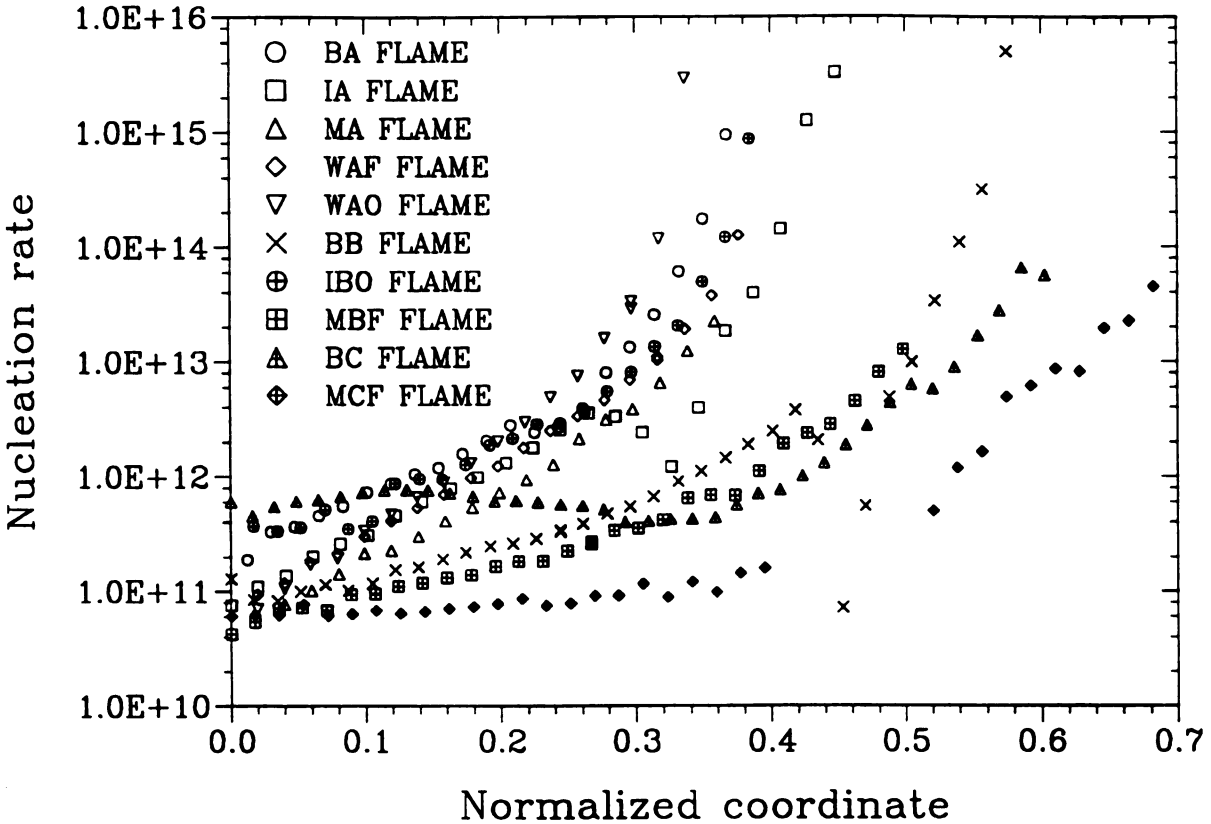

Figure 5-14 Soot particle nucleation rate from the counterflow diffusion flames were plotted against normalized coordinate.

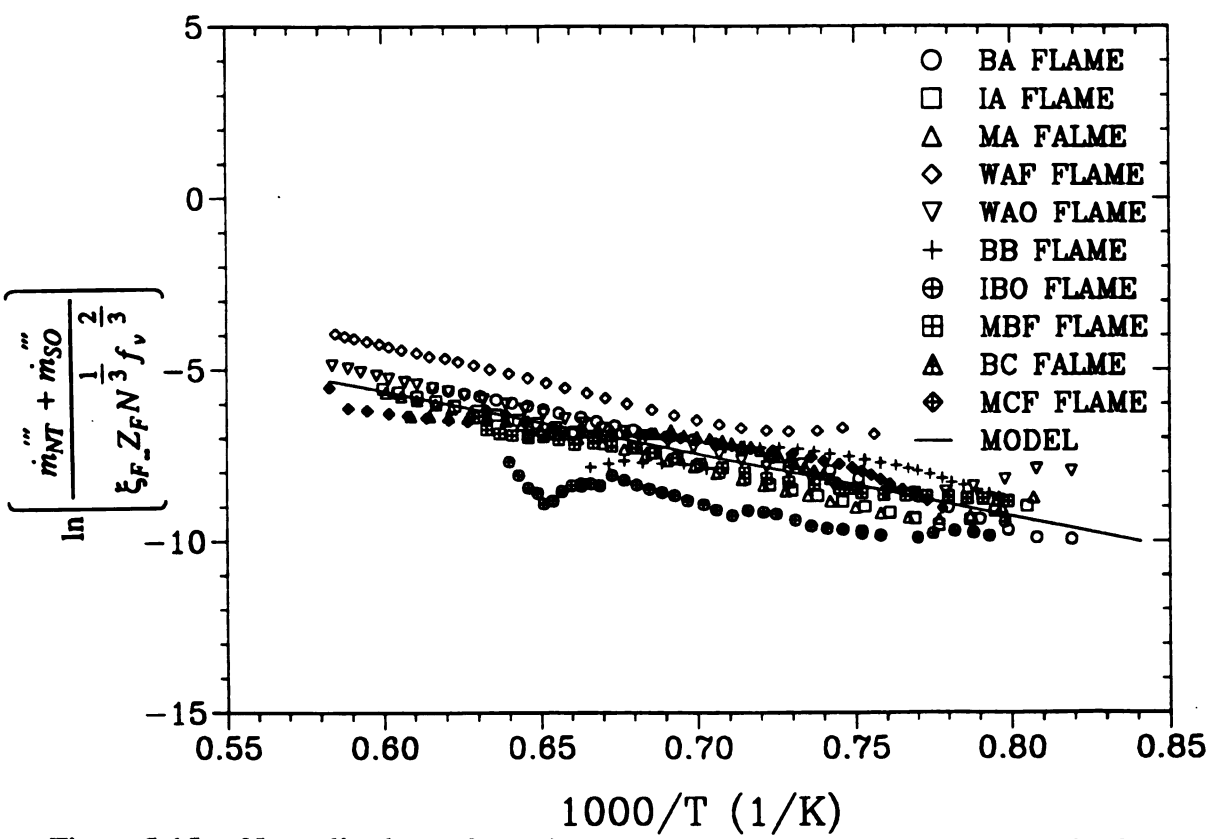

Figure 5-15 Normalized soot formation rates were plotted on the Arrhenius plot for the temperature rang 1200 K to 1700 K. From this plot, E_p = 36.4 Kcal/mole and A_p = 212.7 g/cm²sec were obtained.

Chapter 6

CONCLUSION AND RECOMMENDATIONS

6.1 Conclusion

Significant progress has been made during the last two decades in identifying the probable chemical and physical mechanisms responsible for the formation, growth, and oxidation of soot particles. In the present study, soot formation, growth, and oxidation in axisymmetric counterflow diffusion flame was experimentally and analytically investigated. A unique high temperature axisymmetric counterflow diffusion flame burner was constructed for these experiments. This burner provided a well defined one-dimensional diffusion flame approximately 6.5 *cm* in diameter. In addition, chemical and optical measurement systems were constructed to measure chemical composition of the flame and soot particles in the flame, accurately. Temperature profiles were also measured along the axial direction.

Experiments were conducted such that the variables affecting soot formation, growth, and oxidation in the flames could be independently studied. It was essential to keep strain rate and fuel concentration for given pre-heat temperature constant while oxygen concentration and additive gas concentration were varied. This set of experiments made it possible to investigate the effect only of chemistry on soot formation and oxidation. It also shows that it is possible to isolate one variable from another.

The reduction of oxygen concentration along with increased pre-heat shows that it is possible to establish a condition at which soot particles are formed without oxygen. This experimental result will be invaluable to quantify pure soot formation rate directly.

Velocity profiles, species production rates, and heat release rates were obtained by solving fundamental governing equations with measured quantities. Soot production rate was modeled using conserved scalar equations based on the atomic conservation. This model shows that the pure soot formation rate in a diffusion flame may be obtained in an Arrhenius form. The soot production rates at given strain rate, fuel concentration, soot particles number density, and soot particles volume fraction were plotted along the inverse temperature. This may be applied to predict soot formation rate in turbulent diffusion flames.

The following conclusions are supported by the experimental and analytical work conducted in the present study.

6.1.1 Experimental Work

1. Sooting structure in diffusion flame was observed by three zones. Figure 6-1 shows the flame and sooting structure in axisymmetric counterflow diffusion flame. The first zone is the primary reaction zone which all oxygen is depleted and hence becomes main energy source. The temperature range in this zone is 1800 K to 2000 K and color is blue. The second zone is the soot particle precursor zone and the color is bright yellow or whitish yellow. In this zone, soot particle precursors are developed among the big hydrocarbon molecules. The temperature range of this zone is 1500 K to 1800 K. The last step of soot particle creation in axisymmetric counterflow diffusion flame is particle nucleation and growth. In this stage, soot particles are growing mostly by surface growth. This zone is dark yellow or orange color. Soot particle size in this zone is larger than the order of 1 nm. The particle size profile in this zone is linear. Temperature of this zone is between 1200 K and 1500 K. These final stage of soot particles are flowing out through the streamlines. This final stage of soot particles are large enough to follow the streamlines instead of to diffuse. Figure 6-2 show a

photograph of the typical flame used for this work. This photograph show the flame colors and structure clearly.

2. Oxidation occurs in any stage of soot formation and growth in counterflow diffusion flame. Based on the experimental results of adding carbon dioxide or water vapor, volume fraction of soot particles were reduced in whole range of sooting zone.

3. Soot particle size in axisymmetric diffusion flame increases linearly. If residence time increases without changing in physical and chemical properties of the flame, then particle size will be increased by coagulation mechanism. This was observed from the several experiments performed for this experimental work. If the particle is formed in an earlier position, then the particle size is larger than when the particle is formed later. For all flames, the slope of soot particle size against the normalized coordinate is almost constant.

4. Soot particle nucleation rate has the same characteristics for all flames. The nucleation rate reduces from above 10^{15} order at nucleation zone to 10^{11} order at the stagnation plane for any flame.

5. Soot particles can be nucleated by coagulation mechanism among the big hydrocarbon molecules. This can be explained by the sharp reductions of number density in that area. After nucleated, the number density reduces slowly and then become almost constant at the value of 1.0×10^9 $counts/cm^3$ around the stagnation plane. In that region, soot particles grow by surface growth mechanism. But even in this area, soot number density reduces slowly. This indicates that there are coagulation growth in that region.

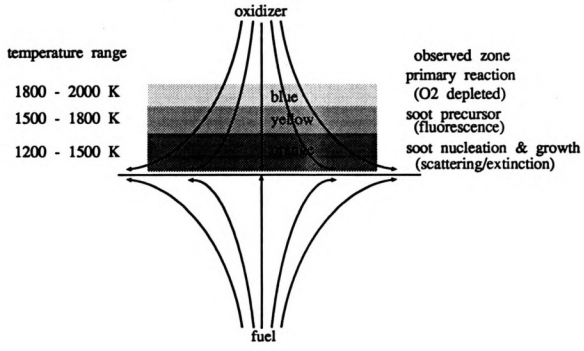

Figure 6-1 Flame and sooting structure in axisymmetric countrflow diffusion flame. Colors and temperature ranges observed in the flame were also shown in the figure.

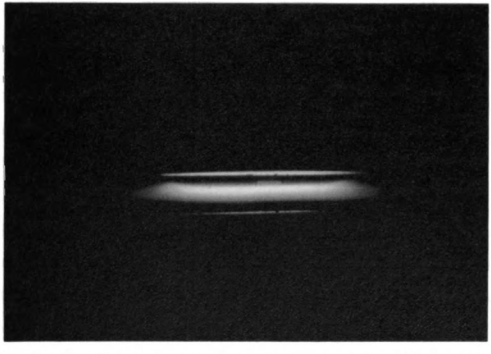

Figure 6-2 Photograph of the axisymmetric countrflow diffusion flame.

6. The Effect of pre-heat temperature on soot formation in diffusion flame was investigated. Increasing pre-heat temperature increases flame temperature as well as hydrocarbon and PAH concentrations. Soot volume fraction also increased along the pre-heat temperature. Soot particles in the higher pre- heat temperature are formed in earlier location, so, the residence time increases and hence particle sizes. But soot particle number density around stagnation plane was almost independent from the pre-heat temperature.

7. CO_2 is one of main combustion products in diffusion flame. So, CO_2 effect on the soot particles in the flame was investigated. Adding CO_2 in fuel inlet stream reduces hydrocarbon and PAH concentrations. And soot particles are formed in later position, which is closer to the stagnation plane, then decrease residence time and hence particle sizes. Soot volume fraction also decreases along the increments of CO_2 concentration in fuel inlet stream.

8. H_2O was also investigated as additive species in diffusion flame because H_2O is also important species among combustion products. Adding water vapor in fuel inlet stream has same trend of adding CO_2. But it was found that the water vapor has much stronger effect to oxidize the soot particles in the flame than CO_2. The effect of 3.6 % of water vapor was comparable to 21 % of CO_2.

9. Adding these major combustion products into the oxidizer inlet stream was investigated. When these species were added into the oxidizer inlet stream reduces much more hydrocarbon and PAH concentrations than when they were added into the fuel inlet stream. Soot residence time reduces much more and hence particle sizes. Soot volume fraction reduces a lot more than when they were added into the fuel stream. For this case, soot number density increased around stagnation

plane. When these species added into the oxidizer inlet stream, these species pass through the high temperature zone. At there, more strong oxidizers such as CO and OH can be generated from these added CO_2 or H_2O. These oxidizers may diffuse into the sooting zone and oxidize soot particles and hydrocarbons. This may cause the reduction of increasing rate of particle size. Also oxidation of an agglomerated soot particle surface can be cause of separation from a large agglomerated soot particle to two or more small individual particles. So, the particle number density may be increased.

6.1.2 Analytical Work

1. All experimental and analytical results are normalized by the thickness between maximum temperature location and stagnation plane. The calculation and their comparisons show this characteristic length is useful for the axisymmetric counterflow diffusion flames.

2. Velocity profile can be calculated using measured stable species concentrations and temperature profiles with continuity and momentum equations. Finding the correct velocity information is one of the main task in combustion research. But for low strain rate, counterflow diffusion flames, it is hard to find the appropriate methods to measure the accurate velocity profile without disturbing flames. From this semi-empirical calculation results, it is verified that this velocity calculation is one of the best ways to get information about velocity profiles.

3. Pure soot nucleation rate can be obtained from the conservation equation for the soot number density profile with given soot coagulation rate. Along this calculation, thermophoretic diffusion coefficient was defined. And the result showed that this diffusion coefficient is valid for the axisymmetric counterflow diffusion

flame.

4. Soot production rate was calculated by a model written as:

$$m'''_{SP} = A_P \; \xi_F \; Z_F \; N^{1/3} \; f_v^{2/3} \exp\left[-\frac{E_P}{RT}\right] \tag{5-1}$$

with given m'''_{SO} and measured net soot formation rate. The calculation results can be plotted on the Arrhenius plot. The results showed that the soot formation rate may be represented by a single overall reaction rate. For the present study, it showed that the activation energy of soot formation is 36 ± 3 Kcal/mol and pre-exponential constant is 213 g/cm^2 sec (ln A_p = 5.4 ± 0.9) in axisymmetric counterflow diffusion flame.

The present study developed a unique experimental facility to separate out the individual influences of temperature, strain rate, oxygen concentration, and concentrations of combustion products on soot formation and oxidation. The result showed for the first time that the pure soot production rate followed Arrhenius kinetics.

6.2 Recommendations

Extensive further study is necessary fully to understand the sooting mechanism and to control soot formation, growth and oxidation in diffusion flames. Fortunately, however, the devices which was developed for the present research can be utilized for further research work.

1. Extension of this research, for example, more gases other than CO_2 and water vapor, can be used to investigate the effect of additives. In this set of experiments, the effects of small amount of oxygen added into fuel stream on the soot

formation can be studied. Numerous other additives, for example, halogens, sulfur, and its oxides, alkaline earth and alkali metals, etc., can be used as an additive gas.

2. The validity of the model used for the present study should be further examined by replicating the experiments with different fuels and pre-heat temperatures.

3. Using the burner, a flame can be established on the fuel side of the stagnation plane. This flame may give different aspect of the soot formation and oxidation in flames. In this flame, fuel and additive gas from the fuel side will path the high temperature region. So, this experiment may give different results from the results in the present study.

4. The results of the present study can be extended to apply for the turbulent diffusion flames.

5. For the ideal study for soot formation, a new burner, which has same configuration, may be constructed with materials which can be used above the 2000 K. And if this burner can heat the oxidizer high enough, then one can perform the experiment for pure soot formation without oxidation.

6. Finally, for practical purpose, the results of the study can be utilized to develop combustion chambers such as burners for industrial boilers or internal combustion chamber such as diesel engines.

Appendix A

APPENDIX A: Burner Model Calculation and Testing

The high temperature axisymmetric counterflow diffusion flame burner was designed and built to meet the experimental requirements. Design of this burner was guided by the calculated streamlines and the model testing with a full scale prototype Plexiglass model. Details of the numerical calculations and the model testing are explained in Appendix A.

A.1 Introduction

The primary target of this burner set is to provide the flow pattern close to the ideal stagnation point flow, and hence one-dimensional flat flame in the gap between the upper and lower parts of the burner without any distortion or disturbances. Most of disturbances in the counterflow diffusion flame come from the draft flow around the burner gap and from the flow separation around injection ports.

The flow separation around injection port may cause temperature short circuit so that the one-dimensional temperature profile along axial direction can be distorted. Also this flow separation can cause rotating flow, thus, create velocity components in the radial direction, r, the circumferential direction, ϕ, and axial direction, z. This will make the problem complex. Therefore, it is important to investigate the shape of the flow guide flange to create flow pattern close to an ideal stagnation point flow without the separation.

Due to the lack of literature on the counterflow stagnation point flow, the best way to determine the flow guide flange shape is through experiments. But experiments are so limited. Therefore, a combination of numerical calculation and experiment was used to determine the optimized flange shape.

A.2 Model Calculations

To calculate streamlines, velocity, and pressure field, steady, incompressible Navier-Stokes equations were employed for the observation area. In the absence of body forces, the dimensionless axisymmetric equations in the vorticity-stream function can be written as (Atreya, Lee, and Foss, 1987):

$$r\left[\frac{\partial(u\,\omega)}{\partial r}+\frac{\partial(v\,\omega)}{\partial z}\right]=\frac{2}{\mathrm{Re}_D}E^2(r\,\omega) \tag{A.1}$$

and

$$E^2(\psi)=2r\,\omega \tag{A.2}$$

where

$$u=\frac{1}{2r}\frac{\partial\psi}{\partial z} \tag{A.3a}$$

$$v=-\frac{1}{2r}\frac{\partial\psi}{\partial r} \tag{A.3b}$$

Where, r and z are the coordinate of radial and axial direction, respectively. u and v are the velocity components in r- and z-direction. ω is vorticity and ψ is stream function. And the operator is given as:

$$E^2\equiv\left[\frac{\partial^2}{\partial r^2}-\frac{1}{r}\frac{\partial}{\partial r}+\frac{\partial^2}{\partial z^2}\right]$$

Boundary conditions are

$$\begin{aligned}
&\psi=0 && \textit{on the stagnation plane and along the } z\textit{-axis},\\
&\psi=1 && \textit{along the flange surface},\\
&\frac{\partial\psi}{\partial r}=0 && \textit{along the inlet and outlet.}
\end{aligned} \tag{A.4}$$

The origin of cylindrical coordinate system was fixed to the stagnation point and Equations (A.1), (A.2), and (A.3) were solved in the domain for different shapes of the boundary which means the different flange shapes. Finite different method was

employed for these numerical calculations. For the calculation, body fitted coordinate system (Thompson, Thomas & Mastin, 1974; Thompson, Warsi & Mastin, 1982; Anderson, Tannahil & Pletcher, 1984) was adopted. This body fitted coordinate system is very useful to transform various shape of the flange to the rectangular plane in calculation coordinate system. This transformation improves accuracy of calculation along the boundaries, and hence reduces experimental trials.

There arises in all fields concerned with the numerical solution to partial differential equations the need for accurate numerical representation of boundary conditions. Such representation is best accomplished when the boundary is such that it is coincident with some coordinate line, for them the boundary may be made to pass through the points of a finite difference grid constructed on the coordinate lines. Finite difference expression at, and adjacent to, the boundary may then be applied using only grid points on the intersections of coordinate lines without the need for any interpolation between points of the grid. The avoidance of interpolation is particularly important to the boundaries with strong curvature or slope discontinuities, both of which are in physical applications for this calculations. Likewise, interpolation between grid points not coincident with the boundaries is particularly inaccurate with differential systems that produce large gradients in the vicinity of the boundaries, and the character of the solution may be significantly altered in such cases.

The coordinate system so generated is not necessarily orthogonal, orthogonality is not required, and its lack only requires that the partial differential system to be solved on the coordinate system when generated must be transformed directly through implicit partial differentiation rather than by use of the scale factors and differential operators developed for orthogonal curvilinear systems. Any orthogonal system can not be achieved with arbitrary spacing of the natural coordinate lines around the boundary, and the capability for such arbitrary spacing is of more importance than orthogonality.

Since the calculation was needed for the irregular shapes of flange boundaries, the irregular boundary shapes were transformed to the boundaries in the non-orthogonal coordinate system. The transformation form a quarter part of two dimensional physical plane (x,y) into the rectangular transformed plane (ξ,η) is shown in Figure A-1. The general transformation from the physical plane to the transformed plane is given:

$$\xi = \xi(x,y),$$

$$\eta = \eta(x,y).$$

Similarly, the inverse transformation is given by:

$$x = x(\xi,\eta),$$

$$y = y(\xi,\eta).$$

Derivatives are transformed as follows:

$$\frac{\partial f}{\partial x} = \frac{\dfrac{\partial(f,y)}{\partial(\xi,\eta)}}{\dfrac{\partial(x,y)}{\partial(\xi,\eta)}} = \frac{\left[\dfrac{\partial y}{\partial \eta}\right]\left[\dfrac{\partial f}{\partial \xi}\right] - \left[\dfrac{\partial y}{\partial \xi}\right]\left[\dfrac{\partial f}{\partial \eta}\right]}{J} \tag{A.5a}$$

$$\frac{\partial f}{\partial y} = \frac{\dfrac{\partial(x,f)}{\partial(\xi,\eta)}}{\dfrac{\partial(x,y)}{\partial(\xi,\eta)}} = \frac{-\left[\dfrac{\partial x}{\partial \eta}\right]\left[\dfrac{\partial f}{\partial \xi}\right] + \left[\dfrac{\partial x}{\partial \xi}\right]\left[\dfrac{\partial f}{\partial \eta}\right]}{J} \tag{A.5b}$$

where J is the Jacobian of the transformation,

$$J = \left[\frac{\partial x}{\partial \xi}\right]\left[\frac{\partial y}{\partial \eta}\right] - \left[\frac{\partial x}{\partial \eta}\right]\left[\frac{\partial y}{\partial \xi}\right]$$

Since the basic idea of the transformation is to generate transformation functions such that all boundaries are coincident with coordinate lines, the body fitted

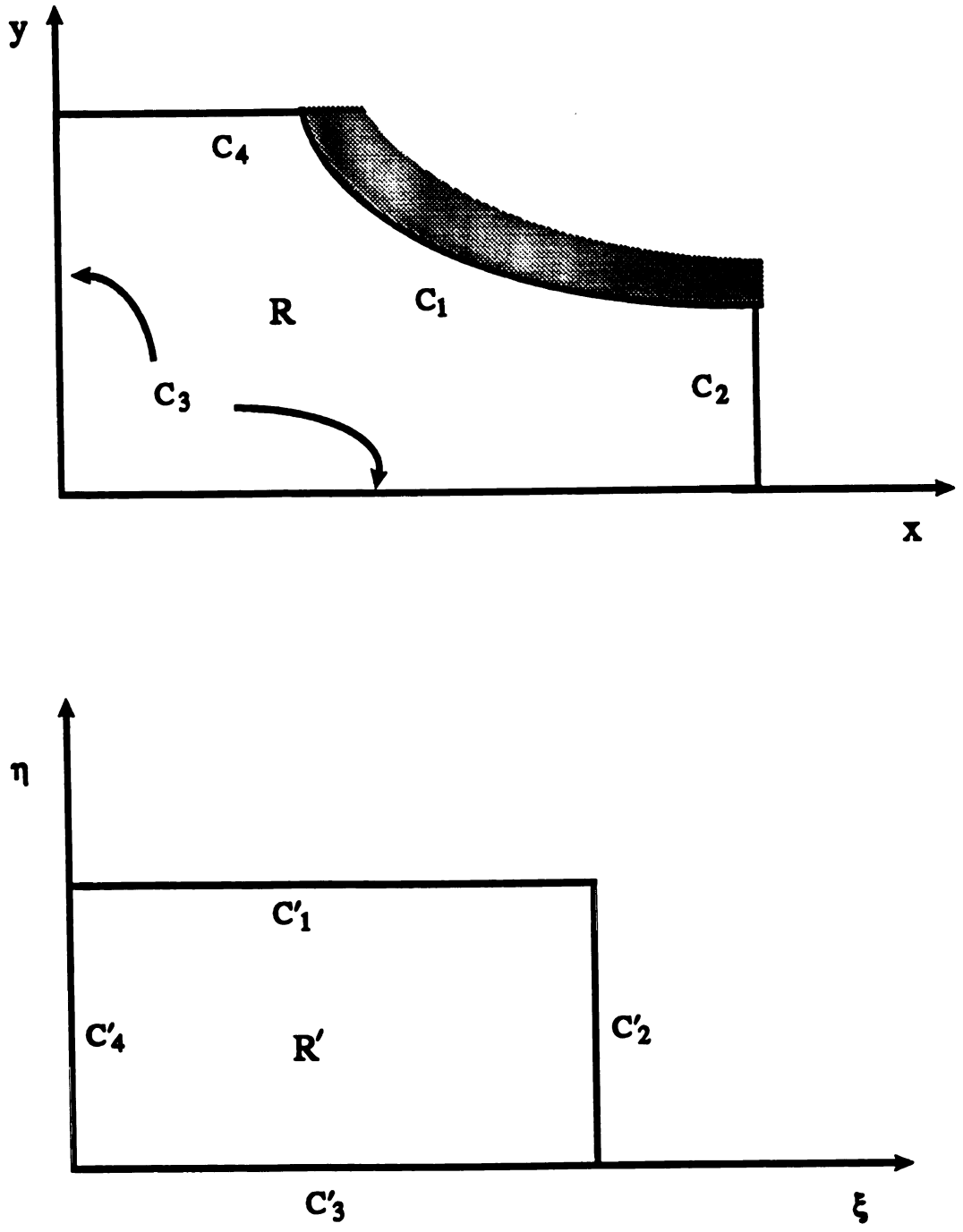

Figure A-1 Transformation of a quadrant of two-dimensional physical plane (x,y) to rectangular transformed plane (ξ,η). (a) Physical plane, (b) Transformed plane.

coordinates (ξ,η) are taken as solution of some suitable elliptic boundary value problem with one of these coordinate constant on the boundaries. To simplify the calculation for the present research, transformation was performed from Cartesian coordinate. Using Laplace's equation as the generating elliptic system, we have:

$$\frac{\partial^2 \xi}{\partial x^2} + \frac{\partial^2 \xi}{\partial y^2} = 0 \tag{A.6a}$$

$$\frac{\partial^2 \eta}{\partial x^2} + \frac{\partial^2 \eta}{\partial y^2} = 0 \tag{A.6b}$$

with Dirichlet boundary conditions,

$$\begin{aligned} \eta &= constant = \eta_1 \qquad on\ C'_1 \\ \eta &= constant = \eta_2 \qquad on\ C'_3 \end{aligned} \tag{A.7}$$

The right and left boundaries of the rectangular transformed plane, C'_4 and C'_2, are inlet and outlet in the physical plane.

To perform all numerical computation in rectangular transformed plane, it was necessary to interchange the dependent and independent variables in Equation (A.6). Applying Equation (A.5) to Equations (A.6) and (A.7) gave:

$$\alpha \frac{\partial^2 x}{\partial \xi^2} - 2\beta \frac{\partial^2 x}{\partial \xi \partial \eta} + \gamma \frac{\partial^2 x}{\partial \eta^2} = 0 \tag{A.8a}$$

$$\alpha \frac{\partial^2 y}{\partial \xi^2} - 2\beta \frac{\partial^2 y}{\partial \xi \partial \eta} + \gamma \frac{\partial^2 y}{\partial \eta^2} = 0 \tag{A.8b}$$

where

$$\alpha = \left[\frac{\partial x}{\partial \eta}\right]^2 + \left[\frac{\partial y}{\partial \eta}\right]^2 \tag{A.8c}$$

$$\beta = \left[\frac{\partial x}{\partial \xi}\right]\left[\frac{\partial x}{\partial \eta}\right] + \left[\frac{\partial y}{\partial \xi}\right]\left[\frac{\partial y}{\partial \eta}\right] \tag{A.8d}$$

$$\gamma = \left[\frac{\partial x}{\partial \xi}\right]^2 + \left[\frac{\partial y}{\partial \xi}\right]^2 \tag{A.8e}$$

with the transformed boundary conditions,

$$\begin{aligned} x &= f_1(\xi,\eta_1) \quad on\ C'_1 \\ y &= g_1(\xi,\eta_1) \quad on\ C'_1 \\ x &= f_2(\xi,\eta_2) \quad on\ C'_3 \\ y &= g_2(\xi,\eta_2) \quad on\ C'_3 \end{aligned} \tag{A.8f}$$

The results is a quasi-linear elliptic system with Dirichlet boundary conditions for the physical coordinates in the transformed plane. The differential equations of the system (A.8) are considerably more complicate than those equations presented in (A.6). However, the boundary conditions of Equations (A.8) are specified on straight boundaries, and the computation field is rectangular. That is, a problem having simple equations but complex boundary conditions was transformed to a problem having complex equations and simple boundary conditions.

For the stream function, the same transformation was applied, and it became:

$$\alpha\frac{\partial^2\psi}{\partial\xi^2} - 2\beta\frac{\partial^2\psi}{\partial\xi\partial\eta} + \gamma\frac{\partial^2\psi}{\partial\eta^2} = 0 \tag{A.9}$$

where α, β, and γ are given by Equations (A.8c), (A.8d), and (A.8e), and transformed boundary conditions were

$$\begin{aligned} \psi(\xi,\eta) &= 1 \qquad on\ \eta = \eta_1\ \ (i.e.,\ on\ C'_1) \\ \psi(\xi,\eta) &= 0 \qquad on\ \eta = \eta_3\ \ (i.e.,\ on\ C'_3) \end{aligned} \tag{A.10}$$

Equation (A.9) was approximated by using second-order, central differences for all derivatives, and the resulting difference equation was solved by accelerated Gauss-Seidel iteration on the rectangular transformed field.

Figure A-2 shows the generated grids in physical plane and computational plane. The calculations were completed for three different shapes, which are right angle, rounded corner, and rounded corner and inclined surface, and for three different burner gaps, which are 19 *mm*, 38 *mm*, and 50 *mm* with Reynolds number of 300, based on burner throat diameter.

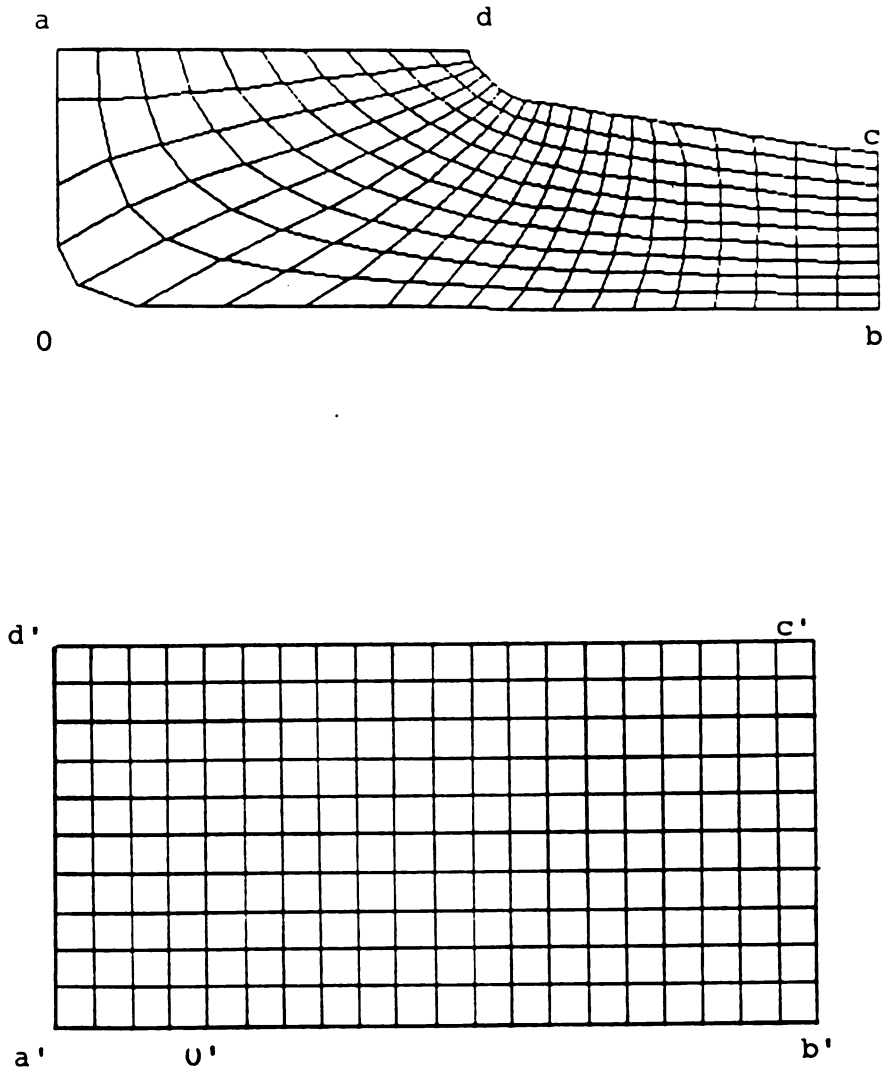

Figure A-2 The generated grids in physical plane and computational plane for rounded corner of the guide flange. (a) Grids in physical plane, (b) Grids in computational plane).

Figure A-3 shows the calculated streamlines in a single quadrant corresponding to burner gap of 19 *mm* for three different flange shapes. In these calculations, separation occurred only in case 1-1 (right angle case). Although separation is not clearly visible in this figure, it is obvious from the calculation.

For a larger burner gap of 38 *mm* the calculated streamlines show in Figure A-4. In this burner gap, the flow clearly separates for case 2-1 and 2-2. Separation did not occur for rounded and inclined surface flange.

Finally, Figure A-5 shows the calculated streamlines for the burner gap of 50 *mm*. For this burner gap separation occurs for all the cases. However, for case 3-3 the flow almost re-attaches at the end of flange.

A.3 Model Testing

A full-scale prototype Plexiglass burner model was built to obtain very low Reynolds number (based on the burner throat diameter) flows that correspond to the hot gas flow. A schematic of the experimental apparatus is shown in Figure A-6 in chapter 3. Water flows from two separate bottles into the upper and lower parts of the apparatus. The flow rate is controlled by flowing metered amounts of N_2 into the water bottles from a pressurized cylinder.

Figure A-7 shows the test section of this apparatus. The flange shapes were followed the shapes used for calculation. Dye was injected into the flow for flow visualization purpose. The various injection ports are also visible in this photograph. Timed photographs of dye particles were taken to determine the flow velocities. Different flange shapes as discussed in the numerical calculations have been examined. Reynolds number is varied by changing the flow velocity and the viscosity of water by adding sugar.

Most of the model experiments were conducted in 40% (by weight) sugar solution with viscosity which is five times larger than pure water. This was done to obtain

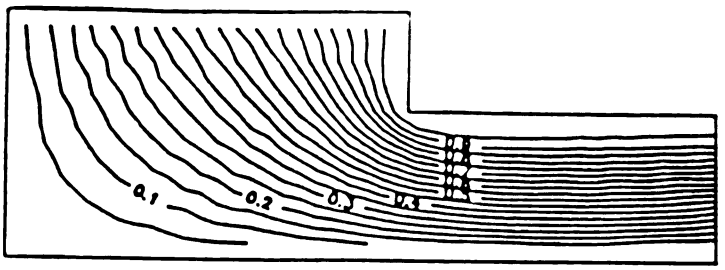

STREAMLINES case # 1-1 Re = 300
Gap = 3/4"
Rignt Angle

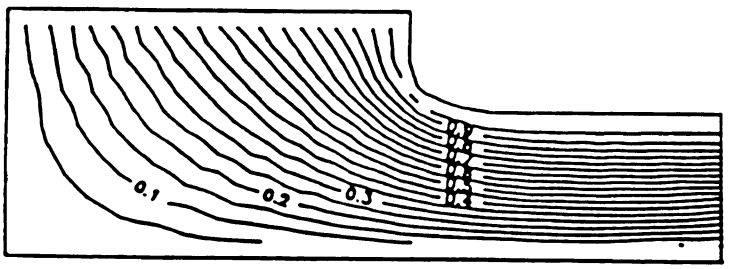

STREAMLINES case # 1-2 Re = 300
Gap = 3/4"
Round Corner

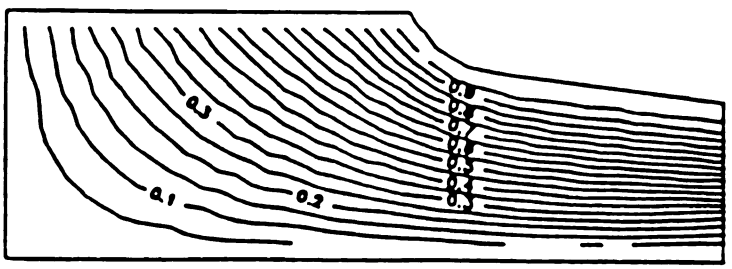

STREAMLINES case # 1-3 Re = 300
Gap = 3/4"
Round & Inclined

Figure A-3 Calculated streamlines for a burner gap of 19 mm (0.75 inches) of three different flange shapes (top : right angle corner, middle : round corner, bottom : round and incline corner).

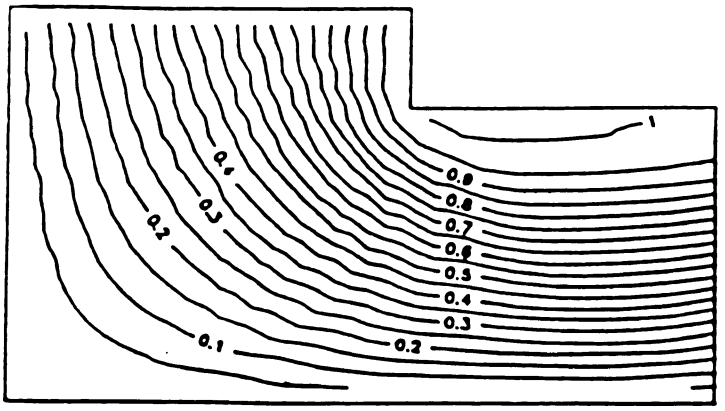

STREAMLINES case # 2-1 Re = 300
Gap = 1½"
Right Angle

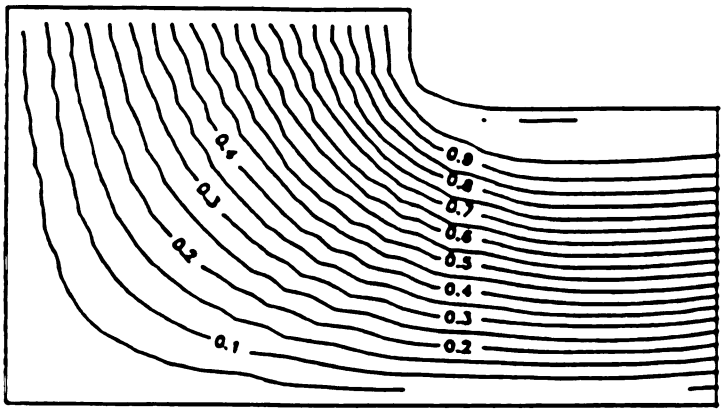

STREAMLINES case # 2-2 Re = 300
Gap = 1½"
Round Corner

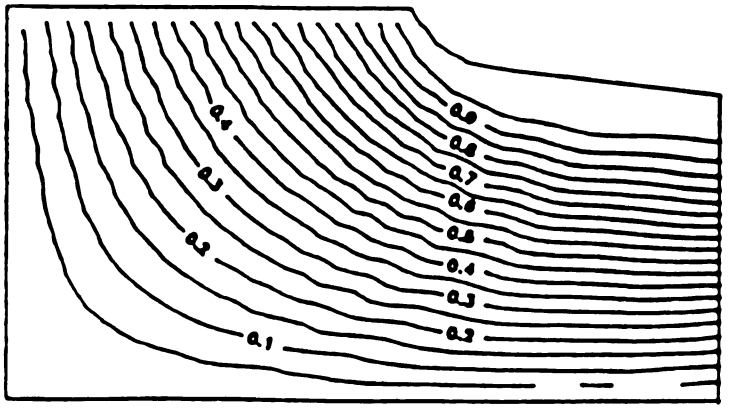

STREAMLINES case # 2-3 Re = 300
Gap = 1½"
Round & Inclined

Figure A-4 Calculated streamlines for a burner gap of 38 mm (1.50 inches) of three different flange shapes (top : right angle corner, middle : round corner, bottom : round and incline corner).

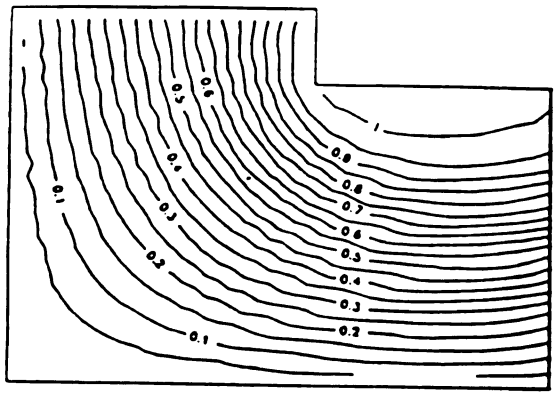

STREAMLIES case # 3-1 Re = 300
Gap = 2"
Right Angle

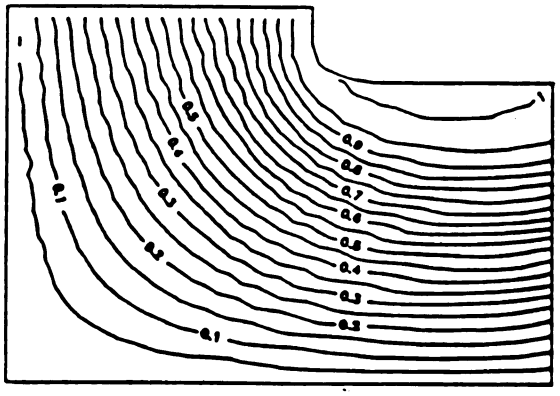

STREAMLINES case # 3-2 Re = 300
Gap = 2"
Round Corner

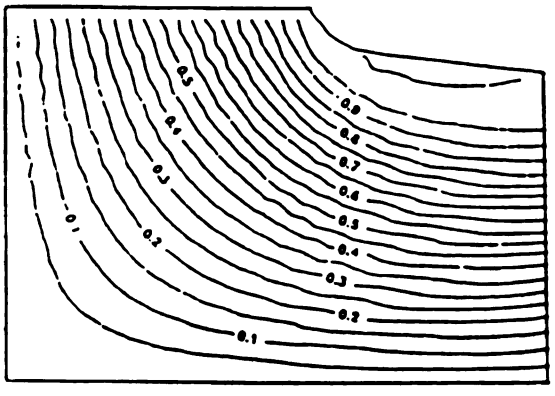

STREAMLINES case # 3-3 Re = 300
Gap = 2"
Round & Inclined

Figure A-5 Calculated streamlines for a burner gap of 50 mm (2.00 inches) of three different flange shapes (top : right angle corner, middle : round corner, bottom : round and incline corner).

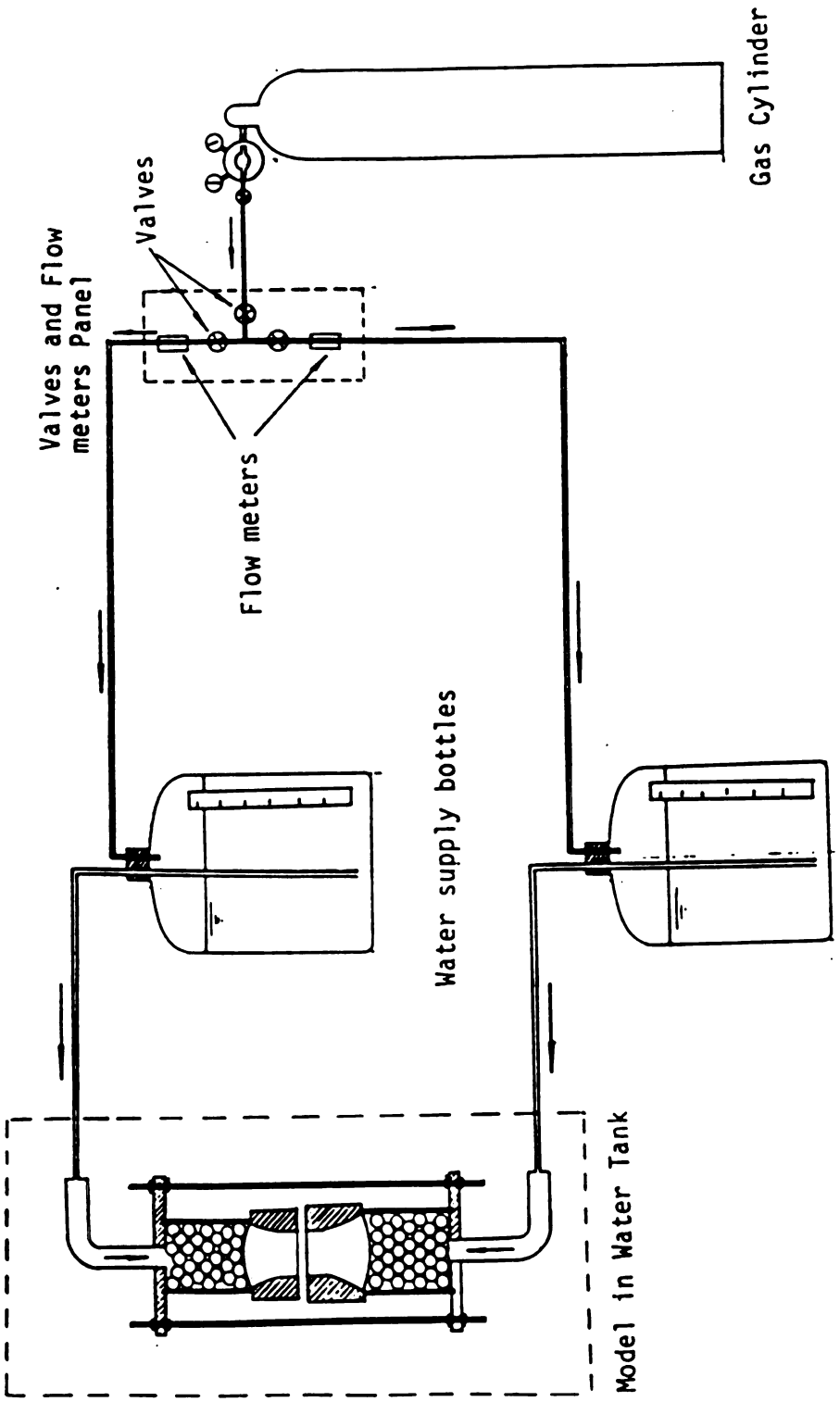

Figure A-6 Schematic of experimental apparatus for the guide flange model testing.

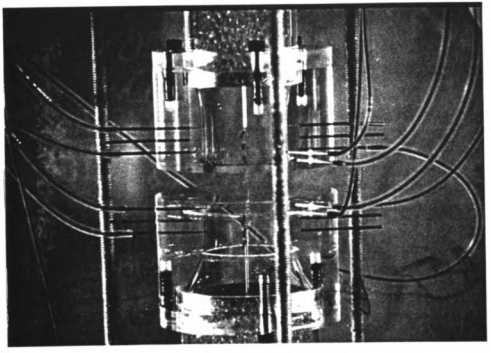

Figure A-7 Photograph of the apparatus used for guide flange model testing. All dye injection ports are visible.

very low Reynolds number flows that correspond to the hot gas flow in the observation area. The objective of these experiments was to determine the maximum permissible burner gap and minimum flow velocity for a given flange shape without flow separation at the boundaries. The burner gap was varied from 1.27 *cm* to 3.81 *cm* and the Reynolds number from 30 to 160. This corresponds to gas velocities in the actual burner from 3 to 12 *cm/sec*.

For 3.81 *cm* burner gap, separation was observed for all flow velocities (or Re_D) tested. This separation and the recirculation zone can be clearly seen in Figure A-8. The dye injected at the flange surface travels toward the throat and then turns around to join the rest of the fluid. The streaklines (or streamlines) at the center are also clearly visible. For 2.54 *cm* burners gap, separation occurred only at high velocities ($Re_D > 100$). For lower velocities separation did not occur, as can be clearly seen in Figure A-9 where the dye streakline exactly follows the flange contour. For burners gap less than 2.54 *cm* flow separation was not observed at all the flow velocities that were tested.

A.4 Strain Rate for Model Testing of Guide Flange Shape

Strain rates were calculated according to the invicid theory for stagnation point flow. By the definition of strain rate, ε:

$$\varepsilon = -\frac{1}{r}\frac{\partial V_r}{\partial r} \tag{A.11}$$

here for invicid flow, radial component of velocity, V_r is

$$V_r = ar. \tag{A.12}$$

Also, radial component of velocity along the stagnation plane can be expressed by

$$V_r = \frac{\partial r}{\partial t} \tag{A.13}$$

where t is a variable for time.

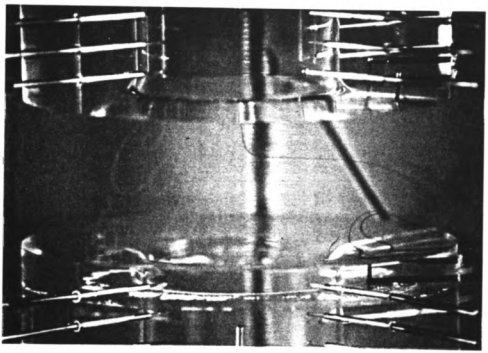

Figure A-8 Photograph showing flow separation and recirculation for 38.1 mm burner gap with round and incline corner flange shape.

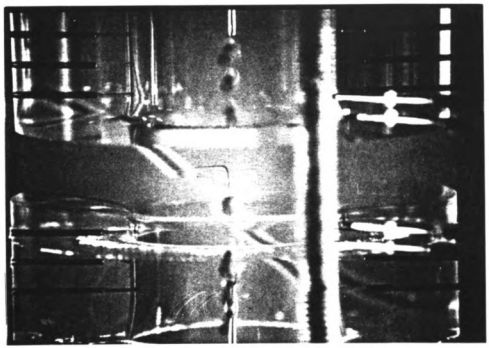

Figure A-9 Photograph showing no flow separation at low velocity for 25.4 mm burner gap with round and incline corner flange shape.

Then, one can get the relation between strain rate and the constant a along the stagnation plane, such as

$$\varepsilon = a = \frac{1}{t} \ln \frac{r}{r_0} \tag{A.14}$$

Let define a quantity y as $\ln \frac{r}{r_0}$. Then the correlation between the defined quantity y and time, t will be

$$y = \varepsilon t \tag{A.15}$$

So, the strain rate can be obtained from the slope of the graph which is plotted quantity y (actually, $\ln \frac{r}{r_0}$) vs. time.

A.5 Results and Conclusions

In addition to determining the flow separation, flow velocities were also measured by taking timed photographs of an expanding dye ring injected at the center. A photograph of such a ring is shown in Figure A-10. Since the dye was injected at the center of the nozzle, the ring is showing the stagnation plane. The stagnation plane shown by the dye is flat just as expected.

The radius of the sharp outer edge of the ring was measured as a function of time. These measurements are plotted on Figures A-11, A-12, and A-13 for 1.9 *cm*, 2.54 *cm* and 3.81 *cm* burners gaps, respectively and for different Reynolds numbers. It is evident that for a non-dimensional radius of about 5 (which corresponds to a physical dimension of 3.81 *cm*) a constant strain rate field is obtained. For a non-dimensional radius greater than 5, the data deviates from the ideal inviscid flow solution.

Figures A-14, A-15, and A-16 are replotted for same Reynolds number with different burner gaps. Figure A-14 shows that invicid theory valid within non-

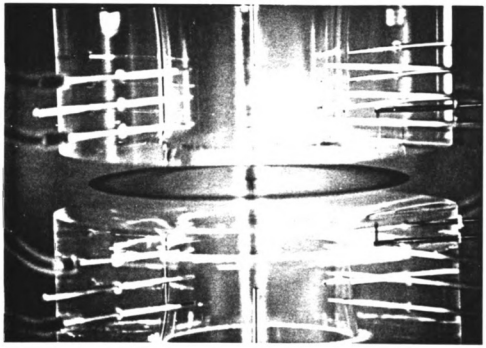

Figure A-10 Photograph of an expanding ring injected at center. This ring is expanding through stagnation point streamline.

dimensional radius about 5 for the Reynolds number 52.5. Increasing Reynolds number reduces the invicid theory valid range for all burners gaps. About 50 % increase in Reynolds number (Rd_D = 76.4) still has same radius of validity (see Figure A-15). For the Reynolds number 114.7, the radius of validity is about 3 which corresponds to a physical dimension of about 2.64 *cm*.

From these observation, one can conclude that;

(i) The range of ideal stagnation plane flow varies with Reynolds number.

(ii) Beyond this range the radial velocity decreases. So increase angle of inclined will be helpful to enlarge the valid range.

(iii) Physical valid range is large enough for given Reynolds numbers.

Thus, it was concluded for the burner design for the present research that a stable unseparated flow can be obtained for (i) burner gap of at about 2.54 *cm*; (ii) Reynolds number of about 30, which corresponds to a hot gas velocity of 3.0 *cm/sec*; and (iii) ideal inviscid flow regime extending over diameters as large as 7.62 *cm*.

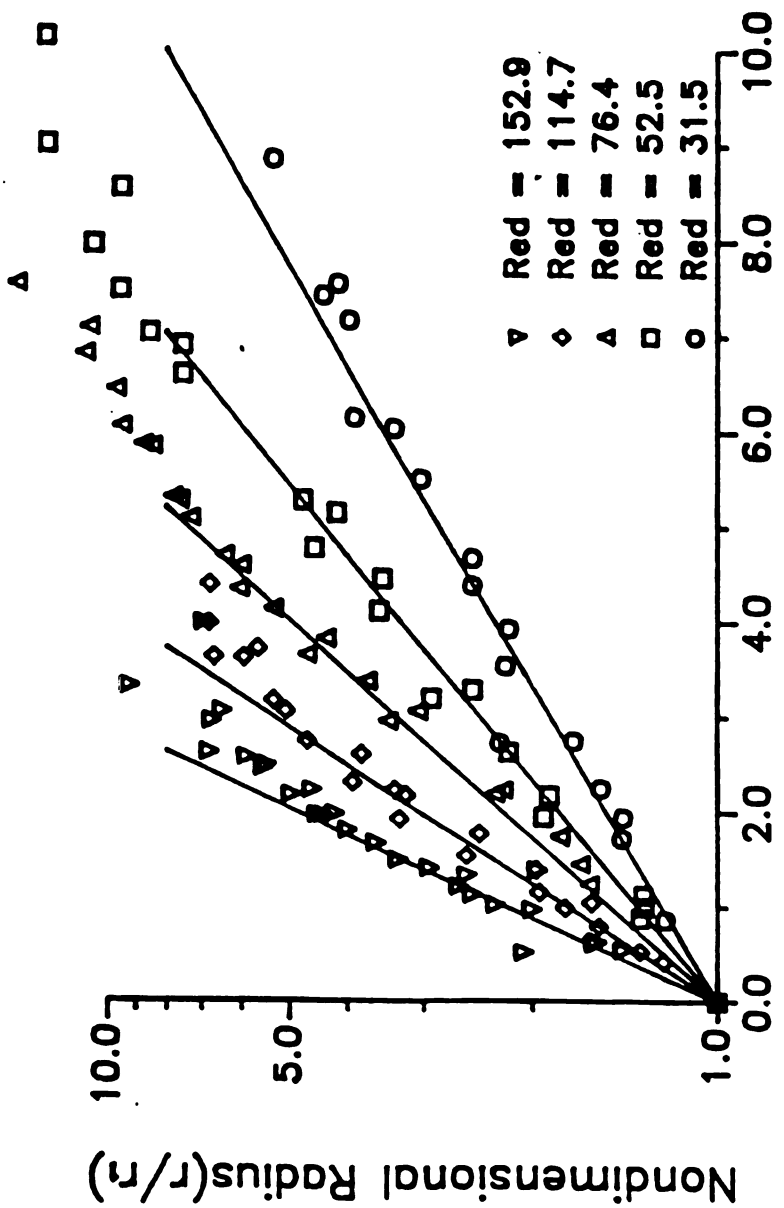

Figure A-11 Experimental results for various Reynolds numbers between 30 to 160 and obtained strain rates for 19 mm burner gap.

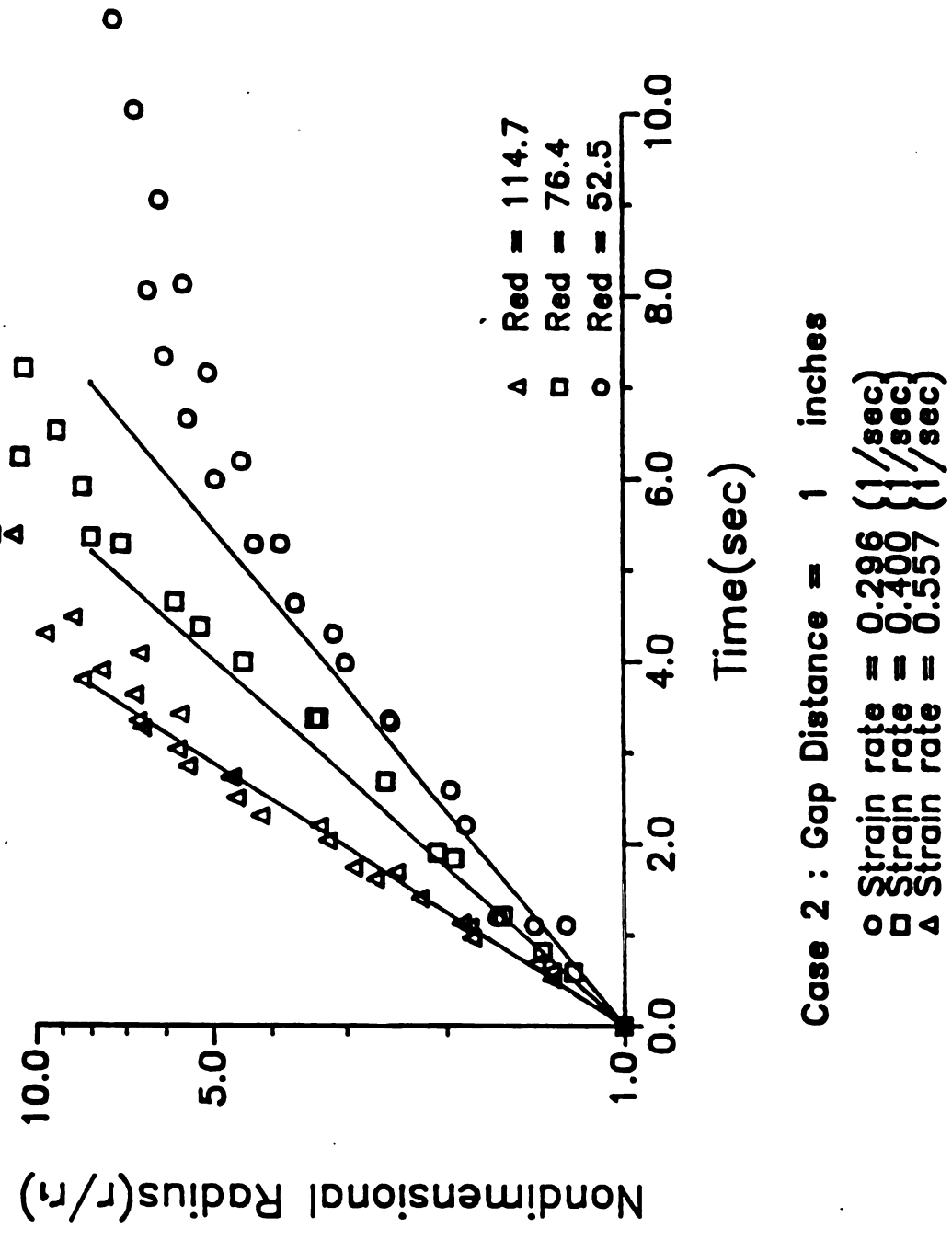

Figure A-12 Experimental results for Three Reynolds numbers (52.5, 76.4 and 114.7) and obtained strain rates for 25.4 mm burner gap.

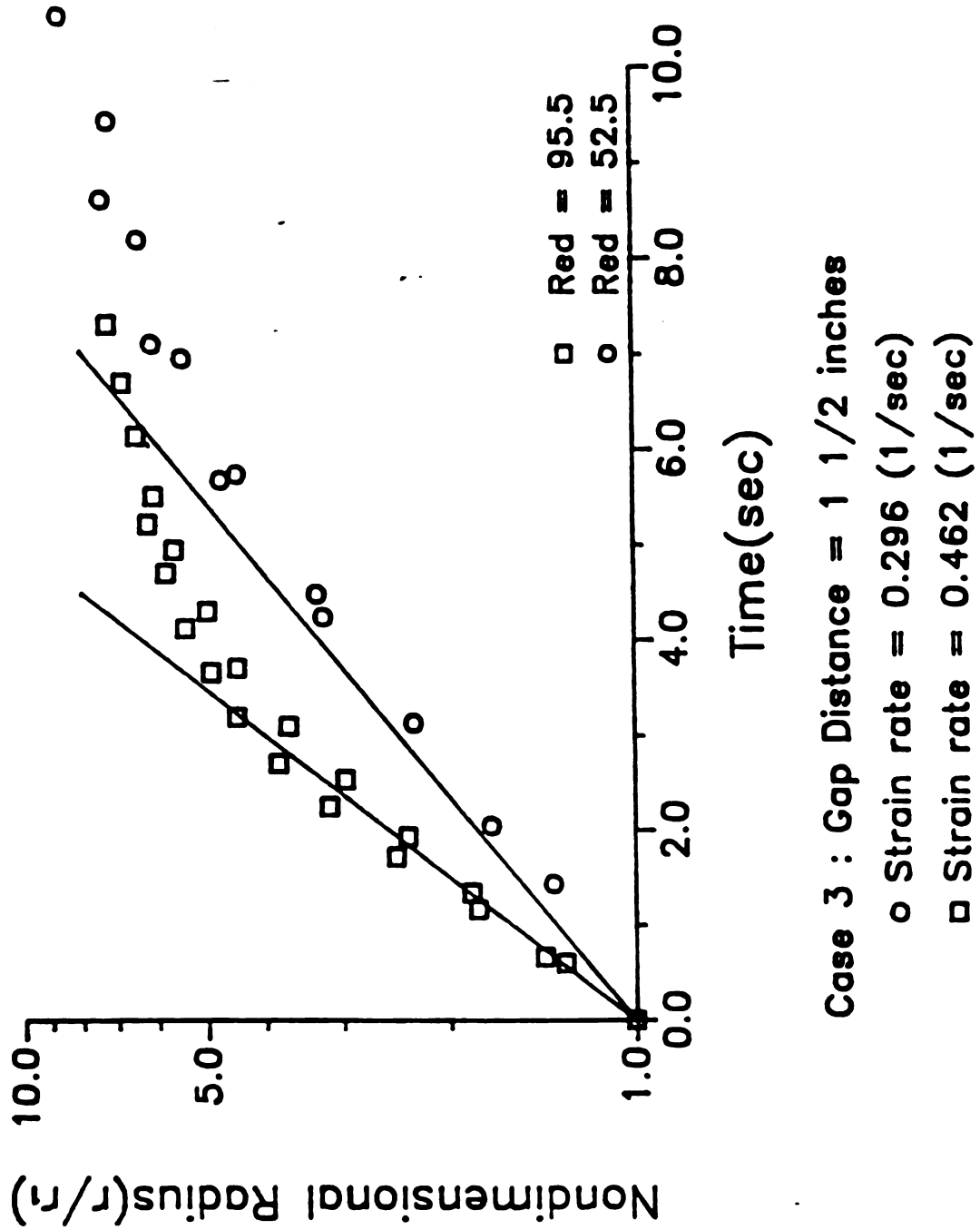

Figure A-13 Experimental results for two Reynolds numbers (52.5 and 95.5) and obtained strain rates for 38.1 mm burner gap.

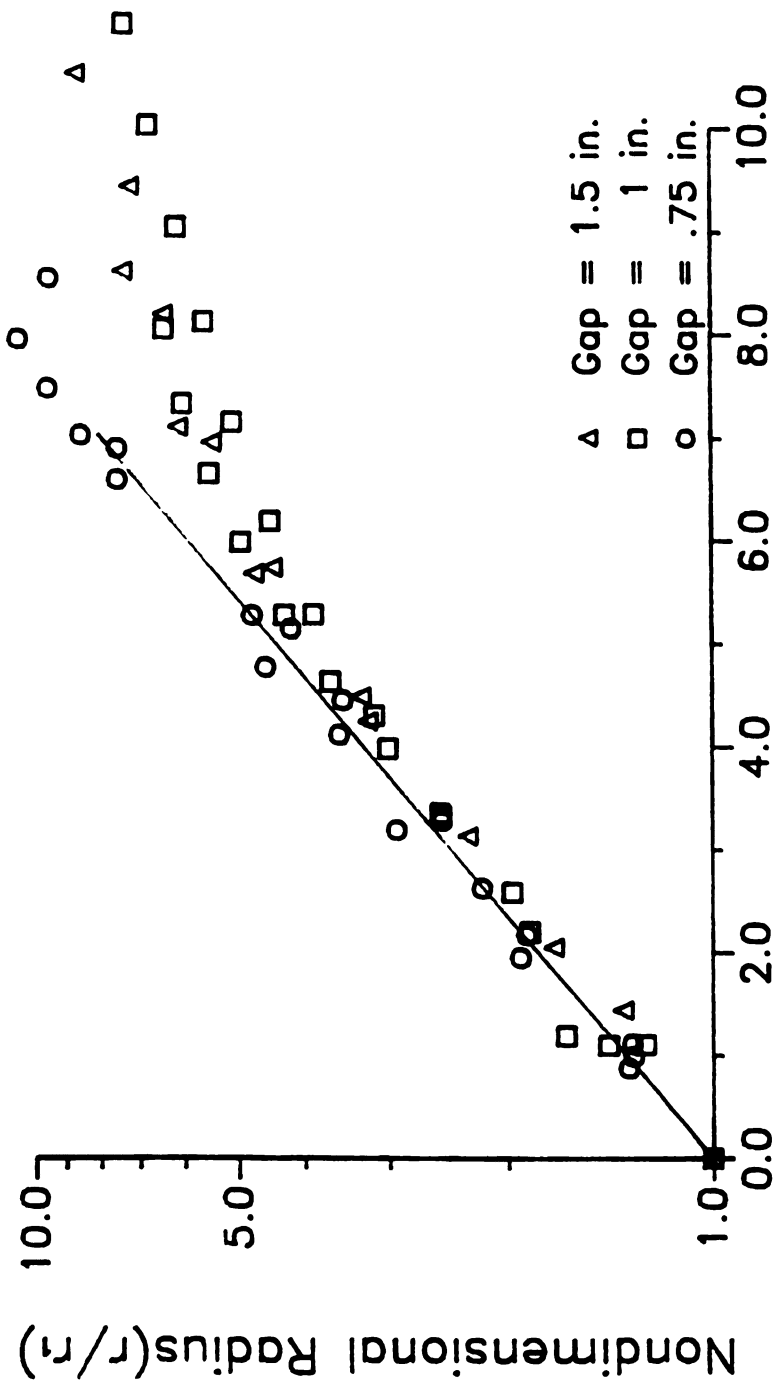

Figure A-14 Experimental results for same Reynolds number (52.5) with different burner gaps (19.0, 25.4 and 38.1 mm) and obtained strain rate (0.296/sec).

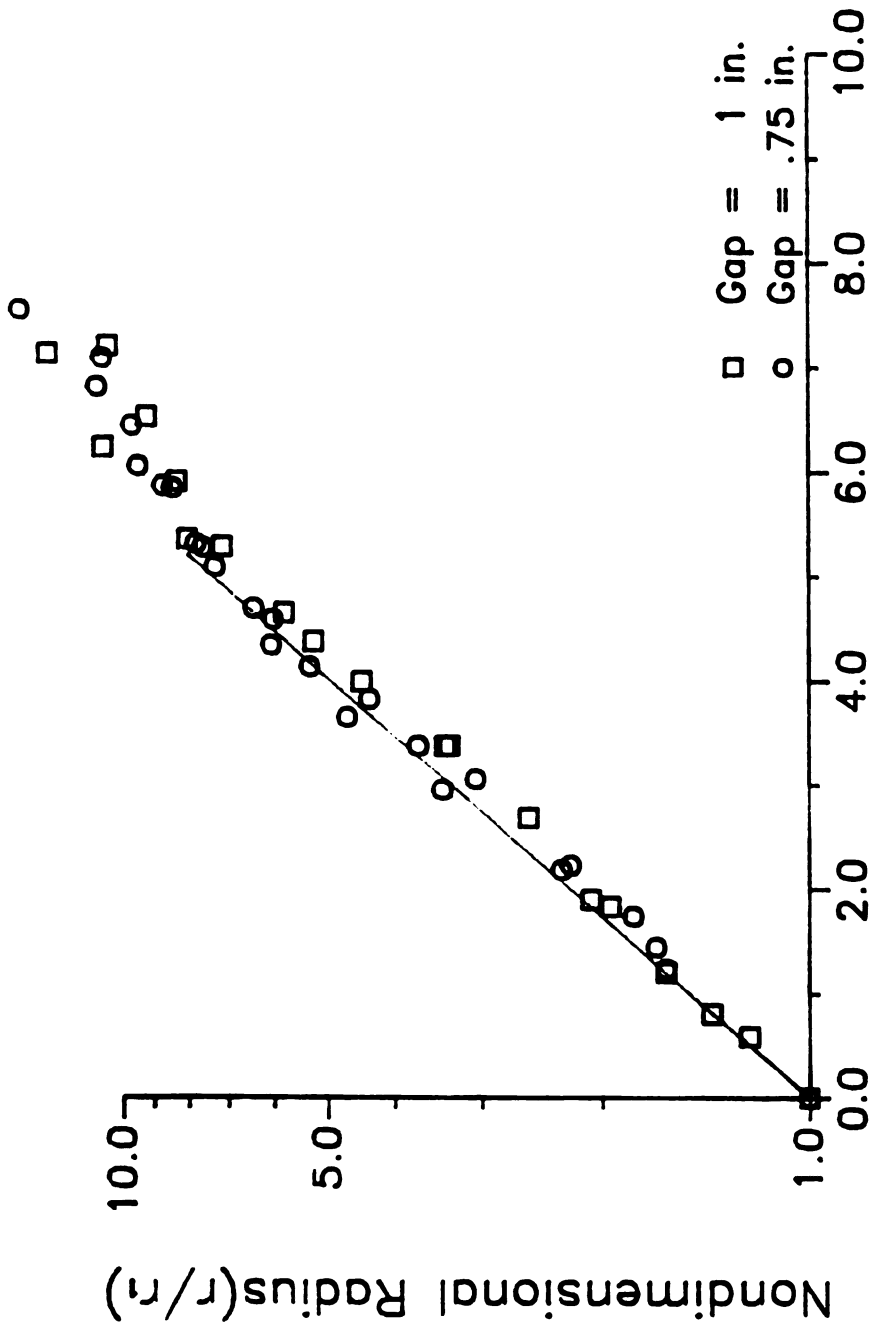

Figure A-15 Experimental results for same Reynolds number (76.4) with different burner gaps (19.0 and 25.4 mm) and obtained strain rate (0.400 /sec).

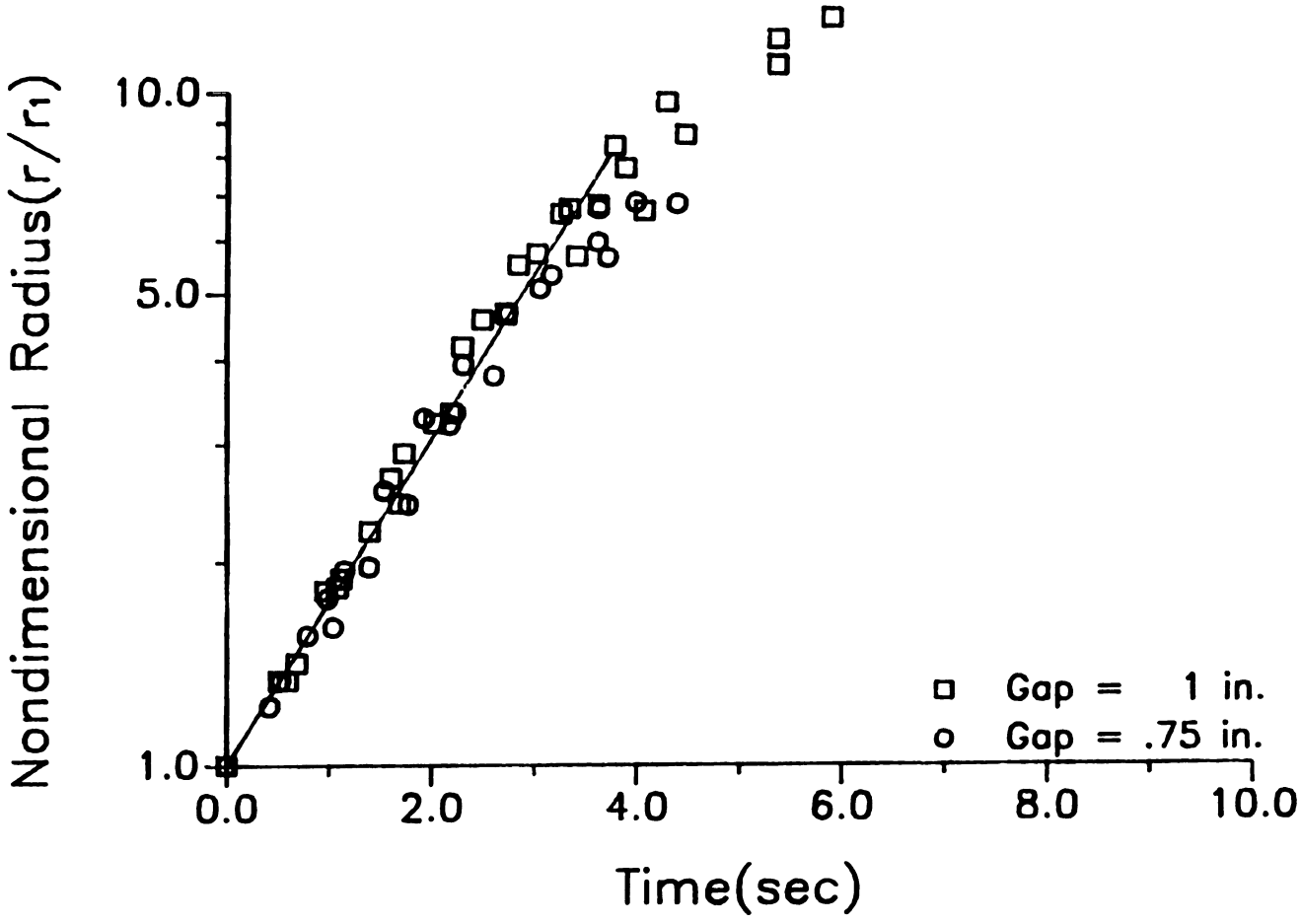

Figure A-16 Experimental results for same Reynolds number (114.7) with different burner gaps (19.0 and 25.4 mm) and obtained strain rate (0.557 /sec).

Appendix B

APPENDIX B: The Time Particle travels along Streamline

To verify the soot field in axisymmetric counterflow diffusion flame is one-dimensional, it is necessary to confirm that the particles travel the same distance in axial coordinat even along the different streamlines. If the distances in axial direction the particles traveled are different, the particles created at same location in axial coordinate may be in different location in axial coordinate after certain time period. Then the soot particles in axisymmetric counterflow diffusion flame which is established in stagnation point flow field are not in one-dimensional. So, the time a soot particles travels along streamline is investigated in Appendix B.

For the present study, two different cases were examined. First the particles in two-dimensional flow and then the particles in axisymetric counterflow were investigated.

B.1 The Particles in 2-D flow

The time period for a particle in flow to take to travel from one point to another, can be calculated by the defintion as:

$$t_{p_1, p_2} = \int_{p_1}^{p_2} \frac{ds}{V} \tag{B.1}$$

where, $t_{p_1 p_2}$ is time to travel form point p_1 to point p_2. The particle velocity is V and the distance is denoted by s.

In 2-D flow, the stream function can be written as:

$$\psi = Axy \tag{B.2}$$

where, ψ is stream function, A is constant.

Then the infinitismal distance ds can be written as:

$$ds = \left[(dx)^2 + (dy)^2 \right]^{\frac{1}{2}} \tag{B.3}$$

$$= \left[\left(\frac{dx}{dy} \right)^2 + 1 \right]^{\frac{1}{2}} dy$$

$$= \left[\left(-\frac{\psi}{A}\frac{1}{y^2} \right)^2 + 1 \right]^{\frac{1}{2}} dy$$

x- and y- components of velocity can be expressed by stream function as:

$$u = \frac{\partial \psi}{\partial y} = Ax \tag{B.4}$$

$$v = -\partial\frac{\psi}{\partial}x = -Ay \tag{B.5}$$

And, resultant velocity V is :

$$V = \sqrt{u^2 + v^2} = Ay\left[\left(\frac{\psi}{Ay^2} \right)^2 + 1^2 \right]^{\frac{1}{2}} \tag{B.6}$$

Apply Equationa (B.3) and (B.6) to Equation (B.1). Then:

$$t_{p_1 p_2} = \int_{p_1}^{p_2} \frac{ds}{V} \tag{B.7}$$

$$= \int_{p_1}^{p_2} \frac{\left[1 + \left(\frac{\psi}{A}\frac{1}{y^2} \right)^2 \right]^{\frac{1}{2}} dy}{Ay\left[\left(\frac{\psi}{ay^2} \right)^2 + 1 \right]^{\frac{1}{2}}}$$

$$= \frac{1}{A}\ln\left| y_{p2} - y_{p1} \right|$$

Equation (B.7) shows that the time a particle flows along streamline from one point to another depends only on the y-coordinate. So, it takes for soot particles

exactely same time to flow from y_1 to y_2. That is, only Δy affects to the time to flow.

B.2 Particles in Axisymmetric Counterflow

Stream function in axisymmetric counterflow is given by:

$$\psi = Ar^2 z \tag{B.8}$$

From the symmetry, the flow is independent from the ϕ-direction. So, the infinitismal distance ds can be written as:

$$ds = \left[\left[dr \right]^2 + \left[dz \right]^2\right]^{\frac{1}{2}} \tag{B.9}$$

$$= \left[\left[\frac{dr}{dz} \right]^2 + 1 \right]^{\frac{1}{2}} dz$$

Here,

$$\frac{dr}{dz} = \frac{d}{dz}\left[\sqrt{\frac{\psi}{Az}}\right] = -\frac{1}{2}\sqrt{\frac{\psi}{A}}\frac{1}{z\sqrt{z}}$$

So, ds becomes:

$$ds = \left[1 + \frac{\psi}{4AZ^3} \right]^{\frac{1}{2}} dz. \tag{B.10}$$

r- and z-components of velocities with stream function are:

$$u = \frac{1}{r}\frac{\partial \psi}{\partial z} = Ar$$

$$v = -\frac{1}{r}\frac{\partial \psi}{\partial r} = -2Az$$

The resultant velocity, V is:

$$V = \left[u^2 + v^2 \right]^{\frac{1}{2}} \tag{B.11}$$

$$= 2Az\left[1 + \frac{\Psi}{4Az^3}\right]^{\frac{1}{2}}$$

From the definition, Equation (B.1) the time period is:

$$t_{p1,p2} = \int_{p1}^{p2} \frac{ds}{V} \tag{B.12}$$

$$= \int_{p_1}^{p_2} \frac{\left[1 + \frac{\Psi}{4Az^3}\right]^{\frac{1}{2}} dz}{2Az\left[1 + \frac{\Psi}{4Az^3}\right]^{\frac{1}{2}}}$$

$$= \frac{1}{2A} \ln\left| z_2 - z_1 \right|$$

The calculation result for the axisymmetric counterflow case is exactly same as that of 2-D flow. This indicates that the time from one position to another in stagnation point flow depends only on the distance in axial coordinate.

Above two investigations show that the time period that a particle in stagntion point flow takes, to travel one point to another depends only on the change of altitude. This can be implies that the soot particles created at the same location in axial coordinate can reach exactly same axial location after traveling same time period. This expresses that the soot particles are in one-dimensional profiles in stagnation point flow.

Appendix C

APPENDIX C: Measuring Soot Particle Size by Dynamic Light Scattering

Soot particles were measured primarily by laser light scattering/extinction technique for the present study. In addition, soot particle size was measured by dynamic scattering measurement technique. The dynamic scattering theory and measurement result are explained in this Appendix C.

C.1 Theoretical Formulation

The intensity autocorrelation function for a suspension of Brownian diffusing particles can be written as:

$$< I(t)I(0) > = < I >^2 + A\exp\left[-2\Gamma t \right] \tag{C-1}$$

where the linewidth, Γ is given by:

$$\Gamma = |\ \mathbf{q}\ |^2 D_i \tag{C-2}$$

where D_i is the diffusion coefficient, A is a constant that depends on coherence of the scattered light on the PMT, and $\mathbf{q}$ is the scattered wave vector, which is given by

$$|\mathbf{q}| = \frac{4\pi m}{\lambda_0} \sin\frac{\theta}{2} \tag{C-3}$$

Here, m is the complex refractive index of the suspension, λ_0 is incident wavelength, and θ is the scattering angle.

Let us define the normalized intensity autocorrelation function as:

$$g^{(2)}(t) = \frac{1}{C_n} < I(t)I(0) > \tag{C-4}$$

Here, the normalization constant C_n is chosen so that $g^{(2)}(\infty) = 1$.

If a distribution of particle sizes is present, there is a corresponding distribution coefficients, or equivalently, a distribution of linewidths. Hence the correlation function can be written as:

$$g^{(2)}(t) = 1 + A\left| \int_0^\infty d\Gamma\, G(\Gamma) \exp(-\Gamma t) \right|^2 \tag{C-5}$$

Here, $G(\Gamma)d\Gamma$ is the fraction of the total intensity of light scattered from the particle between linewidth Γ and $\Gamma + d\Gamma$.

Before starting to explain the calculation methods, it is useful to define the diffusion coefficients. The diffusion coefficient D_i depends on the ratio of mean free path of the molecules l_m to the particle's diameter D. When $l_m/D \ll 1$, the particles are in the hydrodynamic regime, it can be given by the Stokes-Einstein diffusion constant,

$$D_{SE} = \frac{K_B T}{3\pi\eta D} \tag{C-6}$$

where K_B is the Boltzmann constant, T is the temperature, and η is the shear viscosity of the suspension. In the other extreme, $l_m/D \gg 1$, the particle is in the kinetic regime, and the diffusion coefficient is given by:

$$D_{CE} = \frac{3}{2\rho D^2}\left[\frac{m_p K_B T}{2\pi}\right]^{1/2} \tag{C-7}$$

where ρ is the mass density of the surrounding medium, and m_p is the particle mass. At intermediate value of l_m/D, an empirical relation which matches Equations (C-6) and (c-7) in the two limits is used to relate particle size to the particle diffusion coefficient:

$$D_i = \frac{K_B T}{3\pi\eta D}\left\{1 + \left[A_1 + A_2 \exp\left[-A_3 \frac{D}{l_m}\right]\right]\frac{l_m}{D}\right\} \tag{C-8}$$

where A_1, A_2, and A_3 are constants. Although it is an empirical equation, the correction factor shows the proper limiting forms: For $D \gg l_m$, correction factor becomes

1.0 and D_i approaches Equation (C-6), whereas for $D \ll l_m$, D_i approaches the form of the kinetic theory expression Equation(C-7).

Values of the constants A_1, A_2, and A_3 are based on experimental measurements of the drag on the small particles. Such measurements were made by Millikan and his students in their oil drop experiments carried out to determine the electric charge. A later compilation of the experimental data led to the following results: A_1 = 1.728, A_2 = 0.580, and A_3 = 0.625 (Lhuissier, Gouesbet, & Weill, 1989). Values for the diffusion coefficient and setting velocity of the soot particles in the flames can be calculated over the entire particle size range using Equation (C-8).

There are several methods to obtain the line width Γ which is used to calculate particle size by Equation (C-2) with diffusion coefficient by Equation (C-8). But here cumulant method was used for the present work.

Cumulants Method

Koppel (1972) proposed a cumulant technique as a method of analysis for polydisperse systems. From the definition of the average of measured quantities:

$$\int_0^\infty d\Gamma G(\Gamma) \exp\left[-\Gamma t \right] = < \exp\left[-\Gamma t \right] >. \tag{C-9}$$

Let

$$f(t) \equiv < \exp\left[-\Gamma t \right] > \tag{C-10}$$

And take the logarithm of both sides (C-10) and expand the right-hand side in a Taylor's series in t. This gives:

$$\ln f(t) = 1 + a_1 t + \frac{1}{2} a_2 t^2 + \frac{1}{3!} a_3 t^3 + \frac{1}{4!} a_4 t^4 + ... \tag{C-11}$$

Where

$$a_n = \left[(-1)^n \frac{d^n}{dt^n} f(t) \right]_{t=0}$$

is the n^{th} cummulant of $f(t)$. The explicit forms of the first few cumulants are:

$$a_1 = <\Gamma> \equiv <q^2 D>$$

$$a_2 = <(\Gamma - <\Gamma>)^2>$$

$$a_3 = <(\Gamma - <\Gamma>)^3>$$

$$a_4 = <(\Gamma - <\Gamma>)^4> - 3 a_2^2$$

Therefore, Equation (C-5) can be expressed by cumulant technique in the form of:

$$g^{(2)}(t) = 1 + A\left[\exp\left[\sum_{n=1}^{\infty} (-1)^n \frac{\mu_n}{n!} t^n \right] \right]^2 \qquad \text{(C-12)}$$

Here μ_n is the n^{th} cumulant, and the cumulants are related to moments of the scattered intensity distribution function. The first cumulant is the mean linewidth,

$$\mu_1 = <\Gamma> \qquad \text{(C-13)}$$

and second cumulant is the variance of the intensity distribution about the mean,

$$\mu_2 = <\Delta\Gamma^2> \qquad \text{(C-14)}$$

with $\Delta\Gamma = \Gamma - <\Gamma>$. Using the first two cumulants a polydispersity index can be defined as:

$$Q = \frac{\mu_2}{\mu_1^2} = \frac{<\Delta\Gamma^2>}{<\Gamma>^2} \qquad \text{(C-15)}$$

While the linewidth distribution $G(\Gamma)\, d\Gamma$ is in some sense a measure of polydispersity, it is most desirable to determine the actual size distribution $P(D)\, dD$. The distinction between these two distributions cannot be overemphasized.

Equation (C-12) can be linearized to polynomial to fit to a weighted least square technique. The function to be fit is:

$$\ln\left[g^{(2)}(\tau) - 1\right]^{1/2} = \ln A^{1/2} - \mu_1 \tau + \frac{\mu_2}{2!} \tau^2 - ..... \qquad \text{(C-15)}$$

μ_1, μ_2, and the value A can be obtained by using weighted least square method with this function and measured values.

C.2 Measurement Apparatus

Figure C.1 shows the schematic of the dynamic scattering measurement apparatus. Measurement appratus can be divided into two different systems. They are optical system and correlator. Optical system is apparatus to detect the signal of the particle fluctuation and correlator calculates the correlation among the detected signals.

For the optical system, it is desirable to achieve good special resolution while maintaining an appreciable signal level. This was accomplished by focusing the incident laser beam by focus lens. For the present study, the laser spot size at focal point is 0.15 *mm* in diameter. To increase desired signal, it is necessary to decrease the ratio of the area A, of the photocathode which is exposed to the scattered light, to the coherent area A_{coh}. Here, for the light scattering experiments, coherent area can be defined by:

$$A_{coh} = \frac{\lambda^2}{\Omega} \qquad \text{(C-16)}$$

Where λ is wavelength and Ω is the solid angle subtended by the scattering volume when viewed from the detector. For the present study, focus lens (200 mm focal length) and pin whole (0.7 mm in diameter) in front of focus lens were used. The ratio of this system is 0.48 which is sufficient to provide strong signal enough to detect.

The signals detected by the photomultiplier tube (PMT) are send to the correlator to be analyzed for the soot particle size. Correlator BI-2030AT from Brookhaven

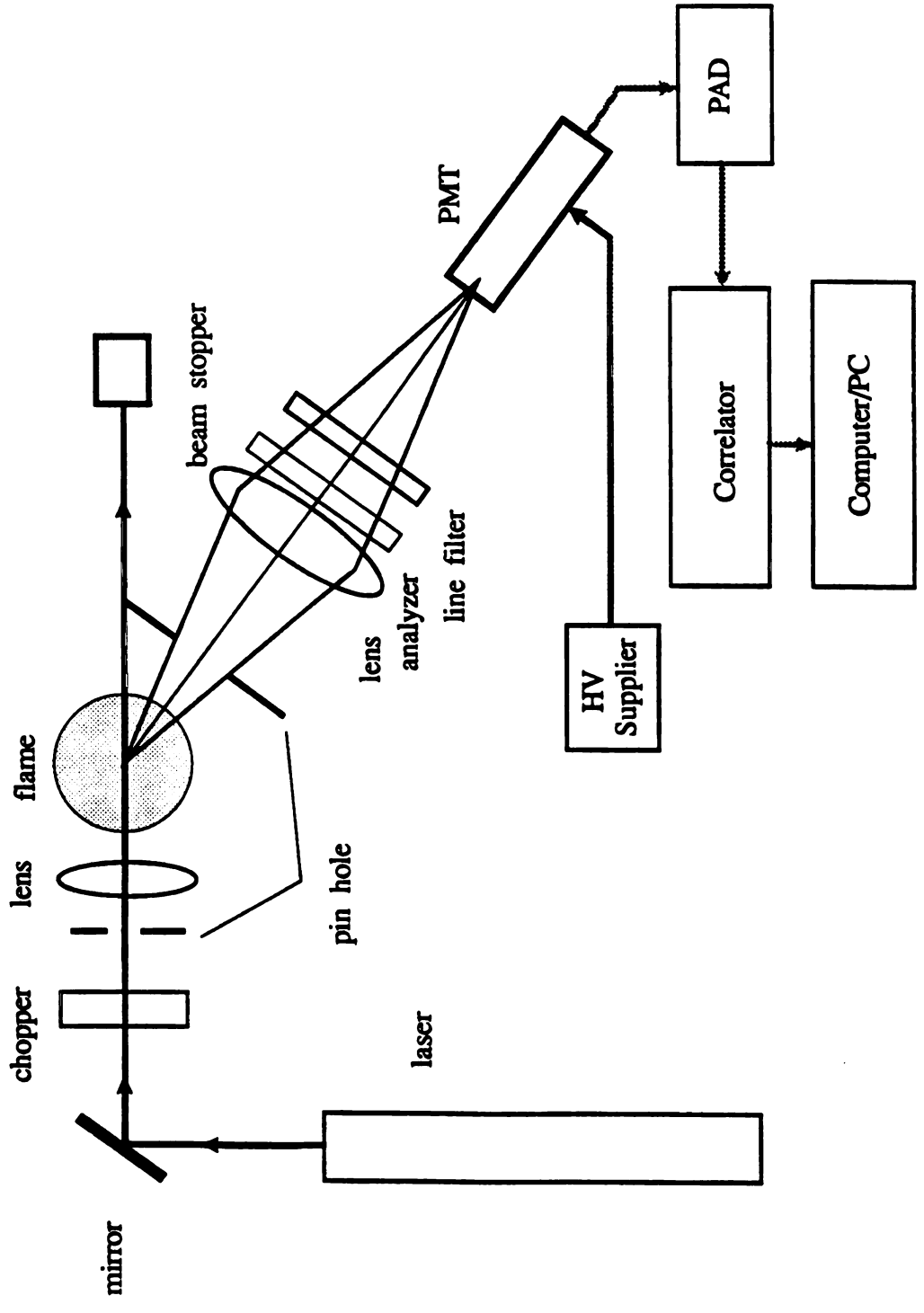

Figure C-1 Schematic of dynamic scattering measurement apparatus.
PAD : Pulse Amplifier Discriminator.

Instruments Corporation was installed. This BI-2030AT is an entirely digital, high speed, signal processor which can be used as an autocorrelator. It operates entirely in real-time and it incorporates an IBM-AT compatible computer.

The correlation function $g^{(2)}(t)$ in Equation (C-12) can be obtained form the digital signals the pulse rate n(t), which is proportional to the signal amplitude. Therefore, the correlation function can be written as:

$$g^{(2)}(j\Delta\tau) = \lim_{N\to\infty} \frac{1}{N} \sum_{i}^{N} 1 n_i n_{i-j}, \qquad j = 1, 2, 3, ..., M \tag{C-17}$$

Where, $\Delta\tau$ discrete time interval to count photons, the $j\Delta\tau$ is the time shift.

Figure C.2 is a simplified diagram of part of the correlator. The signals from the PMT are separated and synchronized with the sample time clock. The number of pulses, n_i is prescaled in the deadtime and derandomization circuitry. The randomized pulses are counted by the 4-bit counter. The value in 4-bit counter is entered into the first stage of a 4-bit shift register. Values already in the shift register are up by one stage. Thus after i^{th} sample periods, the j^{th} stage contains the value n_{i-j}, representing the history of the signal. During every sample period the number of pulses, n_i, applied to the input of channel B to be separated and derandomized in independent circuitry from channel A. Every sampling period the instantaneous value n_i is multiplied by the values in each of the multiplier shift registers, each one of these corresponding to a real-time. After N samples the contest of the j^{th} correlator channel will be

$$g'^{(2)}(j\Delta\tau) = \sum_{i=1}^{N} n_i n_{i-j} \tag{C-18}$$

If N is large enough then Equation (C-18) becomes Equation (C-17). For the present study the system has 136 data channels.

In addition to the data channels, there are 8 more channels to calculate baseline. These channels are accessed after 1024 sample periods by a 1024×4 delay shift register. The baseline are obtained based on the average values of the last 6 delay channels.

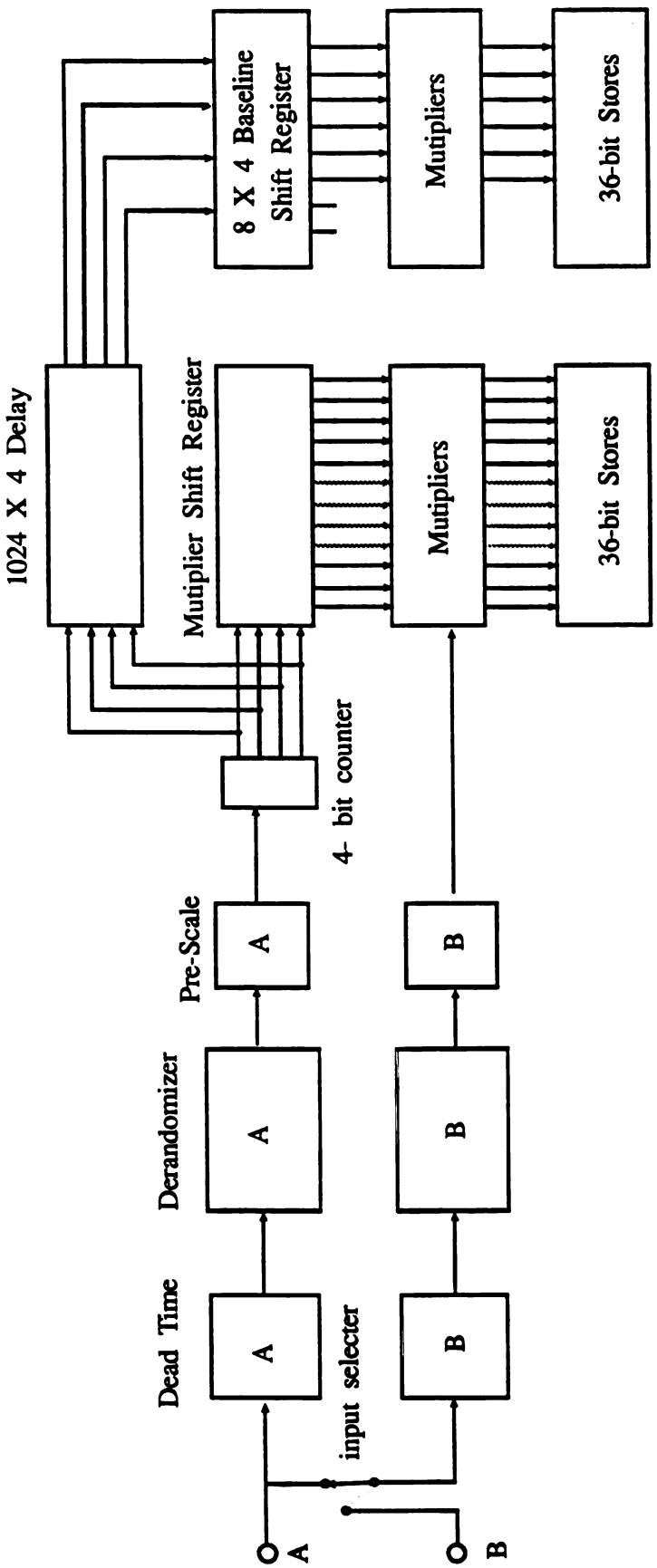

Figure C-2 Diagram of simplified operating principles of digital correlator. (from instruction manual).

If the contents of the last 6 channels are uniform which means sufficiently flat, then their average value is used to normalize the remaining channel contents.

C.3 Results and Discussion

The value for $g^{(2)}(t)$ from the correlator and Equation (C-15) gives line width, Γ. This Γ and wave vector **q** were used to calculate diffusion coefficient of the soot particle at the location of the scattering volume. Viscosity was calculated based on the measured chemistry concentration and temperature profiles. Soot particle sizes were calculated based on the diffusion coefficient corrected with Cunningham correction factor and Equation (C-2).

The particle sizes for each of the flames exhibit the same behavior. The particles decrease in size with distance from the stagnation plane. Table C.1 shows the soot particle sizes obtained from the dynamic scattering technique and from the classical scattering and extinction technique. The sizes from the dynamic scattering technique are always bigger as about twice as those from the scattering and extinction technique. The ratios are between 2.5 and 3.0 around the stagnation plane and between 1.9 and 2.5 when the particles are above the stagnation plane for 900 K flames. For 300 K flames the ratios are between 1.3 and 2.2. This shows that for the larger particles the ratio is larger than that for the smaller particles.

Measuring particle size smaller than 50 nm by the dynamic scattering technique was limited by the equipments. The correlator has limitation for the sampling time, τ. The shortest sampling time of the BI2030-AT is 0.1 μsec. For the particles smaller than the 50 nm, the exponential fits were decayed too fast. It almost looks like 90 ° turning.

From this limitation, it was hard to obtain the entire soot particle size profile across the flame, especially for the less sooty flames. So, the sets data from the dynamic scattering technique were used to check the soot particle sizes around the

Table C.1: Comparison of soot particle size measured by dynamic scattering and by extinction and scattering technique.

Flame	Location Zn	Diameter(nm) By dynamic.	Diameter(nm) By classic.	Ratio Dyn./Class.
BA	0.04	180.3	95.0	1.897
	0.09	124.3	76.6	1.622
	0.14	113.0	68.1	1.659
	0.19	116.2	63.6	1.827
	0.25	108.3	83.5	1.297
IA	0.00	127.5	74.5	1.710
	0.05	102.0	62.1	1.642
	0.10	107.6	55.9	1.926
	0.15	91.1	50.2	1.813
	0.20	97.8	44.0	2.223
MA	0.04	119.4	55.0	2.172
BB	0.00	181.4	88.9	2.041
	0.00	239.9	88.9	2.699
	0.04	208.5	89.9	2.319
	0.07	179.4	84.2	2.130
	0.11	166.4	81.2	2.050
	0.14	149.0	76.1	1.957
	0.18	148.3	71.5	2.075
	0.21	145.4	66.1	2.200
	0.25	127.8	63.8	2.003
	0.28	118.1	58.9	2.005
	0.32	112.6	54.5	2.066
	0.35	103.3	48.9	2.115
IBF	0.02	239.4	87.5	2.736
	0.05	199.2	83.4	2.388
	0.05	202.7	83.4	2.430
	0.05	202.7	83.4	2.430
	0.09	180.6	78.1	2.314
	0.12	160.7	73.4	2.189
	0.12	159.4	73.4	2.171
	0.12	164.1	73.4	2.235
	0.16	112.2	68.7	1.633
	0.16	128.4	68.7	1.868
	0.16	127.4	68.7	1.853
MBF	0.03	244.7	78.3	3.125
	0.07	190.5	74.5	2.556
	0.10	174.2	69.5	2.506
	0.10	167.8	69.5	2.414
	0.12	151.6	67.1	2.260
	0.12	148.9	67.1	2.220
	0.14	126.9	65.4	1.941
	0.14	127.7	65.4	1.952

stagnation plane. The soot particle size profile of entire range for for each flame was decided by using laser light scattering and extinction technique.

Appendix D

Table D.1: The comparison of temperatures corrected and measured by thermocouple for BA-flame in the sooting zone. (Zn = 0.0 ; stagnation plane, Zn = 1.0 Flame location.)

unit : Kelvin

Zn	T(corr.)	T(uncorr.)	Diff.
0.000	1,309.3	1,220.1	89.2
0.016	1,320.1	1,229.3	90.8
0.032	1,331.0	1,238.6	92.4
0.048	1,341.9	1,247.9	94.0
0.065	1,353.1	1,257.4	95.7
0.081	1,364.4	1,267.0	97.4
0.097	1,375.8	1,276.7	99.1
0.113	1,387.4	1,286.5	100.9
0.129	1,398.7	1,296.2	102.6
0.145	1,410.0	1,305.7	104.3
0.161	1,420.8	1,314.9	105.9
0.177	1,431.2	1,323.7	107.5
0.194	1,441.4	1,332.4	109.0
0.210	1,451.5	1,340.9	110.6
0.226	1,461.7	1,349.6	112.1
0.242	1,472.0	1,358.3	113.7
0.258	1,482.5	1,367.2	115.3
0.274	1,493.1	1,376.2	116.9
0.290	1,504.0	1,385.5	118.6
0.306	1,515.3	1,395.0	120.3
0.323	1,526.9	1,404.9	122.0
0.339	1,538.8	1,415.0	123.8
0.355	1,550.6	1,424.9	125.6
0.371	1,562.3	1,434.9	127.4
0.387	1,573.5	1,444.4	129.1
0.403	1,585.5	1,454.6	130.9
0.419	1,597.6	1,464.9	132.7
0.435	1,610.4	1,475.7	134.6
0.452	1,622.8	1,486.3	136.5
0.468	1,634.9	1,496.6	138.3
0.484	1,646.4	1,506.4	140.0
0.500	1,657.0	1,515.5	141.5
0.516	1,667.0	1,524.0	143.0
0.532	1,676.8	1,532.3	144.4
0.548	1,687.2	1,541.3	145.9
0.565	1,699.2	1,551.5	147.7
0.581	1,712.2	1,562.6	149.5
0.597	1,726.5	1,574.9	151.6
0.613	1,740.3	1,586.7	153.5
0.629	1,753.9	1,598.5	155.4
0.645	1,766.1	1,609.0	157.1
0.661	1,777.4	1,618.7	158.7
0.677	1,787.6	1,627.5	160.1
0.694	1,797.0	1,635.6	161.4
0.710	1,806.3	1,643.7	162.6

Table D.1 : Continued

Zn	T(corr.)	T(uncorr.)	Diff.
0.726	1,815.8	1,651.8	163.9
0.742	1,825.5	1,660.3	165.2
0.758	1,835.2	1,668.7	166.5
0.774	1,845.3	1,677.4	167.8
0.790	1,855.7	1,686.5	169.2
0.806	1,867.0	1,696.4	170.6
0.823	1,878.3	1,706.2	172.1
0.839	1,889.0	1,715.6	173.4
0.855	1,899.5	1,724.8	174.7
0.871	1,908.1	1,732.3	175.8
0.887	1,918.1	1,741.1	177.0
0.903	1,930.5	1,752.0	178.5
0.919	1,955.7	1,774.3	181.4
0.935	1,960.5	1,778.6	182.0
0.952	1,962.9	1,780.7	182.2
0.968	1,969.4	1,786.4	183.0
0.984	1,973.7	1,790.2	183.5
1.000	1,974.9	1,791.3	183.6

Table D.2: The comparison of temperatures corrected and measured by thermocouple for IA-flame in the sooting zone. (Zn = 0.0 ; stagnation plane, Zn = 1.0 Flame location.)

unit : Kelvin

Zn	T(corr.)	T(uncorr.)	Diff.
0.000	1,283.8	1,198.4	85.4
0.016	1,295.3	1,208.2	87.1
0.032	1,306.5	1,217.7	88.8
0.048	1,317.3	1,227.0	90.4
0.065	1,327.8	1,235.8	91.9
0.081	1,338.0	1,244.6	93.4
0.097	1,348.0	1,253.1	94.9
0.113	1,358.3	1,261.8	96.5
0.129	1,369.1	1,271.0	98.1
0.145	1,380.4	1,280.6	99.8
0.161	1,392.2	1,290.6	101.6
0.177	1,404.1	1,300.7	103.4
0.194	1,415.8	1,310.6	105.1
0.210	1,426.9	1,320.1	106.8
0.226	1,437.6	1,329.2	108.5
0.242	1,448.5	1,338.4	110.1
0.258	1,459.6	1,347.8	111.8
0.274	1,471.5	1,357.9	113.6
0.290	1,484.0	1,368.5	115.5
0.306	1,496.9	1,379.4	117.5
0.323	1,509.9	1,390.5	119.5
0.339	1,519.3	1,398.4	120.9
0.355	1,531.1	1,408.4	122.7
0.371	1,540.9	1,416.8	124.2
0.387	1,552.5	1,426.6	125.9
0.403	1,566.5	1,438.5	128.0
0.419	1,576.7	1,447.2	129.6
0.435	1,591.4	1,459.6	131.8
0.452	1,606.4	1,472.4	134.0
0.468	1,617.5	1,481.8	135.7
0.484	1,628.9	1,491.5	137.4
0.500	1,640.5	1,501.4	139.1
0.516	1,652.3	1,511.4	140.8
0.532	1,664.0	1,521.4	142.5
0.548	1,675.5	1,531.2	144.2
0.565	1,686.7	1,540.8	145.9
0.581	1,697.6	1,550.2	147.4
0.597	1,708.1	1,559.2	149.0
0.613	1,718.4	1,568.0	150.4
0.629	1,728.5	1,576.6	151.9
0.645	1,738.4	1,585.1	153.3
0.661	1,748.2	1,593.5	154.6
0.677	1,757.9	1,601.9	156.0
0.694	1,767.7	1,610.4	157.4

Table D.2 : Continued

Zn	T(corr.)	T(uncorr.)	Diff.
0.710	1,777.5	1,618.8	158.7
0.726	1,787.5	1,627.4	160.1
0.742	1,797.8	1,636.3	161.5
0.758	1,808.5	1,645.6	162.9
0.774	1,819.3	1,654.9	164.4
0.790	1,830.2	1,664.4	165.8
0.806	1,841.2	1,673.9	167.3
0.823	1,852.1	1,683.4	168.7
0.839	1,863.3	1,693.2	170.1
0.855	1,875.3	1,703.6	171.7
0.871	1,888.0	1,714.7	173.3
0.887	1,900.0	1,725.2	174.8
0.903	1,910.7	1,734.6	176.1
0.919	1,918.3	1,741.3	177.0
0.935	1,931.7	1,753.1	178.6
0.952	1,942.3	1,762.5	179.9
0.968	1,950.6	1,769.8	180.8
0.984	1,955.7	1,774.3	181.4
1.000	1,957.2	1,775.6	181.6

Table D.3: The comparison of temperatures corrected and measured by thermocouple for MA-flame in the sooting zone. (Zn = 0.0 ; stagnation plane, Zn = 1.0 Flame location.)

unit : Kelvin

Zn	T(corr.)	T(uncorr.)	Diff.
0.000	1,301.1	1,213.2	88.0
0.016	1,314.2	1,224.3	89.9
0.032	1,327.3	1,235.5	91.8
0.048	1,340.3	1,246.5	93.8
0.065	1,352.9	1,257.2	95.7
0.081	1,365.2	1,267.7	97.5
0.097	1,376.9	1,277.7	99.3
0.113	1,388.2	1,287.2	101.0
0.129	1,399.0	1,296.4	102.6
0.145	1,409.5	1,305.3	104.2
0.161	1,419.9	1,314.1	105.8
0.177	1,430.1	1,322.8	107.3
0.194	1,440.6	1,331.7	108.9
0.210	1,451.6	1,341.0	110.6
0.226	1,463.0	1,350.7	112.3
0.242	1,475.0	1,360.9	114.1
0.258	1,487.3	1,371.3	116.0
0.274	1,499.9	1,381.9	117.9
0.290	1,512.7	1,392.8	119.9
0.306	1,525.7	1,403.8	121.8
0.323	1,538.8	1,415.0	123.8
0.339	1,552.0	1,426.2	125.8
0.355	1,564.5	1,436.8	127.7
0.371	1,575.2	1,445.9	129.3
0.387	1,586.0	1,455.0	131.0
0.403	1,597.4	1,464.7	132.7
0.419	1,610.6	1,475.9	134.6
0.435	1,625.5	1,488.6	136.9
0.452	1,632.0	1,494.2	137.8
0.468	1,644.7	1,505.0	139.7
0.484	1,657.3	1,515.7	141.6
0.500	1,666.6	1,523.6	142.9
0.516	1,677.3	1,532.8	144.5
0.532	1,689.5	1,543.3	146.3
0.548	1,699.7	1,551.9	147.7
0.565	1,709.6	1,560.4	149.2
0.581	1,719.6	1,569.0	150.6
0.597	1,729.5	1,577.5	152.0
0.613	1,739.3	1,585.9	153.4
0.629	1,748.8	1,594.1	154.7
0.645	1,758.2	1,602.2	156.1
0.661	1,767.2	1,609.9	157.3
0.677	1,775.6	1,617.2	158.5
0.694	1,783.8	1,624.2	159.6

Table D.3 : Continued

Zn	T(corr.)	T(uncorr.)	Diff.
0.710	1,791.7	1,631.0	160.7
0.726	1,799.9	1,638.1	161.8
0.742	1,808.1	1,645.2	162.9
0.758	1,816.9	1,652.9	164.1
0.774	1,826.2	1,660.9	165.3
0.790	1,836.0	1,669.4	166.6
0.806	1,845.8	1,677.9	167.9
0.823	1,855.6	1,686.5	169.2
0.839	1,865.2	1,694.8	170.4
0.855	1,874.4	1,702.9	171.6
0.871	1,884.8	1,711.9	172.9
0.887	1,895.0	1,720.8	174.1
0.903	1,904.5	1,729.2	175.3
0.919	1,912.3	1,736.1	176.3
0.935	1,921.2	1,743.9	177.4
0.952	1,929.1	1,750.8	178.3
0.968	1,938.8	1,759.4	179.4
0.984	1,949.5	1,768.8	180.7
1.000	1,951.1	1,770.2	180.9

Table D.4: The comparison of temperatures corrected and measured by thermocouple for WAF-flame in the sooting zone. (Zn = 0.0 ; stagnation plane, Zn = 1.0 Flame location.)

unit : Kelvin

Zn	T(corr.)	T(uncorr.)	Diff.
0.007	1,336.0	1,245.4	90.6
0.015	1,341.7	1,250.2	91.5
0.023	1,347.3	1,255.0	92.3
0.031	1,352.9	1,259.7	93.2
0.040	1,364.2	1,269.3	94.9
0.050	1,370.5	1,274.7	95.9
0.059	1,376.9	1,280.1	96.9
0.067	1,383.3	1,285.5	97.8
0.074	1,390.1	1,291.2	98.9
0.082	1,396.4	1,296.6	99.9
0.091	1,402.5	1,301.7	100.8
0.098	1,407.7	1,306.1	101.6
0.106	1,413.0	1,310.6	102.4
0.114	1,422.7	1,318.8	103.9
0.124	1,432.5	1,327.1	105.4
0.131	1,437.8	1,331.5	106.2
0.140	1,442.6	1,335.7	107.0
0.149	1,447.9	1,340.1	107.8
0.157	1,453.2	1,344.6	108.6
0.168	1,464.8	1,354.4	110.4
0.176	1,469.7	1,358.5	111.2
0.185	1,474.6	1,362.7	111.9
0.193	1,479.9	1,367.1	112.7
0.202	1,491.1	1,376.7	114.5
0.217	1,497.5	1,382.1	115.5
0.226	1,502.8	1,386.5	116.3
0.233	1,514.8	1,396.7	118.1
0.242	1,520.0	1,401.1	118.9
0.250	1,524.9	1,405.2	119.7
0.266	1,531.3	1,410.6	120.7
0.273	1,537.3	1,415.7	121.6
0.281	1,543.7	1,421.1	122.6
0.290	1,549.7	1,426.2	123.5
0.299	1,556.1	1,431.6	124.5
0.306	1,561.7	1,436.4	125.3
0.314	1,566.6	1,440.5	126.1
0.322	1,572.6	1,445.6	127.0
0.330	1,578.2	1,450.4	127.9
0.342	1,589.1	1,459.6	129.5
0.351	1,594.7	1,464.3	130.4
0.359	1,600.0	1,468.8	131.2
0.367	1,604.8	1,472.9	131.9
0.375	1,609.7	1,477.1	132.6
0.383	1,614.9	1,481.5	133.4
0.391	1,620.2	1,485.9	134.2

Table D.4 : Continued

Zn	T(corr.)	T(uncorr.)	Diff.
0.401	1,633.6	1,497.4	136.3
0.411	1,639.2	1,502.1	137.1
0.420	1,644.5	1,506.6	137.9
0.437	1,650.1	1,511.4	138.7
0.444	1,655.3	1,515.8	139.5
0.460	1,660.5	1,520.3	140.3
0.467	1,666.5	1,525.3	141.2
0.475	1,671.7	1,529.8	141.9
0.483	1,676.9	1,534.2	142.7
0.491	1,681.8	1,538.4	143.4
0.500	1,687.4	1,543.1	144.2
0.508	1,693.0	1,547.9	145.1
0.519	1,700.0	1,553.9	146.1
0.541	1,713.8	1,565.7	148.1
0.549	1,718.6	1,569.8	148.8
0.567	1,723.8	1,574.3	149.5
0.576	1,728.6	1,578.4	150.2
0.584	1,734.2	1,583.2	151.0
0.593	1,739.8	1,587.9	151.8
0.602	1,744.9	1,592.4	152.6
0.610	1,749.8	1,596.5	153.2
0.626	1,754.9	1,601.0	154.0
0.635	1,760.5	1,605.7	154.8
0.644	1,766.4	1,610.8	155.6
0.653	1,771.6	1,615.3	156.3
0.662	1,776.4	1,619.4	157.0
0.670	1,781.5	1,623.8	157.7
0.678	1,786.3	1,628.0	158.4
0.687	1,791.1	1,632.1	159.0
0.696	1,796.3	1,636.5	159.7
0.712	1,802.2	1,641.6	160.6
0.721	1,807.3	1,646.1	161.3
0.729	1,812.5	1,650.5	162.0
0.740	1,818.4	1,655.6	162.8
0.748	1,823.1	1,659.7	163.4
0.767	1,829.0	1,664.8	164.2
0.776	1,834.5	1,669.6	164.9
0.785	1,839.3	1,673.7	165.5
0.800	1,845.1	1,678.8	166.3
0.809	1,849.9	1,682.9	166.9
0.817	1,854.6	1,687.1	167.6
0.825	1,860.1	1,691.8	168.3
0.833	1,865.2	1,696.3	168.9
0.842	1,870.7	1,701.0	169.7
0.850	1,875.8	1,705.5	170.3
0.860	1,880.9	1,709.9	171.0

Table D.4 : Continued

Zn	T(corr.)	T(uncorr.)	Diff.
0.870	1,885.6	1,714.1	171.6
0.895	1,890.3	1,718.2	172.2
0.903	1,895.1	1,722.3	172.7
0.919	1,900.9	1,727.4	173.5
0.927	1,904.5	1,730.6	173.9
0.934	1,908.1	1,733.8	174.4
0.950	1,910.7	1,736.0	174.7
0.957	1,915.4	1,740.1	175.3
0.965	1,918.6	1,743.0	175.7
0.972	1,919.7	1,743.9	175.8
0.987	1,920.4	1,744.6	175.9
1.000	1,920.4	1,744.6	175.9

Table D.5: The comparison of temperatures corrected and measured by thermocouple for WAO-flame in the sooting zone. (Zn = 0.0 ; stagnation plane, Zn = 1.0 Flame location.)

unit : Kelvin

Zn	T(corr.)	T(uncorr.)	Diff.
0.009	1,254.1	1,175.5	78.5
0.018	1,259.3	1,180.0	79.3
0.028	1,265.6	1,185.4	80.2
0.043	1,279.1	1,196.8	82.2
0.053	1,285.4	1,202.2	83.2
0.061	1,290.3	1,206.4	83.9
0.070	1,296.3	1,211.4	84.8
0.080	1,308.2	1,221.6	86.6
0.087	1,313.1	1,225.7	87.3
0.095	1,319.1	1,230.8	88.2
0.103	1,325.8	1,236.5	89.3
0.111	1,331.4	1,241.3	90.1
0.120	1,337.4	1,246.4	91.0
0.128	1,343.8	1,251.8	92.0
0.137	1,349.8	1,256.9	92.9
0.146	1,355.4	1,261.6	93.8
0.155	1,361.0	1,266.4	94.6
0.163	1,369.3	1,273.4	95.9
0.172	1,374.5	1,277.8	96.7
0.181	1,380.9	1,283.2	97.7
0.199	1,393.7	1,294.0	99.6
0.208	1,405.7	1,304.2	101.5
0.225	1,416.9	1,313.7	103.2
0.234	1,422.2	1,318.2	104.0
0.241	1,427.5	1,322.6	104.8
0.250	1,433.1	1,327.4	105.7
0.269	1,445.1	1,337.6	107.5
0.276	1,451.5	1,343.0	108.5
0.285	1,457.1	1,347.7	109.4
0.295	1,463.9	1,353.5	110.4
0.305	1,477.4	1,364.9	112.5
0.314	1,483.0	1,369.7	113.4
0.323	1,495.1	1,379.8	115.2
0.342	1,500.3	1,384.3	116.0
0.350	1,509.0	1,391.6	117.4
0.368	1,522.1	1,402.7	119.4
0.385	1,532.2	1,411.3	121.0
0.393	1,538.2	1,416.4	121.9
0.401	1,543.1	1,420.5	122.6
0.408	1,549.1	1,425.6	123.5
0.418	1,554.0	1,429.7	124.3
0.424	1,559.6	1,434.5	125.2
0.431	1,565.3	1,439.2	126.0
0.439	1,571.6	1,444.6	127.0
0.447	1,577.3	1,449.4	127.9

Table D.5 : Continued

Zn	T(corr.)	T(uncorr.)	Diff.
0.456	1,582.5	1,453.9	128.7
0.480	1,595.2	1,464.7	130.6
0.488	1,601.6	1,470.1	131.6
0.496	1,606.5	1,474.2	132.3
0.503	1,612.5	1,479.3	133.2
0.511	1,618.1	1,484.0	134.0
0.521	1,629.3	1,493.6	135.7
0.530	1,634.9	1,498.3	136.6
0.538	1,640.5	1,503.1	137.4
0.546	1,645.4	1,507.2	138.1
0.555	1,656.2	1,516.4	139.8
0.564	1,662.2	1,521.5	140.6
0.581	1,668.1	1,526.6	141.5
0.589	1,674.1	1,531.7	142.4
0.596	1,679.7	1,536.5	143.2
0.604	1,684.9	1,540.9	144.0
0.613	1,690.5	1,545.7	144.8
0.622	1,696.1	1,550.4	145.6
0.632	1,703.5	1,556.8	146.7
0.641	1,709.8	1,562.2	147.6
0.650	1,716.1	1,567.6	148.5
0.660	1,721.7	1,572.4	149.4
0.668	1,728.4	1,578.1	150.3
0.685	1,734.7	1,583.5	151.2
0.693	1,741.4	1,589.2	152.2
0.701	1,746.9	1,594.0	153.0
0.709	1,751.7	1,598.1	153.6
0.717	1,757.3	1,602.9	154.4
0.732	1,763.2	1,607.9	155.3
0.741	1,772.8	1,616.2	156.6
0.748	1,778.0	1,620.7	157.3
0.757	1,783.5	1,625.4	158.1
0.764	1,789.0	1,630.2	158.9
0.773	1,794.9	1,635.3	159.7
0.780	1,800.1	1,639.7	160.4
0.788	1,804.9	1,643.8	161.0
0.797	1,809.7	1,648.0	161.7
0.804	1,814.8	1,652.4	162.4
0.812	1,819.6	1,656.6	163.0
0.819	1,824.3	1,660.7	163.7
0.827	1,829.1	1,664.8	164.3
0.837	1,835.0	1,669.9	165.1
0.845	1,840.5	1,674.7	165.8
0.852	1,846.0	1,679.4	166.5
0.861	1,850.7	1,683.6	167.2
0.871	1,856.6	1,688.6	167.9

Table D.5: Continued

Zn	T(corr.)	T(uncorr.)	Diff.
0.880	1,862.4	1,693.7	168.7
0.889	1,867.9	1,698.5	169.4
0.897	1,873.0	1,702.9	170.1
0.905	1,879.9	1,709.0	170.9
0.912	1,879.9	1,709.0	170.9
0.922	1,884.7	1,713.1	171.5
0.929	1,888.6	1,716.6	172.0
0.936	1,893.7	1,721.1	172.7
0.943	1,893.7	1,721.1	172.7
0.951	1,898.5	1,725.2	173.3
0.958	1,905.4	1,731.2	174.1
0.965	1,909.0	1,734.4	174.6
0.972	1,913.3	1,738.2	175.1
0.982	1,915.1	1,739.8	175.3
0.986	1,915.5	1,740.1	175.4
1.000	1,915.9	1,740.4	175.4

Table D.6: The comparison of temperatures corrected and measured by thermocouple for BB-flame in the sooting zone. (Zn = 0.0 ; stagnation plane, Zn = 1.0 Flame location.)

unit : Kelvin

Zn	T(corr.)	T(uncorr.)	Diff.
0.009	1,128.0	1,084.4	43.6
0.021	1,134.3	1,089.7	44.6
0.033	1,140.5	1,094.9	45.6
0.045	1,146.6	1,100.1	46.5
0.058	1,153.0	1,105.5	47.6
0.070	1,159.2	1,110.6	48.5
0.082	1,165.3	1,115.8	49.5
0.094	1,171.4	1,120.8	50.5
0.107	1,177.1	1,125.6	51.4
0.119	1,182.9	1,130.5	52.4
0.131	1,188.7	1,135.4	53.3
0.143	1,194.0	1,139.8	54.2
0.156	1,199.4	1,144.4	55.0
0.168	1,204.9	1,148.9	55.9
0.180	1,210.9	1,154.0	56.9
0.192	1,216.5	1,158.7	57.8
0.205	1,222.1	1,163.3	58.7
0.217	1,227.6	1,167.9	59.6
0.229	1,233.0	1,172.5	60.5
0.241	1,238.5	1,177.1	61.4
0.253	1,243.9	1,181.6	62.3
0.266	1,248.4	1,185.4	63.0
0.278	1,252.8	1,189.0	63.7
0.290	1,257.2	1,192.7	64.5
0.302	1,262.7	1,197.3	65.4
0.315	1,266.3	1,200.4	66.0
0.327	1,270.0	1,203.4	66.6
0.339	1,275.1	1,207.7	67.4
0.351	1,279.7	1,211.5	68.2
0.364	1,284.6	1,215.7	69.0
0.376	1,288.8	1,219.1	69.7
0.388	1,296.4	1,225.4	70.9
0.400	1,304.6	1,232.3	72.3
0.413	1,314.7	1,240.7	74.0
0.425	1,323.7	1,248.3	75.5
0.437	1,332.8	1,255.8	77.0
0.449	1,342.0	1,263.5	78.5
0.462	1,350.9	1,270.9	80.0
0.474	1,360.0	1,278.5	81.6
0.486	1,369.5	1,286.4	83.2
0.498	1,379.5	1,294.7	84.8
0.510	1,389.8	1,303.2	86.6
0.523	1,400.3	1,312.0	88.3
0.535	1,411.0	1,320.9	90.1
0.547	1,421.9	1,329.9	91.9

Table D.6: Continued

Zn	T(corr.)	T(uncorr.)	Diff.
0.559	1,432.6	1,338.9	93.8
0.572	1,443.8	1,348.2	95.6
0.584	1,455.1	1,357.6	97.5
0.596	1,466.4	1,367.0	99.4
0.608	1,477.6	1,376.3	101.3
0.621	1,488.7	1,385.6	103.1
0.633	1,499.1	1,394.2	104.9
0.645	1,509.6	1,403.0	106.6
0.657	1,519.7	1,411.4	108.3
0.670	1,529.4	1,419.5	109.9
0.682	1,538.8	1,427.3	111.5
0.694	1,548.3	1,435.2	113.0
0.706	1,557.1	1,442.6	114.5
0.719	1,565.6	1,449.7	115.9
0.731	1,573.9	1,456.6	117.2
0.743	1,581.9	1,463.4	118.6
0.755	1,589.6	1,469.8	119.8
0.767	1,597.1	1,476.0	121.0
0.780	1,604.2	1,482.0	122.2
0.792	1,610.0	1,486.9	123.1
0.804	1,616.3	1,492.2	124.1
0.816	1,622.6	1,497.5	125.1
0.829	1,628.1	1,502.1	126.0
0.841	1,634.6	1,507.6	127.0
0.853	1,641.2	1,513.1	128.1
0.865	1,648.0	1,518.8	129.2
0.878	1,654.2	1,524.0	130.2
0.890	1,662.0	1,530.6	131.4
0.902	1,671.1	1,538.2	132.8
0.914	1,681.1	1,546.7	134.4
0.927	1,691.0	1,555.0	136.0
0.939	1,701.4	1,563.8	137.6
0.951	1,711.4	1,572.2	139.1
0.963	1,719.3	1,578.9	140.4
0.976	1,726.1	1,584.7	141.4
0.988	1,728.3	1,586.6	141.7
1.000	1,728.4	1,586.6	141.7

Table D.7: The comparison of temperatures corrected and measured by thermocouple for IBF-flame in the sooting zone. (Zn = 0.0 ; stagnation plane, Zn = 1.0 Flame location.)

unit : Kelvin

Zn	T(corr.)	T(uncorr.)	Diff.
0.010	1,151.7	1,106.0	45.8
0.024	1,156.1	1,109.7	46.5
0.037	1,160.6	1,113.4	47.2
0.051	1,165.4	1,117.4	48.0
0.065	1,169.8	1,121.1	48.7
0.079	1,174.7	1,125.2	49.5
0.092	1,179.3	1,129.0	50.3
0.106	1,184.8	1,133.6	51.2
0.120	1,189.0	1,137.2	51.9
0.134	1,194.0	1,141.3	52.7
0.147	1,199.6	1,146.0	53.6
0.161	1,206.5	1,151.8	54.7
0.175	1,215.0	1,158.9	56.1
0.189	1,223.6	1,166.1	57.6
0.202	1,233.2	1,174.1	59.2
0.216	1,242.0	1,181.4	60.6
0.230	1,249.8	1,187.9	61.9
0.244	1,257.5	1,194.3	63.2
0.257	1,264.5	1,200.1	64.4
0.271	1,271.5	1,205.9	65.6
0.285	1,278.7	1,211.9	66.8
0.299	1,286.6	1,218.5	68.1
0.312	1,295.4	1,225.9	69.6
0.326	1,304.7	1,233.6	71.1
0.340	1,315.1	1,242.2	72.9
0.354	1,325.3	1,250.7	74.6
0.367	1,335.5	1,259.2	76.3
0.381	1,345.8	1,267.8	78.1
0.395	1,356.5	1,276.6	79.9
0.409	1,366.6	1,285.0	81.6
0.422	1,376.4	1,293.1	83.3
0.436	1,386.1	1,301.2	84.9
0.450	1,395.9	1,309.3	86.6
0.464	1,406.3	1,318.0	88.3
0.477	1,416.1	1,326.1	90.0
0.491	1,425.7	1,334.1	91.6
0.505	1,435.5	1,342.2	93.3
0.519	1,445.5	1,350.5	95.0
0.532	1,456.0	1,359.3	96.7
0.546	1,466.7	1,368.1	98.5
0.560	1,477.3	1,376.9	100.3
0.574	1,487.1	1,385.1	102.0
0.587	1,497.3	1,393.6	103.7
0.601	1,507.6	1,402.2	105.4
0.615	1,517.2	1,410.2	107.0

Table D.7: Continued

Zn	T(corr.)	T(uncorr.)	Diff.
0.629	1,526.7	1,418.1	108.6
0.642	1,536.0	1,425.8	110.2
0.656	1,545.1	1,433.4	111.7
0.670	1,553.8	1,440.7	113.1
0.684	1,562.8	1,448.2	114.6
0.697	1,571.0	1,455.1	116.0
0.711	1,578.6	1,461.4	117.2
0.725	1,585.7	1,467.3	118.4
0.739	1,592.5	1,473.0	119.5
0.752	1,599.1	1,478.5	120.6
0.766	1,605.2	1,483.6	121.6
0.780	1,611.2	1,488.6	122.5
0.794	1,617.3	1,493.7	123.5
0.807	1,623.2	1,498.7	124.5
0.821	1,629.4	1,503.9	125.5
0.835	1,635.4	1,508.9	126.5
0.849	1,641.4	1,514.0	127.4
0.862	1,647.9	1,519.4	128.5
0.876	1,655.1	1,525.5	129.6
0.890	1,663.6	1,532.6	131.0
0.904	1,672.9	1,540.4	132.4
0.917	1,683.0	1,549.0	134.1
0.931	1,695.5	1,559.5	136.0
0.945	1,709.9	1,571.6	138.3
0.959	1,724.7	1,584.1	140.6
0.972	1,735.6	1,593.3	142.2
0.986	1,741.8	1,598.6	143.2
1.000	1,742.2	1,598.9	143.2

Table D.8: The comparison of temperatures corrected and measured by thermocouple for IBO-flame in the sooting zone. (Zn = 0.0 ; stagnation plane, Zn = 1.0 Flame location.)

unit : Kelvin

Zn	T(corr.)	T(uncorr.)	Diff.
-0.931	913.6	905.3	8.3
-0.919	914.1	905.7	8.4
-0.907	914.6	906.1	8.5
0.000	1,169.8	1,120.9	48.9
0.011	1,175.3	1,125.6	49.8
0.023	1,180.3	1,129.7	50.6
0.035	1,185.2	1,133.8	51.4
0.046	1,190.4	1,138.1	52.2
0.058	1,195.4	1,142.4	53.1
0.070	1,200.4	1,146.6	53.9
0.081	1,205.3	1,150.6	54.7
0.093	1,210.4	1,154.9	55.5
0.104	1,215.4	1,159.0	56.3
0.116	1,220.5	1,163.3	57.2
0.128	1,225.6	1,167.6	58.0
0.139	1,230.7	1,171.8	58.9
0.151	1,235.8	1,176.1	59.7
0.163	1,241.3	1,180.7	60.6
0.174	1,246.6	1,185.1	61.5
0.186	1,251.9	1,189.5	62.4
0.197	1,257.3	1,194.0	63.3
0.209	1,262.7	1,198.5	64.2
0.221	1,267.9	1,202.8	65.1
0.232	1,272.4	1,206.6	65.8
0.244	1,277.2	1,210.6	66.6
0.256	1,281.9	1,214.5	67.4
0.267	1,286.3	1,218.2	68.1
0.279	1,290.7	1,221.8	68.9
0.291	1,296.0	1,226.3	69.7
0.302	1,300.7	1,230.1	70.5
0.314	1,305.3	1,234.0	71.3
0.325	1,310.0	1,237.9	72.1
0.337	1,314.9	1,242.0	72.9
0.349	1,319.1	1,245.5	73.6
0.360	1,324.0	1,249.6	74.4
0.372	1,328.9	1,253.6	75.2
0.384	1,333.5	1,257.5	76.0
0.395	1,337.9	1,261.1	76.7
0.407	1,342.2	1,264.7	77.5
0.418	1,346.5	1,268.3	78.2
0.430	1,350.8	1,271.9	78.9
0.442	1,355.1	1,275.5	79.6
0.453	1,359.5	1,279.1	80.4
0.465	1,365.3	1,284.0	81.4
0.477	1,370.7	1,288.5	82.3

Table D.8 : Continued

Zn	T(corr.)	T(uncorr.)	Diff.
0.488	1,376.3	1,293.1	83.2
0.500	1,382.4	1,298.2	84.2
0.512	1,388.9	1,303.6	85.3
0.523	1,395.6	1,309.1	86.4
0.535	1,402.8	1,315.1	87.7
0.546	1,409.9	1,321.1	88.9
0.558	1,417.2	1,327.1	90.1
0.570	1,423.8	1,332.6	91.2
0.581	1,431.3	1,338.8	92.5
0.593	1,438.7	1,345.0	93.7
0.605	1,446.0	1,351.0	94.9
0.616	1,453.3	1,357.1	96.2
0.628	1,461.3	1,363.7	97.5
0.639	1,468.3	1,369.6	98.7
0.651	1,475.3	1,375.4	99.9
0.663	1,482.2	1,381.2	101.0
0.674	1,489.0	1,386.9	102.2
0.686	1,496.3	1,392.9	103.4
0.698	1,503.5	1,398.9	104.6
0.709	1,510.1	1,404.4	105.7
0.721	1,517.0	1,410.1	106.8
0.732	1,523.7	1,415.7	108.0
0.744	1,530.2	1,421.1	109.0
0.756	1,536.4	1,426.3	110.1
0.767	1,542.2	1,431.2	111.0
0.779	1,547.8	1,435.8	112.0
0.791	1,553.6	1,440.7	112.9
0.802	1,559.4	1,445.5	113.9
0.814	1,565.3	1,450.5	114.9
0.826	1,571.6	1,455.7	115.9
0.837	1,577.9	1,461.0	116.9
0.849	1,584.2	1,466.3	117.9
0.860	1,591.0	1,471.9	119.1
0.872	1,597.8	1,477.7	120.2
0.884	1,605.1	1,483.8	121.4
0.895	1,613.0	1,490.3	122.6
0.907	1,623.9	1,499.5	124.4
0.919	1,635.0	1,508.8	126.2
0.930	1,646.4	1,518.3	128.1
0.942	1,657.7	1,527.8	129.9
0.953	1,670.0	1,538.2	131.8
0.965	1,682.2	1,548.4	133.8
0.977	1,690.9	1,555.8	135.1
0.988	1,696.2	1,560.2	136.0
1.000	1,697.3	1,561.2	136.1

Table D.9: The comparison of temperatures corrected and measured by thermocouple for MBF-flame in the sooting zone. (Zn = 0.0 ; stagnation plane, Zn = 1.0 Flame

unit : Kelvin

Zn	T(corr.)	T(uncorr.)	Diff.
0.000	1,108.2	1,069.6	38.6
0.011	1,113.1	1,073.7	39.4
0.023	1,118.0	1,077.8	40.2
0.034	1,122.8	1,081.9	41.0
0.046	1,127.6	1,085.8	41.7
0.057	1,132.1	1,089.6	42.5
0.069	1,136.4	1,093.3	43.2
0.080	1,140.5	1,096.7	43.8
0.092	1,144.5	1,100.0	44.5
0.103	1,148.4	1,103.3	45.1
0.115	1,152.7	1,106.9	45.8
0.126	1,156.8	1,110.3	46.4
0.138	1,161.1	1,114.0	47.1
0.149	1,165.5	1,117.7	47.9
0.161	1,170.0	1,121.4	48.6
0.172	1,174.7	1,125.3	49.3
0.184	1,179.5	1,129.4	50.1
0.195	1,184.5	1,133.5	50.9
0.207	1,189.2	1,137.5	51.7
0.218	1,194.4	1,141.8	52.6
0.230	1,199.5	1,146.1	53.4
0.241	1,204.3	1,150.1	54.2
0.253	1,209.0	1,154.1	55.0
0.264	1,213.6	1,157.9	55.7
0.276	1,217.9	1,161.5	56.4
0.287	1,221.8	1,164.7	57.1
0.239	1,225.3	1,167.7	57.6
0.310	1,229.0	1,170.8	58.2
0.322	1,232.8	1,173.9	58.9
0.333	1,236.9	1,177.4	59.5
0.345	1,241.4	1,181.1	60.3
0.356	1,247.6	1,186.3	61.3
0.368	1,253.3	1,191.0	62.2
0.379	1,261.8	1,198.2	63.7
0.391	1,269.5	1,204.5	65.0
0.402	1,278.0	1,211.6	66.4
0.414	1,287.3	1,219.4	67.9
0.425	1,297.0	1,227.4	69.6
0.437	1,305.1	1,234.2	70.9
0.448	1,315.7	1,243.0	72.7
0.460	1,326.1	1,251.6	74.5
0.471	1,336.5	1,260.3	76.3
0.483	1,347.9	1,269.7	78.2
0.494	1,357.4	1,277.6	79.8
0.506	1,366.9	1,285.5	81.4

Table D.9 : Continued

Zn	T(corr.)	T(uncorr.)	Diff.
0.517	1,376.9	1,293.8	83.1
0.529	1,387.3	1,302.4	84.8
0.540	1,398.0	1,311.4	86.7
0.552	1,409.2	1,320.6	88.6
0.563	1,421.4	1,330.7	90.6
0.575	1,433.1	1,340.5	92.6
0.586	1,446.1	1,351.3	94.8
0.598	1,458.7	1,361.8	97.0
0.609	1,470.6	1,371.6	99.0
0.621	1,481.9	1,381.1	100.9
0.632	1,492.0	1,389.4	102.6
0.644	1,501.1	1,397.0	104.1
0.655	1,509.1	1,403.6	105.4
0.667	1,517.4	1,410.5	106.8
0.678	1,525.3	1,417.1	108.1
0.690	1,533.2	1,423.7	109.5
0.701	1,541.6	1,430.8	110.9
0.713	1,550.4	1,438.1	112.3
0.724	1,559.5	1,445.6	113.8
0.736	1,568.3	1,453.0	115.3
0.747	1,577.3	1,460.5	116.8
0.759	1,586.3	1,468.0	118.3
0.770	1,593.6	1,474.2	119.5
0.782	1,600.3	1,479.8	120.5
0.793	1,606.1	1,484.7	121.5
0.805	1,610.9	1,488.6	122.3
0.816	1,615.6	1,492.6	123.0
0.828	1,620.2	1,496.5	123.8
0.839	1,624.5	1,500.0	124.4
0.851	1,628.5	1,503.4	125.1
0.862	1,632.9	1,507.1	125.8
0.874	1,638.5	1,511.8	126.7
0.885	1,644.6	1,516.9	127.7
0.897	1,652.3	1,523.4	128.9
0.908	1,661.0	1,530.7	130.3
0.920	1,670.1	1,538.3	131.7
0.931	1,682.3	1,548.6	133.7
0.943	1,695.6	1,559.8	135.8
0.954	1,710.5	1,572.4	138.1
0.966	1,723.9	1,583.7	140.2
0.977	1,736.6	1,594.5	142.2
0.989	1,744.0	1,600.7	143.3
1.000	1,745.7	1,602.2	143.5

Table D.10: The comparison of temperatures corrected and measured by thermocouple for MBO-flame in the sooting zone. (Zn = 0.0 ; stagnation plane, Zn = 1.0 Flame location.)

unit : Kelvin

Zn	T(corr.)	T(uncorr.)	Diff.
0.009	1,146.2	1,101.6	44.5
0.022	1,151.4	1,106.0	45.4
0.036	1,157.1	1,110.8	46.3
0.050	1,162.9	1,115.6	47.3
0.064	1,168.9	1,120.6	48.2
0.077	1,175.6	1,126.3	49.3
0.091	1,181.9	1,131.5	50.4
0.105	1,188.3	1,136.9	51.4
0.119	1,195.4	1,142.8	52.6
0.132	1,202.4	1,148.7	53.8
0.146	1,209.7	1,154.7	55.0
0.160	1,217.2	1,161.0	56.2
0.174	1,225.4	1,167.9	57.6
0.188	1,233.5	1,174.6	58.9
0.201	1,242.7	1,182.3	60.5
0.215	1,252.3	1,190.2	62.1
0.229	1,261.1	1,197.6	63.5
0.243	1,270.7	1,205.6	65.2
0.256	1,279.5	1,212.8	66.6
0.270	1,288.0	1,219.9	68.0
0.284	1,295.8	1,226.5	69.4
0.298	1,303.4	1,232.8	70.7
0.311	1,310.9	1,239.0	71.9
0.325	1,319.1	1,245.8	73.3
0.339	1,327.4	1,252.7	74.7
0.353	1,335.8	1,259.7	76.1
0.367	1,344.8	1,267.2	77.6
0.380	1,353.6	1,274.5	79.1
0.394	1,362.2	1,281.6	80.6
0.408	1,369.9	1,288.0	81.9
0.422	1,377.4	1,294.2	83.2
0.435	1,384.5	1,300.1	84.4
0.449	1,390.9	1,305.4	85.4
0.463	1,397.0	1,310.5	86.5
0.477	1,403.0	1,315.5	87.5
0.490	1,408.7	1,320.3	88.5
0.504	1,415.3	1,325.7	89.6
0.518	1,421.7	1,331.1	90.7
0.532	1,429.5	1,337.6	92.0
0.546	1,437.5	1,344.2	93.3
0.559	1,445.3	1,350.7	94.6
0.573	1,454.5	1,358.3	96.2
0.587	1,463.1	1,365.4	97.6
0.601	1,471.8	1,372.7	99.1
0.614	1,480.9	1,380.2	100.6

Table D.10 : Continued

Zn	T(corr.)	T(uncorr.)	Diff.
0.628	1,488.8	1,386.8	102.0
0.642	1,496.5	1,393.3	103.3
0.656	1,504.6	1,400.0	104.6
0.670	1,511.8	1,405.9	105.8
0.683	1,518.5	1,411.5	106.9
0.697	1,525.3	1,417.2	108.1
0.711	1,531.5	1,422.4	109.1
0.725	1,538.2	1,428.0	110.2
0.738	1,545.1	1,433.8	111.4
0.752	1,551.5	1,439.0	112.4
0.766	1,558.4	1,444.8	113.6
0.780	1,564.9	1,450.2	114.6
0.793	1,571.4	1,455.7	115.7
0.807	1,577.3	1,460.6	116.7
0.821	1,583.8	1,466.0	117.8
0.835	1,589.0	1,470.4	118.6
0.849	1,594.7	1,475.1	119.5
0.862	1,599.5	1,479.2	120.3
0.876	1,604.5	1,483.4	121.1
0.890	1,614.9	1,492.1	122.8
0.904	1,623.7	1,499.5	124.3
0.917	1,634.1	1,508.1	125.9
0.931	1,647.1	1,519.0	128.0
0.945	1,656.9	1,527.3	129.6
0.959	1,669.6	1,538.0	131.7
0.972	1,680.6	1,547.2	133.4
0.986	1,684.6	1,550.5	134.0
1.000	1,687.2	1,552.8	134.4

Table D.11: The comparison of temperatures corrected and measured by thermocouple for MCF-flame in the sooting zone. (Zn = 0.0 ; stagnation plane, Zn = 1.0 Flame

unit : Kelvin

Zn	T(corr.)	T(uncorr.)	Diff.
0.010	1,240.0	1,176.1	63.9
0.039	1,248.3	1,183.1	65.2
0.067	1,258.1	1,191.3	66.8
0.095	1,267.3	1,199.0	68.3
0.124	1,277.4	1,207.5	69.9
0.152	1,287.2	1,215.7	71.5
0.180	1,297.6	1,224.4	73.2
0.208	1,307.3	1,232.6	74.8
0.237	1,317.1	1,240.7	76.4
0.265	1,326.5	1,248.6	77.9
0.293	1,335.9	1,256.4	79.4
0.321	1,348.1	1,266.6	81.4
0.350	1,361.5	1,277.9	83.6
0.378	1,375.4	1,289.5	85.9
0.406	1,389.9	1,301.6	88.3
0.435	1,406.2	1,315.2	91.0
0.463	1,422.4	1,328.7	93.7
0.491	1,441.5	1,344.6	96.8
0.519	1,463.2	1,362.8	100.4
0.548	1,488.2	1,383.6	104.6
0.576	1,516.3	1,407.1	109.2
0.604	1,548.0	1,433.6	114.4
0.632	1,576.4	1,457.3	119.0
0.661	1,603.3	1,479.9	123.4
0.689	1,629.7	1,502.1	127.6
0.717	1,658.2	1,526.0	132.2
0.746	1,686.6	1,550.0	136.6
0.774	1,716.0	1,574.8	141.1
0.802	1,745.6	1,599.9	145.6
0.830	1,775.2	1,625.2	150.0
0.859	1,804.5	1,650.2	154.3
0.887	1,833.5	1,675.1	158.4
0.915	1,857.9	1,696.1	161.8
0.943	1,874.5	1,710.4	164.1
0.972	1,884.6	1,719.2	165.4
1.000	1,890.3	1,724.1	166.2

Table D.12: The comparison of temperatures corrected and measured by thermocouple for WCF-flame in the sooting zone. (Zn = 0.0 ; stagnation plane, Zn = 1.0 Flame location.)

unit : Kelvin

Zn	T(corr.)	T(uncorr.)	Diff.
0.007	1,219.3	1,158.8	60.5
0.035	1,227.6	1,165.8	61.8
0.063	1,236.5	1,173.2	63.2
0.092	1,244.8	1,180.2	64.6
0.120	1,253.2	1,187.3	65.9
0.149	1,262.3	1,194.9	67.4
0.177	1,272.4	1,203.4	69.0
0.205	1,283.2	1,212.4	70.8
0.234	1,295.1	1,222.4	72.7
0.262	1,308.6	1,233.7	74.9
0.290	1,323.9	1,246.5	77.4
0.319	1,342.5	1,262.0	80.5
0.347	1,361.0	1,277.5	83.5
0.376	1,381.0	1,294.2	86.8
0.404	1,402.6	1,312.2	90.4
0.432	1,425.0	1,330.9	94.1
0.461	1,447.2	1,349.4	97.8
0.489	1,468.9	1,367.5	101.4
0.518	1,492.3	1,387.0	105.3
0.546	1,519.3	1,409.6	109.7
0.574	1,549.5	1,434.8	114.7
0.603	1,580.1	1,460.4	119.7
0.631	1,609.4	1,485.0	124.4
0.659	1,634.4	1,506.0	128.4
0.688	1,657.6	1,525.5	132.1
0.716	1,680.8	1,545.1	135.7
0.745	1,704.8	1,565.4	139.4
0.773	1,729.3	1,586.1	143.2
0.801	1,755.1	1,608.0	147.0
0.830	1,781.9	1,630.9	151.0
0.858	1,808.7	1,653.8	154.9
0.886	1,831.4	1,673.3	158.1
0.915	1,849.3	1,688.7	160.6
0.943	1,861.3	1,699.0	162.3
0.972	1,867.6	1,704.5	163.1
1.000	1,869.2	1,705.9	163.3

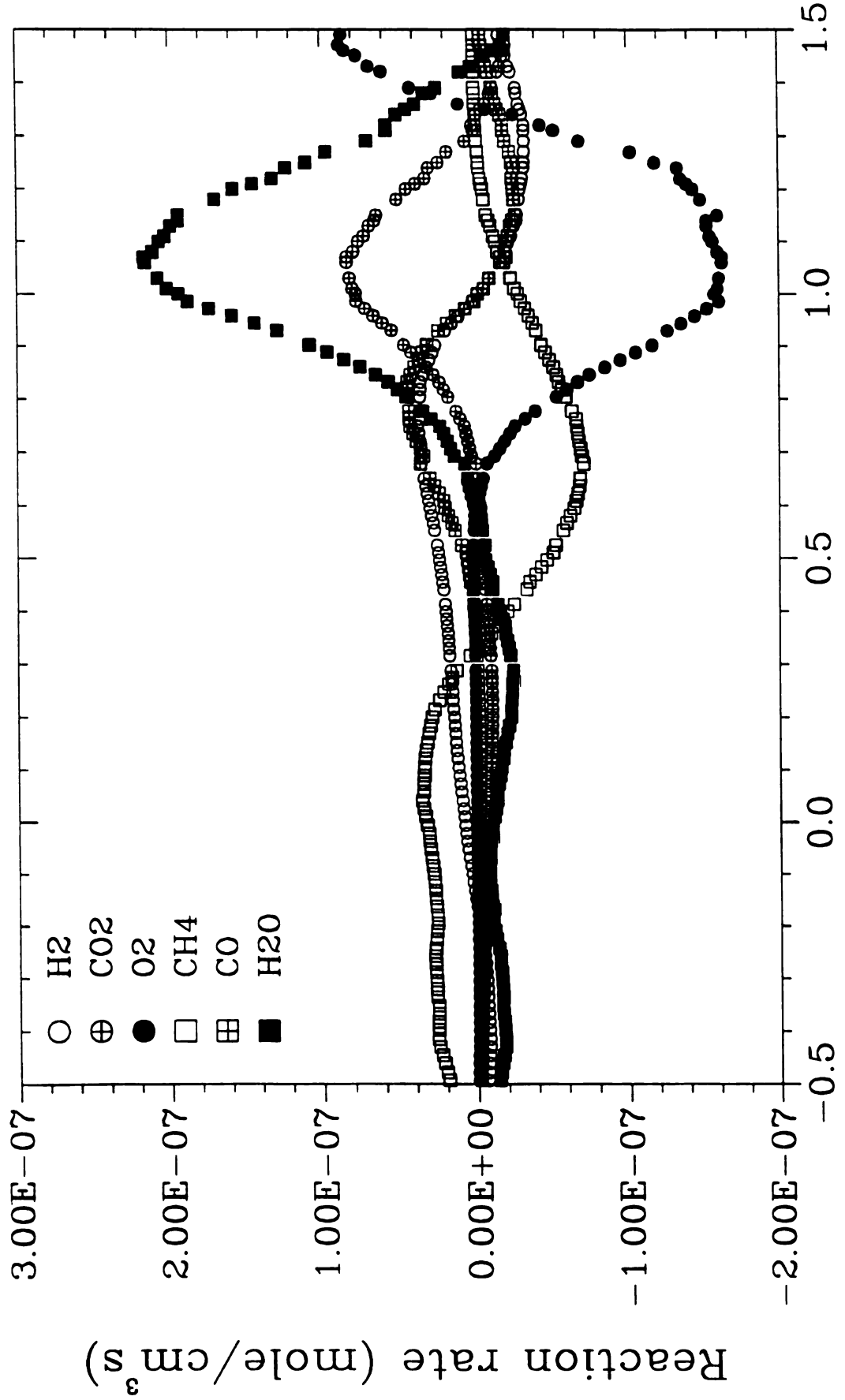

Figure D-1 Chemical reaction rate of major species (H_2, CO_2, O_2, CH_4, CO, and H_2O) in BA-flame

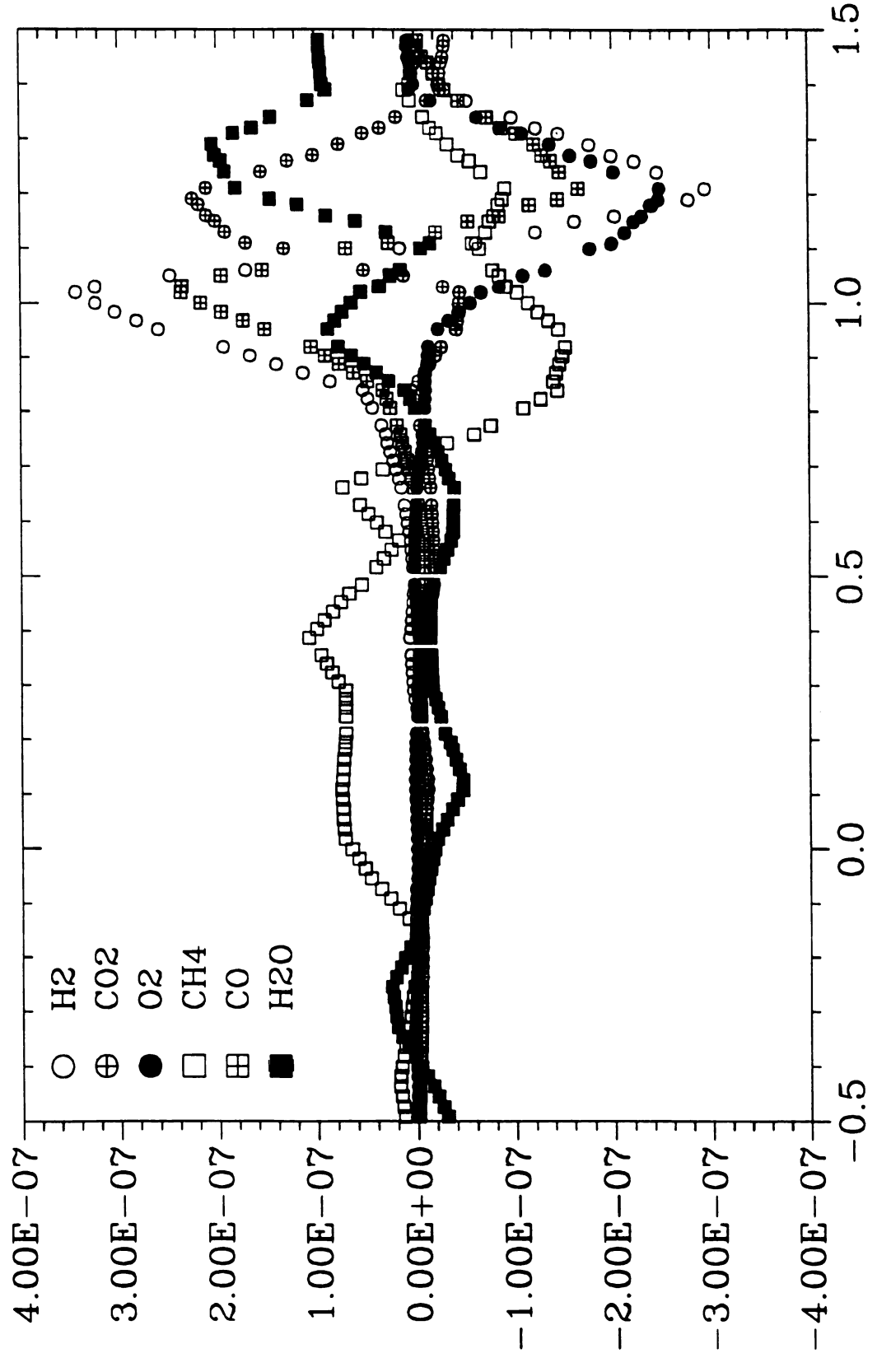

Figure D-2 Chemical reaction rate of major species (H_2, CO_2, O_2, CH_4, CO, and H_2O) in IA-flame

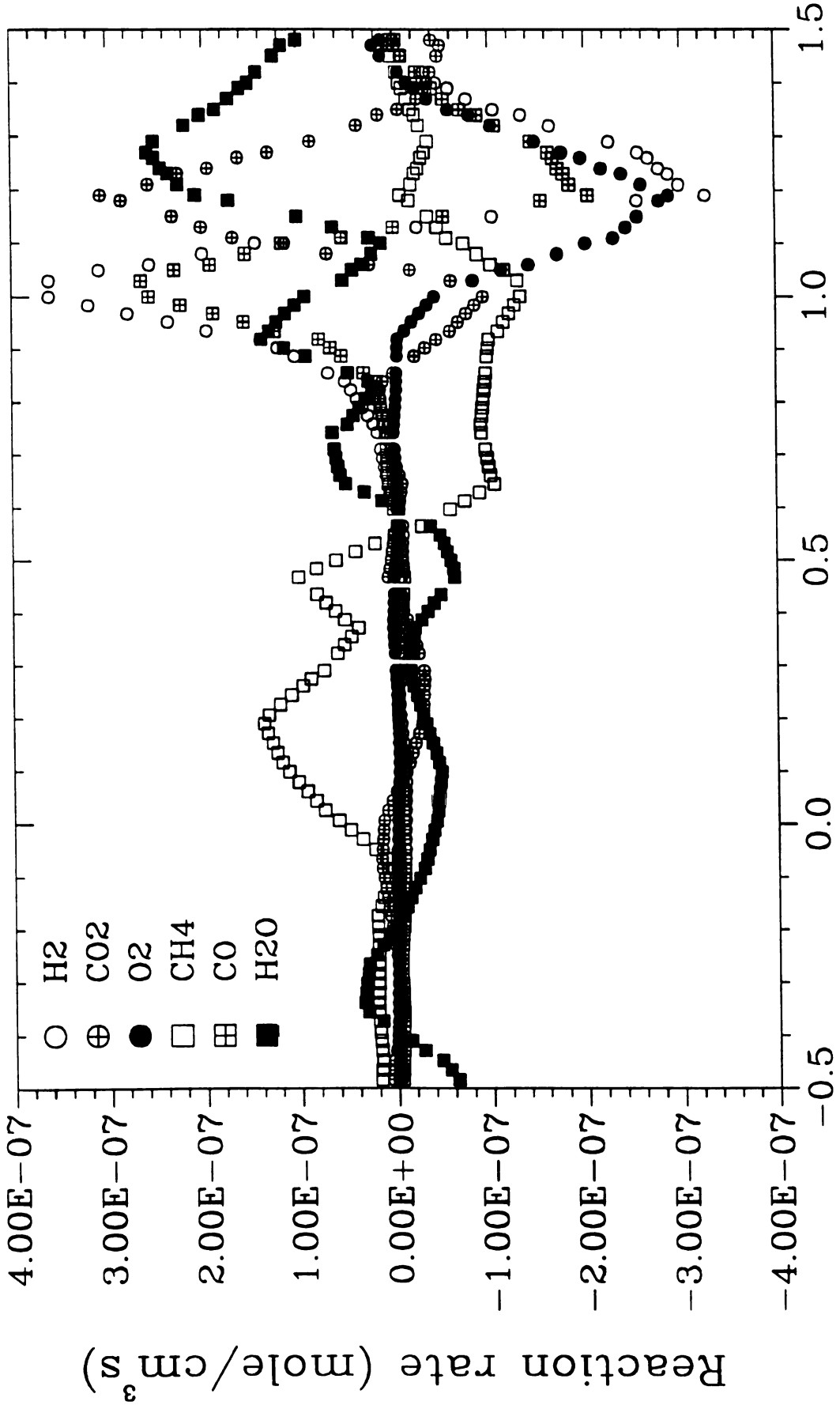

Figure D-3 Chemical reaction rate of major species (H_2, CO_2, O_2, CH_4, CO, and H_2O) in MA-flame

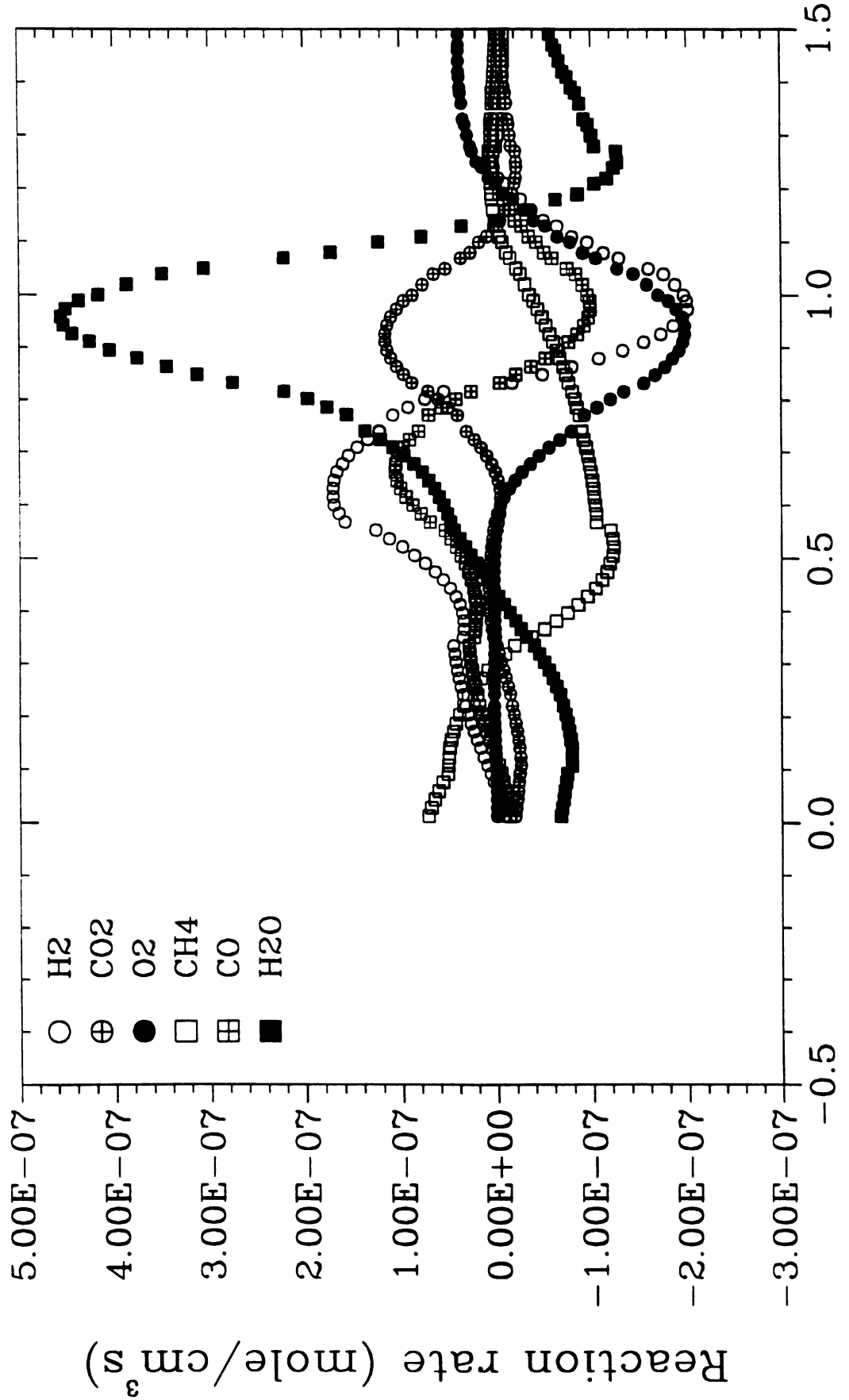

Figure D-4 Chemical reaction rate of major species (H_2, CO_2, O_2, CH_4, CO, and H_2O) in WAF-flame

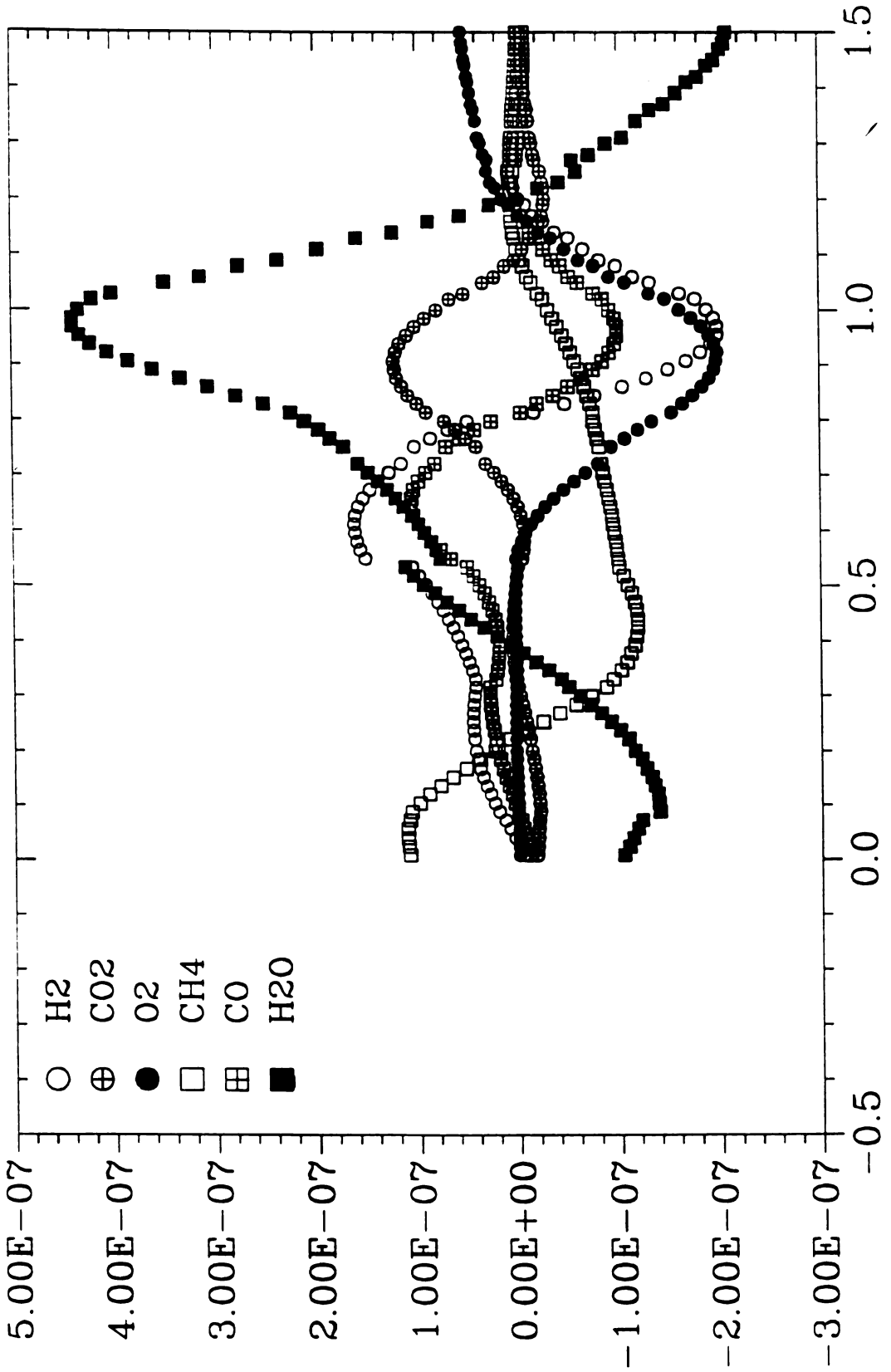

Figure D-5 Chemical reaction rate of major species (H_2, CO_2, O_2, CH_4, CO, and H_2O) in WAO-flame

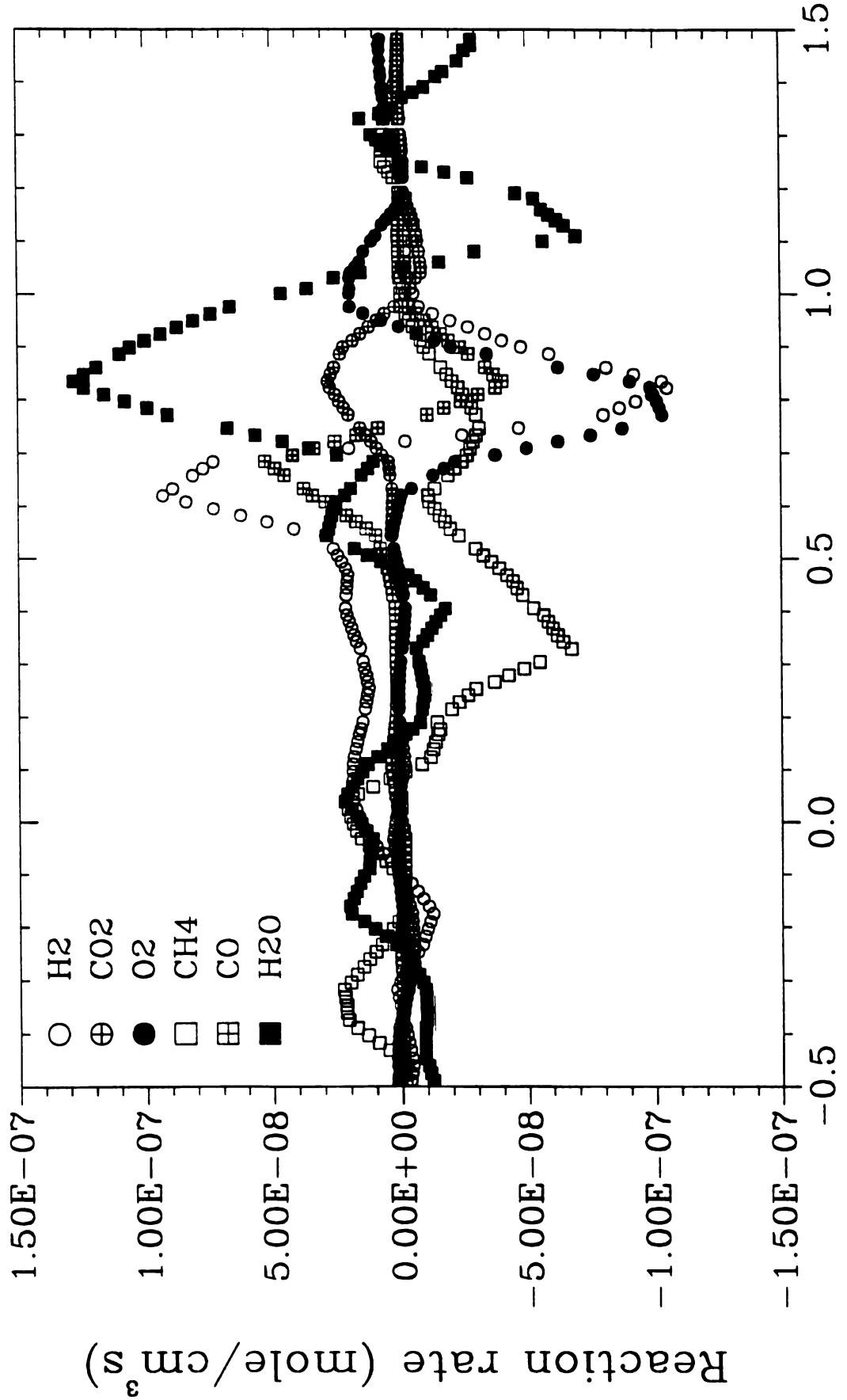

Figure D-6 Chemical reaction rate of major species (H_2, CO_2, O_2, CH_4, CO, and H_2O) in BB-flame

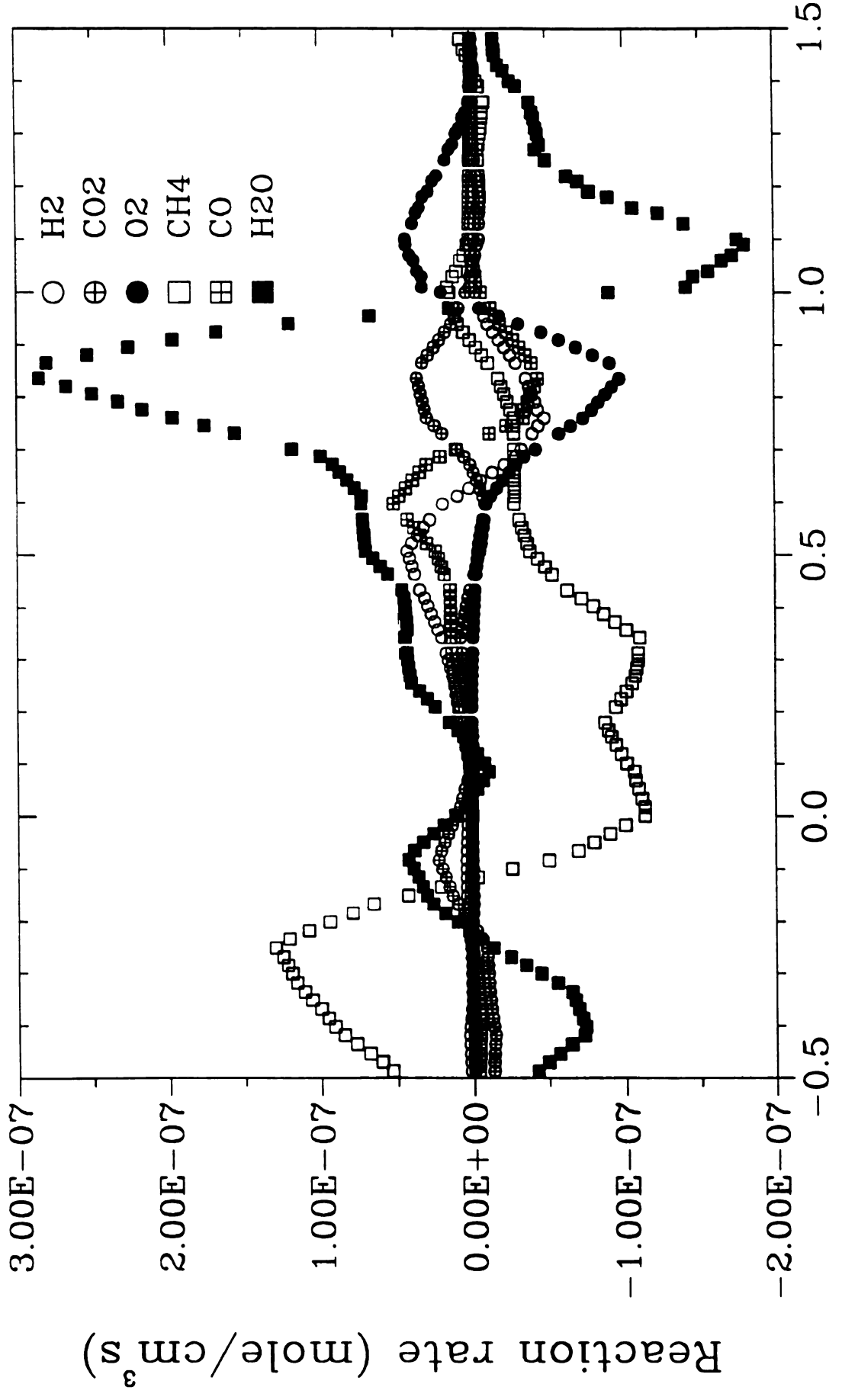

Figure D-7 Chemical reaction rate of major species (H_2, CO_2, O_2, CH_4, CO, and H_2O) in IBO-flame

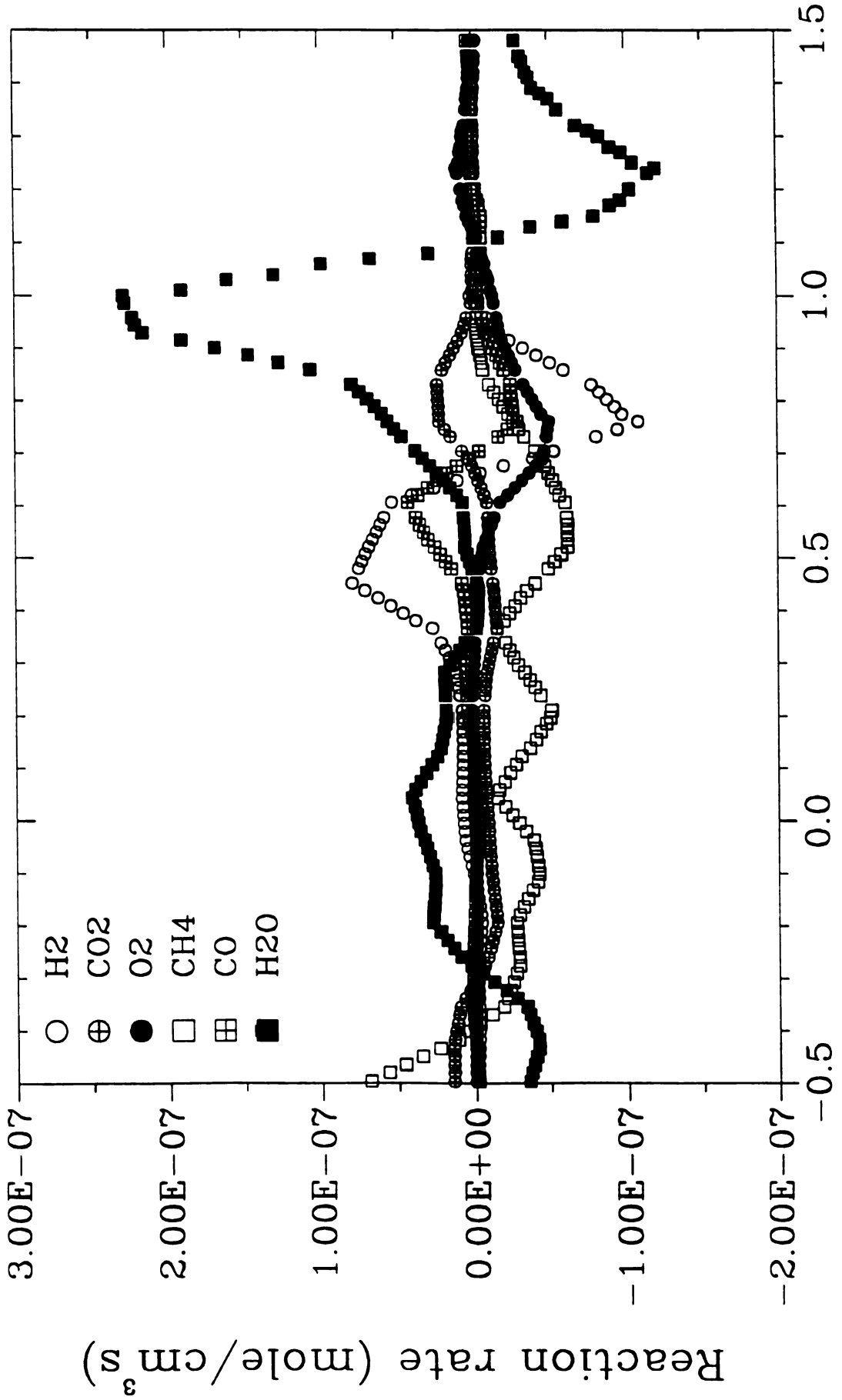

Figure D-8 Chemical reaction rate of major species (H_2, CO_2, O_2, CH_4, CO, and H_2O) in MBF-flame

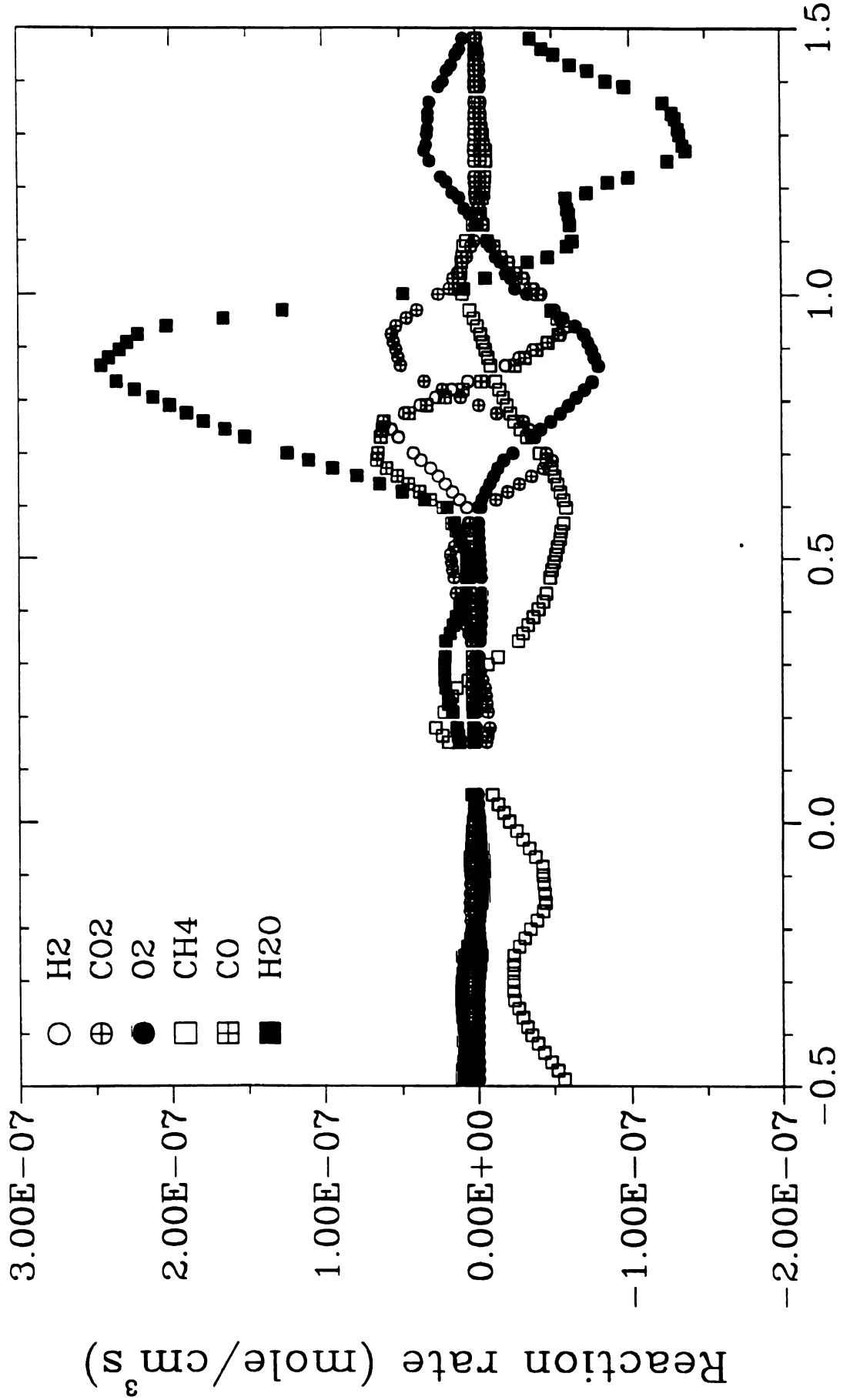

Figure D-9 Chemical reaction rate of major species (H_2, CO_2, O_2, CH_4, CO, and H_2O) in MBO-flame

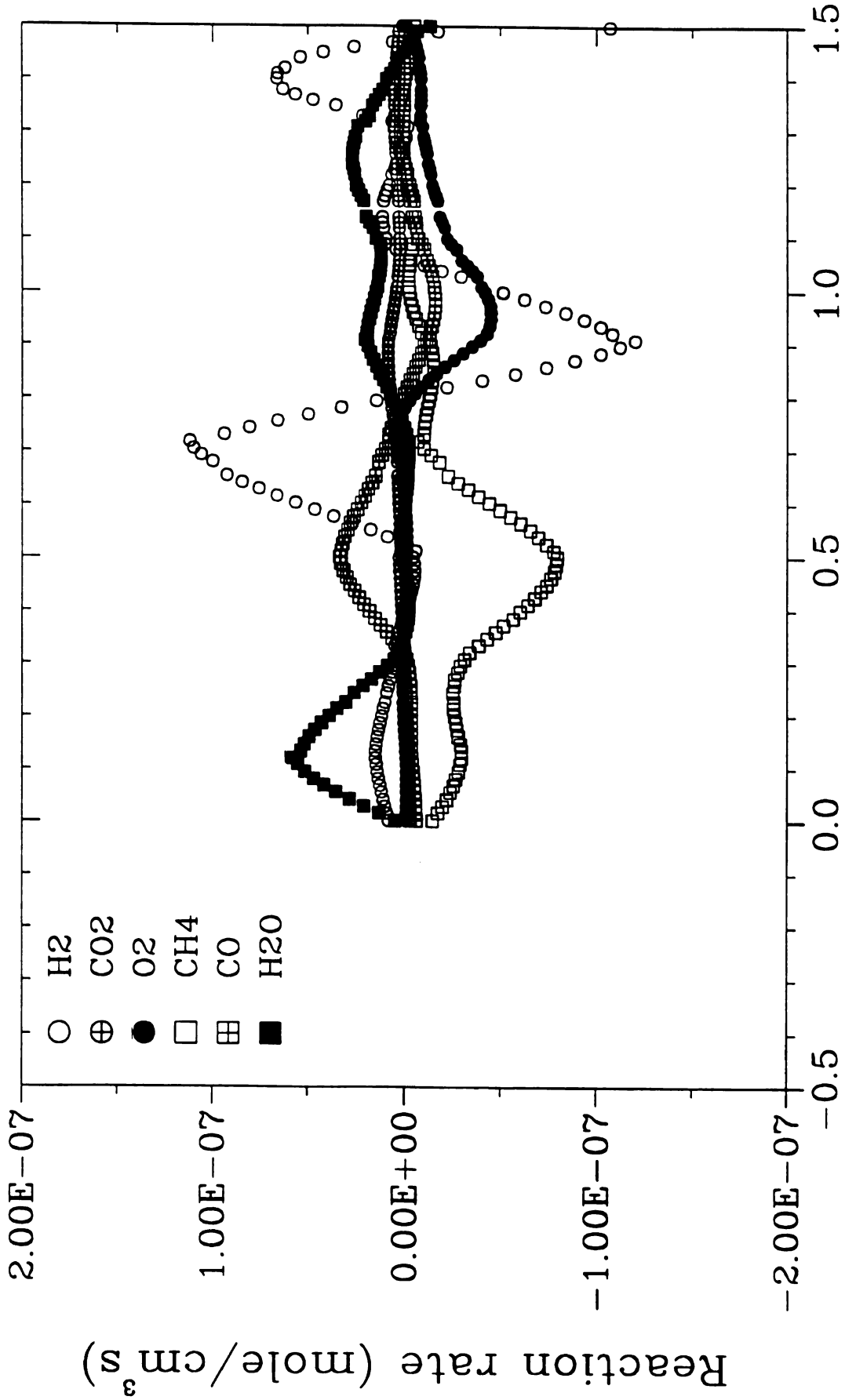

Figure D-10 Chemical reaction rate of major species (H_2, CO_2, O_2, CH_4, CO, and H_2O) in BC-flame

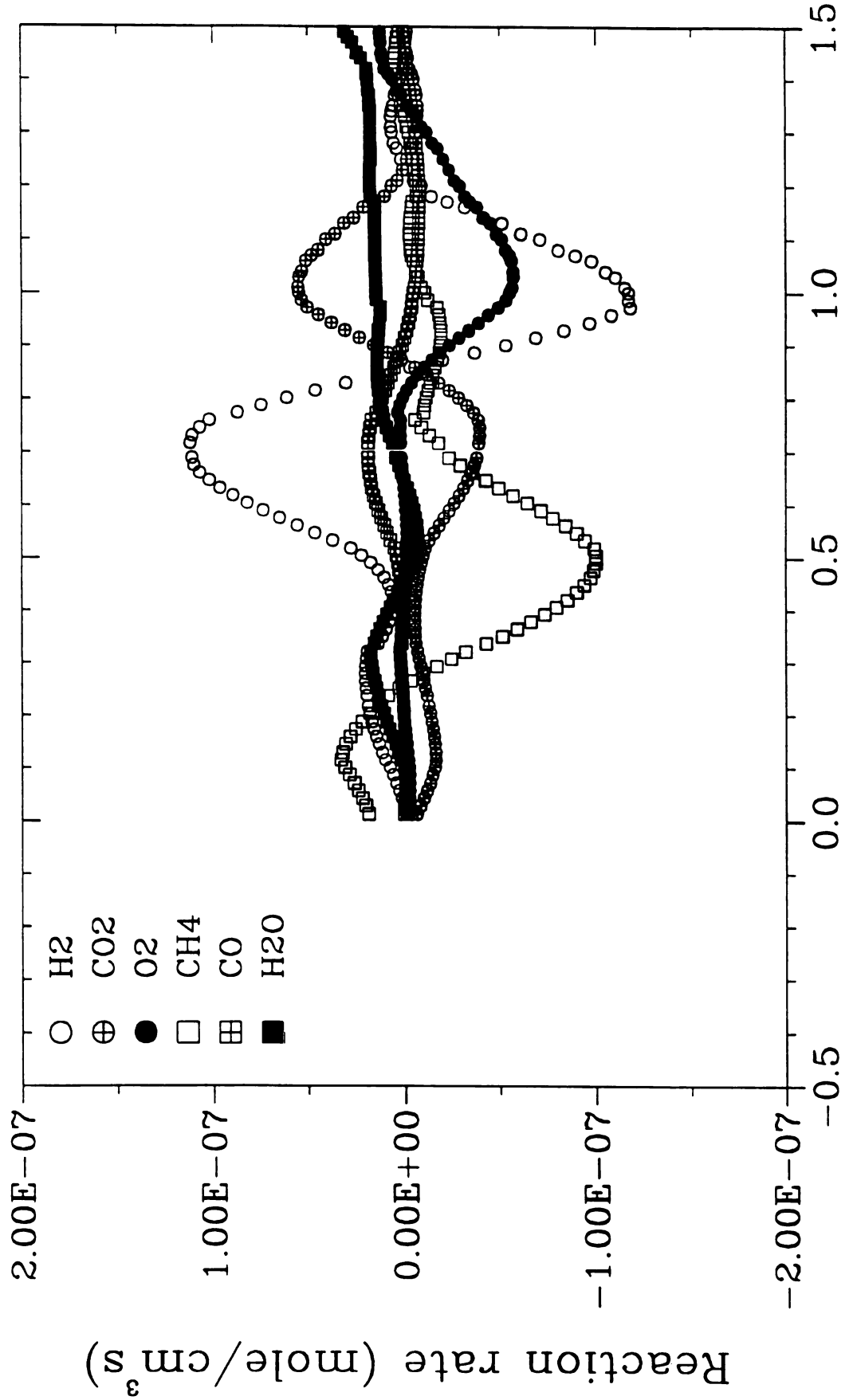

Figure D-11 Chemical reaction rate of major species (H_2, CO_2, O_2, CH_4, CO, and H_2O) in MCF-flame

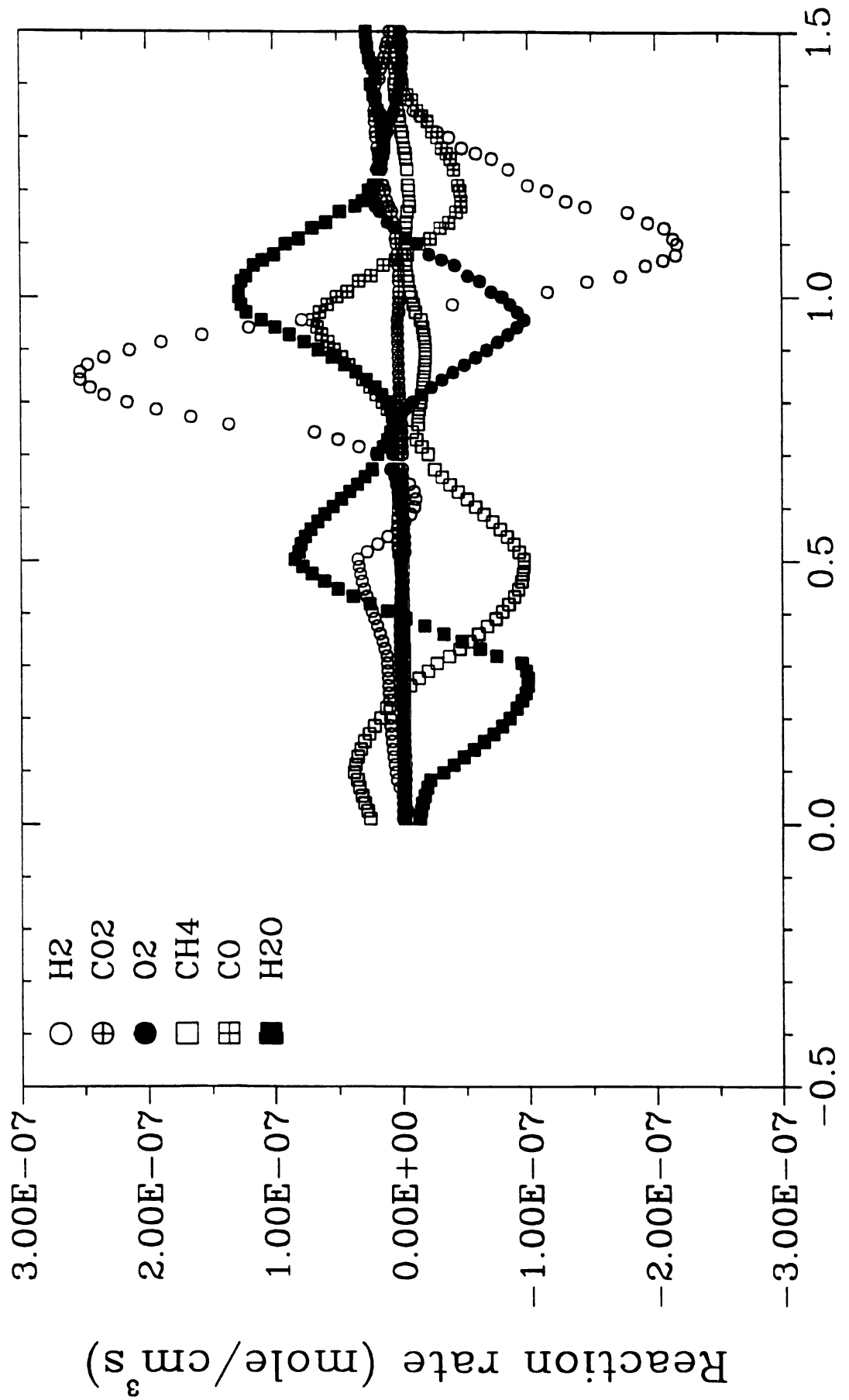

Figure D-12 Chemical reaction rate of major species (H_2, CO_2, O_2, CH_4, CO, and H_2O) in WCF-flame

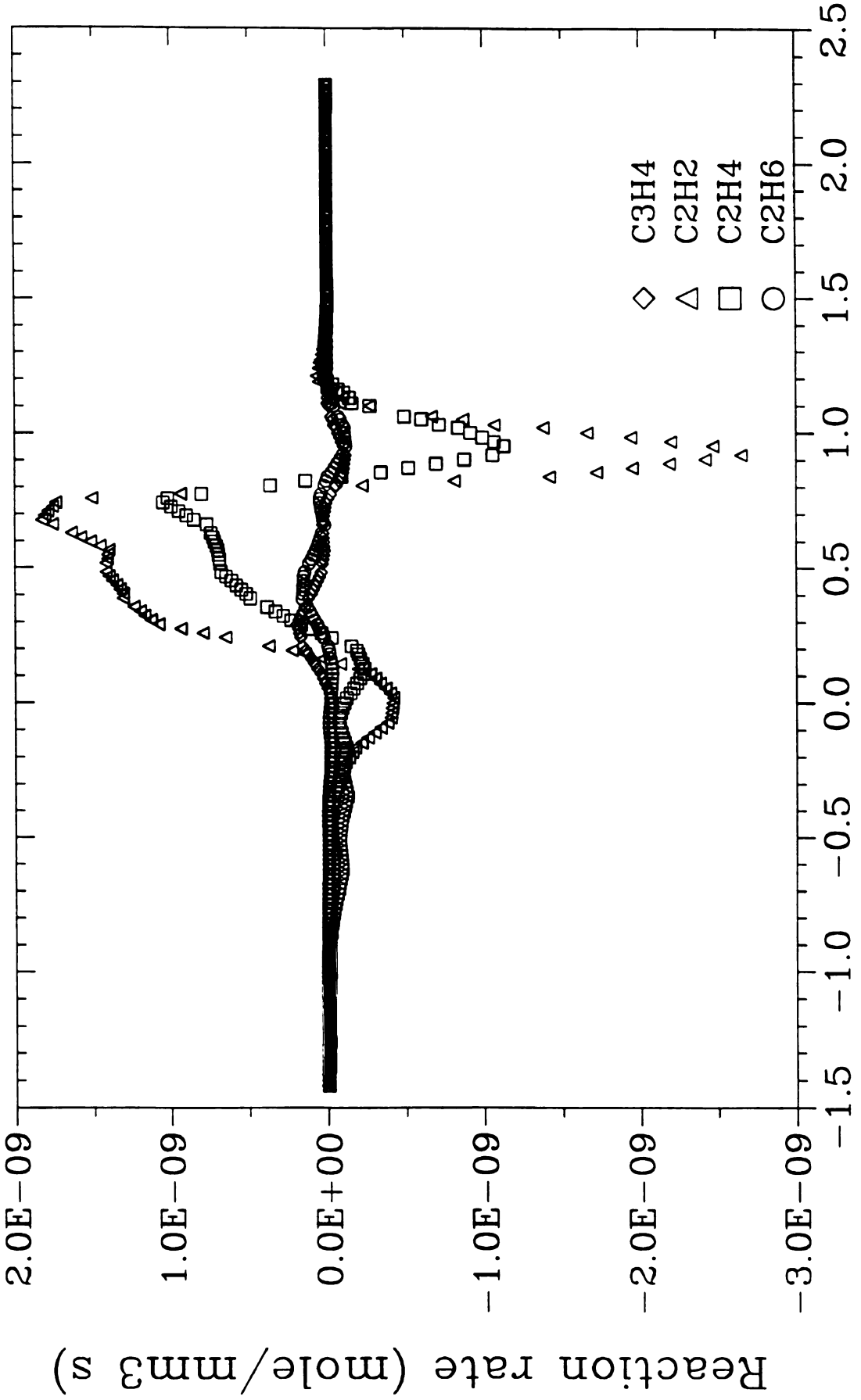

Figure D-13 Chemical reaction rate of hydrocarbons in IA-flame

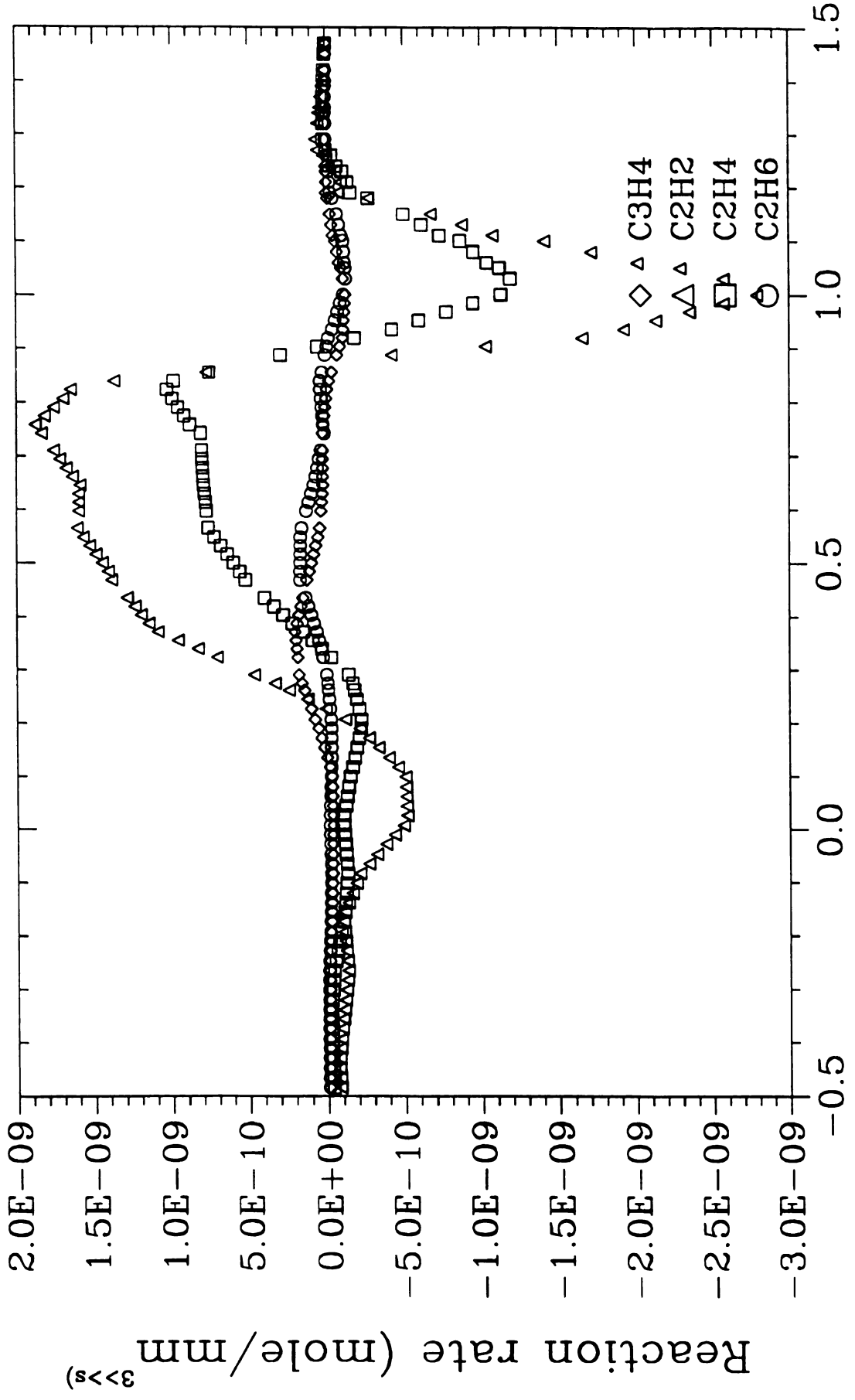

Figure D-14 Chemical reaction rate of hydrocarbons in MA-flame

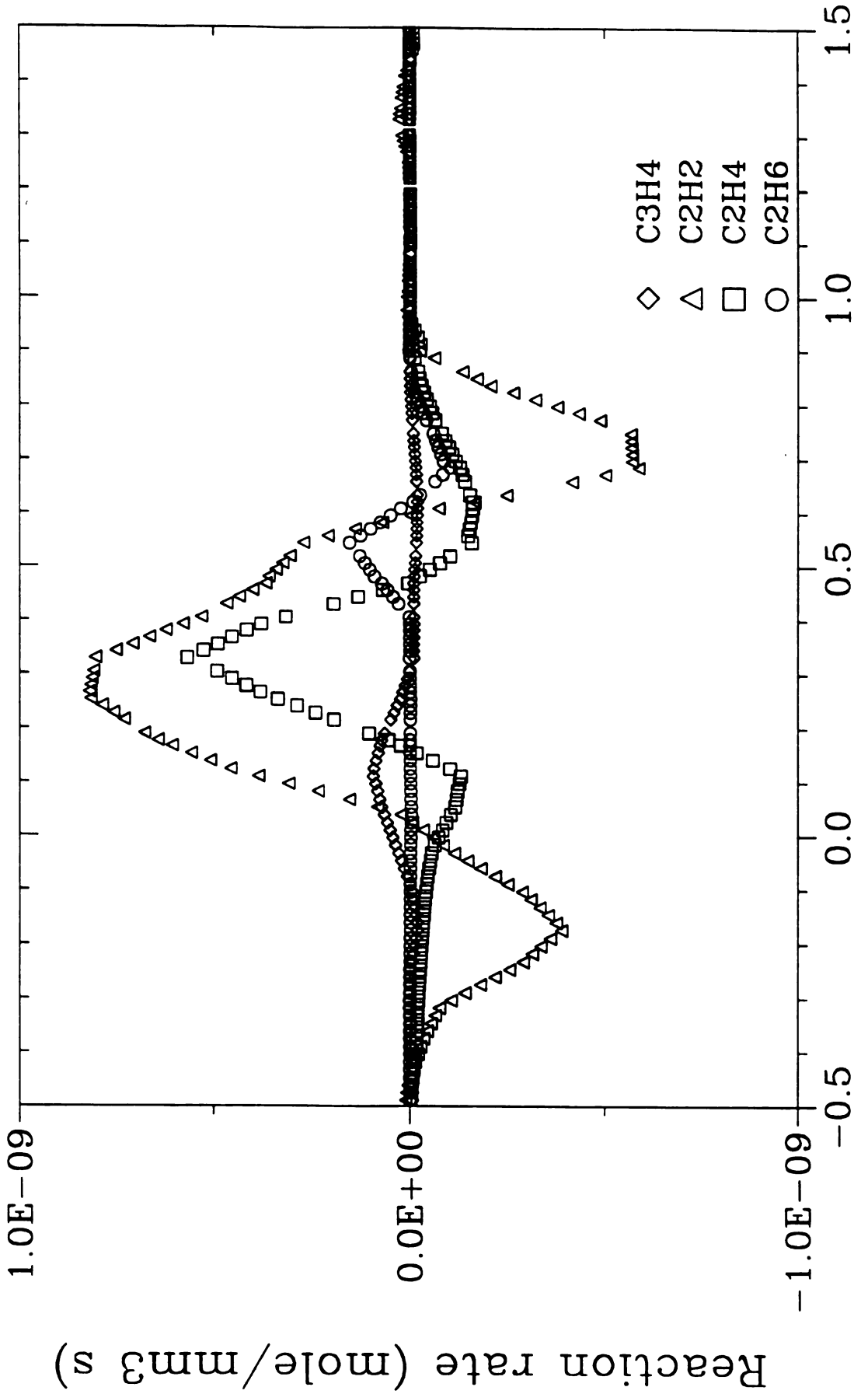

Figure D-15 Chemical reaction rate of hydrocarbons in BB-flame

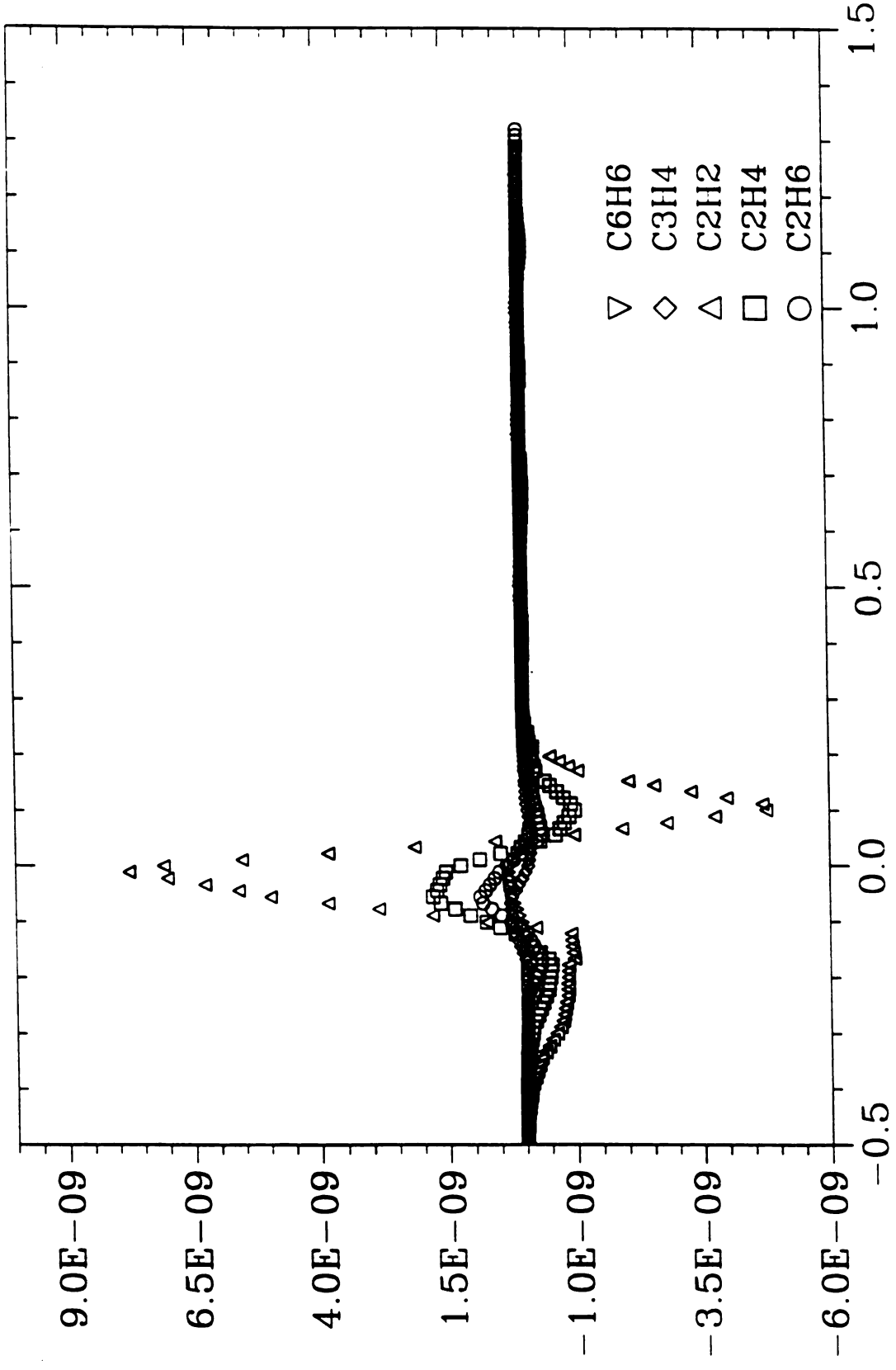

Figure D-16 Chemical reaction rate of hydrocarbons in BC-flame

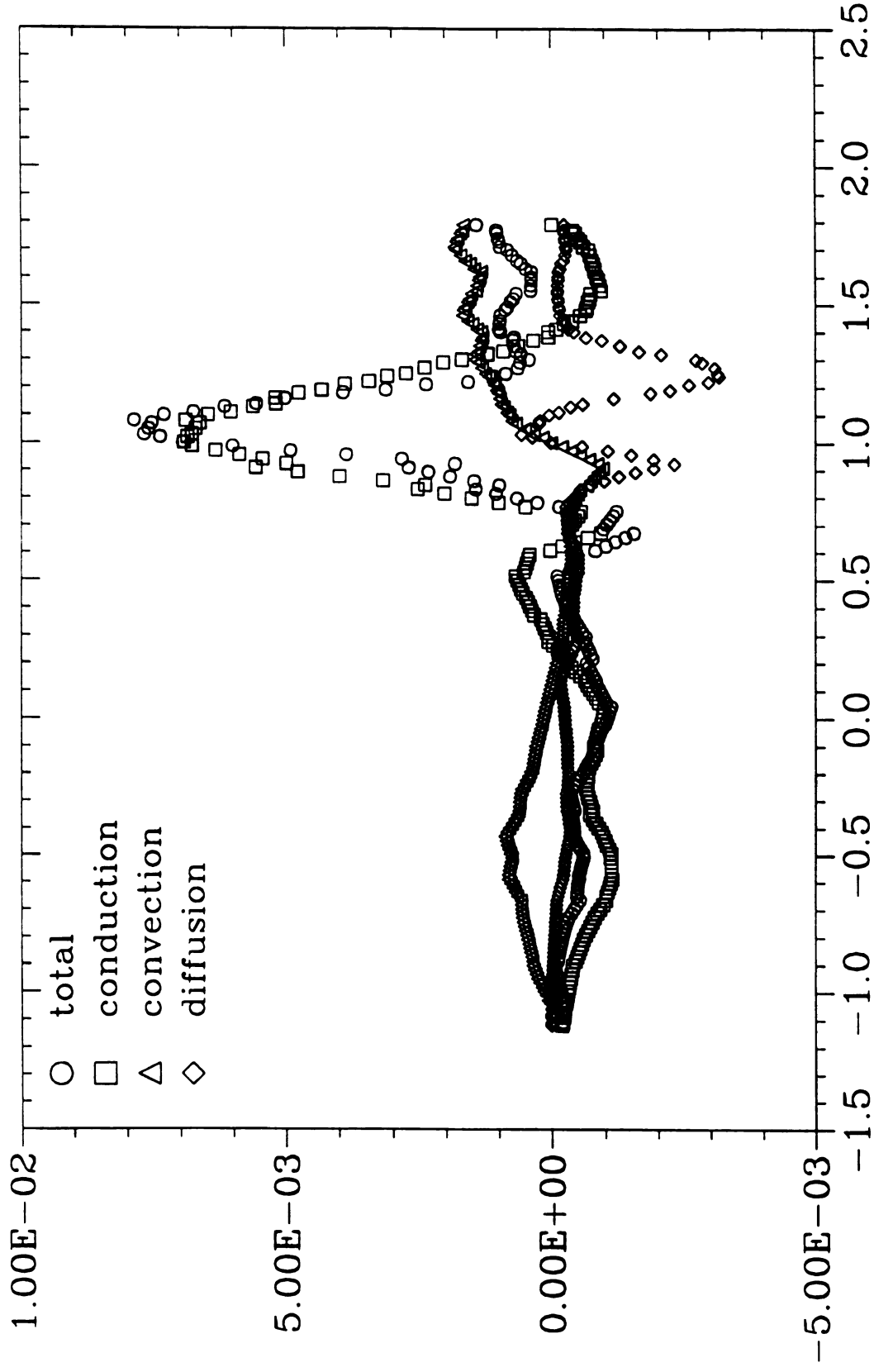

Figure D-17 Comparison of heat release rates by mass diffusion, by convection, and by thermal conduction in axisymmetric counterflow diffusion flames. (BA-flame)

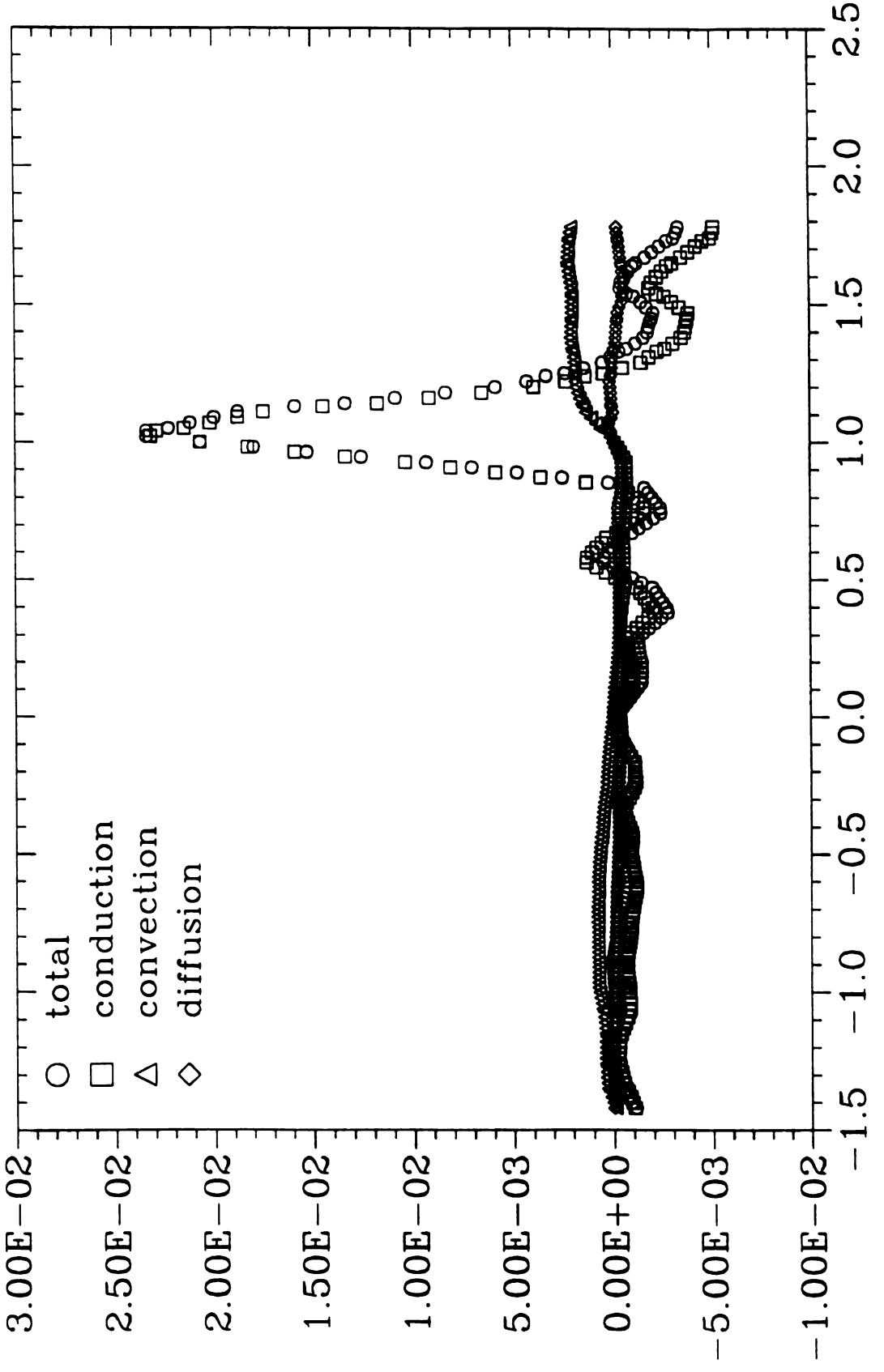

Figure D-18 Comparison of heat release rates by mass diffusion, by convection, and by thermal conduction in axisymmetric counterflow diffusion flames. (IA-flame)

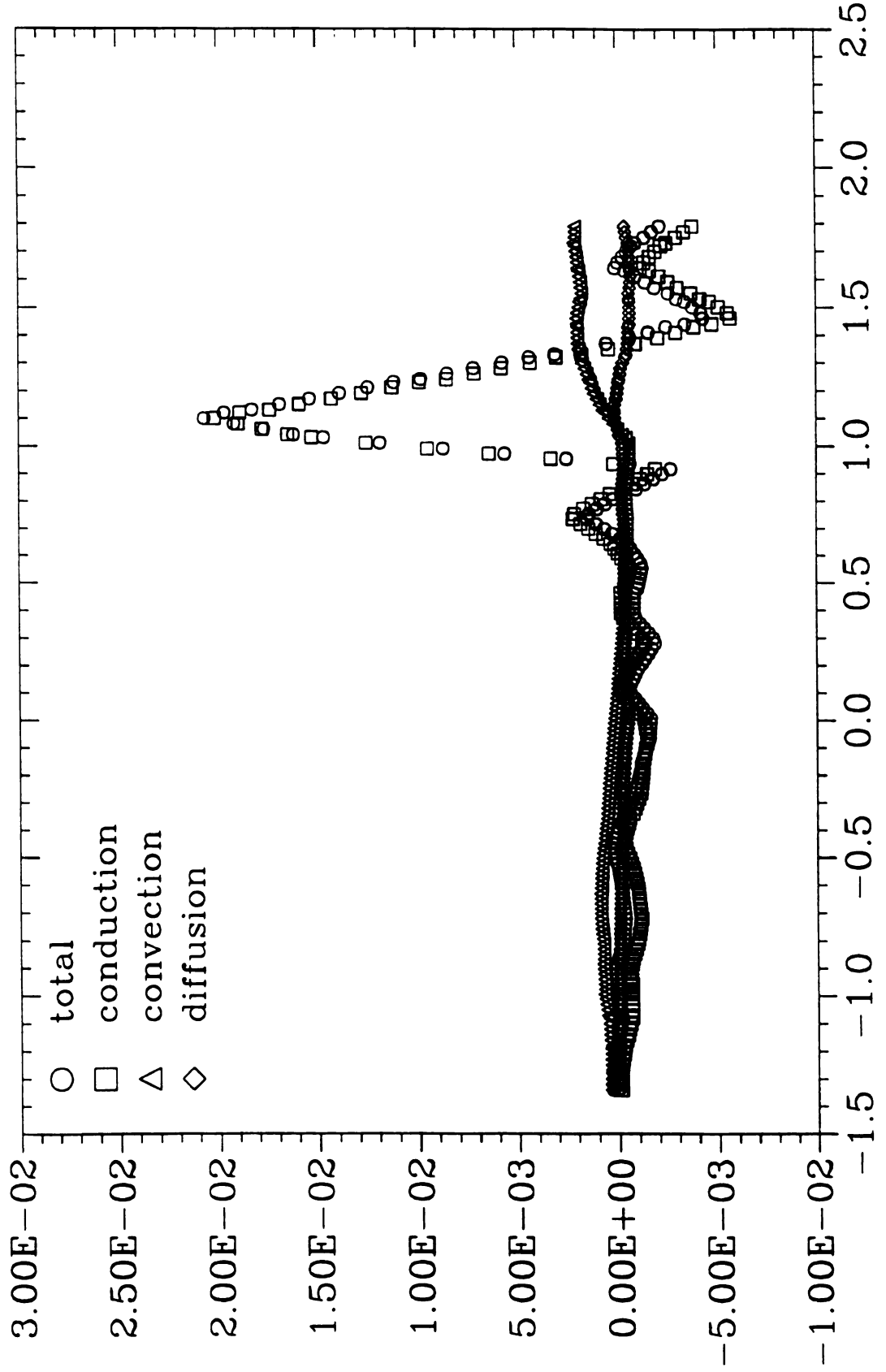

Figure D-19 Comparison of heat release rates by mass diffusion, by convection, and by thermal conduction in axisymmetric counterflow diffusion flames. (MA-flame)

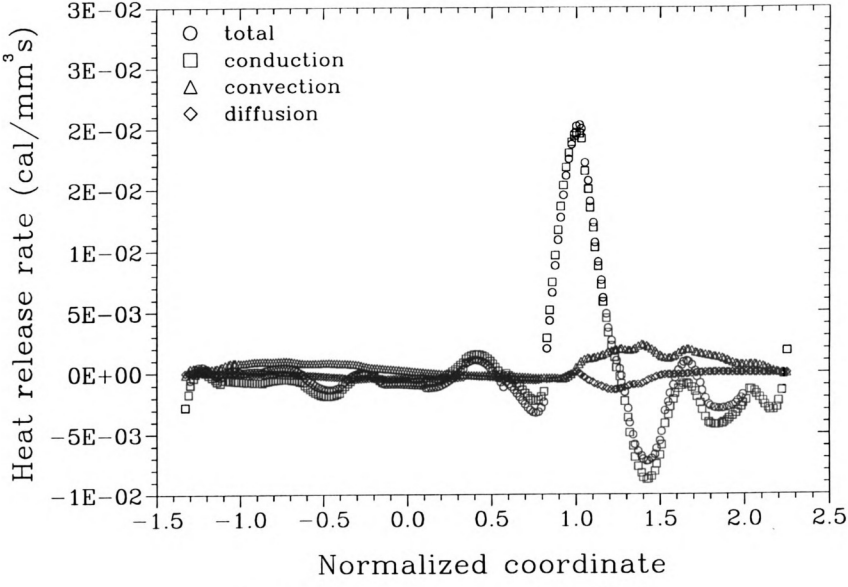

Figure D-20 Comparison of heat release rates by mass diffusion, by convection, and by thermal conduction in axisymmetric counterflow diffusion flames. (WAF-flame)

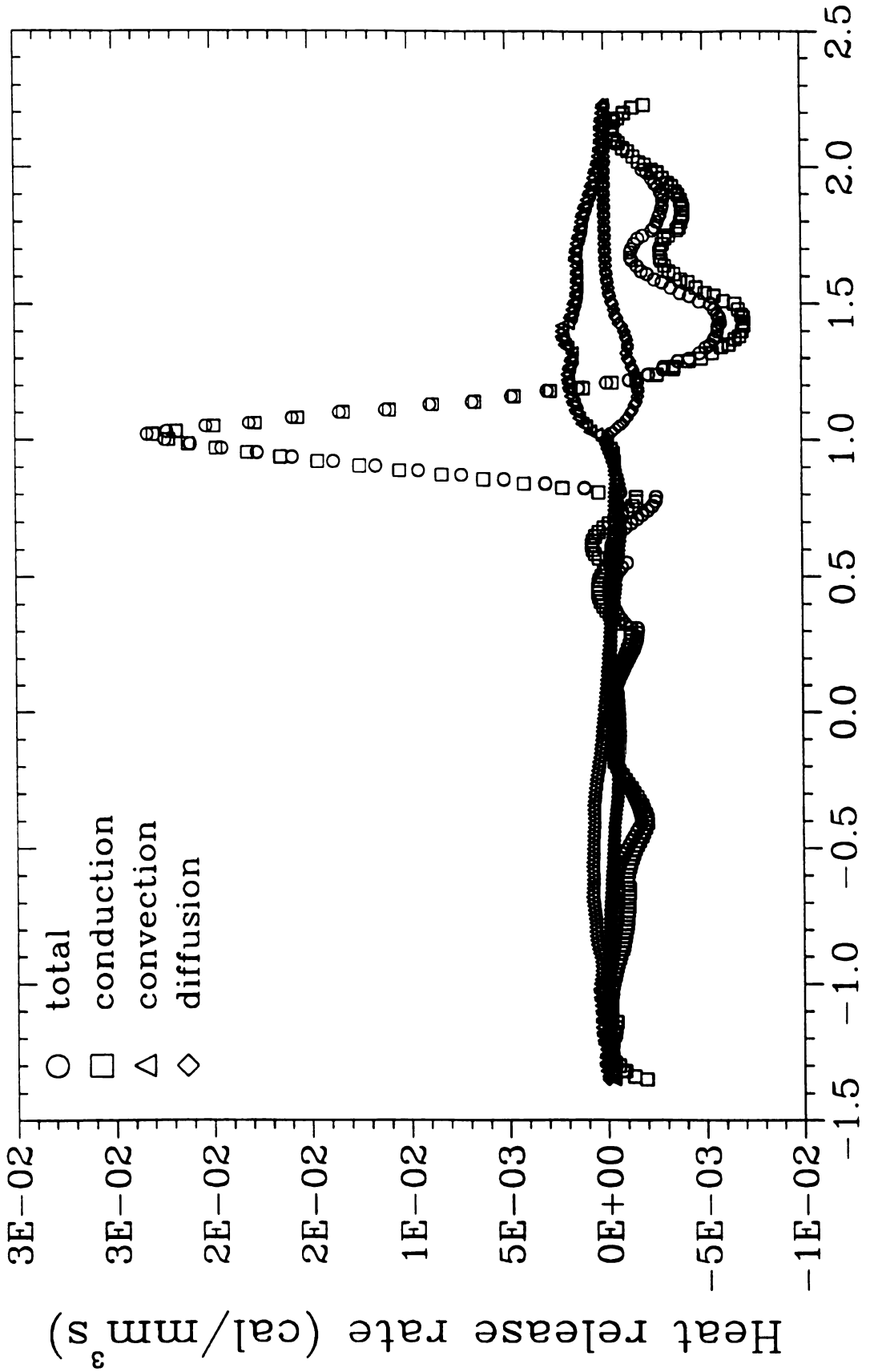

Figure D-21 Comparison of heat release rates by mass diffusion, by convection, and by thermal conduction in axisymmetric counterflow diffusion flames. (WAO-flame)

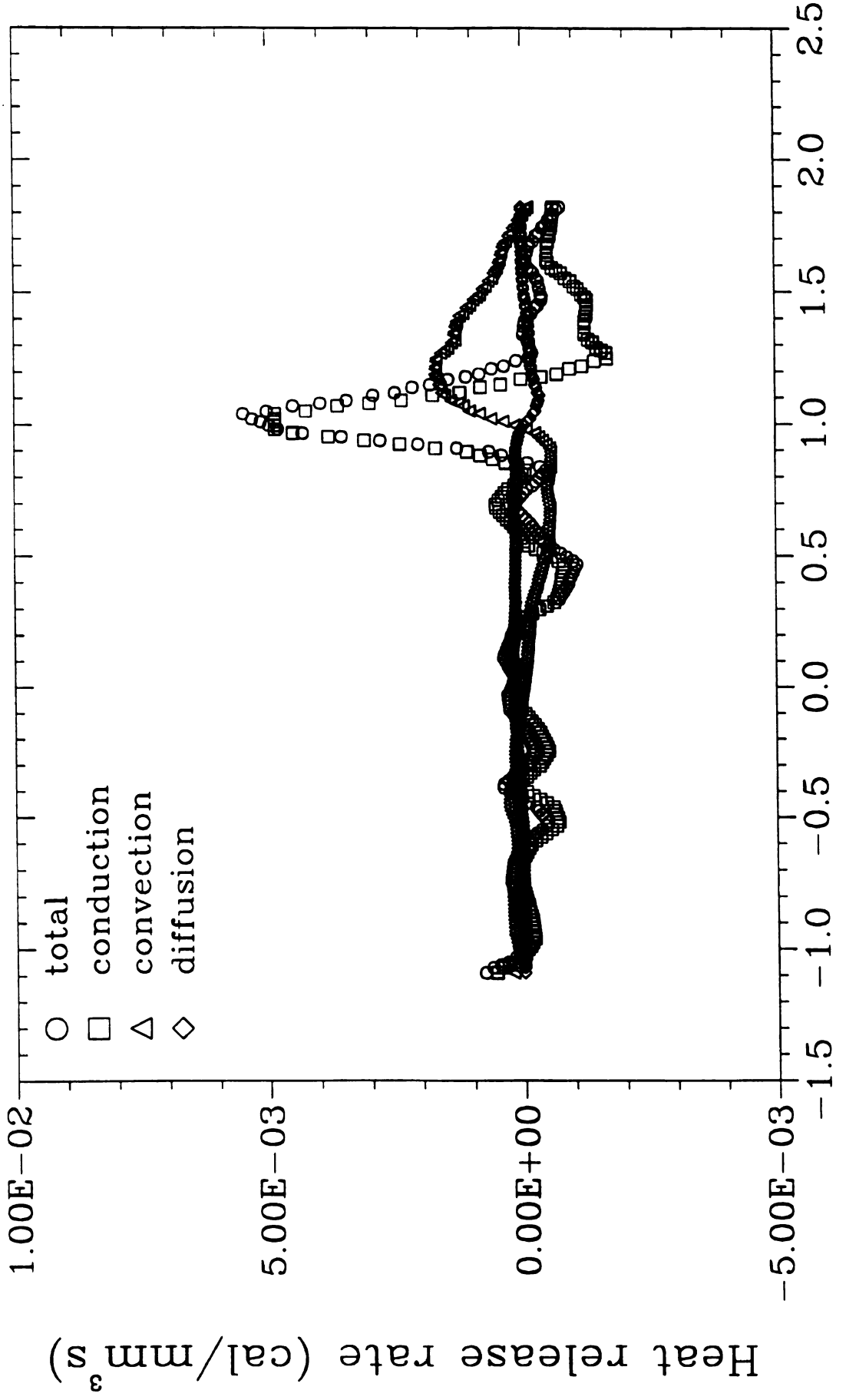

Figure D-22 Comparison of heat release rates by mass diffusion, by convection, and by thermal conduction in axisymmetric counterflow diffusion flames. (BB-flame)

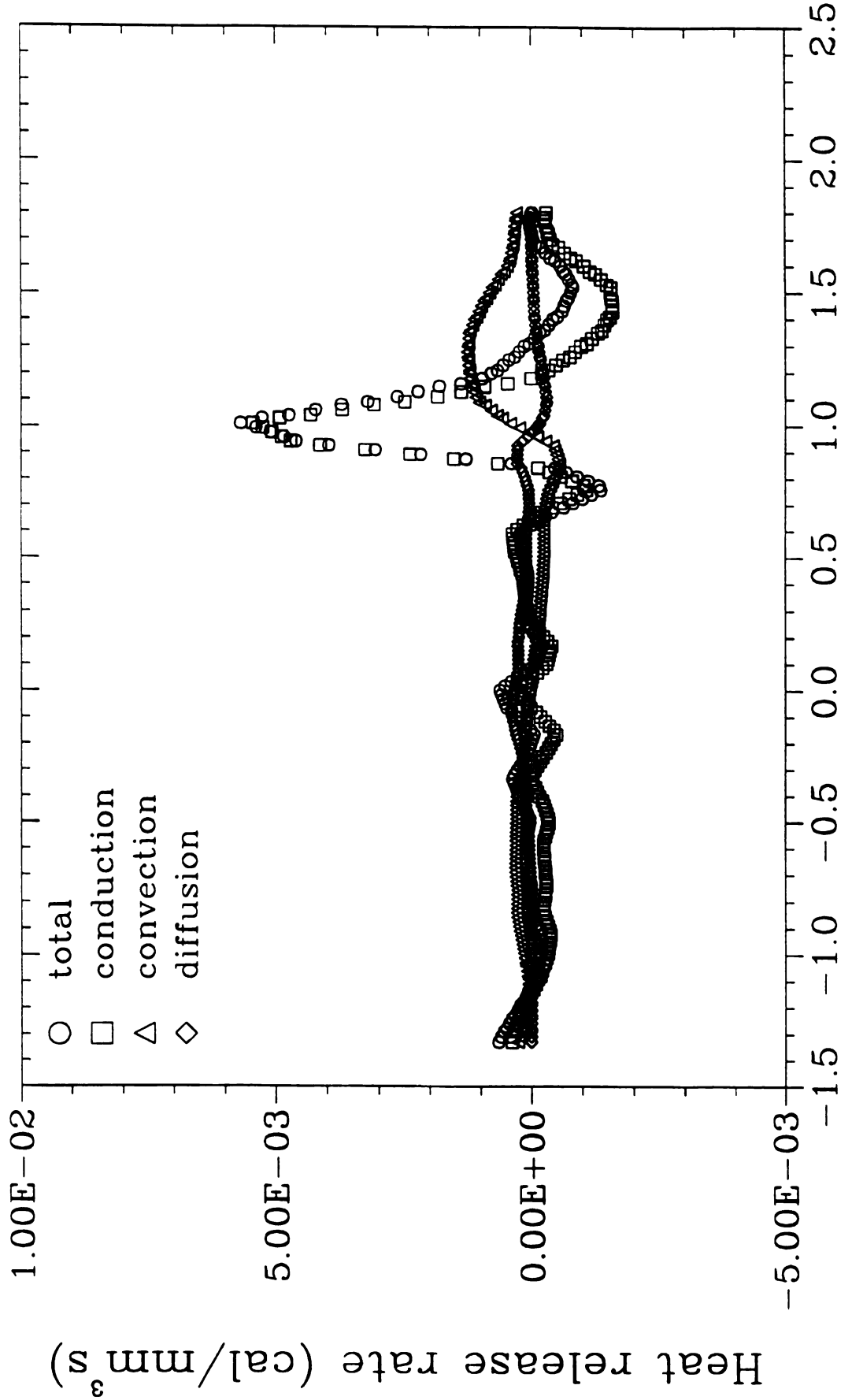

Figure D-23 Comparison of heat release rates by mass diffusion, by convection, and by thermal conduction in axisymmetric counterflow diffusion flames. (IBO-flame)

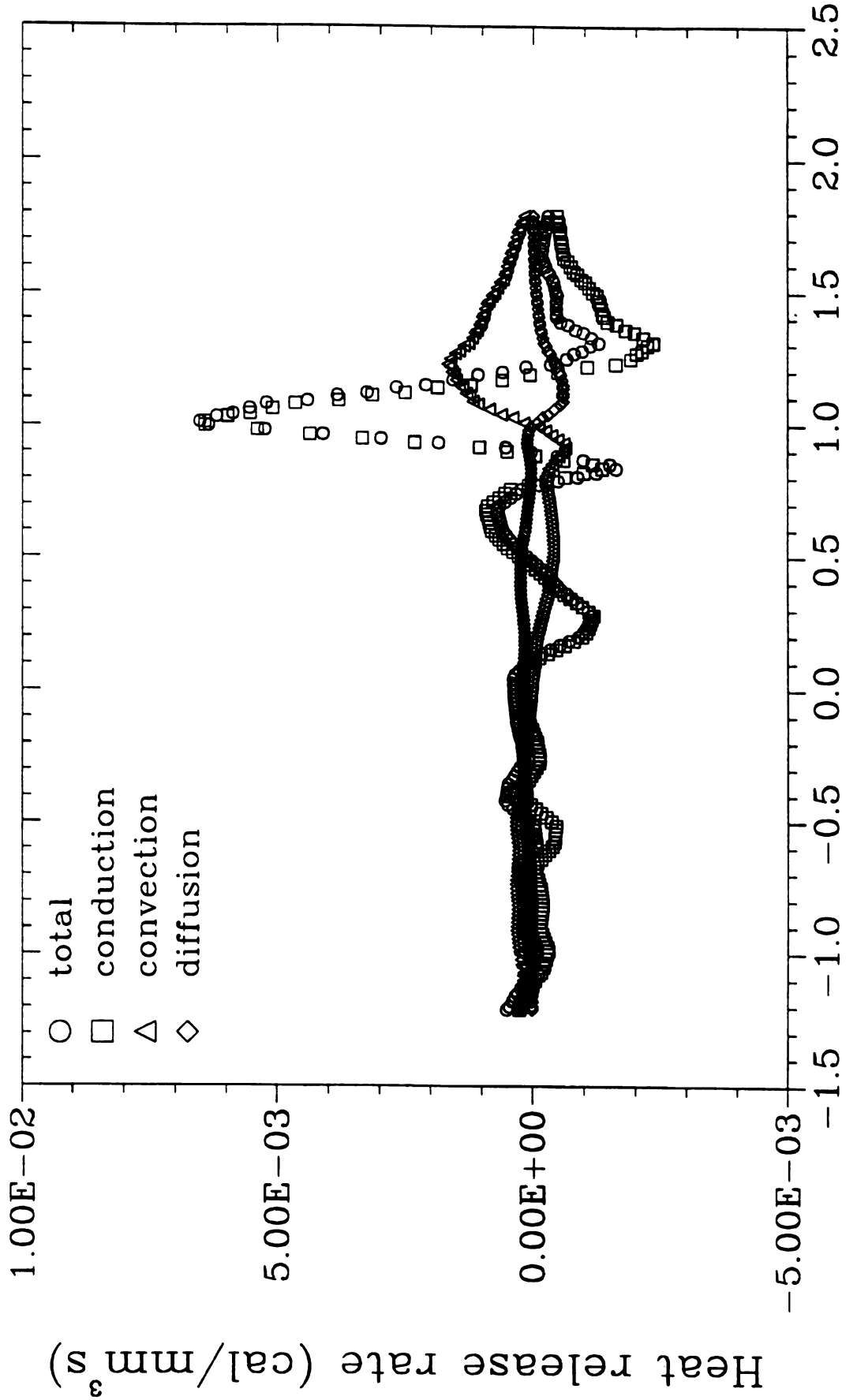

Figure D-24 Comparison of heat release rates by mass diffusion, by convection, and by thermal conduction in axisymmetric counterflow diffusion flames. (MBF-flame)

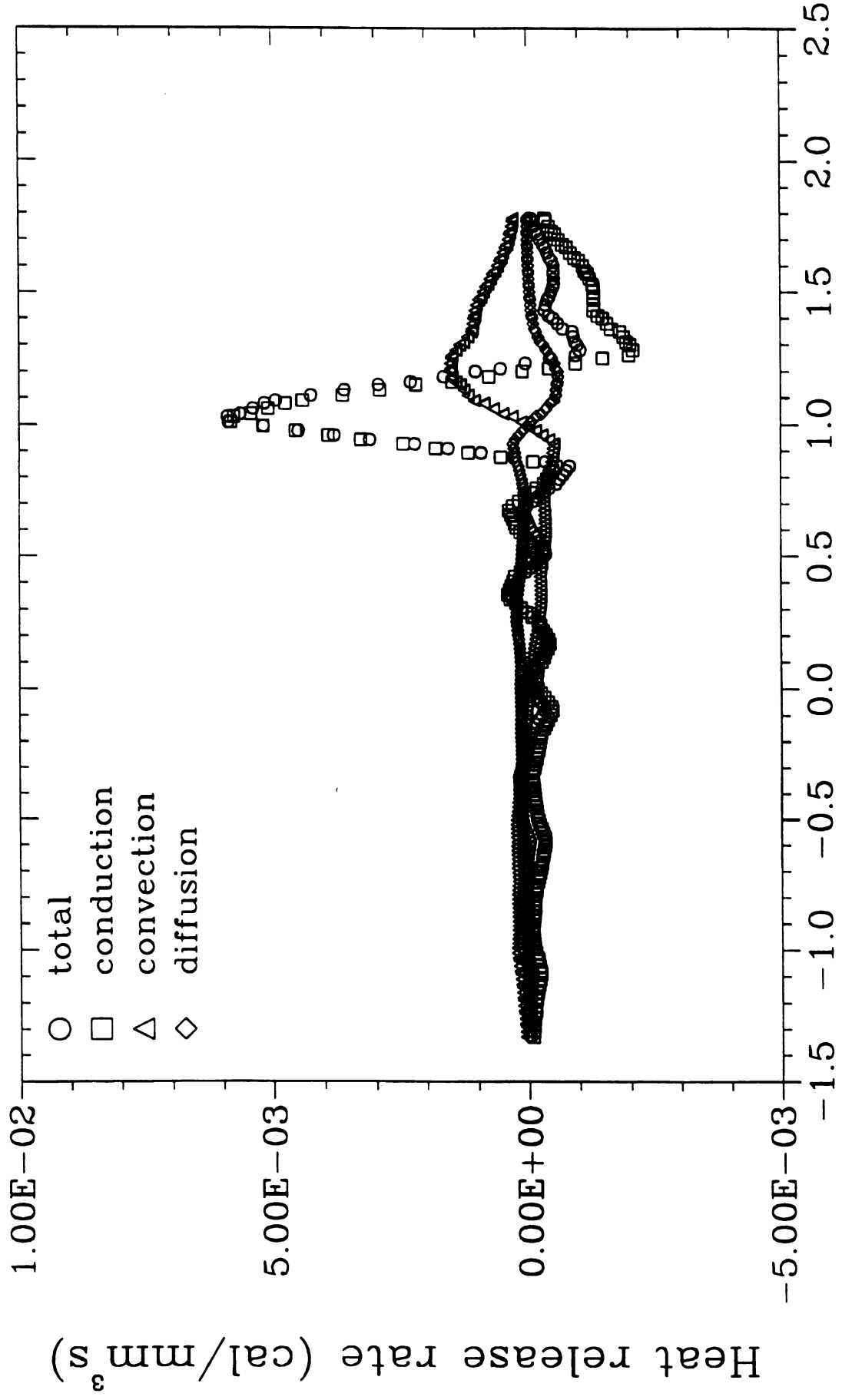

Figure D-25 Comparison of heat release rates by mass diffusion, by convection, and by thermal conduction in axisymmetric counterflow diffusion flames. (MBO-flame)

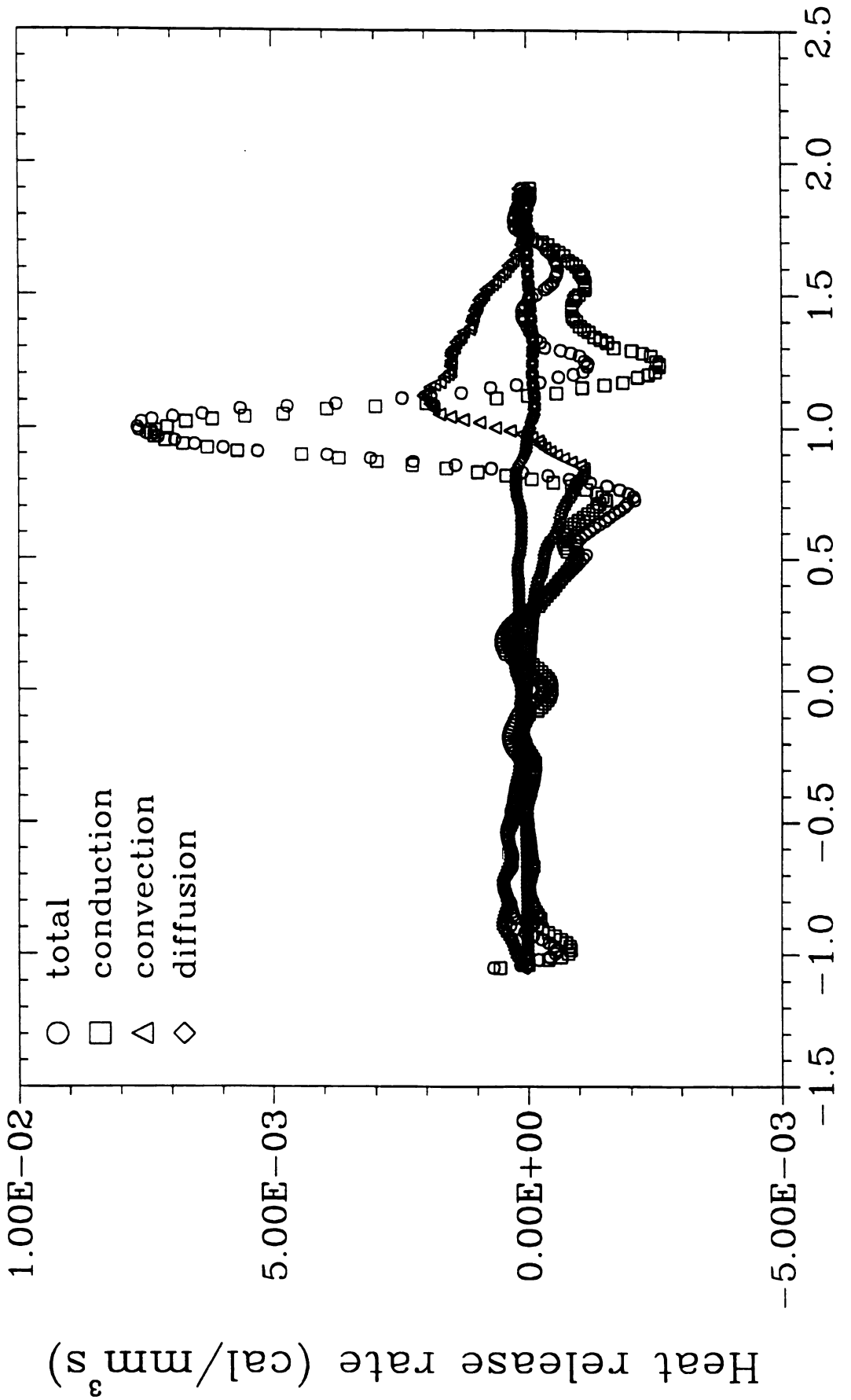

Figure D-26 Comparison of heat release rates by mass diffusion, by convection, and by thermal conduction in axisymmetric counterflow diffusion flames. (BC-flame)

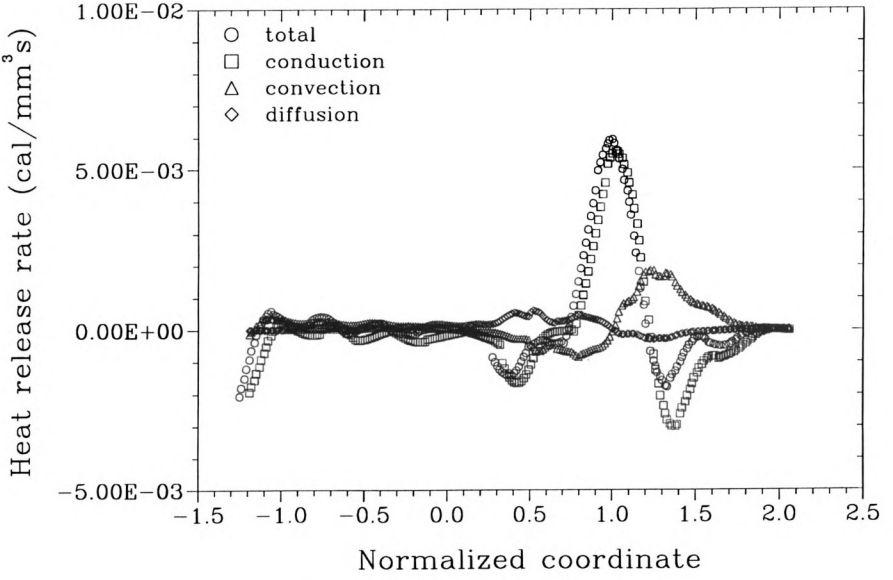

Figure D-27 Comparison of heat release rates by mass diffusion, by convection, and by thermal conduction in axisymmetric counterflow diffusion flames. (MCF-flame)

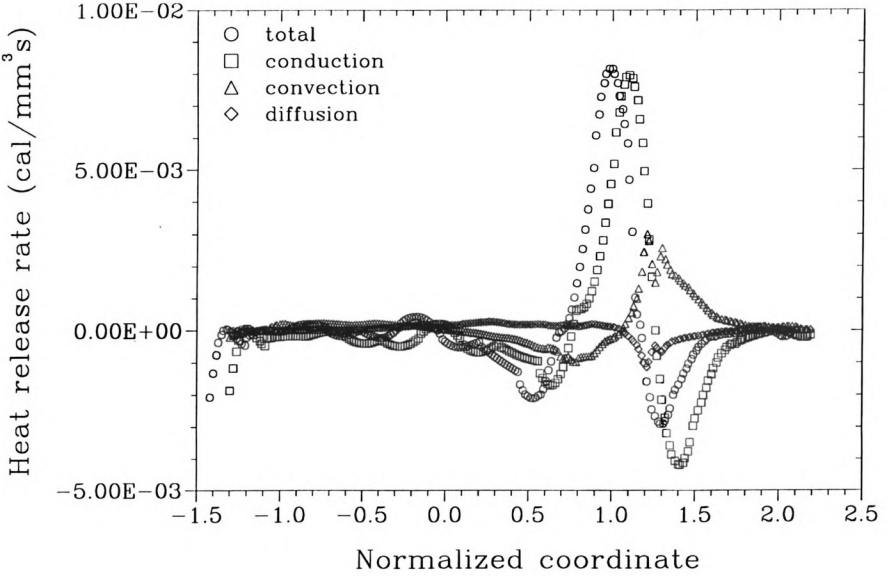

Figure D-28 Comparison of heat release rates by mass diffusion, by convection, and by thermal conduction in axisymmetric counterflow diffusion flames. (WCF-flame)

LIST OF REFERENCES

LIST OF REFERENCES

Anderson, D. A., Tannahil, J. C., & Pletcher, R. H. (1984). Computational fluid mechanics and heat transfer. New York: McGrow-Hill.

Andreussi, P., Borbieri, B. & Petarca, L. (1986). Boundary layer burning of fuel surfaces: The soot field. Combustion Science and Technology, 49, 123-141.

Ang, J. A., Pagni, P. J., Mataga, T. G., Margle, J. M, & Lyons, V. J., (1988, March). Temperature and velocity profiles in sooting free convection diffusion flames. AIAA Journal, 26(3), pp. 323-329.

Atreya, A., Lee, K. C., & Foss, J. F. (1987). Design of a counterflow diffusion flame burner for soot formation studies. Technical Meeting of Central States Section, The Combustion Institute.

Axelbaum, P. L., Flower, W. L.,& Law C. K. (1989, April). Dilution and temperature effects on soot formation in the co-flow flame. Technical Meeting of Eastern Section, The Combustion Institute.

Axelbaum, R. L., Law, C. K., & Flower, W.L..(1988). Preferential diffusion and concentration in sooting counterflow diffusion flame. Twenty-second Symposium (International) on Combustion, The Combustion Institute, pp.

Bertrand, C., & Delfau, J. L., (1985). Mechanism of soot formation in hydrocarbon flames. Combustion Science and Technology, 44, pp. 29

Bittner, J. D., Howard, J. B., & Palmer, R. B., (1982). Chemistry of intermediate species in the rich combustion of benzene soot , in Combustion systems and its toxic properties, edited by Lahaye, J., & Prado, G., Plenum Press. pp. 423.

Burke, S. P. & Schumann, T. E. W. (1928, October). Diffusion flames, Industrial and Engineering Chemistry, 20(10), 998 - 1004.

Calcote, H. F. (1981). Combustion and Flame, 42, p. 215.

Calcote, H.F. (1983). Ionic mechanism of soot formation, in Soot in combustion system and its toxic properties edited by J. Lahye and G. Prado, pp. 197 - 215, Plenum publishing Corporation.

Carrier, G. F., Fendell, F. E., & Marble, F. E. (1975, March). The effect of strain rate on diffusion flames. SIAM. Journal of Applied Mathematics, 28(2), pp.463-500.

Charalampupolos, T. T. & Felske, J. D. (1987). Refractive indices of soot particles deduced from *in-situ* laser light scattering measurements. Combustion and Flame, 68, pp. 283-294.

Chowdhury, D. P., Sorensen, C. M., Taylor, T. W., Merklin, J. F., & Lester, T. W. (1984, November). Application of photon correlation spectroscopy to flowing browian motion systems. Applied Optics, 23(22).

Coe, D. S., Haynes, B. S., & Steinfeld, J. I., (1981). Identification of a source of Argon-Ion-Laser exited Fluorescence in sooting flames. Brief communication, Combustion and Flame, 43, pp. 211-214.

Cristten, B. D. & Long, R., (1973). Formation of polycyclic aromatic in rich, premixed acetylene and ethylene flames. Combustion and Flame, 20, pp. 359-368.

Dalzell, W.H., & Sarofim, A.F. (1969, Feburuary). Optical constants of soot and their application to heat-flux calculations. J. of Heat Transfer, Transaction of the ASME, pp. 100 - 104.

Dearden, P., & Long, R. (1968). Soot formation in ethylene and propane diffusion flames. J. Applied Chemistry, 18, pp. 243.

de Zeeum, J., de Nijs, R. C. M., & Henrich, L. T. (1987). Adsorption chromatography on PLOT (Porous-Layer Open-Tubular) columns: A new look at the future of capillary GC., J. Chromatographic Science, 25, pp.71-83.

Eisner, A. D., & Rosner, D. E., (1985). Experimental studies of soot particle thermophoresis in nonisothermal combustion gases using thermocouple response technique. Combustion and Flame, 42. pp. 111-113.

Espenscheid, W.F., Kerker, M., & Matijevic, E. (1964). Logarithmic distribution functions for colloidal particles. J. of Phys. Chem., 68(11), pp. 3093 - 3097.

Farrow, R. L., Lucht, R. P., Flower, W. L., & Palmer, R. E., (1984). Coherent Anti-Stokes Raman spectroscopy measurements of temperature and acetylene spectra in a sooting diffusion flame. Twentieth Symposium (International) on Combustion, The Combustion Institute. pp. 1307-1312.

Frenklach, M., Clary, D. W., Gardiner, W. C. Jr., & Stein, S. E. (1988). Effect of fuel structure on pathway to soot. Twenty-second Symposium (International) on Combustion, pp..

Freymuth, P., Bank, W., & Palmer, M. (1983, September 6-9). Use of Titanum Tetrachloride for visualization of accelerating flow around airfoils. Third International Symposium on Flow Visualization, Ann Arbor, U.S.A., pp. 800-803.

Fristrom, R. M. (1983). Comments on quenching mechanisms in the microprobe sampling. Brief Communications, Combustion and Flame, 50, pp. 219-242.

Fristrom, R. M., Prescott, R.., & Grunfelder, C., (1957). Flame zone studies III - Techniques for the determination of composition profile of flame fronts. Combustion and Flame, 1, pp. 102-113.

Fristrom, R. M., & Westenberg, A. A. (1965). Flame Structure, McGrow-Hill Publishers, New York.

Glassman, I., & Yaccarino, P. (1981). The temperature effect in sooting diffusion flames. Eighteenth Symposium (International) on Combustion, The Combustion Institute pp. 1175 - 1184.

Graham, S. C., & Homer, J. B., (1973). Coagulation of molten lead aerosols. Faraday Symposium Chem. Soc., 7, pp. 86.

Graham, S.C., & Robinson, A. (1976). J. Aerosol. Sci., 7, pp. 261-273

Hahn, W. A., & Wendt, J. O. L. (1981a). The flat laminar opposed jet diffusion flame: A novel tool for kinetic studies of trace species formation. Chem. Eng. Commun., 9, pp. 121-136.

Haynes, B.S., & Wagner, H.G. (1981). Soot formation. Pro. Energy Combust. Sci., 7, pp. 229 - 273.

Hidy, G. M., & Brock, J. R., (1970). The dynamics of aerocolloidal system. Pergamon Press, Oxford.

Homann, K. H., (1984). Formation of large molecules, particulate and ion in premixed hydrocarbons; Progress and unsolved questions. Tentieth Symposium (International) on Combustion, The Combustion Institute, pp. 857.

Jagoda, I. J., Prado, G., & Lahaye, J. (1980) An experimental investigation into soot formation and distribution in polymer diffusion flames. Combustion and Flames, 37, pp. 261

Jones, J. M., & Rosenfelder, J. L. J. (1972). A model for sooting in diffusion flames. Combustion and Flame, 19, pp. 427.

Kent, J. H., & Honnery, D. R., (1990). A soot formation rate map for a laminar ethylene diffusion flame. Combustion and Flame, 79, pp. 287-298.

Kent, J. H., & Wagner, H. Gg. (1984). Why do diffusion flames emit smoke? Combustion Science and Technology,41, pp 245-269.

Kerker, M., (1969). The scattering of light and other electromagnetic radiation. Academic Press, New York and London.

Kunugi, M., & Jinno, H., (1967). Determination of size and concentration of soot particles in diffusion flames by a light-scattering technique. Eleventh Symposium (International) on Combustion, The Combustion Institute. pp. 257-266.

Lai, F.S., Friedlander, S.K., Pich, S.K., & Hidy, G.M. (1972). J. Colloid and Interface Sci., 39, pp. 395 - 405.

Lhuissier, N., Gouesbet, G., & Weill, M. E., (1989). Extensive Measurements on soot particles in laminar premixed flames by quasi elastic light scattering spectroscopy. Combustion Science and Technology, 67, pp. 17-36.

Lilly, G. P., (1973). Effect of particle size on particle eddy diffusivity. Industrial and Engineering Chemical Fundamentals, 12(3), pp. 268-275.

Lin, T. H., & Sohrab, S. H. (1987). Influence of vorticity on counterflow diffusion flames. Combustion Science and Technology, 52, pp 75-90.

Liñán, A. (1974). The asymtotic structure of counterflow diffusion flames for large activation energies. Acta. Astronautica, 1, pp 1007-1039.

Loehrke, R. I., & Nagib, H. M.(1976, September). Control of free-stream turbulence by means of honeycombs: A balance between suppression and generation. J. of Fluid Engineering, Trans. ASME.

Lumley, J. L. (1964). J. of Basic Engineering, Trans. ASME, Series D, 86, p218, 1964

Lumley, J. L. (1967). J. of Basic Engineering, Trans. ASME, Series D, 89, p764, 1967

Mazumder, M. K., & Kirsch, K. J., (1975). Flow tracing fidelity of scattering aerosol in laser Doppler velocimetry,Applied Optics, 14 (4), pp. 894-901.

Melvin, A., Moss, J. B. & Clarke, J. F. (1971). Combustion Science and Technology. 4, pp 17 - 30.

Mie, G. (1908), Ann. Physik., 25, p. 377.

Millikan, R. C. (1961, May). Measurement of particle and gas temperatures in a slightly luminous premixed flame. Journal of the Optical Society of America, 51(3), pp 535-542.

Palmer, H. B. & Cullis, H. S. (1965). The chemistry and physics of carbon, 1, pp 265, Marcel Dekker, New York.

Peters, N. (1983). Combust. Sci. Tech., 30, p. 1.

Peters, N. (1984). Laminar diffusion flamelet models in non-premixed turbulent combustion. Progr. Energy Combust. Sci., 10, pp.319-339.

Prado, G., Garo, A., Ko, A, & Sarofim, A., (1984). Polycyclic aromatic hydrocarbons formation and destruction in a laminar diffusion flame. Twentieth Symposium (International) on Combustion, The Combustion Institute. pp. 959-996.

Puri, I. K., & Seshadri, K. (1987). The extinction of counterflow premixed flames burning diluted methane-air, and diluted propane-air mixtures. Short Communication, Combustion Science and Technology, 53, pp. 55-65.

Puri, I. K., Seshadri, K., Smook, M. D., & Keyes, D. E., (1987). A comparison between numerical calculation and experimental measurements of the structure of a counterflow methane-air diffusion flame. Combustion Science and Technology, 56. pp. 1-22.

Regan, C. A., Chun, K. S., & Shock, H. J. Jr. (1987). Engine flow visualization using a copper laser, SPIE, 737, pp. 17-27

Roertgen, H. G. & Boltendahl, U.(1975). Second European Symposium on Combustion, The European Section of the Combustion Institute, Orleans. pp 781 -786.

Roper, F. G., (1984). Soot escape from diffusion flames: A comparison of recent work in this field. Short communication, Combustion Science and Technology, 40, pp.323.

Rudder, R. R., & Bach, D. R., (1968, September). Rayleigh scattering of ruby-laser light by neutral gases. J. of the Optical Society of America, 58(9), pp. 1260-1266.

Saito, K., Williams, F. A., & Gordon, A. S. (1986a,). A study of the two-color zone for small hydrogen diffusion flames. Combustion Science and Technology, 51, pp. 285.

Saito, K., Williams, F. A., & Gordon, A. S. (1986b). Effect of oxygen on soot formation in methane diffusion flames. Combustion Science and Technology, 47, pp. 117.

Saito, K., Williams, F. A., & Gordon, A. S. (1986c, August). Structure of laminar coflow methane-air diffusion flames. Transactions of the ASME, 108.

Santoro, R. J., Semerjian, H. G., (1984). Soot formation in diffusion flames: Flow rate, fuel species and temperature effects. Twentieth Symposium (International) on Combustion. The Combustion Institute. pp. 997.

Santoro, R. J., Semerjian, H. G., & Dobbins ,R. A. (1983a, June 1-3). Interpretation of optical measurements of soot in flames. AIAA-83-1516, AIAA 18th Thermophysics Conference, Montreal, Canada.

Santoro, R. J., Semerjian, H. G., & Dobbins, R. A. (1983b). Soot particle measurements in diffusion flames. Combustion and Flame, 51, pp. 203-218.

Santoro, R. J., Yeh, T. T., Horvath, J. J., & Semerjian, H. G., (1987). The transport and growth of soot particles in laminar diffusion flames. Combustion Science and Technology, 53, pp.89.

Schug, K. P. Manheimer-Timnat, Y., Yaccarino, P., & Glassman, I. (1980). Sooting behavior of gaseous hydrocarbon diffusion flames and the influence of additives. Combustion Science and Technology, 22, pp. 235.

Siegel, R.,& Howell, J. R., (1981). Thermal radiation heat transfer, second edition, McGraw-Hill Book Company, New York.

Smith, O. I., (1981). Probe-Induced distortions in the sampling of one-dimensional flames. Combustion and Flame, 40, pp. 187-199.

Smith, S. R. & Gordon, A. S. (1956). J. Phys. Chem., 60, pp 759 - 763.

Smook, M. D., Seshadri, K., & Puri, I. K., (1988). The structure and extinction of partially premixed flames burning methane in air. Combustion and Flame, 73, pp. 45-68.

Smyth, K. C., & Miller, J. H. (1986). Soot inception in hydrocarbon diffusion flames. Chemical and Physical Process in Combustion, Eastern Section of the Combustion Institute, Fall Technical meeting, San Juan, Puerto Rico.

Smyth, K. C., & Miller, J. H. (1987). Science, 236, pp 1540 - 1546.

Smyth, K. C., Mille, J. H., Dorfman, R. C., Mallard, W. G., & Sanmtoro, R. J. (1985). Soot inception in a methane/air diffusion flame as characterized by detailed species profiles. Combustion and Flame, 62, pp 157-181.

Spalding, D. B. (1961). ARS Journal, 31, p 763.

Thompson, J. F., Warsi, Z. U. A., & Mastin, C. W. (1982). Boundary-Fitted coordinate system for numerical solution of partial differential equations - A Review. J. of Computational Physics, 47, pp 1-108.

Thompson, J. F., Thomas, F. C., & Mastin, C. W. (1974). Automatic numerical generation of body-fitted curvillinear coordinate system for field containing any number of arbitrary two-dimensional bodies. J. of Computational Physics, 15, pp 299-319.

Tien, J. H., & Sohrab, S. H., (1990). Effect of air-side oxygen addition on soot formation in methane coflow diffusion flame. Combustion Science and Technology, 73, pp. 617.

Tsuji, H. (1982). Counterflow diffusion flames. Prog. Energy Combust. Sci., 8, pp. 93-119.

Van de Hulst, H. C., (1957). Light scattering by small particles. John Wiley & Sons, Inc., N.Y.

Vandsburger, U., Kennedy, I. M., and Glassman, I. (1984). Sooting counterflow diffusion flames with varying velocity gradients. Twentieth Symposium (International) on Combustion, The Combustion Institute. pp. 1105.

Wall, T. F., Lowe, A., Wibberley, L. J., Mai-Viet, T., & Gupta, R. P. (1981). Fly ash characteristics and radiative heat transfer in pulverized-coal-fired furnaces. Combustion Science and Technology, 26, pp. 107-121.

Way, C., Powell, E. A., & Jagoda, J. I., (1984). The effect on the soot formation of oxigen in the full of a diffusion flame, Twentieth Symposium (International) on Combustion, The Combustion Institute. pp. 1017-1024.

Weiner, A. M. & Harris, S. J. (1989). Optical detection of large soot precursors. Combust.and Flame, 77, pp 261-266.

Weiner, A. M, & Harris, S. J. (1988). Optical detection of large soot precursors. Twenty-second Symposium (International) on Combustion, The Combustion Institute. pp.5

Westenburg, A. A., Raezer, S. D., & Fristrom, R. M., (1957). Interpretation of the sample taken by a probe in a laminar concentration gradient, Combustion and Flame, 1, pp. 467-478.

Williams, F. A. (1975). Turbulent mixing in non-reactive and reactive flows. ed. Murphy, S. N. B., p189, Plenum.

Wolfhard, H. D. & Parker, W. G (1949). Proc. Phys. Soc., Lodan, A62, pp 722 - 730.

Wright, F. J., (1974). Effect of oxygen on the carbon-forming tendencies of diffusion flames. Fuel, 53, pp. 232.